Étude numérique et analyse physique du morphing électroactif pour des ailes et des profils hydrodynamiques à des écoulements turbulents à nombre de Reynolds élevé

Nikolaos Simiriotis

THÈSE

En vue de l'obtention du

DOCTORAT DE L'UNIVERSITÉ DE TOULOUSE

Délivré par :

Institut National Polytechnique de Toulouse (Toulouse INP)

Discipline ou spécialité :

Dynamique des fluides

Présentée et soutenue par :

M. NIKOLAOS SIMIRIOTIS

le jeudi 4 juin 2020

Titre :

Numerical study and physical analysis of electroactive morphing wings and hydrodynamic profiles at high Reynolds number turbulent flows

---

Ecole doctorale :

Mécanique, Energétique, Génie civil, Procédés (MEGeP)

Unité de recherche :

Institut de Mécanique des Fluides de Toulouse (IMFT)

Directeur(s) de Thèse :

MME MARIANNA BRAZA

M. GILLES HARRAN

Rapporteurs :

M. FRANK THIELE, TECHNISCHE UNIVERSITAT BERLIN

M. PAWEL FLASZINSKI, POLISH ACADEMY OF SCIENCES GDANSK

Membre(s) du jury :

M. JEAN-PAUL BONNET, ENSMA POITIERS, Président

M. DAMIEN SZUBERT, DGA, Membre

M. DENIS DESCHEEMAEKER, IRT SAINT-EXUPERY, Membre

M. JEAN FRANCOIS ROUCHON, TOULOUSE INP, Membre

Mme MARIANNA BRAZA, TOULOUSE INP, Membre

M. MICHEL TRINITE, UNIVERSITE DE ROUEN, Membre

Nikolaos Simiriotis

Numerical study and physical analysis of electroactive morphing wings and hydrodynamic profiles at high Reynolds number turbulent flows

Toulouse, 2020

To my friends and family.

Acknowledgements

The work presented here has been conducted in the research group ASI of the Institut de Mécanique des Fluides de Toulouse, and as a result, I was fortunate to profit from the whole group's experience, help and support throughout the years of this thesis.

First of all, I would like to thank DGA for offering this scholarship that provided the necessary funding for this research to take place. I would like to express my gratitude to all the members of the jury for accepting to review this work and participating in the defence. I am very thankful to Prof. Frank Thiele and Prof. Pawel Flasynski for examining this thesis in great detail and for writing exhaustive reports on this manuscript, and thereby contributing to the improvement of the work. I would like to express my sincere gratitude to Dr. Damien Szubert for participating in the commitee and closely following my work during these years.

Foremost, I would like to thank my supervisor Dr. Marianna Braza who welcomed me to her research group and provided me with support, knowledge and guidance. Her advice and vision kept me inspired and motivated throughout the thesis. Same goes for Dr. Gilles Harran, who, as a co-director of the thesis, was always available and supportive. I would also like to thank Prof. Michalis Fragiadakis, Prof. Yannick Hoarau and Prof. Jean-François Rouchon as they all greatly assisted and contributed the work presented here.

Special thanks goes to my collegues and all the SMS partners, all of whom are great researchers that deeply influenced the outcomes of this work through collaboration, long discussion and meetings. Finally, I would like to thank my family for supporting every step I take and all of my friends for being there throughout this journey.

Abstract

The present thesis investigates the effects of electroactive morphing for smart wing designs. Morphing concepts are adopted for future aircraft configurations, targeting increased aerodynamic performance, "greener" air vehicles and efficient air transport. Morphing airfoils and wings are investigated by means of numerical simulation and the physical mechanisms of morphing are analyzed.

The hybrid, partly bio-inspired electroactive morphing is examined. The hybrid concept entails the combination of different classes of electroactive actuators that yield turbulence modifications at multiple scales when realized simultaneously. Shape Memory Alloys (SMA) providing large-amplitude low-frequency deformations and piezoactuators providing low strains at higher frequency are introduced. High Reynolds number calculations around supercritical wings in low-subsonic and transonic regimes are performed and experimental results are employed for a detailed physical analysis. The flow simulations are carried out using the NSMB (Navier Stokes MultiBlock) solver and efficient turbulence modelling approaches, allowing for a physically correct development of related instabilities and coherent structures.

In this context, the Organized Eddy Simulation (OES) approach has been improved to account for upscale energy transfers in strongly sheared flow regions through re-injection of turbulence. This novel approach, based on stochastic forcing of the turbulence transport equations, is extended in the present thesis to three-dimensional flows and applied to the study of the transonic flow. The approach is also examined in the context of Detached Eddy Simulations (DES). The stochastic forcing is proven to inhibit excessive turbulence diffusion effects. As a result, the transonic buffet and the Shock Wave Boundary Layer Interaction (SWBLI) are better captured with this approach. An increase of lift and a decrease of drag are obtained and the force predictions are improved as shown through comparisons with experimental results.

The stochastic forcing effects can be practically realized with the introduction of higher-frequency vibrations and low-amplitude deformations in the near trailing edge region of wings via piezoactuators. The morphing effects are examined on an A320 wing at a Reynolds number of 1 Million in the low-subsonic regime, corresponding to take-off/landing flight phases. The simulations used the OES approach and the analysis employed a large experimental database, obtained in

the context of the “Smart Moprhing and Sensing for Aeronautical configurations” (SMS) H2020 No 723402 European Research program. It is shown that electroactive morphing has the capacity to enhance the aerodynamic performance through lift increase and drag reduction. The aerodynamic enhancement is obtained as a result of the manipulation of turbulence interfacial dynamics interacting with the structure of the wing. Through an extensive parametric study, optimal frequency-amplitude combinations have been determined, able to increase the lift-to-drag ratio.

Furthermore, the present thesis discusses shape control with the use of SMA, introduced to morphing structures inspired by the wings of large-span hunting birds. SMA-based actuators are employed to produce large continuous deformation at low frequencies (order of Hz), adapting the aerodynamic profiles to different flight conditions. The thesis proposes an efficient methodology that allows design smart deformable aeronautical structures, able to achieve pre-defined target shapes. A novel robust algorithm for predicting the nonlinear response of the SMA-structure interaction problem has been developed and validated. The solver is coupled with a method that predicts the optimal structural and operational design parameters to produces safe and “green” morphing structures.

Résumé

La présente thèse étudie par simulation numérique et analyse physique les effets du morphing électroactif pour le design des ailes du futur permettant de réduire l'impact environnemental et d'accroître l'efficacité du transport aérien. La thèse examine les effets du morphing électroactif hybride. Ce concept consiste en une association de diverses classes d'actionneurs électroactifs opérant à des échelles de temps et de longueur multiples, en accord avec la dynamique du spectre turbulent et dans un contexte de bio-inspiration concernant l'actionnement des ailes, ailerons et plumes de grands oiseaux prédateurs. Le morphing électroactif hybride crée des modifications de la turbulence à de multiples échelles dans les zones cisaillées et le sillage proche et crée l'augmentation des performances aérodynamiques par l'action de mécanismes de rétroaction.

La thèse effectue des simulations numériques à nombre de Reynolds élevé autour de configurations de profils d'aile et d'ailes d'avion supercritiques dans les régimes du bas subsonique correspondant aux phases du décollage et atterrissage, et transsonique correspondant au vol de croisière. Toutes les simulations sont effectuées par le code NSMB (Navier Stokes MultiBlock), en utilisant des approches de modélisation de la turbulence efficaces, permettant de prédire en accord avec les expériences physiques, le développement d'instabilités et de structures cohérentes gouvernant la dynamique des écoulements.

Dans ce contexte, l'approche « Organized Eddy Simulation » (OES) a été employée et améliorée par des concepts de cascade inverse utilisant de la réinjection de la turbulence dans les zones fortement cisaillées. Cette méthode, basée sur un forçage stochastique des équations de transport turbulent a été étendue dans la présente thèse aux trois dimensions et ses bénéfices ont été quantifiés concernant l'évaluation des efforts aérodynamiques et le développement d'instabilités fluide. Les avantages de cette approche, qui a été introduite par ailleurs au sein de la « Detached Eddy Simulation », ont été étudiés concernant la prédiction du tremblement en régime transsonique et de l'interaction choc-couche limite.

Les régimes du bas subsonique concernent les écoulements autour de profils et d'ailes de type A320 en configurations statiques et en morphing et sont étudiés en utilisant l'approche de modélisation OES également. Le morphing de la région proche du bord de fuite à l'aide de faibles déformations et de vibrations de fréquences dans le rang de 100-400 Hz a été étudié en synergie avec des résultats

expérimentaux du projet Européen H2020 N° 723402 SMS : « Smart Moprhing and Sensing for Aeronautical configurations ». A l'aide d'une étude paramétrique détaillée, il a été mis en évidence que des combinaisons optimales de fréquence-amplitude de ces actionnements fournissent une augmentation drastique de la finesse aérodynamique. Ces effets ont été obtenus à l'aide de manipulation de la dynamique des interfaces « Turbulent - Non Turbulent » (TNT) et des interactions avec les interfaces « Turbulent-Turbulent » (TT).

De plus, cette thèse a développé un modèle structural efficace permettant le contrôle de forme par des Alliages à Mémoire de Forme (AMF). Ces actionneurs permettent d'obtenir de grandes déformations à de basses fréquences en appliquant une grande cambrure de l'aile pour augmenter la portance et pour adapter la forme de l'aile aux différentes sollicitations aérodynamiques. La présente thèse propose un modèle efficace pour obtenir des formes-ciblées de configurations aérodynamiques utilisant des AMF embarqués. Un nouvel algorithme robuste a été développé et validé pour prédire la réponse non-linéaire de l'interaction AMF-structure. Cet algorithme a été couplé avec une méthode de prédiction de la structure et des paramètres opérationnels optimaux pour le design, fournissant ainsi des architectures de morphing plus performantes et réduisant l'impact environnemental.

Contents

List of Figures

List of Tables

Chapter 1

State of the art

– Complicated problems have... smart solutions –

1.1 Morphing

The present thesis investigates the effects of electroactive morphing for smart wing design. Morphing concepts are adopted for future aircraft configurations, targeting increased aerodynamic performance, "greener" air vehicles and efficient air transport. In this thesis, morphing is defined as an efficient multi-point adaptability [MWH+02] with a possible dynamic adaptation in real-time. They idea of morphing is not new. A detailed historical review of morphing applications and recent developments is included in [CL18]. The wing was born as a flexible element, able to deform itself in order to adapt to the different flight stages. The first flying device constructed by Clément Ader and tested on 9 October 1890, was a bat-like design made of linen and wood. A later version of his flying machine, AVION[1] III, is shown in Fig. 1.1. However, as the operational velocities of the aircrafts increased, the wing became stiffer and these basic capabilities were abandoned. The major question arising: the *smart structure paradox* where any deformable structure should be designed to be flexible, but also able to sustain large external loads [CL18]. The available technologies in the previous years led to simpler solutions that abandoned the idea of morphing wings. Modern scientific developments, however, along with the leveling of the aircraft performance, have enabled to reconsider morphing as one of the main solutions that can be used to improve the capabilities of aeronautical configurations and bring the flexible wings back.

[1] "Appareil Volant Imitant Oiseau Naturel", Clément Ader introduced the term "AVION" (aircraft), coming from the latin word "avis" (bird)

When examining adaptive structural systems, special attention is devoted to the actuators utilized. An extensive overview of the morphing aircraft can be found in [BSFA+14] and a complete review of the historical evolution of the morphing wing technology in [CL18]. A first NASA report [Fer77] referenced morphing parts and concepts targeting the improvement of commercial aircraft performance. The Preliminary Design Department of Boeing later published a study [BHCS80] regarding the introduction of systems that would vary the wing camber smoothly and continuously in order to optimize the performance for civil aircrafts. This study examined the design, the aerodynamic gains and the possibility of integrating systems that would "morph" parts of the wing during selected flight phases, in addition to the already existing high-lift configurations i.e. slats and flaps. A first direct link with the expected benefits that innovative morphing systems can have, from an industrial point of view, is given in [SH88]. The study focused on advances concerning transonic variable camber airfoils, shock-boundary layer control, laminarization techniques and new propulsion systems targeting a novel passenger plane.

Figure 1.1: *Clément Ader's AVION III displayed at the Musée des Arts et Métiers in Paris; photograph ©2011 SA Sharat Ganapati via Flickr.*

The transonic wing and flow control solutions were also the focus of the ADIF project [SMKR14] that tackled various aerodynamic problems. For the first time, systems that incorporated more than one actuation components were designed, and exhibited an enhanced performance when all the components were working simultaneously. Later, the F-111 Mission Adaptive Wing (MAW) research program [Har83] adapted a military aircraft with wings equipped with hinge-less devices and whose camber could be modified continuously by hydraulic actuators. Direct measurements of the aerodynamic efficiency were performed and the morphing systems surpassed existing solutions. However, increased weight and the overall complexity of the morphing system almost overshadowed the aerodynamic benefits [CL18]. Later, NASA published a new analytic investigation [BG99] in which an

algorithm for computing optimal shape control was introduced and wind tunnel testing of deformable models was carried out. The authors demonstrated gains in the aerodynamic performance at all points in the flight envelope of a civil aircraft. Nevertheless, the difficulties associated with the technology readiness, the complexity of the proposed actuation systems and often with cost, weight and space limitations, prevented any real morphing application from being implemented.

1.1.1 Shape Memory Alloys

The design of motor-based actuation systems was one of the first approaches examined for a fully deformable wing. These systems were strong enough to sustain the external loading and achieve the pre-described deformations. However, they also came with sizing and weight penalties especially for distributed actuating systems, i.e. configurations where multiple actuators were employed to deform large parts of the structure. Advances in material technology offered however a possible solution to counter many of the drawbacks of past morphing concepts. New breakthroughs in the Shape Memory Alloy (SMA) research area emerged. The SMAs had been discovered for a long time and their thermo-mechanical behavior is well documented. Due to their unique material properties, SMAs initiated the discussion around the possibility to use "smart" materials in order to construct smart deformable structures. Upon cooling, or under the application of stress (or both), SMAs undergo a change in their crystal structure reaching a pseudo-plastic limit and presenting a residual strain when the load is removed. When these alloys are heated, they are able to recover their original shape. By positioning suitably pairs of SMA actuators within the structure, it is possible to apply large forces by adjusting the temperature of every actuator. SMAs are quite efficient since they produce large (large maximum stress capacity - order of $350MPa$ for Nickel titanium compounds) and they can fully recover from large strains. As transformations occur due to the intrinsic properties of the material, SMAs can be used directly as actuators and any use of external apparatuses becomes redundant, making the actuating system safer and lighter. Such systems of actuation can have many applications as they can offer simplicity in the design, greener solutions and address safety and certification issues.

Industrial applications started quite early [HH75] and SMAs have been involved over the years in patents in various fields of engineering, particularly in automotive, aerospace, robotics, civil and biomedical engineering. SMA-based systems were first developed by NASA for space deployable systems where usually small forces are present. The book of [LA14] is a detailed reference on the use of SMAs that includes not only relevant applications but a detailed analysis on the phenomenology of the material and models describing their behavior. SMAs incorporated in cars, function either as linear actuators (e.g. rear-view mirror folding, climate control flaps adjustment and lock/latch controls) or as active thermal actuators (e.g. engine temperature control, carburetion and engine lubrication, powertrain clutches), significantly reducing the scale, the weight and the cost of automotive

components and providing substantial performance, in comparison to conventional actuators. In civil structures, SMAs are used in braced frames to morph energy dissipation systems, due to their hysteretic behavior and superelasticity. Isolation SMA-based devices and SMA dampers are also very promising applications in seismic engineering. In addition, SMAs are used extensively in structural connections either in steel structures or in reinforced concrete frames, mainly because of their superelastic capacity. Finally, self-rehabilitation using SMA wires has been also considered as a very promising application. Shape memory applying heating, is used in order for a great strain - due to an earthquake [FL11] or other type of failures - to be fully recovered. The materials are quite promising for biomedical applications as well, but in that context they mostly function as a support and not as actuators. SMAs fit the stress-strain behavior of human body parts and this favored medical developments [BVW03].

The use of SMAs in the field of aeronautics was delayed until the 90s. This was mainly due to the fact that impressive developments in the classical electromechanical actuators have led to significantly compact devices [CL18]. These devices were often preferred with respect to SMA-based systems not yet fully certified or even characterized at operational flight conditions (e.g. vibrating environment). This is expected to change as the needs of aircraft manufacturers grow and the necessity for novel multi-actuated architectures will emerge. However, based on a general understanding, the use of SMAs will soon be realistic at an industrial level, mainly for devices operating at a low frequency range. This will answer to the industrial demands for innovative morphing designs heading towards highly efficient green aircrafts. A considerable nujmber of projects were (and still are) devoted in the research of more compact, even simpler solutions that will be smoothly integrated and have a minimal impact on the shape of the aircraft in order to avoid important aerodynamic penalties.

The “Smart Wing” program carried out under the Defense Advanced Research Projects Agency (DARPA) examined the use of SMAs in the development of deformable wings [Kud04]. From numerical calculations, ground and wind tunnel tests performed the authors demonstrated an aerodynamic performance enhancement. Many critical issues were addressed in the systems integrated and the general assessment postponed any exploitation to a full-size aircraft [CL18]. Elzey et al. in [ESW03] developed an agonist-antagonist concept with elements that could rotate relative to one another and SMA sheets that induced curvature due to heating. The actuating system allowed not only to generate a 2D deflection but could also control the twist of wing sections if they were actuated asymmetrically. A similar system has also been developed in [SEW08] to create two-way SMA actuators using a one-way shape memory effect. The “Hingeless Wing” [CL18] led by CIRA, investigated the adaptability of aeronautical structures and developed compact actuators based on SMAs. For the first time it was concluded that an adaptive structure should be designed from the beginning, as a novel system as SMAs could only deform continuous structures that were flexible enough and common architectures were too stiff for these purposes. The same team worked on the re-designing of

a real flap configuration [PBC+11]. Examining various designs and through an extensive experimental and numerical analysis, the authors demonstrated positive results concerning the reliability and the feasibility of morphing concepts utilizing SMA actuators.

More recently, the multidisciplinary team composed by IMFT and LAPLACE laboratories studied the cambering ability of a plate equipped by SMA in interaction with the turbulence structure at Reynolds number 200000 by means of Time-Resolved Particle Image Velocimetry (PIV) [CRD+14] in the context of the research project EMMAV, supported by the STAE[2] Foundation. This study put in evidence the ability of a significant bending by an order of 10% of the chord and discussed the validity of the quasi-static hypothesis. This study quantified the modification of the turbulence stresses for different electrical intensities of the actuations corresponding to different cambered positions. It was demonstrated that morphing has the capacity to attenuate the shear-layer mode and the overall spectral energy at the most deformed position.

1.1.2 Piezoactuators

SMAs transform heat into mechanical energy due to their intrinsic properties. However, this process is slow, rendering SMAs as an unacceptable solution only for control devices with an expected slow - quasistatic - response (e.g. flaps, ailerons, rudders, brakes). Magnetic SMAs on the contrary have a faster response. These systems however are significantly heavier and their prominent nonlinear behavior can cause compatibility issues with the other systems and complicates their characterization in a flight environment. A viable solution for morphing systems with higher-frequency response appears in the form of piezoelectric actuators. These type of actuators utilize the piezoelectric effect which describes the capacity of materials to transform mechanical energy into an electric charge (direct piezoelectric effect). It is the reverse transformation however that finds a special application in actuation systems (inverse piezoelectric effect). Based on this effect, the piezoelectric actuators can transform an electric charge in order to produce large stresses at very low strains, with a low power consumption and at actuation frequencies that can reach up to several hundreds of kHz. Controlling applications utilizing piezoelectric materials mainly incorporate the use of piezoelectric ceramic stacks (piezo-stacks) and Macro Fiber Composites (MFC) [WPIW02].

Similar to the SMAs, the piezoactuators offer the possibility of a direct actuation. This has a significant impact on the complexity of the actuation system, with beneficial consequences on the weight and the safety of the morphing designs. Mainly due to the levels of strain and stress that the piezoactuators are capable of producing, they find extensive use in Unmanned Air Vehicles (UAVs). In these morphing and flow control applications, the energy output of the actuation is usually sufficient for the investigated physics. Vos et al. [VBBT07] proposed a new class of

[2]Sciences et Technologies pour l'Aéronautique et l'Espace, http://www.fondation-stae.net.

flight control actuators using piezoelectric elements which was then improved in [BV08]. In order to achieve higher deflections compared to conventional methods, the researchers applied an axial compression to the piezoelectric actuators. The actuators were modelled and then employed in a deformable wing structure of UAV to modify its camber distribution. The prototype was tested in a wind tunnel for various airspeeds. Testing demonstrated that high deflections could be maintained even at high flight speed while neither flutter nor divergence phenomena appeared.

Similarly, O. Bilgen and I. Friswell [BF14] studied the use of surface-bonded piezoelectric actuators for fixed-wing aircrafts operating at low Reynolds numbers. The partially active surface designed, employed a continuous boundary conditions for chordwise variations of the camber, demonstrating the feasibility of piezoelectric actuated surfaces for UAVs. The experimental evaluation showed the capacity of the structure to support the aerodynamic loads during actuation and sustain its shape. Due to the actuation, he wing was also capable of controlling the lift and drag in real time and achieve a desired aerodynamic response. In [LI14], the authors examined the application of MFC to be used in active flight control on a forward swept Micro Air Vehicle (MAV). The wing incorporated composite material as a passive load-alleviation system, and two MFC actuators for the roll and pitch moment control. This investigation evaluated the performance of the actuators and demonstrated the capacity of proposed design to maximize curvature and load bearing. Along with the aerodynamic performance, the controllability of the aircraft was also increased. Finally, MFC were also employed by Debiasi et al. [DBLR13] to be used for the shape modification of the upper and lower surfaces of a symmetric airfoil. The authors discussed the creation of morphing surfaces, targeting improved aerodynamic performance, enhanced maneuverability and active flow control. In their design, the authors integrated in parts of the skin the thin piezoelectric actuators and performed wind-tunnel measurements in different flow regimes in order to assess the dynamic shape variation and the gains in performance.

The small deformations provided by the piezoelectric materials do necessarily restrict their application to reduced scale aircrafts. In practice, in civil and military aeronautics, the piezoelectric-based actuators find extensive application due to their high frequency bandwidth. A review discussing typical applications of piezoelectric - among others - actuators in aircrafts can be found in [CGC$^+$08]. The piezoelectric actuation allows for controlling the ailerons on rotating blades or actively damping external disturbances. In general, piezoelectric smart materials are capable of controlling smaller scale physical instabilities and, as a result, are widely used in noise cancelling application and on the attenuation of vibrations. In the context of dynamic flow control, an active “smart” skin for turbulent drag reduction in realistic flight conditions was presented by Rediniotis et al. [RLMK02]. Recent advances on SMAs and piezoelectric-based actuators were capitalized in this work and various designs were examined. The active skin, made out of electroactive materials, would generate spanwise traveling waves, optimal in terms of amplitude, wavelength and frequency, in order to reduce the skin friction through interactions with the boundary layer. Based on computational evidence, the authors proposed a flow control

technique that introduced micro-scale wave amplitudes and energy in the flow, and was be able to produce significant benefits. An active flow control technique was also proposed in [OLI14] where multilayer piezoelectric tabs distributed on a cylinder were employed to delay the flow separation and reduce the drag. The actuators were equidistant along the span of the cylinder and placed at various angles with respect to the upstream flow. Several control parameters concerning the applied dynamic forcing (e.g. frequency, amplitude) were evaluated at different Reynolds number regimes and were found to have a large influence on the performance of the piezoelectric actuation. The authors performed measurements of the pressure distribution around the cylinder in order to estimate the drag, and demonstrated a reduction of 30% in the pre-critical regime, while achieving at the same time a suppression of the vortex shedding and a reduce of the energy content due to the forcing.

In the context of the DYNAMORPH research project, supported by the STAE Foundation, the small deformation – higher-frequency vibrations obtained by piezoactuators were proved to have major effects on the flow instabilities, on the wake's structure and on the aerodynamic forces. In this research project, the study by [CSR$^+$13] designed a push-push actuator adapted in the rear part of a NACA0012 wing. This study investigated by means of TRPIV the effect of different actuation frequencies in low amplitudes on the turbulence structure and determined optimal frequency ranges in which a considerable attenuation of the shear-layer mode and of the turbulence stresses was obtained through vortex breakdown mechanisms. Scheller [Sch15] studied the effect of Macro-Fiber Composite (MFC) actuators disposed along the span of a NACA4412 morphing wing able to apply simultaneously high-deformations in very low frequencies and higher-frequency low-amplitude vibrations, giving birth to the "hybrid electroactive morphing" [SJR$^+$16]. This concept "imitates" the actuation of the wings, ailerons and feathers of large-span hunting birds at different length and time scales. This kind of morphing realized on wing prototypes for the first time in the state-of-the-art by the present studies, was proven fully adequate for manipulation of the turbulence spectrum containing a multitude of modes and legth scales. These studies had shown that optimal frequencies of the piezoactuators were able to considerably attenuate the wake's width, by producing eddy-blocking effects.

1.2 Bio-inspiration

A key challenge in the design of morphing structures [LDW13] is to create systems that are able to deform the controlled surface continuously, to carry significant prescribed loading and, at the same time, have a minimal impact on the controlled geometry. The potential gain in the capabilities of future vehicles is broad due to the recent developments in smart materials - such as the ones previously examined - as they provide a continuous multi-point change in shape with no distinction between the structure and the actuation system [BSFA$^+$14]. In addition to this, compliant

structures are needed in order to maintain the actuation forces in low levels and avoid introducing discontinuities in the aerodynamic profile which can affect the aerodynamic performance in a detrimental way. To this end, designs inspired by efficient natural architectures, systems and processes can be proven suitable in developing flexible bio-inspired structures.

Indeed, bio-inspired technologies and designs have been considered in various morphing applications. A clear demonstration of bio-inspiration can be found in the work of Woods et al. [WF12], [WBF14]. The authors presented an experimental investigation on a constructed Fish Bone Active Camber morphing wing which displayed an enhanced aerodynamic performance. This biologically inspired concept consisted of a compliant skeletal structure covered by a composite skin and an antagonistic pair of actuators acting as tendons and deforming the wing. The proposed morphing architecture was able to produce large deflections in order to provide a continuous cambering.

As previously mentioned, a breakthrough in the bio-inspired electroactive morphing technology was achieved by the studies of the multidisciplinary team IMFT-LAPLACE Laboratories through three federative research projects funded by the STAE Foundation: EMMAV, DYNAMORPH and the platform SMARTWING[3]. The hybrid electroactive morphing concept provided wing prototypes able to manipulate different classes of turbulent vortices which in turn produce optimal interactions with the actuations and create a suitable fluid-structure interaction system, able to increase the aerodynamic performance. In these studies, it is worth noticing that the bio-inspiration is only partial, because an airplane flies in much higher speeds than a bird. Only the first phases of take-off and the very last phases of landing can be comparable with the speeds of flight of rapacious. The electroactive morphing concepts that have been studied were adapted in higher speeds, including the transonic regimes. The aforementioned studies led to an extended investigation in collaboration with Airbus "Emerging Technologies and Concepts Toulouse" - ETCT, through two collaborative projects, towards full - scale design on the purpose of applying these concepts in real flight in the next years [JMS$^+$17]. This objective, together with a thorough investigation on closed-loop controllers and sensor systems gave birth to the European research project "Smart Morphing and Sensing (SMS) for aeronautical configurations".

1.2.1 The SMS project

The electroactive morphing is currently being studied in the context of the H2020 European research program "Smart Morphing & Sensing (SMS) for Aeronautical configurations"[4]. The project was born from the collaboration between the IMFT and LAPLACE laboratories that introduced the *hybrid*, partly bio-inspired, electroactive morphing concept ([SCR$^+$15], [SJR$^+$16], [JMS$^+$17]). The hybrid concept, inspired by the large-span wings of hunting birds, entails the combination

[3]The reader can visit www.smartwing.org

[4]Project N° 723402, the reader can refer to: www.smartwing.org/SMS/EU

of different classes of electroactive actuators that yield turbulence modifications at multiple scales when realized simultaneously. This produces interactions with the actuations and creates a fluid-structure interaction system, able to increase the aerodynamic performance.

Hybrid morphing enables the manipulation of turbulence and its interaction with the morphing structure, enhancing the amplification of smaller structures in the wake and attenuating natural flow instabilities. The first realization of hybrid morphing was carried out by Scheller et al. [SJR$^+$16] who studied the effect of MFC patches disposed along the span of a morphing wing in combination with SMA actuators. The actuation system was able to apply simultaneously high-deformations in very low frequencies and higher-frequency low-amplitude vibrations, giving birth to the hybrid electroactive morphing. In this realization, the electroactive patches correspond to the action of bird feathers which passively vibrate at higher frequencies and are able to produce significant vortex breakdown, beneficial for the aerodynamic performance. The cambering of the wing through SMA actuators is inspired by the continuous deformation of the large-span wings of hunting birds. The bio-inspired morphing allows for a "smart wing design through turbulence control" and a clear demonstration on how "science imitates nature". This was shown in the annual scientific exhibition of the Royal Society of 2014, where the interdisciplinary team IMFT-LAPLACE was honorifically invited to present the hybrid electroactive morphing wing. An implementation of the hybrid electroactive morphing approach was also achieved in the design and construction of an electroactive Morphing Wing Prototype which will be denoted as "MWP" in the present thesis.

1.2.2 Electroactive Morphing Wing Prototype

The considered prototype is a reduced scale design of a hybrid electroactive morphing wing. It is equipped with both a camber control system and High-Frequency Vibrating Trailing Edge (HFVTE) actuators. The baseline airfoil is the wing section of A320, with a chord of 700*mm* and a span of 590*mm*. The SMA-based camber control actuators were sized and implemented on a length covering the last 30% of the chord, corresponding to the actual flap placement; the HFVTE actuation employs Macro Fiber Composite (MFC) piezoelectric patches. The area close to the leading edge was retained hollow to provide the space to contain all electronics and tubing necessary for temperature, pressure and position transducers as well as actuator interfaces. A schematic representation of the MWP is illustrated in Fig. 1.2 where both families of actuators used in the context of the hybrid electroactive morphing concept are observed.

The working principle of the camber control relies on distributed structure-embedded actuators. SMA wires are placed under the upper and lower sides of the aluminum sheets constituting the skin of the wing. The selected SMA wires were made of Nickel-Titanium alloys and their properties are controlled by a change in temperature [CRD$^+$14]. When electrically charged, the wires are heated and are able to recover part of the strain by which they have been previously trained.

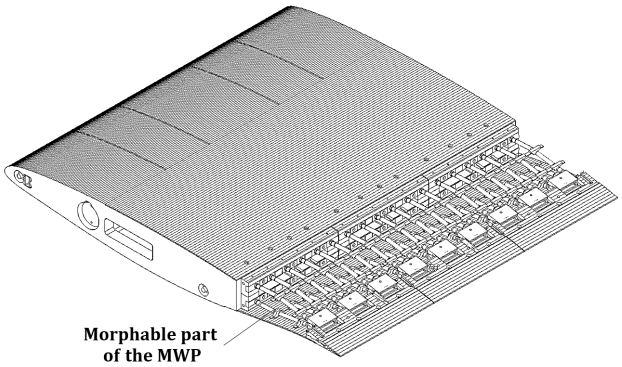

(a) *3D view; upper skin removed on the deformable part of the wing.*

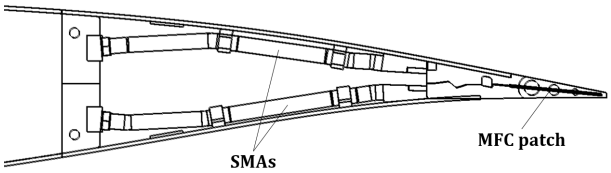

(b) *Side-view; both families of actuators.*

Figure 1.2: *CAD of electroactive the Morphing Wing Prototype (MWP) designed and constructed by LAPLACE/IMFT.*

They are capable of generating intense stress (larger than $600MPa$) under large deformation levels (order of $25-30\%$ of the chord) and can be respectively cooled down by forced air to bring the wing back to the initial neutral position. In this prototype, the actuation of the wires on the suction side causes bending of the trailing edge towards higher cambered shapes (i.e. downwards). On the contrary, the actuation of the wires on the pressure side skin causes a decrease in camber (i.e. upward deformation).

The HFVTE actuators are composed of metallic substrates positioned in between the MFC patches. The MFC, first developed by NASA Langley Research Center [WHB02], include lead-zirconate-titanate (PZT) piezoelectric fibers and electrode networks, encapsulated within epoxy. When supplied by a voltage, the patches stretch out and generate bending. The Multi-Fiber composite piezoelectric actuators were glued on both sides of a metallic substrate and placed in the trailing edge region. The whole ensemble is covered by a flexible molded silicon in order to retain the trailing edge shape and limit the impact on the actuator's performance. The active chord-wise length of the HFVTE is $35mm$. This implementation allows for quasi-static tip deformation amplitude of $0.3-1mm$, and the piezoactuators are able to vibrate with large enough amplitudes up to $500Hz$. For further details, related to the design and the electromechanical characterization of the electroactive morphing wing the reader is invited to refer to [GSR+15].

1.3 Ouline of the thesis

Having introduced the background and context of the present thesis, the outline of the chapters that follow is presented. Morphing airfoils and wings are investigated by means of numerical simulation and the physical mechanisms of morphing are analyzed. High Reynolds number calculations around supercritical wings in low-subsonic and transonic regimes are performed and experimental results are employed for a detailed physical analysis. The flow simulations are carried out using the NSMB (Navier Stokes MultiBlock) solver and efficient turbulence modelling approaches.

The following chapter (Chapter 2) is split into two parts. The first one includes all the essential elements concerning Computational Fluid Dynamics (CFD) that are referenced throughout the thesis and were utilized in the flow simulations. Special attention has been given to the turbulence modelling employed in the following studies. The second part briefly goes over the basics on Computational Structural Mechanics (CSM) and the relevant works on which the development of a Finite Element (FE) code was based. Nonlinear mechanics are extremely relevant when examining controlled (morphed) structures and thus, various aspects and emerging nonlinearities are discussed.

In Chapter 3, an advanced turbulence modelling approach with re-injection of turbulence in sheared regions is examined. The approach is extended in the present thesis to three-dimensional flows and applied to the study of a transonic flow around a “laminar” wing in order to investigate the buffet instability. The method consists of the addition of stochastic source terms in specifically confined regions that in return force the turbulent variables in order to model interfacial shear dynamics and upscale energy transfers. The methodology is examined on its effectiveness to enhance the predictive capabilities of the modelling for complex flows with significant detachment and increased Reynolds number. In this chapter, the effect of turbulent transition and the state of the incoming boundary layer on the suction side of the wing is also evaluated.

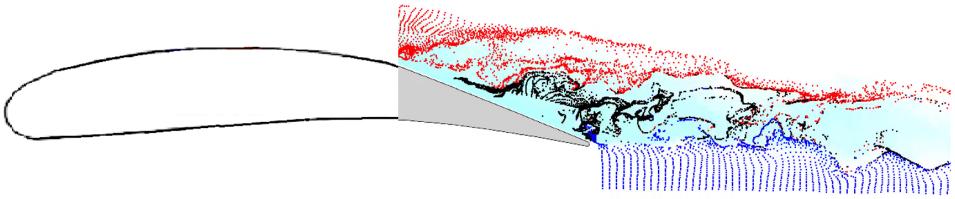

Figure 1.3: *Development of interfaces and vortices in the wake; an illustration of the morphing effects.*

In Chapter 4, the stochastic forcing effects are realized with the introduction of high-frequency low-amplitude vibrations (HFVTE) near the trailing edge of wings. This HFVTE actuation introduces locally in the flow small-scale fluctuating energy

that interacts with the existing flow dynamics. This morphing strategy is examined via extensive numerical simulations and Time-Resolved Particle Image Velocimetry (TRPIV) measurements. In the context of hybrid morphing, the lower-frequency actuation via SMAs is then examined in Chapter 5. In this chapter, we focus on the development of an efficient methodology that accurately predicts the response of the solid structure due to the thermo-mechanical SMA actuation. The proposed method is an efficient way to determine the working capabilities of controlled aeronautical configurations and serves as a design tool for future "smart" wings.

Finally, the conclusions are included in Chapter 6; perspectives regarding future developments and investigations are drawn.

Bibliography

[BF14] O. Bilgen and M. I. Friswell. Piezoceramic composite actuators for a solid-state variable-camber wing. *Journal of Intelligent Material Systems and Structures*, 25(7):806–817, 2014.

[BG99] A. Bolonkin and G. B. Gilyard. *Estimated benefits of variable-geometry wing camber control for transport aircraft*. National Aeronautics and Space Administration, Dryden Flight Research Center ; National Technical Information Service, distributor Edwards, Calif. : Springfield, VA, 1999.

[BHCS80] R. F. Brissenden, A. R. Heath, D. W. Conner, and M. L. Spearman. Assessment of variable camber for application to transport aircraft. Technical report, NASA, November 1980.

[BSFA+14] S. Barbarino, E. Saavedra Flores, R. M. Ajaj, I. Dayyani, and M. I. Friswell. A review on shape memory alloys with applications to morphing aircraft. *Smart Materials and Structures*, 23:63001, June 2014.

[BV08] R. Barrett and R. Vos. Post-buckled precompressed subsonic micro-flight control actuators and surfaces. *Smart Materials and Structures*, 17(5):055011, August 2008.

[BVW03] S. Bokhari, O. Vahdat, and R. Winters. The first clinical experience with a peripheral, self-expanding nitinol stent in the treatment of saphenous vein graft disease: Angiographic evidence of late expansion. *The Journal of invasive cardiology*, 15:418–22, August 2003.

[CGC+08] F. Claeyssen, B. Grohmann, M. Christmann, T. Lorkowski, and R. Le Letty. New Actuators for Aircraft and Space Application. *Proc. 11th International Conference on New Actuators, Bremen*, 2008.

[CL18] A. Concilio and L. Lecce. Chapter 1 - Historical Background and Current Scenario. In A. Concilio, I. Dimino, L. Lecce, and R. Pecora, editors, *Morphing Wing Technologies*, pages 3–84. Butterworth-Heinemann, January 2018.

[CRD+14] M. Chinaud, J. F. Rouchon, E. Duhayon, J. Scheller, S. Cazin, M. Marchal, and M. Braza. Trailing-edge dynamics and morphing of a deformable flat plate at high Reynolds number by time-resolved PIV. *Journal of Fluids and Structures*, 47:41–54, May 2014.

[CSR+13] Maxime Chinaud, Johannes Scheller, Jean François Rouchon, Eric Duhayon, and Marianna Braza. Hybrid electroactive wings morphing for aeronautic applications. In *Mechatronic Systems and Materials IV*, volume 198 of *Solid State Phenomena*, pages 200–205. Trans Tech Publications Ltd, 5 2013.

[DBLR13] M. T. Debiasi, Y. Bouremel, Z. Lu, and V. Ravichandran. Deformation of the Upper and Lower Surfaces of an Airfoil by Macro Fiber Composite Actuators. In *31st AIAA Applied Aerodynamics Conference*. American Institute of Aeronautics and Astronautics, 2013.

[ESW03] D. M. Elzey, A. Y. N. Sofla, and H. N. G. Wadley. A bio-inspired high-authority actuator for shape morphing structures. In *Smart Structures and Materials 2003: Active Materials: Behavior and Mechanics*, volume 5053, pages 92–100. International Society for Optics and Photonics, August 2003.

[Fer77] J. C. Ferris. Wind-tunnel investigation of a variable camber and twist wing. [in the Langley 8-ft transonic wind tunnel]. Technical report, NASA, August 1977.

[FL11] M. Fragiadakis and N. D. Lagaros. An overview to structural seismic design optimisation frameworks. *Computers & Structures*, 89(11):1155 – 1165, 2011.

[GSR+15] J. Gurvan, J. Scheller, K. J. Rizzo, E. Duhayon, J. F. Rouchon, and M. Braza. Dimensionnement d'une maquette pour l'investigation du morphing électroactif hybride en soufflerie subsonique. In *22e Congrès Français de Mécanique*, pages 1–13, Lyon, France, 2015. Thanks to the AFM, Association Française de Mécanique.

[Har83] R. Hardy. AFTI/F-111 mission adaptive wing technology demonstration program. In *Aircraft Prototype and Technology Demonstrator Symposium*. American Institute of Aeronautics and Astronautics, 1983.

[HH75] J. D. Harrison and D. E. Hodgson. Use of TiNi in Mechanical and Electrical Connectors. In Jeff Perkins, editor, *Shape Memory Effects in Alloys*, pages 517–523. Springer US, Boston, MA, 1975.

[JMS+17] G. Jodin, V. Motta, J. Scheller, E. Duhayon, C. Döll, J.F. Rouchon, and M. Braza. Dynamics of a hybrid morphing wing with active open loop vibrating trailing edge by time-resolved PIV and force measures. *Journal of Fluids and Structures*, 74(Supplement C):263–290, October 2017.

[Kud04] J. N. Kudva. Overview of the DARPA Smart Wing Project. *Journal of Intelligent Material Systems and Structures*, 15(4):261–267, April 2004.

[LA14] L. Leonardo and C. Antonio, editors. *Shape Memory Alloy Engineering: For Aerospace, Structural and Biomedical Applications*. Butterworth-Heinemann, Amsterdam, 1 edition edition, October 2014.

[LDW13] X. Lachenal, S. Daynes, and P. M. Weaver. Review of morphing concepts and materials for wind turbine blade applications. *Wind Energy*, 16(2):283–307, March 2013.

[LI14] B. W. LaCroix and P. G. Ifju. Macro Fiber Composites and Substrate Materials for MAV Wing Morphing. In G. P. Tandon, S. A. Tekalur, C. Ralph, N. R. Sottos, and B. Blaiszik, editors, *Experimental Mechanics of Composite, Hybrid, and Multifunctional Materials, Volume 6*, pages 89–101, Cham, 2014. Springer International Publishing.

[MWH+02] AM. R. McGowan, A. E. Washburn, L. G. Horta, R. G. Bryant, D. E. Cox, E. J. Siochi, S. L. Padula, and N. M. Holloway. Recent results from NASA's morphing project. In *Smart Structures and Materials 2002: Industrial and Commercial Applications of Smart Structures Technologies*, volume 4698, pages 97–111. International Society for Optics and Photonics, July 2002.

[OLI14] M. Orazi, D. Lasagna, and G. Iuso. Circular cylinder drag reduction using piezoelectric actuators. *Advances in Aircraft and Spacecraft Science*, 1:27–41, 2014.

[PBC+11] R. Pecora, S. Barbarino, A. Concilio, L. Lecce, and S. Russo. Design and Functional Test of a Morphing High-Lift Device for a Regional Aircraft. *Journal of Intelligent Material Systems and Structures*, 22(10):1005–1023, July 2011.

[RLMK02] O. K. Rediniotis, D. C. Lagoudas, R. Mani, and G. Karniadakis. Active skin for turbulent drag reduction. In Vijay K. Varadan, editor, *Smart Structures and Materials 2002: Smart Electronics, MEMS, and Nanotechnology*, volume 4700, pages 122 – 134. SPIE, 2002.

[Sch15] Johannes Scheller. *Electroactive morphing for the aerodynamic performance improvement of next generation airvehicles*. PhD thesis, INP

Toulouse, 2015. Thèse de doctorat dirigée par Rouchon, Jean-François et Braza, Marianna Génie électrique Toulouse.

[SCR+15] J. Scheller, M. Chinaud, J.F. Rouchon, E. Duhayon, S. Cazin, M. Marchal, and M. Braza. Trailing-edge dynamics of a morphing NACA0012 aileron at high Reynolds number by high-speed PIV. *Journal of Fluids and Structures*, 55(Supplement C):42–51, May 2015.

[SEW08] A.Y.N. Sofla, D.M. Elzey, and H.N.G. Wadley. Two-way Antagonistic Shape Actuation Based on the One-way Shape Memory Effect. *Journal of Intelligent Material Systems and Structures*, 19(9):1017–1027, September 2008.

[SH88] J. Szodruch and R. Hilbig. Variable wing camber for transport aircraft. *Progress in Aerospace Sciences*, 25(3):297–328, January 1988.

[SJR+16] J. Scheller, G. Jodin, K. J. Rizzo, E. Duhayon, JF. Rouchon, M. S. Triantafyllou, and M. Braza. A combined smart-materials approach for next-generation airfoils. *Solid State Phenomena*, vol. 251:pp. 106–112, 2016.

[SMKR14] M. Sinapius, H. P. Monner, M. Kintscher, and J. Riemenschneider. DLR's Morphing Wing Activities within the European Network. *Procedia IUTAM*, 10:416 – 426, 2014.

[VBBT07] R. Vos, R. Barrett, R. de Breuker, and P. Tiso. Post-buckled precompressed elements: a new class of control actuators for morphing wing UAVs. *Smart Materials and Structures*, 16(3):919–926, May 2007.

[WBF14] B. K. S. Woods, O. Bilgen, and M. I. Friswell. Wind tunnel testing of the fish bone active camber morphing concept. *Journal of Intelligent Material Systems and Structures*, 25(7):772–785, May 2014.

[WF12] B. K S. Woods and M. I. Friswell. Preliminary investigation of a fishbone active camber concept. In *Smart Materials, Adaptive Structures and Intelligent Systems*, volume Volume 2: Mechanics and Behavior of Active Materials; Integrated System Design and Implementation; Bio-Inspired Materials and Systems; Energy Harvesting, pages 555–563. American Society of Mechanical Engineers, 09 2012.

[WHB02] W. K. Wilkie, J. W. High, and J. Bockman. Reliability Testing of NASA Piezocomposite Actuators. In *Nasa Technical report*, Bremen; Germany, 2002.

[WPIW02] R. Williams, G. Park, D. Inman, and W. K. Wilkie. An overview of composite actuators with piezoceramic fibers. *Proceedings of SPIE - The International Society for Optical Engineering*, 4753:421–427, 2002.

Chapter 2

Numerical approach

2.1 Computational Fluid Dynamics

The advent of large supercomputers together with the rapid development of numerical schemes in the last two decades have stimulated research towards solving the complete set of Navier-Stokes equations numerically. At the present, numerical solutions are available for a considerable number of complex flow problems around real configurations. An extensive and comprehensive reference to Computational Fluid Dynamics (CFD) theory and practice can be found in the book of C. Hirsch [Hir07]. The present thesis the NSMB (Navier-Stokes MultiBlock) code; NSMB is the fruit of a European Consortium consisting of multiple research institutes strongly collaborating with the main European aeronautical industries. The NSMB code solves the compressible Navier-Stokes equations and is also adapted for low Mach aerodynamics. It employs a wide range of advanced turbulence modelling approaches for non-equilibrium turbulent flows, high-order schemes and grid-handling methods (e.g. multigrid, chimera grids) for moving/deformable structures and large scale complex configurations. The present section follows closely the book of K. J. Blasek [Bla01] and the utilization handbook of the NSMB (Navier-Stokes Multi-Block) code [HPV+16].

2.1.1 Governing equations

The Navier-Stokes equations in three-dimensional (3D) Cartesian coordinates, for a viscous perfect gas with no external sources can be expressed in conservative form as:

$$\frac{\partial}{\partial t}(W) + \frac{\partial}{\partial x}(f - f_v) + \frac{\partial}{\partial y}(g - g_v) + \frac{\partial}{\partial z}(h - h_v) = 0 \tag{2.1}$$

where t denotes time. The state vector W is given by:

$$W = (\rho \;\; \rho u \;\; \rho v \;\; \rho w \;\; \rho E)^T$$

and the convective fluxes are defined as:

$$f = \left\{ \begin{array}{c} \rho u \\ \rho u^2 + p \\ \rho uv \\ \rho uw \\ u(\rho E + p) \end{array} \right\}, \; g = \left\{ \begin{array}{c} \rho v \\ \rho vu \\ \rho v^2 + p \\ \rho vw \\ v(\rho E + p) \end{array} \right\}, \; h = \left\{ \begin{array}{c} \rho w \\ \rho wu \\ \rho wv \\ \rho w^2 + p \\ w(\rho E + p) \end{array} \right\}$$

where ρ the density, u, v, w the Cartesian velocity components, p the pressure and E the total energy. The viscous fluxes are defined:

$$f_v = \left\{ \begin{array}{c} 0 \\ \tau_{xx} \\ \tau_{xy} \\ \tau_{xz} \\ (\tau U)_x - q_x \end{array} \right\}, \; g_v = \left\{ \begin{array}{c} 0 \\ \tau_{yx} \\ \tau_{yy} \\ \tau_{yz} \\ (\tau U)_y - q_y \end{array} \right\}, \; h_v = \left\{ \begin{array}{c} 0 \\ \tau_{zx} \\ \tau_{zy} \\ \tau_{zz} \\ (\tau U)_z - q_z \end{array} \right\}$$

The τ the shear tensor is given by:

$$\tau_{xx} = \frac{2}{3}\mu(2\frac{\partial u}{\partial x} - \frac{\partial v}{\partial y} - \frac{\partial w}{\partial z}) \;, \;\; \tau_{xy} = \tau_{yx} = \mu(\frac{\partial u}{\partial y} + \frac{\partial v}{\partial x})$$

$$\tau_{yy} = \frac{2}{3}\mu(-\frac{\partial u}{\partial x} + 2\frac{\partial v}{\partial y} - \frac{\partial w}{\partial z}) \;, \;\; \tau_{yz} = \tau_{zy} = \mu(\frac{\partial v}{\partial z} + \frac{\partial w}{\partial y})$$

$$\tau_{zz} = \frac{2}{3}\mu(-\frac{\partial u}{\partial x} - \frac{\partial v}{\partial y} + 2\frac{\partial w}{\partial z}) \;, \;\; \tau_{zx} = \tau_{xz} = \mu(\frac{\partial w}{\partial y} + \frac{\partial u}{\partial z})$$

where the Stokes hypothesis ($\lambda + \frac{2}{3}\mu = 0$) has been employed, with μ the molecular viscosity. The viscous dissipation in the energy equation is calculated from:

$$(\tau U)_* = \tau_{*x}u + \tau_{*y}v + \tau_{*z}w$$

The heat flux q_* due to conduction is calculated according to Fourier's law $q_* = -k\partial T/\partial(*)$ with T the temperature and k the heat conductivity. For a caloric perfect gas flow, Sutherland's law for air at standard atmosphere states:

$$\frac{\mu}{\mu_\infty} = \left(\frac{T}{T_\infty}\right)^{3/2} \frac{(T_\infty + 110.3)}{(T + 110.3)}$$

where μ_∞ the viscosity at the reference temperature T_∞. Assuming a constant Prandtl number (Pr) the heat conductivity is found by $k = \mu c_p/Pr$. The specific heat at constant temperature and at constant volume can be calculated for a caloric perfect gas as $c_p = \gamma c_v$ and $c_v = R/(\gamma - 1)$ where γ the heat capacity ration (1.4 for air) and

R the gas constant (equal to $287 J/kgK$ for air). The system of equations is closed by relating the pressure to the state vector. For a caloric perfect gas, the constitutive gas relationship writes:

$$p = \rho e(\gamma - 1) = \rho c_v T(\gamma - 1) = \rho RT$$

where $e = C_v T$ the internal energy for a calorically perfect fluid, related to the total energy by: $e = E - \frac{1}{2}(u^2 + v^2 + w^2)$.

Finite volume formulation

The cell centered finite volume method is used for the spatial discretization of the Navier-Stokes equations. Starting from the Navier-Stokes in conservative form (Eq. 2.1) and using a direct discretization of the integral form of the conservation laws, it has been proven that the mass, momentum and energy will remain conserved by the numerical scheme on the grid. This ensures automatically that the discretized equation are able to capture discontinuities that often arise when solving the Navier-Stokes for compressible flows. The approach is deals with arbitrary complex geometries. The computational domain is subdivided into a number of grid cells with unique $(i, j.k)$ coordinates. Integrating Eq. 2.1 over a volume Ω yields:

$$\int_\Omega \frac{\partial W}{\partial t} d\Omega + \int_\Omega div(\bar{F}) d\Omega = 0 \tag{2.2}$$

where $\bar{F} = (f - f_v, g - g_v, h - h_v)$ is the flux tensor. Applying the Gauss divergence theorem gives:

$$\int_\Omega \frac{\partial W}{\partial t} d\Omega + \oint_{\partial\Omega} \bar{F} \cdot \vec{n} dS = 0 \tag{2.3}$$

with $\vec{n}$ the unit normal vector, always pointing in the outward direction of the $\partial\Omega$ boundary of Ω. Eq. 2.3 states that the time rate of the change in W inside the domain Ω should equal the sum of the fluxes entering or leaving the boundaries of the domain. For a structured grid, if $\Omega_{i,j,k}$ the cell volume and $W_{i,j,k}$ the approximate average value of W in this cell, located at its center for cell-centered schemes. Eq. 2.3 can be approximated as:

$$\frac{d}{dt}(\Omega_{i,i,k} W_{i,j,k}) = -R_{i,j,k} \tag{2.4}$$

where we use the residual term $R_{i,j,k}$ to denote every term on the right hand side of the equation. This term includes the discretization of source terms. However, when no source terms are taken into account the term $R_{i,j,k}$ is the net flus leaving and entering the cell from each face, i.e.:

$$\begin{aligned} R_{i,j,k} &= r_{i+1/2,j,k} - r_{i-1/2,j,k} + r_{i,j+1/2,k} - \\ & \quad r_{i,j-1/2,k} + r_{i,j,k+1/2} - r_{i,j,k-1/2} &= \sum_{m=1}^{N_F} F_m \Delta S_m \end{aligned}$$

with N_F the number of control volume faces, F_m the flux projected on the surface and $\Delta S_m = ||\vec{S}^m||$ the area of the face with surface vector $\vec{S}^m = (S_x^m, S_y^m, S_z^m)$.

2.1.2 Flux calculation

To approximate the flux tensor F at each surface, a distinction is made between the inviscid and the viscous part ($F = F^I + F^V$) of the fluxes. In the following, we focus on the numerical schemes used in the present studies.

Central scheme

Starting with the inviscid fluxes, in the cell-centered central scheme [JST81], the flux F^I at the m surface is calculated using the arithmetic average of the state vector W at this cell side from the conservative variables on both side of the face. As an example, for the $(i-1/2, j, k)$ face of the control volume (i, j, k) the respective convective flux with a second-order of accuracy scheme can be built as:

$$F^I_{i-1/2,j,k} = F^I(W_{i-1/2,j,k}) \;\; with \;\; W_{i-1/2,j,k} = \frac{1}{2}(W_{i,j,k} + W_{i-1,j,k})$$

This evaluation is generally used for steady state solutions. Instead of averaging the state variables, another approach can use the average of the flux tensors. Following [RS14], the 3D Navier-Stokes equations can be re-written in a skew-symmetric form as:

$$\frac{\partial \rho}{\partial t} + \frac{\partial \rho u_m}{\partial x_m} = 0$$

$$\frac{1}{2}\left(\frac{\partial \rho}{\partial t} + \rho\frac{\partial}{\partial t}\right)u_l + \frac{1}{2}\left(\frac{\partial \rho u_m}{\partial x_m} + u_m\rho\frac{\partial}{\partial x_m}\right)u_l + \frac{\partial p}{\partial x_l} = \frac{\partial \tau_{lm}}{\partial x_m}$$

$$\frac{1}{\gamma-1}\frac{\partial p}{\partial t} + \frac{\gamma}{\gamma-1}\frac{\partial p u_m}{\partial x_m} - u_l\frac{\partial p}{\partial x_l} = -u_l\frac{\partial \tau_{lm}}{\partial x_m} + \frac{\partial u_l \tau_{lm}}{\partial x_m} + \frac{\partial q_l}{\partial x_l}$$

Therefore, an equivalent formulation for the nonlinear tensor:

$$F = \begin{Bmatrix} \frac{\partial \rho u_k}{\partial x_k} \\ \frac{1}{2}\left(\frac{\partial \rho u_k}{\partial x_k} + u_k\rho\frac{\partial}{\partial x_k}\right)u + \frac{\partial p}{\partial x} \\ \frac{1}{2}\left(\frac{\partial \rho u_k}{\partial x_k} + u_k\rho\frac{\partial}{\partial x_k}\right)v + \frac{\partial p}{\partial y} \\ \frac{1}{2}\left(\frac{\partial \rho u_k}{\partial x_k} + u_k\rho\frac{\partial}{\partial x_k}\right)w + \frac{\partial p}{\partial z} \\ \frac{\gamma}{\gamma-1}\frac{\partial p u_k}{\partial x_k} - u_l\frac{\partial p}{\partial x_l} \end{Bmatrix}$$

can be used in calculating each component of the flux tensor from the computed state vector from a direct discretization. This approach adds stability in the central scheme.

Artificial dissipation

The central scheme needs to be augmented by the addition of artificial viscosity. Following [ST87], second and fourth order differences of the state vector - multiplied by a scaling factor and weights - are added to the central fluxes. The second order

artificial viscosity term is used near discontinuities for stability while the fourth order dissipation term to suppress odd/even decoupling of the solution. After addition of the dissipative terms, Eq.2.4 writes:

$$\frac{d}{dt}(\Omega_{i,i,k}W_{i,j,k}) = -R_{i,j,k} + D_{i,j,k} \tag{2.5}$$

with D the dissipation operator. Analogous to the discretization of the convective fluxes, the dissipative fluxes are introduced for each equation to preserve the conservative form of the discretized equation. The operator is split as:

$$\begin{aligned} D_{i,j,k} &= d_{i+1/2,j,k} - d_{i-1/2,j,k} + d_{i,j+1/2,k} - \\ &\quad d_{i,j-1/2,k} + d_{i,j,k+1/2} - d_{i,j,k-1/2} \end{aligned} \tag{2.6}$$

For the $(i-1/2, j, k)$ face of the control volume (i, j, k) the respective dissipative flux can be calculated:

$$\begin{aligned} d_{i-1/2,j,k} &= \Lambda_{i-1/2,j,k}\Big[\varepsilon^{(2)}_{i-1/2,j,k}(W_{i,j,k} + W_{i-1,j,k}) - \\ &\quad \varepsilon^{(4)}_{i-1/2,j,k}(W_{i+1,j,k} - 3W_{i,j,k} + 3W_{i-1,j,k} - W_{i-2,j,k})\Big] \end{aligned}$$

where Λ a scaling factor used to relate the dissipative flux to the magnitude of the convective flux through the cell side. Performing the addition in Eq. 2.6 only second and fourth order differences are produced. The coefficients $\varepsilon^{(2)}$ and $\varepsilon^{(4)}$ are used to locally adapt the dissipative fluxes. It is desirable for the second order dissipation term to be small except in regions of large pressure gradients. In addition, the fourth order difference should be used everywhere except in regions where the second order dissipation term is large, in order to disappear in the vicinity of a discontinuity. The $\varepsilon^{(2)}$ coefficient is directly related to the normalized pressure gradient through:

$$\mu_{i,j,k} = \left| \frac{p_{i+1,j,k} - 2p_{i,j,k} + p_{i-1,j,k}}{p_{i+1,j,k} + 2p_{i,j,k} + p_{i-1,j,k}} \right|$$

with which the sensor $\nu_{i+1/2,j,k} = max(\mu_{i-1,j,k},\ \mu_{i,j,k})$ adjusts the values of the coefficients as:

$$\begin{aligned} \varepsilon^{(2)}_{i-1/2,j,k} &= k^{(2)}\nu_{i+1/2,j,k} \\ \varepsilon^{(4)}_{i-1/2,j,k} &= max(0,\ k^{(4)} - \varepsilon^{(2)}_{i-1/2,j,k}) \end{aligned}$$

Typical values for the constant parameters are $0.5 \leq k^{(2)} \leq 1$ and $0.01 \leq k^{(4)} \leq 0.05$. For subsonic flows, the second order artificial dissipation is set to zero. The scaling factor can be estimated by evaluating the spectral radius of the Jacobian matrix $A_c = \partial(\bar{F}^I \cdot S)/\partial W$ as:

$$\Lambda_{i-1/2,j,k} = \lambda^i_{i-1/2,j,k} + \lambda^j_{i-1/2,j,k} + \lambda^k_{i-1/2,j,k}$$

with:

$$\lambda^m_{i-1/2,j,k} = \frac{1}{2}(\lambda^m_{i-1,j,k} + \lambda^m_{i,j,k})$$

and:

$$\lambda^m = |S_x^m u + S_y^m v + S_z^m w| + c\sqrt{(S_x^m)^2 + (S_y^m)^2 + (S_z^m)^2}$$

where c the speed of sound. In order to switch of the artificial dissipation terms in viscous region, a damping function can be included:

$$d_{i-1/2,j,k} = \left(\frac{V}{||\vec{U}_\infty||}\right)^{2n} d_{i-1/2,j,k}$$

with $n = 1,2$ or 3, $V = sqrt(u^2+v^2+w^2)$ and $||\vec{U}_\infty||$ the magnitude of the freestream velocity.

Roe's upwind scheme

The flux-difference splitting schemes evaluate the convective fluxes at a face of the control volume from the left and right state by solving the Riemann problem. The two states are in general discontinuous and the flux-difference splitting computes the intermediate flux according to the propagation of wave components (both the direction and the information itself). In Roe's scheme, an approximate Riemann solver is used. In this section, the second order Total Variation Diminishing (TVD) [Har83] version of Roe's scheme is presented. The Monotone Upwind Schemes for Conservation Laws (MUSCL) extrapolation [Yee97] is also applied. The inviscid flux at the $(i+1/2,j,k)$ cell face of the control volume (i,j,k) reads:

$$\begin{aligned} F^I_{i+1/2,j,k} &= \tfrac{1}{2}\left(F^I(W^L_{i+1/2,j,k}) + F^I(W^R_{i+1/2,j,k})\right) - \\ &\quad \tfrac{1}{2}\left|\bar{A}_{roe}(W^L_{i+1/2,j,k}, W^R_{i+1/2,j,k})\right|\left(W^R_{i+1/2,j,k} - W^L_{i+1/2,j,k}\right) \end{aligned}$$

where $W^L_{i+1/2,j,k}$ and $W^R_{i+1/2,j,k}$ the values of the conservative variables at the left and right state extrapolated on the cell side. The $\bar{A}_{roe}$ matrix is Roe's approximate Riemann solver and is derived directly from the convective flux Jacobian $A_c = \partial F^I/\partial W$ (see Appendix B.1) when the flow variables are replaced by the averaged values:

$$\begin{aligned} \overline{\rho} &= \sqrt{\rho_R \rho_L} \\ \overline{u_j} &= [(u_j\sqrt{\rho})^R + (u_j\sqrt{\rho})^L]/(\sqrt{\rho^R} + \sqrt{\rho^L}) \\ \overline{H} &= [(H\sqrt{\rho})^R + (H\sqrt{\rho})^L]/(\sqrt{\rho^R} + \sqrt{\rho^L}) \end{aligned}$$

with $H = E + \frac{p}{\rho}$ the total enthalpy. Since $\bar{A}_{roe}(W^L, W^R)$ has a complete set of real eigenvalues and eigenvectors, the $|\bar{A}_{roe}|$ is calculated from:

$$|\bar{A}_{roe}| = \bar{T}|\bar{\Lambda}_{roe}|\bar{T}^{-1}$$

where $\bar{T}$ and $\bar{T}^{-1}$ the right and left eigenvectors of $\bar{A}_{roe}$ and $\bar{\Lambda}_{roe}$ the diagonal matrix of its eigenvalues (see Appendix B.1). These can be evaluated from the averaged

values. The absolute eigenvalues are redefined to avoid the violation of the entropy condition due to shock expansion:

$$|\bar{\lambda}^k_{roe}| = \begin{cases} |\bar{\lambda}^k_{roe}| & if \;\; |\bar{\lambda}^k_{roe}| \geq \varepsilon \\ \\ \frac{1}{2\varepsilon}\left[(\bar{\lambda}^k_{roe})^2 + \varepsilon^2\right] & if \;\; \bar{\lambda}^k_{roe} \leq \varepsilon \end{cases}$$

where ε is scaled with the free stream velocity, the speed of sound and the surface vector at the interface as: $\varepsilon = \varepsilon_0(U_\infty + c_\infty)|s|$. The left and right states at the (i,j,k) cell interfaces are derived from the MUSCL interpolation:

$$\begin{aligned} W^L_{i+1/2,j,k} &= W_{i,j,k} + \left(\tfrac{1+\bar{\Phi}}{4}\bar{\Delta}_{i+1/2,j,k} + \tfrac{1-\bar{\Phi}}{4}\bar{\Delta}_{i-1/2,j,k}\right) \\ \\ W^R_{i-1/2,j,k} &= W_{i,j,k} - \left(\tfrac{1+\bar{\Phi}}{4}\bar{\Delta}_{i-1/2,j,k} + \tfrac{1-\bar{\Phi}}{4}\bar{\Delta}_{i+1/2,j,k}\right) \end{aligned}$$

The parameter $\bar{\Phi}$ controls the accuracy of the TVD upwind scheme. Using $\bar{\Phi} = -1$ results in a second order fully upwind scheme and $\bar{\Phi} = 1/3$ in a scheme based on a third-order scheme for the scalar convection. The limited slopes can be calculated as:

$$\begin{aligned} \bar{\Delta}_{i+1/2,j,k} &= minmod\left[W_{i+1,j,k} - W_{i,j,k}, \omega(W_{i,j,k} - W_{i-1,j,k})\right] \\ \\ \bar{\Delta}_{i-1/2,j,k} &= minmod\left[W_{i,j,k} - W_{i-1,j,k}, \omega(W_{i+1,j,k} - W_{i,j,k})\right] \end{aligned}$$

with $1 \leq \omega \leq (3-\bar{\Phi})/(1-\bar{\Phi})$ a compression parameter. Practically, the upper limit of ω is always used. The *minmod* function is defined as:

$$minmod(u,v) = \begin{cases} u & if \;\; |u| < |v| \;\; and \;\; uv > 0 \\ v & if \;\; |u| > |v| \;\; and \;\; uv > 0 \\ 0 & if \;\; uv < 0 \end{cases}$$

Viscous fluxes

The control volume for the viscous fluxes F^V is set the same as for the inviscid fluxes. Similarly to the convective fluxes using a second-order central scheme, the viscous fluxes through the $(i-1/2,j,k)$ face of the control volume (i,j,k) are:

$$F^V_{i-1/2,j,k} = F^V(W_{i-1/2,j,k}) \;\; with \;\; W_{i-1/2,j,k} = \frac{1}{2}(W_{i,j,k} + W_{i-1,j,k})$$

where the viscous flux tensor is given by $\bar{F}^V = (f_v, g_v, h_v)$. The values of the velocity components, the viscosity and the heat conduction coefficient are linearly interpolated at each face. The evaluation of the temperature and velocity gradients is done using Green's theorem. By shifting the control volume appropriately, we define a new domain with its faces passing through the cell centers of the discretized domain. To calculate the gradients of a value ϕ at the center of this shifted control volume:

$$\nabla\phi = \frac{\int_{\tilde{\Omega}} \nabla\phi \tilde{\Omega}}{\int_{\tilde{\Omega}} d\tilde{\Omega}} = \frac{1}{\tilde{\Omega}} \int_{\partial\tilde{\Omega}} \phi d\tilde{S} \tag{2.7}$$

with $\tilde{\Omega}$ the shifted control volume and $d\tilde{S}$ the face pacing through the cell centers. At the cell corners, i.e. the rest of the faces of the shifted control volume, the average values of the variables are used. The contributions of the viscous fluxes can be summed up, completing the spatial discretization.

2.1.3 Temporal discretization

The separate temporal and spatial discretization of the governing equations leads for a control volume $I \equiv (i, j, k)$ to a system of coupled ordinary differential equations to be integrated in time:

$$\frac{d(\Omega W)_I}{dt} = -R_I$$

Assuming a static grid, the time derivative can be approximated [CS88] by the following linear two-step method:

$$(1+\xi)\Omega\frac{\Delta W^n}{\Delta t^n} - \xi\Omega\frac{\Delta W^{n-1}}{\Delta t^{n-1}} = -\left(\theta R^{n+1} + (1-\theta+\beta)R^n - \beta R^{n-1}\right) \tag{2.8}$$

where $\Delta W^n = W^{n+1} - W^n$. For simplicity the cell indices are omitted here. For constant time step, the time increment is $\Delta t^n = \Delta t^{n-1} = \Delta t$. For the family of implicit schemes ($\theta \neq 0$) the condition for second-order accuracy in time is $\beta + \theta = \xi + 1/2$ and the additional condition for third-order accuracy is $\xi = 2\theta - 5/6$. For unsteady flows, the second-order implicit backward-difference scheme is derived with $\theta = 1$, $\xi = 1/2$ and $\beta = 0$ for a constant time step. For the first time step, since W^{-1} is not available, the backward Euler scheme can be used, derived by setting $\xi = 0$. Since this scheme is only first order accurate, the procedure might require the reduction of the first time step.

Dual time stepping

The dual time-stepping technique is based on the second-order time accurate version of Eq. 2.8. We start by building the unsteady residual $\mathscr{R}$ as:

$$\begin{aligned}\mathscr{R}(W^{n+1}) &= (1+\xi)\Omega^{n+1}\tfrac{\Delta W^n}{\Delta t} - \xi\Omega^n\tfrac{\Delta W^{n-1}}{\Delta t} + \theta R^{n+1} + (1-\theta+\beta)R^n - \beta R^{n-1} \\ &= \theta R^{n+1} + (1+\xi)\Omega^{n+1}\tfrac{W^{n+1}}{\Delta t^n} + Q\end{aligned} \tag{2.9}$$

where all the terms constant during the time-stepping are gathered in the source term Q. The following system of ordinary differential equations can be solved:

$$\frac{d(\Omega^{n+1}U)}{dt'} + \mathscr{R}(U) = 0 \tag{2.10}$$

where $U \approx W^{n+1}$ and t' a fictitious time. Integrating Eq. 2.10 until a steady state is reached will provide a solution for each Δt time step. In the case of moving/deformable grids, the Ω^{n+1} has to satisfy the Geometry Conservation Laws

(GCL). Any appropriate (explicit or implicit) time integration method can be used for the solution of Eq. 2.10. The implementation for an implicit scheme for the solution is examined. Linearization of the unsteady residual reads:

$$\mathscr{R}(U^{l+1}) \approx \mathscr{R}(U^l) + \left.\frac{\partial \mathscr{R}}{\partial U}\right|_l (U^{l+1} - U^l) \tag{2.11}$$

and the the flux Jacobian defined from Eq. 2.9:

$$\frac{\partial \mathscr{R}}{\partial U} = \theta \frac{\partial R}{\partial W} + (1+\xi)\frac{(\Omega^{n+1})}{\Delta t}\bar{\bar{I}}$$

with $\bar{\bar{I}}$ the identity matrix. Formulating Eq. 2.10 as an implicit scheme:

$$\frac{d(\Omega^{n+1}U^l)}{dt'} = -\mathscr{R}(U^{l+1}) \tag{2.12}$$

and combining with Eq. 2.11 and 2.1.3 gives:

$$\underbrace{\left(\frac{\Omega^{n+1}}{\Delta t'}\bar{\bar{I}} + (1+\xi)\frac{\Omega^{n+1}}{\Delta t}\bar{\bar{I}} + \theta \left.\frac{\partial R}{\partial W}\right|_l\right)}_{\text{implicit operator}} \Delta U^l = -\mathscr{R}(U^l) \tag{2.13}$$

where $\Delta U^l = U^{l+1} - U^l$. The above written equation can be solved with any methodology employed for a steady state problem.

Implicit time integration for steady state problems

The implicit operator is a sparse, nonsymmetric block matrix with a dimension equal to the total number of cells. It only affects the convergence rate of the scheme and has no influence on the accuracy of the steady state solution which depends only on the explicit operator on the right hand side of Eq. 2.13. The solution of Eq. 2.13 requires the inversion of the implicit operator. Iterative methods are employed in practical problems to limit the amount of memory and the computational cost needed in this procedure. In the absent of source terms, the Jacobian flux reads:

$$\frac{\partial R}{\partial W} = \sum_{m=1}^{N_F} \frac{\partial (F^I)_m}{\partial W}\Delta S_m - \sum_{m=1}^{N_F} \frac{\partial (F^V)_m}{\partial W}\Delta S_m$$

The derivative of the fluxes at the face $m = i+1/2$ can be written:

$$\begin{aligned} \frac{\partial (F^{I,V})_{i+1/2,j,k}}{\partial W} &= \frac{\partial}{\partial W}\left\{\frac{1}{2}\left[F^{I,V}(W^n_{i+1,j,k}) + F^I(W^n_{i,j,k})\right]\right\} \\ &= \frac{1}{2}\left[(A_{c,v})_{i+1,j,k} + (A_{c,v})_{i,j,k}\right] \end{aligned}$$

where $A_{c,v}$ the convective/viscous Jacobian flux. Equation 2.13, for $\theta = 1$ and constant volume, after linearization of the numerical fluxes, ca be re-written in a diagonally dominant form as:

$$\left[\Omega I \tfrac{1}{\Delta t'} + \Omega I \tfrac{(1+\xi)}{\Delta t}\right] \Delta U_{i,j,k} +$$

$$\left[A^+_{i+1/2} - A^-_{i-1/2} + A^+_{j+1/2} - A^-_{j-1/2} + A^+_{k+1/2} A^-_{k-1/2}\right] \Delta U_{i,j,k} +$$

$$A^-_{i+1/2} \Delta U_{i+1,j,k} + A^-_{j+1/2} \Delta U_{i,j+1,k} + A^-_{k+1/2} \Delta U_{i,j,k+1} -$$

$$A^+_{i-1/2} \Delta U_{i-1,j,k} - A^+_{j-1/2} \Delta U_{i,j-1,k} - A^+_{k-1/2} \Delta U_{i,j,k-1} \quad = \quad \mathscr{R}(U)_{i,j,k}$$

where the split Jacobian matrix in the term $A^-_{i+1/2}$ is evaluated at the cell side $i+1/2$ from the state in cell $(i+1, j, k)$, the term $A^+_{i-1/2}$ at the cell side $i-1/2$ from cell $(i-1, j, k)$ etc. Following Yoon and Jameson [YJ86], the approximation used:

$$A^{\pm} = \frac{1}{2}(A \pm r_A I) \;\; with \;\; r_A = \kappa max(|\lambda_{A_c}|)$$

where λ_{A_c} the eigenvalues of A_c. The convergence and stability properties can be controlled through κ. The implementation of the Lower-Upper Symmetric Gauss-Seidel (LU-SGS) method is presented by decomposing the implicit operator into a sum of three matrices:

$$(\mathscr{L} + \mathscr{D} + \mathscr{U})\Delta U = -\mathscr{R}^n \tag{2.14}$$

with

$$\mathscr{L} \equiv -(A^+_{i-1/2})_{i-1,j,k} - (A^+_{j-1/2})_{i,j-1,k} - (A^+_{k-1/2})_{i,j,k-1}$$

$$\mathscr{D} \equiv \Omega_{i,j,k} I \tfrac{1}{\Delta t'} + \Omega_{i,j,k} I \tfrac{(1+\xi)}{\Delta t} +$$

$$\left(A^+_{i+1/2} - A^-_{i-1/2} + A^+_{j+1/2} - A^-_{j-1/2} + A^+_{k+1/2} A^-_{k-1/2}\right)_{i,j,k}$$

$$\mathscr{U} \equiv (A^-_{i+1/2})_{i+1,j,k} + (A^-_{j+1/2})_{i,j+1,k} + (A^-_{k+1/2})_{i,j,k+1}$$

The matrix $\mathscr{L}$ contains the lower triangular part, $\mathscr{U}$ the upper triangular part and $\mathscr{D}$ the main diagonal of the implicit operator. The system can be inverted using a Symmetric Successive Over Relaxation (SSOR) method which sweeps through the mesh on planes with constant $i+j+k$ (oblique planes). The SSOR method performs two seeps per iteration, one forward and one backward as:

$$(\mathscr{L} + \mathscr{D})\Delta U^{p+1/2} = -\mathscr{R}^n - \mathscr{U}\Delta U^p$$

$$(\mathscr{U} + \mathscr{D})\Delta U^{p+1} = -\mathscr{R}^n - \mathscr{L}\Delta U^{p+1/2}$$

In this way, the off-diagonal terms $\mathscr{U}\Delta U^p$ and $\mathscr{L}\Delta U^{p+1/2}$ become known from the previous part of the sweep and can be added to the right hand side. The LU-SGS method is obtained by factorizing the left hand side of Eq. 2.14 as:

$$(\mathscr{L}+\mathscr{D})\mathscr{D}^{-1}(\mathscr{D}+\mathscr{U})\Delta U = -\mathscr{R}^n$$

The scheme is inverted by a forward and a backward sweep:

$$\begin{aligned}(\mathscr{L}+\mathscr{D})\Delta U^* &= -\mathscr{R}^n \\ (\mathscr{U}+\mathscr{D})\Delta U &= \mathscr{D}\Delta U^*\end{aligned}$$

The LU-SGS method corresponds to the SSOR method if only one iteration is performed. Increasing the number of iterations - i.e. the number of forward and backward sweeps - improves the convergence rate particularly for high-aspect ratio cell grids. As the time step increases, the LU-SSOR method reduces to an approximate Newton's method and increases the dependence of the convergence rate on the initial solution.

Implicit treatment of the viscous terms

The contribution of the viscous terms should also be taken into account to ensure the stability of the LU-SGS method. The viscous flux vector F^V, being a function of the state vector and its gradients, can be linearized as:

$$\Delta F^V = \frac{\partial F^V}{\partial U_x}\Delta U_x + \frac{\partial F^V}{\partial U_y}\Delta U_y + \frac{\partial F^V}{\partial U_z}\Delta U_z + \frac{\partial F^V}{\partial U}\Delta U \tag{2.15}$$

where U_* the $(*)$ spatial derivative of the state vector. This can be simplified by expressing the state vector in primitive variables $W_p = (\rho, u, v, w, p)^T$ as:

$$\Delta F^V = \frac{\partial F^V}{\partial (W_p)_x}\frac{\partial W_p}{\partial U}\Delta U_x + \frac{\partial F^V}{\partial (W_p)}\frac{\partial W_p}{\partial U}\Delta U_y + \frac{\partial F^V}{\partial (W_p)_z}\frac{\partial W_p}{\partial U}\Delta U_z \tag{2.16}$$

where the last term of Eq. 2.15 is neglected. The derivation of the transformation matrix $\partial W_p/\partial U$ between primitive and conservative variables is straightforward. Performing a transformation to curvilinear coordinates:

$$\Delta U_\kappa = \frac{\partial(\Delta U)}{\partial \xi}\frac{\partial \xi}{\partial \kappa} + \frac{\partial(\Delta U)}{\partial \eta}\frac{\partial \eta}{\partial \kappa} + \frac{\partial(\Delta U)}{\partial \zeta}\frac{\partial \zeta}{\partial \kappa}$$

for $\kappa = x_1, x_2, x_3 (= x, y, z)$. The cross derivatives can be neglected and only derivatives normal to the surface are considered. Applying this to Eq. 2.16 for the viscous flux at the $i+1/2$ cell side gives in one dimension:

$$\Delta F^V = \frac{\partial F^V}{\partial (W_p)_{x_i}}\frac{\partial \xi}{\partial x_i}\bigg|_{i+1/2}\frac{\partial W_p}{\partial U}\bigg|_{i+1/2}(\Delta U_{i+1} - \Delta U_i) = B(\Delta U_{i+1} - \Delta U_i)$$

where all the terms can be evaluated at the cell surfaces using linear interpolation. The viscous Jacobian matrices with respect to primitive variables can be easily derived (see Appendix B.2). The metrics can be calculated as:

$$\left.\frac{\partial \xi}{\partial \kappa}\right|_{i+1/2} = \frac{1}{\tilde{\Omega}} S_{\kappa}^{i+1/2}$$

where $\tilde{\Omega} = 1/2(\Omega_{i+1} + \Omega_i)$ denotes the shifted control volume.

LU-SGS version for Roe's upwind scheme

Linearization of the numerical flux based on Roe's upwind scheme results in a diagonally dominant - but not overstabilized - linear system where the left hand side better matches the explicit residual. For one dimension[1], the linearization leads to the following scheme:

$$\begin{aligned}
\left[\Omega I \tfrac{1}{\Delta t'} + \Omega I \tfrac{(1+\xi)}{\Delta t}\right] \Delta U_i \quad &+ \\
\tfrac{1}{2}\alpha \left[|(\bar{A}_{roe})_{i+1/2}| + |(\bar{A}_{roe})_{i-1/2}|\right] \Delta U_i \quad &+ \\
\tfrac{1}{2}\alpha \left[A(U^R_{i+1/2}) - |(\bar{A}_{roe})_{i+1/2}|\right] \Delta U_{i+1} \quad &- \\
\tfrac{1}{2}\alpha \left[A(U^L_{i-1/2}) - |(\bar{A}_{roe})_{i-1/2}|\right] \Delta U_{i-1} \quad &= \quad \mathscr{R}(U)_i^{upw}
\end{aligned} \tag{2.17}$$

where $|\bar{A}_{roe}|$ has been assumed to be constant and α a factor resulting from the upwind extrapolation when the limiters are neglected. Finally, the inclusion of the viscous fluxes in the linearization gives:

$$\begin{aligned}
\left[\Omega I \tfrac{1}{\Delta t'} + \Omega I \tfrac{(1+\xi)}{\Delta t} + B_{i+1/2} + B_{i-1/2}\right] \Delta U_i \quad &+ \\
\tfrac{1}{2}\alpha \left[|(\bar{A}_{roe})_{i+1/2}| + |(\bar{A}_{roe})_{i-1/2}|\right] \Delta U_i \quad &+ \\
\left[\tfrac{1}{2}\alpha A(U^R_{i+1/2}) - \tfrac{1}{2}\alpha |(\bar{A}_{roe})_{i+1/2}| - B_{i+1/2}\right] \Delta U_{i+1} \quad &- \\
\left[\tfrac{1}{2}\alpha A(U^L_{i-1/2}) - \tfrac{1}{2}\alpha |(\bar{A}_{roe})_{i-1/2}| + B_{i-1/2}\right] \Delta U_{i-1} \quad &= \quad \mathscr{R}(U)_i^{upw}
\end{aligned} \tag{2.18}$$

LU-SGS version for the central scheme

In order to use a central scheme for the discretization of the convective fluxes, the implicit operator has to be modified. The fourth-order artificial dissipation terms have to be included for numerical stability. The same structure as in Eq. 2.17 is kept

[1] For ease of notation.

but the Roe matrices are replaced by the convective Jacobian A_c calculated with the arithmetic average of the state vector at the cell face. Once more, after linearization, the implicit operator for the central scheme can be written in one dimension as:

$$\begin{aligned}
&\left[\Omega I \tfrac{1}{\Delta t'} + \Omega I \tfrac{(1+\xi)}{\Delta t}\right] \Delta U_i + \varepsilon^{(4)}_{i+1/2} \Delta U_{i+2} + \varepsilon^{(4)}_{i-1/2} \Delta U_{i-2} \quad + \\
&\left[\tfrac{1}{2}\left(|A_{i+1/2}| + |A_{i-1/2}|\right) + 3(\varepsilon^{(4)}_{i+1/2} + \varepsilon^{(4)}_{i-1/2}) I\right] \Delta U_i \quad + \\
&\left[\tfrac{1}{2} A(U_{i+1}) - \tfrac{1}{2}|A_{i+1/2}| - (3\varepsilon^{(4)}_{i+1/2} + \varepsilon^{(4)}_{i-1/2}) I\right] \Delta U_{i+1} \quad - \\
&\left[\tfrac{1}{2} A(U_{i-1}) - \tfrac{1}{2}|A_{i-1/2}| + (3\varepsilon^{(4)}_{i-1/2} + \varepsilon^{(4)}_{i+1/2}) I\right] \Delta U_{i-1} \quad = \quad \mathscr{R}(U)^{cent}_i
\end{aligned} \tag{2.19}$$

The fourth-order dissipation coefficient is calculated as presented in Section 2.1.2. The resulting pentadiagonal (in 1D) block system is solved using the LU-SGS method. The viscous fluxes can easily be included in the linearization as in Eq. 2.18.

Convergence criterion

The L_2-norm of the residual is used as a measure of the rate of convergence. For implicit time stepping methods, the L_2-norm of the residual is calculated as:

$$||Res^n||_{L_2} = \frac{1}{\sum \Omega_{i,i,k}} \sqrt{\sum \left(\frac{\mathscr{R}^2_{i,j,k}}{V_{i,j,k}}\right)} \tag{2.20}$$

with $\mathscr{R}$ the explicit residual.

2.1.4 Boundary conditions

Boundary conditions are imposed using ghost cells, added outside the computational domain. The values of the state vector W are calculated from the prescribed boundary conditions. It is possible to fill the ghost cells with physical values only for the free-stream boundary condition; for a solid wall, no physical values exist. It is necessary to use extrapolation techniques that have correct damping properties, do not produce a false entropy layer on the wall and work independent of the flow case. Finally, for a multiblock strategy is, the block connectivity boundary conditions are introduced. Across the block boundary interfaces, the values of the state vector in the ghost cells are taken directly from the neighboring block.

For a multiblock strategy, the convergence rate degrades with the number of blocks, and the number of time steps needed to obtain a steady state solution increases significantly, especially for subsonic flows. To improve convergence and to avoid stability problems related to the large number of blocks, the LU-SGS method can be modified so that an update of the block connectivity boundary conditions is performed between each Gauss-Seidel sweep. Performing several sweeps can

help to better propagate information from one block to the other. The modified LU scheme converges to the singleblock solution of the linear system, the computational efficiency, however, is reduced due to the increase of the performed operations. Using the update between sweeps for a large number of blocks leads to a higher computational efficiency than the pure explicit coupling.

Wall boundary conditions

For an inviscid (slip) wall condition, the velocity vector must remain tangent to the surface. This translates to $\vec{u} \cdot \vec{n} = 0$. The vector of convective fluxes reduces to:

$$F^I\big|_{wall} = [0 \;\; n_x p_{wall} \;\; n_y p_{wall} \;\; n_z p_{wall} \;\; 0]^T$$

with p_{wall} the wall pressure and n_* the unit normal vector components of the wall surface. The wall pressure is extrapolated from the interior of the computational domain using a two-point:

$$p_{wall} = \frac{1}{2}(3p_1 - p_2)$$

or a three-point extrapolation formula:

$$p_{wall} = \frac{1}{8}(15p_1 - 10p_2 + 3p_3)$$

with p_i the pressure value of the i^{th} from the wall cell. To account for the stretching of the grid, the exact shell distance can be used to replace the constant coefficients in these expressions. The state vector values in the ghost cells can be calculated from the interior as:

$$W_0 = 2W_1 - W2$$

$$W_{-1} = 3W_1 - 2W2$$

where 0 and -1 the first and second ghost cells inside the wall region and 1,2 and 3, the first cell points just above the wall.

For a viscous flow over a solid wall, the nonslip boundary condition should be enforced. For a stationary wall this translate to $u = v = w = 0$ at the surface. The wall pressure and the convective fluxes are treated in the same was as before. For completing the state vector in the ghost cells:

$$\rho_0 = \rho_1 \;\; , \;\; \rho_{-1} = \rho_2 \;\; , \;\; E_0 = E_1 \;\; , \;\; E_{-1} = E_2$$

$$\vec{u}_0 = -\vec{u}_1 \;\; , \;\; \vec{u}_{-1} = -\vec{u}_2$$

for an adiabatic wall. For a given wall temperature, the pressure is prescribed as $p_{-1} = p_0 = p_1$ and the temperature can be linearly interpolated. The density and the total energy are evaluated from the interpolated values.

Characteristic boundary conditions

The size of the physical domain is, in general, infinite. In the finite computational domain, artificial far field boundaries are introduced to prevent waves leaving the domain from being reflected. To this end, the physical variables are extrapolated using the characteristic variables. As the wave propagation is connected to the convective part of the Navier-Stokes, only the convective flux Jacobian A_c has to be considered. Depending on the sign of the eigenvalues of A_c, the information can be travelling towards (for positive eigenvalues) or outwards with respect to the computational domain. The number of conditions imposed outside the boundary is equal to the number of positive eigenvalues. The rest are determined from inside the domain.

For a supersonic inflow, all the conservative variables on the boundary are determined from the freestream values. Likewise, in a supersonic outflow, all the conservative variables at the boundary must be calculated from the solution inside the domain. However, for a subsonic inflow, only four characteristic variables are prescribed based on the freestream values and one should be extrapolated from the interior of the computational domain. This leads to:

$$\begin{aligned} p_{boundary} &= 1/2\{p_a + p_{in} - \rho_0 c_0\,[\vec{n}\cdot(\vec{u}_a - \vec{u}_{in})]\} \\ \rho_{boundary} &= \rho_a + (p_{boundary} - p_a)/c_0^2 \\ \vec{u}_{boundary} &= \vec{u}_a - \vec{n}(p_a - p_{boundary})/(\rho_0 c_0) \end{aligned}$$

where the index 0 refers to the reference state, the *in* to the interior point and *a* to the point outside the boundary. The unit normal vector $\vec{n} = [n_x \;\; n_y \;\; n_z]^T$ of the boundary surface points always out of the domain.

Subsonic inlet & outlet

As mentioned, one characteristic variable has to be interpolated from inside the computational domain for the subsonic inlet case. The speed of sound at the boundary is calculated from:

$$c_{boundary} = \frac{-\mathscr{H}^-(\gamma-1)}{(\gamma-1)cos^2\theta+2}\left\{1 + cos\theta\sqrt{\frac{[(\gamma-1)cos^2\theta+2]c_0^2}{(\gamma-1)(\mathscr{H}^-)^2} - \frac{\gamma-1}{2}}\right\}$$

where $\mathscr{H}$ the outgoing Riemann invariant:

$$\mathscr{H}^- = \vec{u}_{in}\cdot\vec{n} - \frac{2c_{in}}{\gamma-1}$$

c_0 the stagnation speed of sound and θ the flow angle relative to the boundary. The static temperature, pressure, density and velocity magnitude at the inlet are

calculated from:

$$\begin{aligned} T_{boundary} &= T_{t0}\left(\frac{c^2_{boundary}}{c^2_0}\right) \\ p_{boundary} &= p_{t0}\left(\frac{T_{boundary}}{T_{t0}}\right)^{\gamma/(\gamma-1)} \\ \rho_{boundary} &= \frac{p_{boundary}}{RT_{boundary}} \\ ||\vec{u}_{boundary}||_2 &= \sqrt{2c_p(T_{t0}-T_{boundary})} \end{aligned}$$

The index t here refers to total quantities. The velocity components at the inlet are obtained for the prescribed flow angles. The subsonic outlet boundary can be treated similar to the outflow boundary condition previously examined, by replacing the p_a ambient value with a prescribed static pressure at the outlet.

2.1.5 Preconditioning method

Solving the compressible equations for very low Mach numbers can significantly increase the computational cost until convergence is reached. Preconditioning methods are implemented to control the eigenvalues of the system and maintain effective convergence rates at low Mach numbers by changing the differential equations to be solved. Preconditioning methods are applicable to all Mach numbers making the solution of the compressible Navier-Stokes the best approach to examine high-speed flow cases with regions of low velocity or low-speed flows with density changes due to heat sources.

Here, the preconditioning method developed for the Euler equations is examined. The method can be directly applied to the full Navier-Stokes equations by adding the inviscid, viscous and artificial fluxes and multiply them with the preconditioning matrix. In 3D Cartesian coordinates, the unsteady compressible Euler equations in conservative form are written:

$$\frac{\partial W}{\partial t}+\frac{\partial f}{\partial x}+\frac{\partial g}{\partial y}+\frac{\partial h}{\partial z}=0 \tag{2.21}$$

where:

$$W=(\rho \;\; \rho u \;\; \rho v \;\; \rho w \;\; \rho E)^T$$

and

$$f=\begin{Bmatrix} \rho u \\ \rho u^2+p \\ \rho uv \\ \rho uw \\ u(\rho E+p) \end{Bmatrix},\; g=\begin{Bmatrix} \rho v \\ \rho vu \\ \rho v^2+p \\ \rho vw \\ v(\rho E+p) \end{Bmatrix},\; h=\begin{Bmatrix} \rho w \\ \rho wu \\ \rho wv \\ \rho w^2+p \\ w(\rho E+p) \end{Bmatrix}$$

the convective fluxes. The preconditioned Euler equations are written:

$$P^{-1}\frac{\partial W}{\partial t}+\frac{\partial f}{\partial x}+\frac{\partial g}{\partial y}+\frac{\partial h}{\partial z}=0$$

where:

$$P^{-1}=\left\{\begin{array}{ccccc}
\frac{(\gamma-1)V^2}{2\beta^2} & \frac{(\gamma-1)u}{\beta^2} & \frac{(\gamma-1)v}{\beta^2} & \frac{(\gamma-1)w}{\beta^2} & \frac{(\gamma-1)}{\beta^2} \\
u\frac{(\gamma-1)V^2}{2\beta^2}-1 & \frac{(\gamma-1)u^2}{\beta^2}+1 & \frac{(\gamma-1)uv}{\beta^2} & \frac{(\gamma-1)uw}{\beta^2} & \frac{(\gamma-1)u}{\beta^2} \\
v\frac{(\gamma-1)V^2}{2\beta^2}-1 & \frac{(\gamma-1)uv}{\beta^2} & \frac{(\gamma-1)v^2}{\beta^2}+1 & \frac{(\gamma-1)vw}{\beta^2} & \frac{(\gamma-1)v}{\beta^2} \\
w\frac{(\gamma-1)V^2}{2\beta^2}-1 & \frac{(\gamma-1)uw}{\beta^2} & \frac{(\gamma-1)vw}{\beta^2} & \frac{(\gamma-1)w^2}{\beta^2}+1 & \frac{(\gamma-1)w}{\beta^2} \\
\frac{(\theta+2)(\gamma-1)V^2}{2}-\gamma E & u\psi & v\psi & w\psi & \psi+1
\end{array}\right\}$$

with $\psi=(\gamma-1)(\theta+1)$, $\theta=(\rho E+p)/(\rho\beta^2)-1$, $V^2=(u^2+v^2+w^2)$ and β a free parameter. For the solution of the system, only the spatial derivatives are multiplied with the preconditioning matrix. The solution is no longer time-accurate, the stationary solution however remains the same. A new set of eigenvalues and eigenvectors are derived that correspond to the matrix PA_c with $A_c=\partial F^I/\partial W$, $F^I=(f,g,h)$. The new eigenvalues are:

$$\lambda_{pre}=[U\ \ U\ \ U\ \ \lambda_+\ \ \lambda_-]^T$$

with

$$\lambda_\pm=\frac{1}{2}(\zeta V\pm\sqrt{\zeta^2V^2+4\beta^2(1-\frac{V^2}{\alpha^2})})$$

and $\zeta=1+\beta^2/\alpha^2$. The parameter β^2 should be proportional to V^2 and is typically expressed as: $\beta^2=max(V^2,K)$ where K is a constant that depends on the inflow conditions and the number of mesh nodes. For the artificial compressibility method, the parameter can be computed as:

$$\beta^2=max(K||\vec{U}_\infty||,CV^2)$$

with C a constant for the local velocity. The preconditioning matrix is added in the calculation of the residual. The new eigenvalues are included in the numerical scaling of the artificial dissipation and the characteristic boundary conditions.

2.1.6 Arbitrary Lagrangian Eulerian method for deformable grids

In order to take into account the mesh deformation in time, the Arbitrary Lagrangian Eulerian (ALE) formulation is introduced in the Navier-Stokes system of equations. The formulation is based on the spatial discretization of the moving fluid. A system of mixed coordinates is used, expressed by:

$$\vec{\xi}=\vec{\xi}(\vec{x},t)$$

where $\vec{\xi} = (\xi_1, \xi_2, \xi_3)$ the coordinates of a point P in an arbitrary domain of volume Ω' and $\vec{x} = (x, y, z) = (x_1, x_2, x_3)$ a point P_0 in a the reference domain with Ω_0. The determinant of the transformation Jacobian between the two domains is:

$$J = \left| \frac{\partial \xi_i}{\partial x_j} \right|$$

with J satisfying the following equations:

$$d\Omega' = J(\vec{x}, t) d\Omega_0 \text{ and } \left. \frac{\partial J}{\partial t} \right|_{\vec{x}} = J(\nabla_{\vec{\xi}} \cdot \vec{u_g})$$

where $\vec{u_g} = \partial \xi_i / \partial t$ the velocity of the point P with respect to the reference domain. A physical variable ϕ at the point P can be expressed in the reference domain as:

$$\phi(\vec{\xi}(\vec{x}, t)) = \hat{\phi}(\vec{x}, t)$$

Multiplying by J and applying a derivation in time gives:

$$\left. \frac{\partial (J\hat{\phi})}{\partial t} \right|_{P_0} = \left. \frac{\partial (J\phi)}{\partial t} \right|_P + \frac{\partial (J\phi)}{\partial \xi_i} \frac{\partial \xi_i}{\partial t} = J \left[\left. \frac{\partial \phi}{\partial t} \right|_P + \nabla_{\vec{\xi}} \cdot (\phi \vec{u_g}) \right]$$

Applying this to the state vector written in the reference domain and integrating:

$$\int_{\Omega_0} \frac{\partial (J\hat{W})}{\partial t} d\Omega_0 = \int_{\Omega_0} J \left[\frac{\partial W}{\partial t} + \nabla_{\vec{\xi}} \cdot (W \vec{u_g}) \right] d\Omega_0$$

In the same manner, the numerical fluxes can be expressed as:

$$\int_{\Omega_0} \nabla_{\vec{x}} \hat{\bar{F}} d\Omega_0 = \int_{\Omega_0} J \nabla_{\vec{\xi}} \bar{F} d\Omega_0$$

As a result, Eq. 2.2 can be written:

$$\int_{\Omega_0} J \left[\frac{\partial W}{\partial t} + \nabla_{\vec{\xi}} \cdot (W \vec{u_g}) \right] d\Omega_0 + \int_{\Omega_0} J \nabla_{\vec{\xi}} \bar{F} d\Omega_0 = 0$$

$$\int_{\Omega'} \left[\frac{\partial W}{\partial t} + \nabla_{\vec{\xi}} \cdot (W \vec{u_g}) \right] d\Omega' + \int_{\Omega'} \nabla_{\vec{\xi}} \bar{F} d\Omega' = 0$$

$$\frac{\partial}{\partial t} \int_{\Omega'} W d\Omega' + \int_{\Omega'} W \frac{\partial (d\Omega')}{\partial t} + \int_{\Omega'} \nabla_{\vec{\xi}} \cdot (\bar{F} - W \vec{u_g}) \, d\Omega' = 0$$

and applying the Gauss divergence theorem:

$$\frac{\partial}{\partial t} \int_{\Omega'} W d\Omega' + \int_{\partial \Omega'} (F - W \vec{u_g}) \cdot \vec{n}(t) dS' = 0 \tag{2.22}$$

where the temporal variation of the domain has been eliminated. It can be seen that Eq. 2.22 which is the expression of the Navier-Stokes equations for a arbitrarily

moving grid is identical to the formulation derived for fixed grids. As a result, the solving procedure demonstrated up to now is directly applicable to the solution of the moving grid. The mesh movement is taken into account through a flux term to be added to the convective fluxes. The fluxes through a moving face can be expressed as:

$$\tilde{F} = F - (W\vec{u_g}) \cdot \vec{n}$$

Geometric Conservation Laws (GCL) can be added to preserve the conservative properties of the numerical schemes used and avoid the apparition of numerical discontinuities. In [ZRTC93] a Volume Conservation Law (VCL) and a Surface Conservation Law (SCL) methodology can be found.

Modification of Roe's upwind scheme

We will examine the modifications of Roe's upwind scheme in the context of an ALE formulation. By replacing the inviscid fluxes with $\tilde{F}$ containing the mesh movement fluxes, we get at the $(i+1/2, j, k)$ cell face of the control volume (i, j, k):

$$\begin{aligned}\tilde{F}_{i+1/2,j,k} &= \tfrac{1}{2}\Big[F^I(W^L_{i+1/2,j,k}) + F^I(W^R_{i+1/2,j,k}) - \\ &\quad (\vec{u}_{g_{i+1/2,j,k}} \cdot \vec{S}^{i+1/2,j,k})(W^L_{i+1/2,j,k} - W^R_{i+1/2,j,k})\Big] - \\ &\quad \tfrac{1}{2}\Big|\bar{A}_{roe}(W^L_{i+1/2,j,k}, W^R_{i+1/2,j,k}) - \\ &\quad (\vec{u}_{g_{i+1/2,j,k}} \cdot \vec{S}^{i+1/2,j,k})\bar{\bar{I}}\Big|\left(W^R_{i+1/2,j,k} - W^L_{i+1/2,j,k}\right)\end{aligned}$$

with $\bar{\bar{I}}$ the identity tensor. The grid movement adds a term in the flux calculation and results in the modification of the eigenvalues used in the calculation of the Roe matrix. The calculation now writes:

$$|\tilde{\bar{A}}_{roe}| = \bar{T}|\bar{\Lambda}_{roe} - (\vec{u}_{g_{i+1/2,j,k}} \cdot \vec{S}^{i+1/2,j,k})\bar{\bar{I}}|\bar{T}^{-1}$$

2.1.7 Turbulence modelling

The Navier-Stokes equations for a compressible Newtonian fluid are written without source terms:

$$\begin{aligned}\frac{\partial \rho}{\partial t} + \frac{\partial}{\partial xi}(\rho u_i) &= 0 \\ \frac{\partial}{\partial t}(\rho u_i) + \frac{\partial}{\partial x_j}(\rho u_j u_i) &= -\frac{\partial p}{\partial x_i} + \frac{\partial \tau_{ij}}{\partial x_j} \\ \frac{\partial}{\partial t}(\rho E) + \frac{\partial}{\partial x_j}(\rho u_j H) &= \frac{\partial u_i \tau_{ij}}{\partial x_j} + \frac{\partial q_j}{\partial x_j}\end{aligned} \tag{2.23}$$

The viscous stress tensor τ_{ij} is defined as:

$$\tau_{ij} = \mu\left(\frac{\partial u_i}{\partial x_j} + \frac{\partial u_j}{\partial x_i}\right) - \frac{2\mu}{3}\frac{\partial u_m}{\partial x_m}\delta_{ij} = 2\mu s_{ij} - \frac{2\mu}{3}\frac{\partial u_m}{\partial x_m}\delta_{ij}$$

with δ_{ij} the Kronecker delta and s_{ij} the strain-rate tensor. Considering the Reynolds ensemble averaging on a flow quantity ϕ:

$$\bar{\phi} = \lim_{N\to\infty} \frac{1}{N} \sum_{m=1}^{N} \phi_m$$

and the Favre (mass) ensemble averaging:

$$\tilde{\phi} = \frac{1}{\bar{\rho}} \lim_{N\to\infty} \frac{1}{N} \sum_{m=1}^{N} \phi_m$$

the various flow quantities are decomposed into a mean and a fluctuating part as:

$$\rho = \bar{\rho} + \rho' \ , \ p = \bar{p} + p' \ , \ q_i = \bar{q}_i + q_i'$$

$$u_i = \tilde{u}_i + u_i'' \ , \ H = \tilde{H} + H'' \ , \ E = \tilde{E} + E''$$

where the Reynolds decomposition is employed for the density, pressure and the heat flux vector and the Favre decomposition for the velocity, the total enthalpy and the total energy. The mass averaged conservation equations are written:

$$\begin{aligned}
\tfrac{\partial \bar{\rho}}{\partial t} + \tfrac{\partial}{\partial xi}(\bar{\rho}\tilde{u}_i) &= 0 \\
\tfrac{\partial}{\partial t}(\bar{\rho}\tilde{u}_i) + \tfrac{\partial}{\partial x_j}(\bar{\rho}\tilde{u}_j\tilde{u}_i) &= -\tfrac{\partial \bar{p}}{\partial x_i} + \tfrac{\partial}{\partial x_j}(\tilde{\tau}_{ij} - \bar{\rho}\widetilde{u_j'' u_i''}) \\
\tfrac{\partial}{\partial t}(\bar{\rho}\tilde{E} + \tfrac{\bar{\rho}\widetilde{u_j'' u_i''}}{2}) + \tfrac{\partial}{\partial x_j}(\bar{\rho}\tilde{u}_j\tilde{H} + \tilde{u_j}\tfrac{\bar{\rho}\widetilde{u_i'' u_i''}}{2}) &= \tfrac{\partial}{\partial x_j}[\tilde{u}_i(\tilde{\tau}_{ij} - \bar{\rho}\widetilde{u_j'' u_i''})] \\
&+ \tfrac{\partial}{\partial x_j}(\bar{q}_j - \bar{\rho}\widetilde{u_j'' H''} + \widetilde{\tau_{ij} u_i''} - \tfrac{1}{2}\bar{\rho}\widetilde{u_j'' u_i'' u_i''})
\end{aligned}$$

with $\bar{P} = \bar{\rho} R \tilde{T}$ and $\widetilde{\rho u_i} = \bar{\rho}\tilde{u}_i$. The Favre-averaged Reynolds stress tensor is defined as:

$$t_{ij} = -\bar{\rho}\widetilde{u_i'' u_j''}$$

and the turbulent kinetic energy per unit volume (i.e. the kinetic energy of the turbulent fluctuations) as:

$$\bar{\rho}K = \frac{1}{2}\bar{\rho}\widetilde{u_i'' u_i''}$$

The turbulent transport of heat is given from:

$$q_{ti} = \bar{\rho}\widetilde{u_i'' H''}$$

The term $\widetilde{\tau_{ij} u_i''}$ corresponds to the molecular diffusion of the turbulent kinetic energy K and the term $1/2\bar{\rho}\widetilde{u_j'' u_i'' u_i''}$ to the turbulent transport of K. To derive the K transport equation, the primitive-variable form of the momentum equation is multiplied by

u_i'' and the average is taken. After proper mathematical manipulations, the exact equation writes:

$$\bar{\rho}\frac{\partial K}{\partial t}+\bar{\rho}\tilde{u}_j\frac{\partial K}{\partial x_j} = \underbrace{t_{ij}\frac{\partial \tilde{u}_i}{\partial x_j}}_{\text{production}} - \underbrace{\widetilde{\tau_{ij}\frac{\partial u_i''}{\partial x_j}}}_{\text{dissipation rate}} - \underbrace{\widetilde{u_i''}\frac{\partial \bar{p}}{\partial x_i}}_{\text{pressure work}} + \underbrace{\widetilde{p'\frac{\partial u_i''}{\partial x_i}}}_{\text{pressure dilatation}}$$

$$+ \frac{\partial}{\partial x_j}\Big(\underbrace{\widetilde{\tau_{ij}u_i''}}_{\text{molecular diffusion}} - \underbrace{\bar{\rho}\widetilde{u_j''K}}_{\text{turbulent transport}} - \underbrace{\widetilde{p'u_j''}}_{\text{pressure diffusion}} \Big)$$

The equation for the complete Reynolds stress tensor can be derived in the same manner and assumes a similar form. We denote the production term as $\mathscr{P}$ and the dissipation rate is written as $\bar{\rho}\varepsilon$. It should be noted that both the pressure work and the dilatation terms vanish for incompressible flows. The whole set of Favre-averaged equation in conservative form is summarized:

$$\begin{aligned}
\frac{\partial \bar{\rho}}{\partial t}+\frac{\partial}{\partial xi}(\bar{\rho}\tilde{u}_i) &= 0 \\
\frac{\partial}{\partial t}(\bar{\rho}\tilde{u}_i)+\frac{\partial}{\partial x_j}(\bar{\rho}\tilde{u}_j\tilde{u}_i) &= -\frac{\partial \bar{p}}{\partial x_i}+\frac{\partial}{\partial x_j}(\tilde{\tau}_{ij}+t_{ij}) \\
\frac{\partial}{\partial t}(\bar{\rho}E_t)+\frac{\partial}{\partial x_j}(\bar{\rho}\tilde{u}_jH_t) &= \frac{\partial}{\partial x_j}[\tilde{u}_i(\tilde{\tau}_{ij}-t_{ij})] \\
&+ \frac{\partial}{\partial x_j}(\bar{q}_j-q_{tj}+\widetilde{\tau_{ij}u_i''}-\bar{\rho}\widetilde{u_j''K}) \\
\bar{\rho}\frac{\partial K}{\partial t}+\bar{\rho}\tilde{u}_j\frac{\partial K}{\partial x_j} &= \mathscr{P}-\bar{\rho}\varepsilon-\widetilde{u_i''}\frac{\partial \bar{p}}{\partial x_i}+\widetilde{p'\frac{\partial u_i''}{\partial x_i}} \\
&+ \frac{\partial}{\partial x_j}\left(\widetilde{\tau_{ij}u_i''}-\bar{\rho}\widetilde{u_j''K}-\widetilde{p'u_j''}\right)
\end{aligned}$$

with $E_t=\tilde{E}+K$ and $H_t=\tilde{H}+K$. As the $\mathscr{P}$ and the $\bar{\rho}\varepsilon$ terms describe inter-scale energy transfers, they should cancel out, leaving only two terms of turbulent spatial transfers (i.e. the molecular diffusion and the turbulent transport of K) in the conservation of energy equation.

Modelling closure

Based on the Boussinesq hypothesis, the Favre/Reynolds stress tensor can be rewritten as a linear function of the mean strain rate, in analogy to the shear tensor for the laminar flow. This reads:

$$t_{ij}=2\mu_t\tilde{s}_{ij}-\frac{2}{3}\left(\mu_t\frac{\partial \tilde{u}_m}{\partial x_m}\delta_{ij}-\bar{\rho}K\right)\delta_{ij}$$

where μ_t stands for the eddy viscosity that depends on local flow conditions and expresses the proportionality between the Reynolds stresses and the strain rate. The

turbulent heat-flux vector can be set proportional to the mean temperature gradient as:

$$q_{ti} = -\frac{\mu_t C_p}{Pr_t}\frac{\partial \tilde{T}}{\partial x_i} = -k_t \frac{\partial \tilde{T}}{\partial x_i}$$

with k_t the turbulent thermal conductivity coefficient and Pr_t the turbulent Prandtl number, assumed to be constant. The molecular diffusion and the turbulent transport of K can be grouped together and approximated as:

$$\widetilde{\tau_{ij}u_i''} - \bar{\rho}\widetilde{u_j''K} = (\mu + \frac{\mu_t}{\sigma_K})\frac{\partial K}{\partial x_j}$$

with σ_K a constant balancing the effects of turbulent and molecular viscosity on the diffusion of the turbulent kinetic energy. The dissipation rate is written according to the turbulent kinetic energy as:

$$\bar{\rho}\varepsilon = \widetilde{\tau_{ij}\frac{\partial u_i}{\partial x_j}}$$

Concerning the remaining terms (i.e. pressure dilatation, diffusion and work), there is a lack of a generally accepted modelling approach. These terms are often ignored for incompressible flows while various (non-universal) empirical proposals exist for compressible flows, depending on the turbulent modelling approach followed.

First-order closures: $K-\varepsilon$ model

The $K-\varepsilon$ model introduces two transport equations, one for the turbulent kinetic energy and one for the dissipation. Inherently, it is a model well adapted to high Reynolds number flows. The Navier-Stokes equations for turbulent flows for a viscous, perfect gas can be written for the averaged variables and with the addition of a source term:

$$\frac{\partial}{\partial t}(W) + \frac{\partial}{\partial x}(f - f_v) + \frac{\partial}{\partial y}(g - g_v) + \frac{\partial}{\partial z}(h - h_v) = S \tag{2.24}$$

where W is given by:

$$W = (\bar{\rho}\ \ \bar{\rho}\tilde{u}\ \ \bar{\rho}\tilde{v}\ \ \bar{\rho}\tilde{w}\ \ \bar{\rho}\tilde{E}\ \ \bar{\rho}K\ \ \bar{\rho}\varepsilon)^T$$

The convective fluxes are:

$$f = \begin{Bmatrix} \bar{\rho}\tilde{u} \\ \bar{\rho}\tilde{u}^2 + p^* \\ \bar{\rho}\tilde{u}\tilde{v} \\ \bar{\rho}\tilde{u}\tilde{w} \\ \tilde{u}(\bar{\rho}\tilde{E} + p^*) \\ \bar{\rho}\tilde{u}K \\ \bar{\rho}\tilde{u}\varepsilon \end{Bmatrix},\ g = \begin{Bmatrix} \bar{\rho}\tilde{v} \\ \bar{\rho}\tilde{v}\tilde{u} \\ \bar{\rho}\tilde{v}^2 + p^* \\ \bar{\rho}\tilde{v}\tilde{w} \\ \tilde{v}(\bar{\rho}\tilde{E} + p^*) \\ \bar{\rho}\tilde{v}K \\ \bar{\rho}\tilde{v}\varepsilon \end{Bmatrix},\ h = \begin{Bmatrix} \bar{\rho}\tilde{w} \\ \bar{\rho}\tilde{w}\tilde{u} \\ \bar{\rho}\tilde{w}\tilde{v} \\ \bar{\rho}\tilde{w}^2 + p^* \\ \tilde{w}(\bar{\rho}\tilde{E} + p^*) \\ \bar{\rho}\tilde{w}K \\ \bar{\rho}\tilde{w}\varepsilon \end{Bmatrix}$$

where $p^* = \bar{p} + 2/3\bar{\rho}K$. The viscous fluxes and the source term are defined as:

$$f_v = \begin{Bmatrix} 0 \\ \delta\tau_{xx} \\ \delta\tau_{xy} \\ \delta\tau_{xz} \\ (\delta\tau\tilde{U})_x - \delta q_x + \sigma_x^K \\ -\sigma_x^K \\ -\sigma_x^\varepsilon \end{Bmatrix}, \; g_v = \begin{Bmatrix} 0 \\ \delta\tau_{yx} \\ \delta\tau_{yy} \\ \delta\tau_{yz} \\ (\delta\tau\tilde{U})_y - \delta q_y + \sigma_y^K \\ -\sigma_y^K \\ -\sigma_y^\varepsilon \end{Bmatrix}$$

$$h_v = \begin{Bmatrix} 0 \\ \delta\tau_{zx} \\ \delta\tau_{zy} \\ \delta\tau_{zz} \\ (\delta\tau\tilde{U})_z - \delta q_z + \sigma_z^K \\ -\sigma_z^K \\ -\sigma_z^\varepsilon \end{Bmatrix}, \; S = \begin{Bmatrix} 0 \\ 0 \\ 0 \\ 0 \\ 0 \\ \mathscr{S}_K \\ \mathscr{S}_\varepsilon \end{Bmatrix}$$

with $\delta\tau_{ij} = \tilde{\tau}_{ij} + t_{ij}$, $\delta q_i = \bar{q}_i + q_{ti}$, $\sigma_i^K = -(\mu + \frac{\mu_t}{\sigma_K}\frac{\partial K}{\partial x_i})$ and $\sigma_i^\varepsilon = -(\mu + \frac{\mu_t}{\sigma_\varepsilon}\frac{\partial \varepsilon}{\partial x_i})$. The source terms are treated differently in the various model versions. The low-Reynolds version of the model requires the addition of damping functions to stay valid through the viscous sublayer up to the wall boundary. These should ensure that $K \sim y_w^2$ and $\varepsilon/K \sim 2\nu/y_w^2$ as $y_w \to 0$, with y_w the normal wall distance. However, the addition of damping functions results in stiff source terms that requires high grid resolution close to the wall boundaries and implicit time-stepping schemes.

Chien's low-Reynolds number model

Chien's version of $K-\varepsilon$ model [Chi82] employs low-Reynolds number turbulence damping towards the wall. It differ from the standard version in the form of the source terms, the values of the closure coefficients and the surface boundary conditions. Two dimensionless parameters are introduced:

$$Re_t = \frac{K^2}{\nu\varepsilon} \;\text{ and }\; y^+ = \frac{u_\tau y_w}{\nu}$$

where Re_t the turbulent Reynolds number and $u_\tau = \sqrt{\tilde{\tau}_w/\bar{\rho}}$ the friction velocity with $\tilde{\tau}_w$ the shear stress on the wall. The source terms are written as:

$$\mathscr{S}_K = \mathscr{P} - \bar{\rho}\varepsilon - \frac{2\mu K}{y_w^2}$$

$$\mathscr{S}_\varepsilon = C_{\varepsilon 1} f_1 \frac{\varepsilon}{K}\mathscr{P} - C_{\varepsilon 2} f_2 \bar{\rho}\frac{\varepsilon^2}{K} - \frac{2\mu\varepsilon}{y_w^2}e^{-0.5y^+}$$

The damping function employed by Chien were:

$$f_\mu = 1 - e^{-0.0115y^+} \;\;,\;\; f_1 = 1 \;\text{ and }\; f_2 = (1 - 0.22e^{-\frac{Re_t^2}{36}})$$

and the closure coefficients:

$$C_\mu = 0.09 \ , \ C_{\varepsilon 1} = 1.35 \ , \ C_{\varepsilon 2} = 1.8 \ , \ \sigma_K = 1.0 \ \text{and} \ \sigma_\varepsilon = 1.3$$

The boundary conditions at the solid wall for the turbulent kinetic energy and the dissipation rate are $K = 0$ and $\varepsilon = 0$. This implies that $\mu_t = 0$ at the wall as the turbulent viscosity is calculated from:

$$\mu_t = C_\mu f_\mu \bar{\rho} \frac{K^2}{\varepsilon}$$

At the inflow boundary, K and ε can be computed from pre-described values of the turbulent intensity T_u and the length scale l_t as:

$$K_\infty = \frac{3}{2}(T_u||\vec{U}_\infty||)^2 \ \text{and} \ \varepsilon_\infty = \frac{C_\mu K_\infty^{3/2}}{l_t}$$

Organised Eddy Simulation

The Organised Eddy Simulation (OES) approach enhances the physically correct development of flow instabilities and coherent structures in the high Reynolds numbers, especially in regions of non-equilibrium turbulence where the efficiency of traditional statistical models degrades. For non-homogeneous turbulent flows, the turbulent spectrum in the inertial range takes a different form, compared to equilibrium turbulent flows. This was shown experimentally by rapid Particle Image Velocimetry (PIV) measurements in [BPH06] and consequently, these modifications should be taken into account by the turbulence modelling. In OES, the decomposition of a variable $u(x,t)$, based on the ensemble (phase) averaging of the flow, takes the form:

$$u(x,t) = < u(x,t) > + u'(x,t) \tag{2.25}$$

where $< u(x,t) > = \overline{u}(x) + u_c(x,t)$ the ensemble average value which is a sum of a temporal mean $\overline{u}(x)$, and coherent (resolved) fluctuations $u_c(x,t)$. This decomposition reduces to a phase-averaging if only one periodicity is pronounced. The approach splits the turbulence energy spectrum in two parts as shown in Fig.2.1. The first, regroups all the organized (coherent) in space and time motions to be resolved, and the second, the chaotic turbulence motion to be modelled. The present approach does not differentiate vortex structures according to their size, as in the Large Eddy Simulation (LES) approach, but instead, according to their organised or chaotic character. The chaotic part of the turbulence spectrum is extended over all the wavenumbers as in statistical modelling approaches. In OES however, the turbulence stresses are modelled by re-evaluating the length and time turbulence scales, to account for the modifications occurring on the inertial range of the turbulent spectrum [PCC$^+$07].

This non-intrinsically 3D approach targets the treatment of non-equilibrium and near-wall turbulence. Traditional turbulence modelling approaches based on the Reynolds/Favre averaging of the flow (URANS[2]) relate the unresolved turbulent

[2]Unsteady Reynolds Averaged Navier-Stokes

stresses to the velocity deformations through the eddy viscosity. In regions of non-equilibrium turbulence, it has been found that strong misalignments appear between the principal axes of the turbulent stresses and the local strain rates. This stress-strain misalignment due to non-equilibrium turbulence and the existence of coherent structures has been experimentally investigated by Bourguet et al. [BBPH07]. The effect of turbulent stresses is not purely dissipative and these non-equilibrium effects should be appropriately modelled.

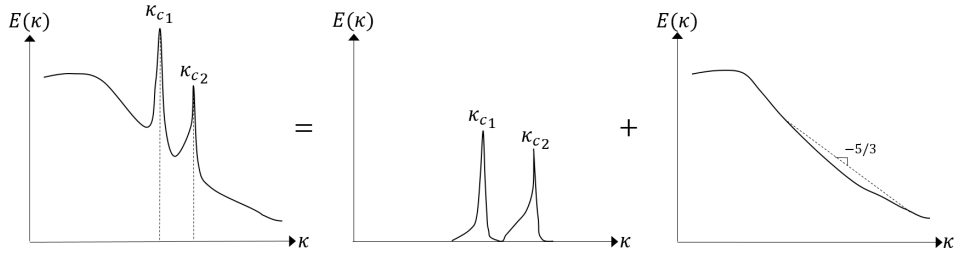

Figure 2.1: *Turbulence energy spectrum split in OES: the organized motions to be resolved, and the chaotic motion to be modelled; κ_c the wavenumbers of the coherent processes.*

This modification of the structural properties of turbulence due to the development of coherent structures were modelled by Y. Hoarau [Hoa02] for strongly separated flows around wings. The cross-term of the turbulence anisotropy tensor was found to increase in the near-wall regions for adverse pressure gradient boundary layers. As a result, a reduced C_μ value has been derived through DNS studies and second-order model closures, and was adopted in the OES approach. The non-constant behavior of the turbulence cross-stress $u'v'/K$ had also been evaluated in non-equilibrium turbulent boundary layers by Bourdet et al. [BBH$^+$07] and was found to retain lower values when compared to measurements in equilibrium boundary layers.

The modelling of the stress-strain misalignment gave birth to the anisotropic extension of the OES approach developed in [BBHEA08]. A tensorial eddy-viscosity model was adopted to capture the stress-strain misalignment and the complete set of equations derived from second-order closure modelling was presented in detail. This formulation led to a directional C_μ coefficient which admitted the equilibrium turbulence value (0.09) in flow regions where turbulence production is equal to the dissipation, and lower values $(0.02 - 0.03)$ in flow regions deviating from equilibrium. Furthermore, the Improved OES (IOES) approach was developed in [SGJG$^+$15] where a reinjection of small scale turbulence through stochastic source terms led to mitigation of the excessive (due to the downscale assumptions) turbulence diffusion in shear layers and provided improved predictions. This approach is examined in detail in the following section.

For the simplified OES version, the transport equations produced via the ensemble (phase) averaging take the same form with Eq. 2.24 previously examined,

where the Reynolds/Favre averaged quantities are replaced by the ensemble (phase) averaged ones and the turbulent stresses are expressed:

$$t_{ij} = 2\mu_t < s_{ij} > -\frac{2}{3}\left(\mu_t \frac{\partial < u_m >}{\partial x_m}\delta_{ij} - \bar{\rho}K\right)\delta_{ij}$$

i.e. in relation to the ensemble averaged quantities. This simplified version of the OES has been adopted in the present study and implemented based on Chien's version of the $K-\varepsilon$ model. In order to account for non-equilibrium turbulence and the modifications on the continuous part of the (modelled) spectrum, OES consists of a reconsideration of the closure constants and an adapted eddy-viscosity damping towards the wall:

$$f_\mu = 1 - e^{-0.0002y^+ - 0.000065(y^+)^2} \ , \ f_1 = 1 \ \text{ and } \ f_2 = (1 - 0.22e^{-\frac{Re_t^2}{36}})$$

$$C_\mu = 0.02 - 0.04 \ , \ C_{\varepsilon 1} = 1.35 \ , \ C_{\varepsilon 2} = 1.8 \ , \ \sigma_K = 1.0 \ \text{ and } \ \sigma_\varepsilon = 1.3$$

where a reduced C_μ value is adopted in accordance with what has been previously examined. The improved damping function f_μ, introduced in [JB94], has been proposed in order to provide a milder attenuation of the eddy viscosity towards the wall, compared to RANS modelling for turbulence flows in statistical equilibrium.

Stochastic forcing

The decomposition in Eq. 2.25 can be further expanded by splitting the turbulent fluctuation as follows:

$$u'(x,t) = \hat{u}(x,t) + \check{u}(x,t)$$

where the downscale $\hat{u}(x,t)$ part of the turbulent fluctuations, responsible for the direct energy cascade (forward scatter), was separated from the upscale $\check{u}(x,t)$ part, responsible for the backscatter of the turbulent energy. The direct turbulent energy cascade assumption, where energy flows from larger structures to smaller ones, and the upscaling, where the reverse energy transfer is observed, will be discussed in more detail in Chapter 3. The additional decomposition results in multiple second-order correlation terms to be modelled; the $\hat{u}_i(x,t)\check{u}_j(x,t)$, $\hat{u}_j(x,t)\check{u}_i(x,t)$ and $\check{u}_i(x,t)\check{u}_j(x,t)$ tensors are introduced.

In the approach here presented, all the additional terms appearing in the turbulent transport equations are regrouped and their effect is accounted for through a reinjection of turbulence. The turbulence reinjection is introduced by forcing terms added in the transport equations of turbulence kinetic energy and dissipation. These terms act as production terms and represent the effects of small scale fluctuations that produce upscale energy transfers (back-scatter) in the case of inhomogeneous turbulent flows. They are included in the turbulent transport equations in order to limit the effects of turbulent diffusion which is a product of the direct cascade assumptions. The direct cascade is widely employed in the majority of turbulence modelling approaches and may provide excessive turbulence diffusion rates which

is detrimental to the force prediction. The present approach can mitigate this inconvenience without significantly increasing the grid size to prohibitive - in the context of industrial applications - levels.

The stochastic terms are built from low energy high-order modes educted from a Proper Orthogonal Decomposition (POD - see Appendix A) of the flow. In this way, the regions of intense shearing can be identified. In these regions, the small scale turbulence kinetic energy is then reinjected, modifying the local turbulent length scales. The stochastic nature of the upscaling dynamics can be represented with a random variation of the forcing in time. The approach was developed first in [SGJG$^+$15] (IOES) for 2D simulations and it was extended in the present thesis to three-dimensional flows. The $K-\varepsilon-$OES model can be rewritten with the addition of the stochastic forcing terms:

$$\begin{aligned}
\frac{\partial(\bar{\rho}K)}{\partial t}+\frac{\partial}{\partial x_j}(\bar{\rho}\tilde{u_j}K) &= \frac{\partial}{\partial x_j}\left[\left(\mu+\frac{\mu_t}{\sigma_K}\right)\frac{\partial K}{\partial x_j}\right]+t_{ij}\tilde{s_{ij}}-\bar{\rho}\varepsilon-\frac{2\mu K}{y_w^2}+S_{POD} \\
\frac{\partial(\bar{\rho}\varepsilon)}{\partial t}+\frac{\partial}{\partial x_j}(\bar{\rho}\tilde{u_j}\varepsilon) &= \frac{\partial}{\partial x_j}\left[\left(\mu+\frac{\mu_t}{\sigma_\varepsilon}\right)\frac{\partial \varepsilon}{\partial x_j}\right]+C_{\varepsilon 1}f_1\frac{\varepsilon}{K}t_{ij}\tilde{s_{ij}}-C_{\varepsilon 2}f_2\bar{\rho}\frac{\varepsilon^2}{K} \\
&- \frac{2\mu\varepsilon}{y_w}e^{-0.5y^+}+\frac{C_{\varepsilon 2}S_{POD}^2}{K_\infty}
\end{aligned}$$

where the source terms, after a dimensional analysis, take the following form:

$$S_{POD}=\tilde{r}C_\mu\bar{\rho}\frac{K_\infty^2+K_{POD}^2}{\nu_{t_\infty}}$$

with ν_{t_∞} the upstream turbulent viscosity, C_μ the coefficient calibrated by the OES approach and $\tilde{r}$ a randomly generated number varying in the interval $[0,1]$. The K_{POD} is calculated from the time average of the POD reconstructed velocity field:

$$K_{POD}=\frac{1}{2}(\overline{u'^2}_{recon}+\overline{v'^2}_{recon}+\overline{w'^2}_{recon})$$

These source terms can be added to the right hand side of the turbulent equations and be treated as constants in the linearization of the source terms, as it will be presented in the following section.

Treatment of the source terms

The turbulent transport equations can be decoupled from the system and be solved separately. Freezing the eddy viscosity, the mean flow is updated. Then, turbulence is calculated in the next time step. The numerical schemes adopted for the discretization of the convective and viscous fluxes apply for the turbulent equations as well. In practice however, various discretization approaches dedicated to the turbulent equations have been developed and can be found in the literature [Wil06]. In this section, only the treatment of the source terms is examined. For implicit schemes, the source terms should be evaluated at the $n+1$ time step:

$$\mathscr{S}_K^{n+1}=\mathscr{S}_K^n+\frac{\partial\mathscr{S}_K}{\partial(\bar{\rho}K)}\left[(\bar{\rho}K)^{n+1}-(\bar{\rho}K)^n\right]+\frac{\partial\mathscr{S}_K}{\partial(\bar{\rho}\varepsilon)}\left[(\bar{\rho}\varepsilon)^{n+1}-(\bar{\rho}\varepsilon)^n\right]$$

$$\mathscr{S}_{\varepsilon}^{n+1} = \mathscr{S}_{\varepsilon}^{n} + \frac{\partial \mathscr{S}_{\varepsilon}}{\partial(\bar{\rho}K)}\left[(\bar{\rho}K)^{n+1} - (\bar{\rho}K)^{n}\right] + \frac{\partial \mathscr{S}_{\varepsilon}}{\partial(\bar{\rho}\varepsilon)}\left[(\bar{\rho}\varepsilon)^{n+1} - (\bar{\rho}\varepsilon)^{n}\right]$$

The source Jacobian matrix is written:

$$J = \frac{\partial \mathscr{S}}{\partial U} = \begin{bmatrix} \frac{\partial \mathscr{S}_K}{\partial(\bar{\rho}K)} & \frac{\partial \mathscr{S}_K}{\partial(\bar{\rho}\varepsilon)} \\ \frac{\partial \mathscr{S}_{\varepsilon}}{\partial(\bar{\rho}K)} & \frac{\partial \mathscr{S}_{\varepsilon}}{\partial(\bar{\rho}\varepsilon)} \end{bmatrix}$$

The term $\varepsilon/K = \mu_t/(\bar{\rho}K)$, remains constant over a time step. Same goes for the y^+ value as τ_w varies slowly per iteration. As mentioned, the stochastic forcing terms is set constants during the times step. Finally, the term $\mathscr{P}/(\bar{\rho}K)$ associated with the turbulent production is treated as constant as well. Using these assumptions and after linearization, the terms of the source Jacobian matrix can be estimated from:

$$\frac{\partial \mathscr{S}_K}{\partial(\bar{\rho}K)} = \frac{\mathscr{P}}{\bar{\rho}K} - \frac{2\varepsilon}{K} + \frac{2\mu}{\bar{\rho}y_w^2} \quad \text{and} \quad \frac{\partial \mathscr{S}_K}{\partial(\bar{\rho}\varepsilon)} = 0$$

$$\frac{\partial \mathscr{S}_{\varepsilon}}{\partial(\bar{\rho}K)} = 0 \quad \text{and} \quad \frac{\partial \mathscr{S}_{\varepsilon}}{\partial(\bar{\rho}\varepsilon)} = C_{\varepsilon 1} f_1 \frac{\mathscr{P}}{\bar{\rho}\varepsilon} - C_{\varepsilon 2} f_2 \frac{3\bar{\rho}\varepsilon}{2K} - \frac{2\mu}{\bar{\rho}y_w} e^{-0.5y^+}$$

From these terms, only the negative part of the Jacobian (i.e. when dissipation exceeds production) are treated implicitly in order to ensure diagonal dominance.

Hybrid turbulence models

Advanced turbulence modelling approaches have been developed to perform as a hybrid between the conventional Favre-Reynolds statistical treatment of turbulence (RANS) and the Large Eddy Simulation (LES) approach. The Hybrid RANS-LES turbulence models had been derived in order to increase the predictive capability of the turbulence modelling at high-Reynolds number flows around bodies, especially for industrial applications.

The LES methodology solves only for the larger structures in the flow that carry most of the energy and models smaller scale structures that are expected to present a homogenous and universal character. LES is based on a spatial filtering procedure of the Navier-Stokes equations through which the filtered (resolved) part of the flow is acquired and the sub-filter (sub-grid) resulting terms remains to be closed by appropriate methodologies. The latter, usually takes into account the local geometric grid properties. The mesh size requirements however, significantly increase with the Reynolds number, especially close to wall regions. As a result, LES is limited to moderate Reynolds numbers since it remains costly for full scale industrial applications. On the other hand, the (U)RANS system of equations offers robustness and efficiency in capturing near-wall physics in high Reynolds numbers. However, the URANS approach offers poor predictive efficiency in outer flow regions because of the excessive turbulence diffusion arising from the direct cascade assumption. To this end, in the second half of the '90s, novel approaches were proposed, in which the calculation resolution is adapted to the level of discretization:

(U)RANS computations are adopted close to the wall and LES in the outer flow regions (e.g. [Spe98a], [Spe98b])

The Detached Eddy Simulation (DES) proposed by Spalart et al. [SJSA97] is a hybrid approach that employs the traditional statistical treatment (RANS) in regions close to the wall and an LES approach for the calculation of eddies in the outer flow. For this switch, a characteristic length is introduced to identify the mode in which DES performs. For the $K-\varepsilon$ formulation, the DES length scale is calculated from:

$$l_{DES} = min(l_{K\varepsilon}, C_{DES}\Delta) \tag{2.26}$$

where Δ the largest dimension of the control volume calculated as $\Delta = max(\Delta x, \Delta y, \Delta z)$ and C_{DES} a constant equal to 0.61 (for $K-\varepsilon$). The $l_{K\varepsilon}$ length scale is calculated from $l_{K\varepsilon} = K^{3/2}/\varepsilon$.

To adress the shortcomings of the DES approach, the Delayed Detached Eddy Simulations (DDES) [SDS$^+$06] was later proposed. DDES is employed to preserve the Favre-Reynolds (RANS) calculation mode throughout thick boundary layers and shallow separation regions. In DDES, the l_{DDES} is calculated from:

$$l_{DDES} = l_{K\varepsilon} - f_d max(0, l_{K\varepsilon} - C_{DES}\Delta)$$

with $f_d = 1 - tanh[(8r_d)^3]$ a delaying function varying between 0 (for a DDES mode) and 1 (for a $K-\varepsilon$ mode). In practice, the methodology delays the transitioning to a DES mode in order to maintain a appropriate approach close to the wall. The f_d function is calculated from:

$$r_d = (\mu + \mu_t)\frac{\kappa^2}{max(\sqrt{\delta u}, 10^{10})y_w^2}$$

with $\kappa = 0.41$ the Karman constant and δu given from:

$$\delta u = \left|\left|\begin{pmatrix}\frac{\partial u}{\partial x} & \frac{\partial v}{\partial x} & \frac{\partial w}{\partial x}\end{pmatrix}\right|\right|_2 + \left|\left|\begin{pmatrix}\frac{\partial u}{\partial y} & \frac{\partial v}{\partial y} & \frac{\partial w}{\partial y}\end{pmatrix}\right|\right|_2 + \left|\left|\begin{pmatrix}\frac{\partial u}{\partial z} & \frac{\partial v}{\partial z} & \frac{\partial w}{\partial z}\end{pmatrix}\right|\right|_2$$

The modification on the turbulent kinetic equation are observed in the following equation:

$$\frac{\partial(\bar{\rho}K)}{\partial t} + \frac{\partial}{\partial x_j}(\bar{\rho}\tilde{u}_j K) = \frac{\partial}{\partial x_j}\left[\left(\mu + \frac{\mu_t}{\sigma_K}\right)\frac{\partial K}{\partial x_j}\right] + \mathscr{P} - \frac{\bar{\rho}K^{3/2}}{l_{D(D)ES}} - \mathscr{S}_K$$

with $l_{D(D)ES} = l_{K\varepsilon} = K^{3/2}/\varepsilon$, the dissipation rate reduces to $-\bar{\rho}\varepsilon$ and the turbulent kinetic energy equation takes a form identical to the statistical modelling. In region where the mesh is sufficiently fine compared to the turbulent length scales (e.g. away from the solid boundaries) the dissipation rate becomes grid-dependent. As the dissipation term grows, the effective turbulent viscosity decreases. At equilibrium, i.e. where turbulent production and dissipation are equal, the model reduces to a Smagorinski-like subgrid-scale model used in LES [SSST08].

An Improved DDES (IDDES) approach was proposed in [SSST08]. IDDES includes empirical functions that, depending on the flow, activate either the DDES branch of the model or the Wall-Modelled LES (WMLES) branch to ensure a physically correct solution. The DES approach and its improved versions have been widely investigated in recent years in European Research projects with strong industrial interest [HBR09a], [HBR09b]. Furthermore, in the context of DES/DDES, the RANS part can be replaced by the OES approach which better captures the non-equilibrium and near-wall turbulence as mentioned before. This approach, namely DES/DDES-OES, has been proven highly efficient for complex flows with strong flow detachment [BBHEA08]. Finally, it is mentioned that the stochastic forcing methodology previously described can be directly added to the right hand side of the DES/DDES equations.

2.2 Computational Structural Mechanics

In this second part of the present chapter, the principles of modelling and solution procedures for structural mechanics are presented. We closely follow [Bat96] and [ZTF05] in deriving the basic formulations of a Finite Element (FE) analysis for steady state elastic equilibrium problems. Some axes of nonlinear analysis are also examined.

2.2.1 Field equations & boundary conditions

In this section only elastic materials are discussed. For the exact solution of the structural problem, an equilibrium of forces must be satisfied. This is expressed in general steady 3D analysis as:

$$\frac{\partial \sigma_{ij}}{\partial x_j} + f_i^b = 0 \tag{2.27}$$

inside the body, where $\boldsymbol{f}^b$ the body (inertial) forces and $\bar{\sigma}$ the (Cauchy) stress tensor given from:

$$\bar{\sigma} = \begin{bmatrix} \sigma_{xx} & \tau_{xy} & \tau_{xz} \\ \tau_{yx} & \sigma_{yy} & \tau_{yz} \\ \tau_{zx} & \tau_{zy} & \sigma_{zz} \end{bmatrix}$$

The equilibrium on the surface boundaries of the body requires:

$$\sigma_{ij} n_j = f_i^S \ \text{ on } \ S_f$$

where S_f part of the surface where forces are applied and n_j the unit vector normal to the surface. Inside the body, the strain-displacement relation writes:

$$\varepsilon_{ij} = \frac{1}{2}\left(\frac{\partial u_i}{\partial x_j} + \frac{\partial u_j}{\partial x_i}\right)$$

for small deformations (i.e. $|\varepsilon_{ij}| << 1$), with $\bar{\varepsilon}$ the strain tensor and $\boldsymbol{u}$ the displacement vector. Similar to stress boundary conditions, the compatibility requires that the deformations are continuous and equal to the ones imposed on the boundaries, i.e.:

$$u_i = u_i^S \ \text{ on } \ S_u$$

where S_u part of the body surface with no common points with S_f ($S = S_f \cup S_u$ the complete boundary). The material behavior is described by constitutive equations. For elastic materials, the stress-strain relation relates the stresses to the arising strain as:

$$\sigma_{ij} = C_{ijkl}(\varepsilon_{kl} - \varepsilon_{kl}^0)$$

where ε_{kl}^0 the strain resulting from initial conditions or other source (e.g. thermal strain). In terms of notation, since both the stress and strain tensor are symmetric they can be rewritten as:

$$\boldsymbol{\sigma} = [\sigma_{xx} \ \ \sigma_{yy} \ \ \sigma_{zz} \ \ \tau_{xy} \ \ \tau_{yz} \ \ \tau_{xz}]^T$$

and

$$\boldsymbol{\varepsilon} = [\varepsilon_{xx} \;\; \varepsilon_{yy} \;\; \varepsilon_{zz} \;\; \gamma_{xy} \;\; \gamma_{yz} \;\; \gamma_{xz}]^T$$

with $\gamma_{ij} = 2\varepsilon_{ij}$. This consequently leads to rewriting the strain-displacement relations as:

$$\boldsymbol{\varepsilon} = \bar{\mathscr{S}}\boldsymbol{u}$$

with $\bar{\mathscr{S}}$ the strain operator, and the constitutive relation as:

$$\boldsymbol{\sigma} = \bar{D}(\boldsymbol{\varepsilon} - \boldsymbol{\varepsilon^0})$$

with $\bar{D}$ the stress-strain material matrix.

Principle of virtual displacements

For a linear analysis, we assume that the displacements are infinitesimal and $\bar{D}$ does not depend on the stress state. Let us consider any arbitrary (large or small) continuous virtual displacement field that satisfies $\tilde{u} = 0$ on S_u. Then from Eq. 2.27 we have:

$$\int_\Omega \left(\frac{\partial \sigma_{ij}}{\partial x_j} + f_i^b \right) \tilde{u}_i d\Omega = 0$$

which can be rewritten as:

$$\int_\Omega \left[\frac{\partial (\sigma_{ij}\tilde{u}_i)}{\partial x_j} - \sigma_{ij}\frac{\partial \tilde{u}_i}{\partial x_j} + f_i^b \tilde{u}_i \right] d\Omega = 0$$

$$\int_\Omega \left[-\sigma_{ij}\frac{\partial \tilde{u}_i}{\partial x_j} + f_i^b \tilde{u}_i \right] d\Omega + \int_S (\sigma_{ij}\tilde{u}_i) n_j dS = 0$$

$$\int_\Omega \sigma_{ij}\frac{\partial \tilde{u}_i}{\partial x_j} d\Omega = \int_\Omega f_i^b \tilde{u}_i d\Omega + \int_{S_f} f_i^S \tilde{u}_i^S dS_f$$

with Ω the body volume. Since:

$$\sigma_{ij}\frac{\partial \tilde{u}_i}{\partial x_j} = \sigma_{ij}\frac{1}{2}\left(\frac{\partial \tilde{u}_i}{\partial x_j} + \frac{\partial \tilde{u}_j}{\partial x_i} \right) = \sigma_{ij}\tilde{\varepsilon}_{ij}$$

due to the symmetry of the stress tensor, we can write:

$$\int_\Omega \sigma_{ij}\tilde{\varepsilon}_{ij} d\Omega = \int_\Omega f_i^b \tilde{u}_i d\Omega + \int_{S_f} f_i^S \tilde{u}_i^S dS_f \tag{2.28}$$

for the virtual strain field $\tilde{\boldsymbol{\varepsilon}}$ calculated from the virtual displacements. Equation 2.28 is the expression of the virtual work principle, expressed through the equivalent principle of virtual displacements[3] in a weak form, which states that the internal virtual work is equal to the external virtual work. Consequently, the stresses and forces are in equilibrium if and only if the principle of virtual work is satisfied. We can rewrite Eq. 2.28 with the addition of p concentrated loads as:

$$\int_\Omega \tilde{\boldsymbol{\varepsilon}}^T \boldsymbol{\sigma} d\Omega = \int_\Omega \tilde{\boldsymbol{u}}^T \boldsymbol{f}^b d\Omega + \int_{S_f} (\tilde{\boldsymbol{u}}^S)^T \boldsymbol{f}^S dS_f + \sum_p (\tilde{\boldsymbol{u}}^p)^T \boldsymbol{f}^p \tag{2.29}$$

[3] This directly relates to the principle of stationarity of the total potential.

2.2.2 Finite Element formulation

The body is approximated by dividing the domain in discrete finite elements connected with each other at nodal points. The continuous displacements for each m element, measured in a local coordinate system $\boldsymbol{\xi} = (\xi, \eta, \zeta)$, can be written as a function of the displacements of the element nodal points. This reads:

$$\boldsymbol{u}^{(m)}(\boldsymbol{\xi}) = \bar{N}^{(m)}(\boldsymbol{\xi})\hat{\boldsymbol{U}}$$

where $\bar{N}^{(m)}$ the displacement interpolation matrix and $\hat{\boldsymbol{U}}$ the vector with every displacement component for all the element nodes. The construction of $\bar{N}$ depends on the type of elements chosen for the solution. For iso-parametric elements, the same shape functions (matrix $\bar{N}^{(m)}$) are used for the interpolation of the coordinates $\boldsymbol{x} = (x, y, z)$ of the element.

$$\boldsymbol{x}^{(m)}(\boldsymbol{\xi}) = \bar{N}^{(m)}(\boldsymbol{\xi})\hat{\boldsymbol{X}}$$

The corresponding strains are taken from the strain-displacement relation:

$$\boldsymbol{\varepsilon}^{(m)}(\boldsymbol{x}) = \bar{B}^{(m)}(\boldsymbol{x})\hat{\boldsymbol{U}}$$

where $\bar{B}^{(m)}$ is obtained by differentiating $\bar{N}^{(m)}$ according to $\bar{\mathscr{D}}^{(m)}$. This procedure uses the derivatives of the shape functions:

$$\frac{\bar{N}^{(m)}}{\partial \boldsymbol{x}} = \bar{J}^{-1}\frac{\bar{N}^{(m)}}{\partial \boldsymbol{\xi}} \quad \text{with} \quad \bar{J} = \begin{bmatrix} \frac{\partial x}{\partial \xi} & \frac{\partial y}{\partial \xi} & \frac{\partial z}{\partial \xi} \\ \frac{\partial x}{\partial \eta} & \frac{\partial y}{\partial \eta} & \frac{\partial z}{\partial \eta} \\ \frac{\partial x}{\partial \zeta} & \frac{\partial y}{\partial \zeta} & \frac{\partial z}{\partial \zeta} \end{bmatrix}$$

The element stresses are related to the element strains from:

$$\boldsymbol{\sigma}^{(m)} = \bar{D}^{(m)}(\boldsymbol{\varepsilon}^{(m)} - \boldsymbol{\varepsilon}_{\mathbf{0}}^{(m)})$$

Let us rewrite Eq. 2.29 in the context of finite elements, as a sum of integrations:

$$\begin{aligned} \sum_m \int_{\Omega^{(m)}} (\tilde{\boldsymbol{\varepsilon}}^{(m)})^T \boldsymbol{\sigma}^{(m)} d\Omega^{(m)} &= \sum_m \int_{\Omega^{(m)}} (\tilde{\boldsymbol{u}}^{(m)})^T \boldsymbol{f}^b_{(m)} d\Omega^{(m)} \\ &+ \sum_m \int_{S_f^{(m)}} (\tilde{\boldsymbol{u}}^S)^{(m)T} \boldsymbol{f}^S_{(m)} dS_f \\ &+ \sum_p (\tilde{\boldsymbol{u}}^p)^{(m)T} \boldsymbol{f}^p_{(m)} \end{aligned} \tag{2.30}$$

where $S_f^{(m)}$ the surfaces of the element that are also part of the body surface. Substituting in Eq. 2.30 the interpolations for the virtual displacements and stresses:

$$\tilde{\hat{\boldsymbol{U}}}^T \left[\sum_m \underbrace{\int_{\Omega^{(m)}} (\bar{B}^{(m)})^T \bar{D}^{(m)} \bar{B}^{(m)} d\Omega^{(m)}}_{\bar{K}^{(m)}} \right] \hat{\boldsymbol{U}} = \tilde{\hat{\boldsymbol{U}}}^T \left[\sum_m \underbrace{\int_{\Omega^{(m)}} (\bar{H}^{(m)})^T \boldsymbol{f}^b_{(m)} d\Omega^{(m)}}_{\boldsymbol{R}_b^{(m)}} \right.$$

$$+ \sum_m \underbrace{\int_{S_f^{(m)}} (\tilde{\bar{N}}^S)^{(m)T} \boldsymbol{f}^S_{(m)} dS_f}_{\boldsymbol{R}_S^{(m)}} + \boldsymbol{R}_p$$

$$\left. + \sum_m \underbrace{\int_{\Omega^{(m)}} (\bar{B}^{(m)})^T \bar{D}^{(m)} \boldsymbol{\varepsilon}_{\mathbf{0}}^{(m)} d\Omega^{(m)}}_{-\boldsymbol{R}_0^{(m)}} \right]$$

Assembling all the elements results in:

$$\bar{K}\hat{\boldsymbol{U}} = \boldsymbol{R} \tag{2.31}$$

with $\boldsymbol{R} = \boldsymbol{R}_b + \boldsymbol{R}_S + \boldsymbol{R}_p - \boldsymbol{R}_0$ the force vector and $\bar{K}$ the stiffness matrix of the structure. The solution of the above written equation satisfies simultaneously both element and nodal point equilibrium.

2.2.3 Nonlinear analysis

In the previous section we derived the finite element equilibrium equation for static linear analysis. Several assumptions have entered the derivation of Eq. 2.31. If the boundary conditions change during loading (e.g. contact between elements, following force) or if the displacements are large, several of the assumptions used for the evaluation of $\bar{K}$ and $\boldsymbol{R}$ fail. The nonlinear analysis is introduced to solve the structural problem. In the general case, the relation between external loads and displacements can be nonlinear as the stiffness matrix can vary with displacements, i.e. $\bar{K} = \bar{K}(\hat{\boldsymbol{U}})$. The most common approach to handle nonlinear problems is the introduction of the Newton-Raphson methodology.

Newton-Raphson method

The basic problem is to identify the equilibrium for a body under externally applied loads. This is expressed as:

$$\boldsymbol{R} = \boldsymbol{P}$$

with $\boldsymbol{P}$ the vector of internal forces, calculated from the deformed state of the structure by integrating the stresses over the whole volume. Starting from a point of

equilibrium i we can apply a load increment $\Delta\boldsymbol{R}$ so that $\boldsymbol{R}_{i+1} = \boldsymbol{R}_i + \Delta\boldsymbol{R}$. For static analysis, the load increment can represent solely the passage to the final deformed equilibrium state (moving from $i = 0$ to $i = 1$) or a pseudo-time marching to achieve numerical convergence. Searching for the new equilibrium point we can write:

$$\boldsymbol{R}_{i+1} = \boldsymbol{P}_{i+1} = \bar{K}(\boldsymbol{U}_{i+1})\boldsymbol{U}_{i+1}$$

where $\boldsymbol{U} \equiv \hat{\boldsymbol{U}}$. Linearizing the $\boldsymbol{P}_{i+1}$[4] term gives:

$$\boldsymbol{P}_{i+1} = \boldsymbol{P}_i + \left.\frac{\partial \bar{K}}{\partial \boldsymbol{U}}\right|_i \Delta\boldsymbol{U} = \boldsymbol{P}_i + (\bar{K}_t)_i \Delta\boldsymbol{U}$$

with $\bar{K}_t$ the tangent stiffness matrix. The equilibrium is written:

$$(\bar{K}_t)_i \Delta\boldsymbol{U} = \boldsymbol{R}_{i+1} - \boldsymbol{P}_i$$

where $\boldsymbol{U}_{i+1} = \boldsymbol{U}_i + \Delta\boldsymbol{U}$. The above written equilibrium stands if the load increment is small. If this is not true, additional iterations should be performed within each load increment:

$$(\bar{K}_t)_{i+1}^{n-1} \Delta\boldsymbol{U}^n = \boldsymbol{R}_{i+1} - \boldsymbol{P}_{i+1}^{n-1} \tag{2.32}$$

with $\boldsymbol{U}_{i+1}^n = \boldsymbol{U}_{i+1}^{n-1} + \Delta\boldsymbol{U}^n$, to be repeated until $\mathscr{R}_{i+1} = \boldsymbol{R}_{i+1} - \boldsymbol{P}_{i+1}^{n-1} = 0$. In practice, a common convergence criterion can be:

$$\frac{||\boldsymbol{R}_{i+1} - \boldsymbol{P}_i^n||}{||\boldsymbol{R}_{i+1}||} < e_{tol}$$

with e_{tol} a small number (order of 10^{-3} to 10^{-5}). When the pseudo-time steps are omitted in the above described approach, we retrieve the pure Newton-Raphson procedure. Otherwise, the incremental Newton-Raphson methodology is followed. The latter provides a quadratic rate of convergence meaning that only a few iterations per time step are required. However, building and inverting a new stiffness matrix at each iteration can significantly increase the computational cost for large systems. The modified Newton-Raphson approach only uses the stiffness matrix calculated at the first iteration. In principle, the choice of the stiffness matrix only affects the convergence rate of the solution as accuracy is related to the calculation of the internal forces[5].

Principle of virtual work in nonlinear mechanics

We can write the principle of virtual work at a time $t + \Delta t$ at which the body is in an equilibrium state. The difference with the procedure examined in a linear analysis is that the current configuration is now unknown. Then, Eq. 2.28 can be rewritten as:

$$\begin{aligned} \int_{\Omega|_{t+\Delta t}} \sigma_{ij}|_{t+\Delta t} \delta\varepsilon_{ij}|_{t+\Delta t} d\Omega|_{t+\Delta t} &= \int_{\Omega|_{t+\Delta t}} f_i^b|_{t+\Delta t} \delta u_i d\Omega|_{t+\Delta t} \\ &+ \int_{S_f|_{t+\Delta t}} f_i^S|_{t+\Delta t} \delta u_i^S dS_f|_{t+\Delta t} = R|_{t+\Delta t} \end{aligned} \tag{2.33}$$

[4]The subscript i used here refers to a time-marching increment.

[5]See also remark for the solution of the equations of a dynamic fluid system in Section 2.1.3.

where we changed the notation for the virtual displacements and strains to δu and $\delta\varepsilon$ to associate the virtual work principle with the variational formulation. All the derivatives and integrations in Eq. 2.33 are carried out in the current (latest) configuration. The calculation of the stresses and strains must take into account the deformation of the body. In the analysis, we will adopt a Lagrangian formulation, following the body during its deformation. We define the deformation gradient as:

$$\bar{F}^T = \begin{bmatrix} \frac{\partial x}{\partial X} & \frac{\partial y}{\partial X} & \frac{\partial z}{\partial X} \\ \frac{\partial x}{\partial Y} & \frac{\partial y}{\partial Y} & \frac{\partial z}{\partial Y} \\ \frac{\partial x}{\partial Z} & \frac{\partial y}{\partial Z} & \frac{\partial z}{\partial Z} \end{bmatrix}$$

where $\boldsymbol{x} = (x, y, z)$ the body coordinates at a time t and $\boldsymbol{X} = (X, Y, Z)$ at the time 0. From large-strain theory, the Lagrangian-Green strain tensor is given from:

$$e_{ij} = \frac{1}{2}\left(\frac{\partial u_i}{\partial x_j} + \frac{\partial u_j}{\partial x_i} + \frac{\partial u_k}{\partial x_i}\frac{\partial u_k}{\partial x_j}\right)$$

where the derivatives are written with respect to the initial configuration. It can also be expressed as:

$$\delta e_{ij} = F_{mi} F_{mj} \delta\varepsilon_{mn}$$

where $\delta\varepsilon_{mn}$ the variation of the linear strain expressed for the current configuration. An appropriate stress tensor should be used as well. The second Piola-Kirchhoff stress tensor reads:

$$\tau_{ij} = |\bar{F}|(F^{-1})_{im}(F^{-1})_{jn}\sigma_{mn}$$

with σ_{mn} the stress at the latest configuration. It can be proven [Bat96] that for a stationary coordinate system, both the Green-Lagrange strain tensor and the Piola-Kirchhoff stress tensor are invariant under rigid body rotation. This leads into rewriting Eq. 2.33 as:

$$\int_{\Omega|_{t+\Delta t}} \sigma_{ij}|_{t+\Delta t}\delta\varepsilon_{ij}|_{t+\Delta t} d\Omega|_{t+\Delta t} = \int_{\Omega} \tau_{mn}\delta e_{mn} d\Omega = R|_{t+\Delta t}$$

where the derivations and integrations carried out in the right hand side are performed with respect to the initial (known) configuration. After splitting $e_{ij} = \varepsilon_{ij} + n_{ij}$[6] and linearizing the equations using $\tau_{ij} = D_{ijmn}\varepsilon_{mn}$ and $\delta\varepsilon_{ij} \approx \delta e_{ij}$[7], we end up with:

$$\int_{\Omega} D_{ijmn}\varepsilon_{mn}\delta\varepsilon_{ij} d\Omega + \int_{\Omega} \tau_{ij}\delta n_{ij} d\Omega = R|_{t+\Delta t} - \int_{\Omega} \tau_{ij}\delta\varepsilon_{ij} d\Omega$$

which constitutes the total Lagrangian formulation of the off-balance virtual work. Due to the linearization, an error is introduced in the calculation of the internal work.

[6] It can be deduced that $n_{ij} = \frac{1}{2}\frac{\partial u_k}{\partial x_i}\frac{\partial u_k}{\partial x_j}$.

[7] This is written with respect to the initial configuration.

Multiple iterations should be executed for the minimization of this error and the identification of the equilibrium. The above written equation can be modified as:

$$\underbrace{\int_{\Omega} D_{ijmn}\Delta\varepsilon_{mn}\delta\varepsilon_{ij}d\Omega}_{\text{linear part}} + \underbrace{\int_{\Omega} \tau_{ij}^{k}\delta\Delta n_{ij}d\Omega}_{\text{nonlinear part}} = R|_{t+\Delta t} - \int_{\Omega} \tau_{ij}^{k}\delta e_{ij}^{k}d\Omega \tag{2.34}$$

with $\Delta\varepsilon_{mn} = \varepsilon_{mn}^{k+1} - \varepsilon_{mn}^{k}$ and $\Delta n_{ij} = n_{ij}^{k+1} - n_{ij}^{k}$, where we assumed that the material properties do not vary with the deformation. If the applied forces vary with deformation, the external virtual work at $k+1$ can be estimated from the geometry at k and then updated at each iteration. The effect of the incremental displacements should be included in the stiffness matrix. Finally, the FE expression of Eq. 2.34 can be derived following the same procedure examined for linear mechanics. The direct correspondence between Eq. 2.34 and Eq. 2.32 leads Eq. 2.34 to be written as:

$$(\bar{K}_{L}^{k-1} + \bar{K}_{NL}^{k-1})_{i+1}\Delta\boldsymbol{U}^{k} = \boldsymbol{R}_{i+1} - \boldsymbol{P}_{i+1}^{k-1} \tag{2.35}$$

where $\bar{K}_L$ the stiffness matrix coming for the linear part (Eq. 2.34) and $\bar{K}_{NL}$ from the nonlinear part respectively.

2.2.4 Corotational beam formulation

The corotational concept introduces a local reference frame following the translation and rotation (rigid body) movement of the element. In this way, only the strain that produces deformation at a local (element) level remains. The strain is directly related to the internal forces induced in the beam element. In this section, we follow [BCRV12] in deriving a 2D corotational beam element using Kirchhoff theory.

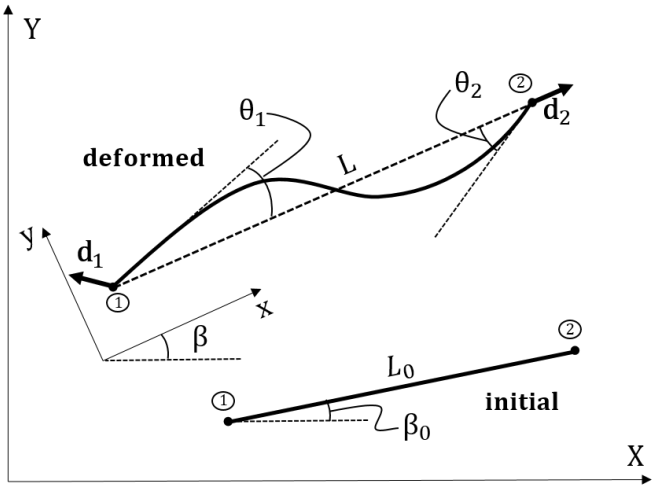

Figure 2.2: *Initial (L_0) and deformed (L) configuration of a 2D corotational frame element.*

The 2D frame element in Fig. 2.2 at its initial and deformed configuration is considered. The beam undergoes a translation (due to $\boldsymbol{d}_1$ and $\boldsymbol{d}_2$) and a rotation (from β_0 to β) with respect to the global (X,Y) reference system. At its final position, the local (x,y) reference system is introduced. The flexural deformations θ_1 and θ_2 are measured in the local coordinate system. The local extension is calculated from:

$$u_e = L - L_0 = \frac{L^2 - L_0^2}{L + L_0}$$

were the latter expression is adopted to avoid a ill-conditioned formulation. The length of each configuration is calculated from:

$$L_0 = \sqrt{(X_2 - X_1)^2 + (Y_2 - Y_1)^2}$$

and

$$L = \sqrt{[(X_2 + u_2) - (X_1 + u_1)]^2 + [(Y_2 + v_2) - (Y_1 + v_1)]^2}$$

where the indices 1 and 2 denote the nodes as shown in Fig. 2.2 with $\boldsymbol{d}_1 = (u_1, v_1)$, $\boldsymbol{d}_2 = (u_2, v_2)$ the deformation vectors. The current angle of the corrotating frame with respect to the global coordinate system can be calculated from:

$$\beta = atan\left[\frac{(Y_2 + v_2) - (Y_1 + v_1)}{(X_2 + u_2) - (X_1 + u_1)}\right]$$

while

$$\beta_0 = atan\left[\frac{Y_2 - Y_1}{X_2 - X_1}\right]$$

The induced axial strain is assumed constant and calculated from u_e/L_0. The axial force in the frame is given from:

$$N = EA\frac{u_e}{L_0}$$

The flexural deformations are given from:

$$\theta_1 = \theta_{g1} - \beta + \beta_0 = \beta_1 - \beta \;\text{ and }\; \theta_2 = \theta_{g2} - \beta + \beta_0 = \beta_2 - \beta \tag{2.36}$$

where θ_{g1}, θ_{g2} the deformation with respect to the initial configuration in the global coordinate system. In practice, to allow the rotations to take arbitrarily large values, the calculation uses:

$$\theta_* = atan\left(\frac{cos\beta sin\beta_* - sin\beta cos\beta_*}{cos\beta cos\beta_* + sin\beta sin\beta_*}\right)$$

Following the beam-theory, the local end moments are linked to the local nodal rotations with:

$$\left\{\begin{array}{c} M_1 \\ M_2 \end{array}\right\} = \frac{2EI}{L_0}\left[\begin{array}{cc} 2 & 1 \\ 1 & 2 \end{array}\right]\left\{\begin{array}{c} \theta_1 \\ \theta_2 \end{array}\right\}$$

The shear forces at the two nodes are calculated from:

$$V_1 = -V_2 = \frac{M_1 + M_2}{L}$$

In this way, a relation between the local forces $\boldsymbol{p}_l = (N \;\; M_1 \;\; M_2)^T$ and the local strain inducing deformations is established.

Virtual local displacements

We define $c = cos\beta$ and $s = sin\beta$. For a small movement $\delta \boldsymbol{d}_{12}$ (see Fig. 2.3) from the current configuration defined as:

$$\delta \boldsymbol{d}_{12} = \left\{ \begin{array}{c} \delta u_2 - \delta u_1 \\ \delta v_2 - \delta v_1 \end{array} \right\}$$

we can express the small local extension as:

$$\delta u_e = c(\delta u_2 - \delta u_1) + s(\delta v_2 - \delta v_1) = \underbrace{[-c \;\; -s \;\; 0 \;\; c \;\; s \;\; 0]}_{\boldsymbol{r}^T} \delta \boldsymbol{q}$$

where we denote with $\boldsymbol{q} = (u_1 \;\; v_1 \;\; \theta_{g1} \;\; u_2 \;\; v_2 \;\; \theta_{g2})$ the nodal displacement vector. The small rigid rotation $\delta\alpha$ (see Fig. 2.3) from the current configuration results in

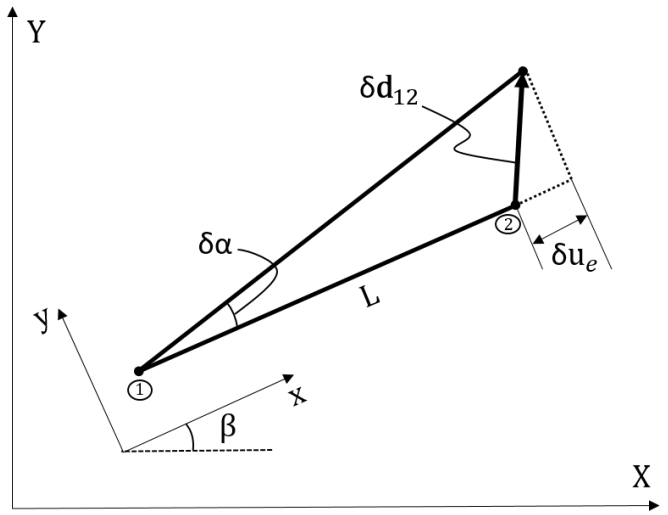

Figure 2.3: *Infinitesimal deformation.*

an arc length change given from:

$$L\delta\alpha = -s(\delta u_2 - \delta u_1) + c(\delta v_2 - \delta v_1) = \underbrace{[s \;\; -c \;\; 0 \;\; -s \;\; c \;\; 0]}_{\boldsymbol{z}^T} \delta \boldsymbol{q}$$

Differentiating Eq. 2.36 gives:

$$\delta\boldsymbol{\theta} = \left\{ \begin{array}{c} \delta\theta_{g1} + \delta\beta_0 - \delta\beta \\ \delta\theta_{g2} + \delta\beta_0 - \delta\beta \end{array} \right\} = \left\{ \begin{array}{c} \delta\theta_{g1} - \delta\alpha \\ \delta\theta_{g2} - \delta\alpha \end{array} \right\}$$

as $\delta\beta_0 = 0$ and $\delta\beta = \delta\alpha$. We can write:

$$\delta\boldsymbol{\theta}_g = \left[\begin{array}{cccccc} 0 & 0 & 1 & 0 & 0 & 0 \\ 0 & 0 & 0 & 0 & 0 & 1 \end{array} \right] \delta\boldsymbol{q}$$

and finally:

$$\delta\boldsymbol{\theta} = \underbrace{\left(\left[\begin{array}{cccccc} 0 & 0 & 1 & 0 & 0 & 0 \\ 0 & 0 & 0 & 0 & 0 & 1 \end{array} \right] - \frac{1}{L} \left[\begin{array}{c} \boldsymbol{z}^T \\ \boldsymbol{z}^T \end{array} \right] \right)}_{\bar{A}^T} \delta\boldsymbol{q}$$

The complete vector of local displacements is summarized:

$$\delta\boldsymbol{q}_l = \left\{ \begin{array}{c} \delta u_e \\ \delta\theta_1 \\ \delta\theta_2 \end{array} \right\} = \left[\begin{array}{c} \boldsymbol{r}^T \\ \bar{A}^T \end{array} \right] \delta\boldsymbol{q} = \bar{B}\delta\boldsymbol{q}$$

Virtual work principle

The virtual work can be expressed as:

$$\delta\boldsymbol{q}^T\boldsymbol{p} = N\delta u_l + M_1\delta\theta_1 + M_2\delta\theta_2 = \delta\boldsymbol{q}_l^T\boldsymbol{p}_l = \delta\boldsymbol{q}^T\bar{B}^T\boldsymbol{p}_l$$

As this expression holds for arbitrarily large virtual deformations, it is deduced:

$$\boldsymbol{p} = \bar{B}^T\boldsymbol{p}_l \tag{2.37}$$

Differentiating Eq. 2.37 leads to:

$$\delta\boldsymbol{p} = \bar{B}^T\delta\boldsymbol{p}_l + \delta\bar{B}^T\boldsymbol{p}_l$$

For linear material behavior, we can write:

$$\bar{B}^T\delta\boldsymbol{p}_l = \bar{B}^T\bar{D}\delta\boldsymbol{q}_l = \bar{B}^T\bar{D}\bar{B}\delta\boldsymbol{q} = \bar{K}_L\delta\boldsymbol{q}$$

where

$$\bar{D} = \frac{1}{L_0} \left[\begin{array}{ccc} EA & 0 & 0 \\ 0 & 4EI & 2EI \\ 0 & 2EI & 4EI \end{array} \right]$$

The geometric stiffness matrix comes from:

$$\delta\bar{B}^T\boldsymbol{p}_l = N\delta\boldsymbol{r} + \frac{M_1+M_2}{L^2}(L\delta\boldsymbol{z} + \boldsymbol{z}\delta u_e) = \underbrace{\left[\frac{N}{L}\boldsymbol{z}\boldsymbol{z}^T + \frac{M_1+M_2}{L^2}(\boldsymbol{r}\boldsymbol{z}^T + \boldsymbol{z}\boldsymbol{r}^T) \right]}_{\bar{K}_{NL}} \delta\boldsymbol{q}$$

The complete tangent stiffness matrix is given by:

$$\bar{K}_t = \bar{K}_L + \bar{K}_{NL}$$

2.2.5 Nonconservative forces

The analysis previously examined does not take into account the variation of boundary conditions during loading. In general, as the body deforms, the externally applied forces vary with the displacement. This dependency of the forces to the degrees of freedom should be included in the nonlinear analysis. In this section, we follow J. H. Argyris and S. Symeonidis [AS81] in deriving a finite element formulation that accounts for nonconservative forces.

Starting from the term $R|_{t+\Delta t}$ in Eq. 2.34, the virtual work of the nonconservative forces is written:

$$\delta W_{nc} = R|_{t+\Delta t} = \delta \boldsymbol{u} \boldsymbol{R}_{nc}|_{t+\Delta t}$$

where for each element:

$$\boldsymbol{R}_{nc} = \boldsymbol{R}_b^{(m)} + \boldsymbol{R}_S^{(m)} + \boldsymbol{R}_p^{(m)} - \boldsymbol{R}_0^{(m)}$$

The linearization of the forces reads:

$$\boldsymbol{R}_{nc}|_{t+\Delta t} = \boldsymbol{R}|_t + \frac{\partial \boldsymbol{R}_{nc}}{\partial \boldsymbol{U}} \Delta \boldsymbol{U}$$

and this leads to:

$$\Delta(\delta W_{nc}) \approx \delta \boldsymbol{u} \left(\boldsymbol{R}|_t + \frac{\partial \boldsymbol{R}_{nc}}{\partial \boldsymbol{U}} \Delta \boldsymbol{U} \right)$$

Consequently, Eq. 2.35 is augmented as:

$$(\bar{K}_L^{k-1} + \bar{K}_{NL}^{k-1})_{i+1} \Delta \boldsymbol{U}^k = \boldsymbol{R}_{i+1}^{k-1} + \underbrace{\left. \frac{\partial \boldsymbol{R}_{nc}}{\partial \boldsymbol{U}} \right|_{i+1}^{k-1}}_{\bar{K}_{NC}} \Delta \boldsymbol{U}^k - \boldsymbol{P}_{i+1}^{k-1}$$

$$(\bar{K}_L^{k-1} + \bar{K}_{NL}^{k-1} - \bar{K}_{NC}^{k-1})_{i+1} \Delta \boldsymbol{U}^k = \boldsymbol{R}_{i+1}^{k-1} - \boldsymbol{P}_{i+1}^{k-1}$$

Newton-Raphson iterations are performed to minimize the error introduced due to linearization. The matrix $\bar{K}_{NC}$ is obtained by differentiating the force expression. This procedure is straightforward in the case of point loads for which:

$$\bar{K}_{NC} = \sum_m \frac{\partial \boldsymbol{R}_{nc}^{(m)}}{\partial \boldsymbol{U}^{(m)}}$$

Circulatory distributed loading

For distributed loads, the derivation of the stiffness correction matrix becomes more complicated. In this section we will examine linearly varying distributions on straight 2D beams. We follow [AS81] where the generalized displacement vector $\boldsymbol{\rho}$ is introduced:

$$\boldsymbol{\rho} = \{\boldsymbol{\rho}_0 | \boldsymbol{\rho}_N\} = \bar{a} \boldsymbol{U} \tag{2.38}$$

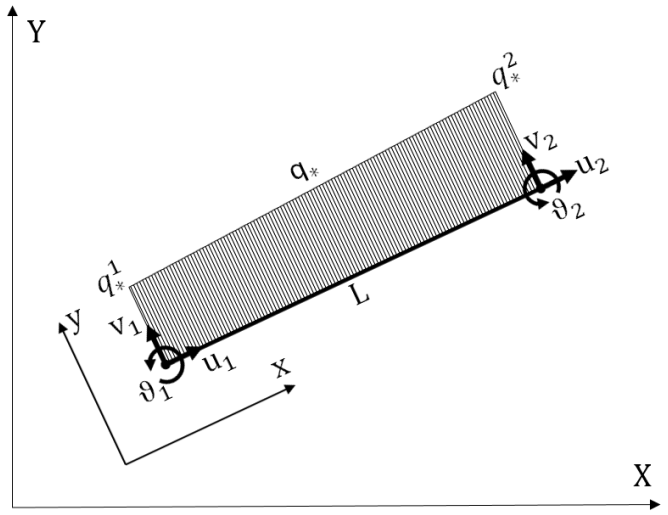

Figure 2.4: *Beam element under distributed nonconservative loading.*

The local beam movement $\boldsymbol{U} = (u_1 \;\; v_1 \;\; \theta_1 \;\; u_2 \;\; v_2 \;\; \theta_2)^T$ (see Fig. 2.4) into rigid body $(\boldsymbol{\rho}_0)$ and natural $(\boldsymbol{\rho}_N)$ modes. In two dimensions, the matrix $\bar{a}$ writes:

$$\bar{a} = \begin{bmatrix} 1/2 & 0 & 0 & 1/2 & 0 & 0 \\ 0 & 1/2 & 0 & 0 & 1/2 & 0 \\ 0 & 1/L & 0 & 0 & -1/L & 0 \\ -1 & 0 & 0 & 1 & 0 & 0 \\ 0 & 0 & -1 & 0 & 0 & 1 \\ 0 & 2/L & -1 & 0 & -2/L & -1 \end{bmatrix}$$

with L the beam element length. In 2D, for the nonconservative distributed loading $\boldsymbol{q}_{nc} = (q_x, q_y)$, the mean mid-point values and the differences of the nodal values are introduced:

$$q_{*m} = \frac{1}{1}(q_*^2 + q_*^1) \;\text{ and }\; q_{*d} = q_*^2 - q_*^1$$

At the undeformed position:

$$\boldsymbol{q}_{nc}^0 = \boldsymbol{q}_m + \xi \boldsymbol{q}_d$$

where

$$\boldsymbol{q}_m = (q_{xm}, q_{ym}) \;\;,\;\; \boldsymbol{q}_d = (q_{xd}, q_{yd}) \;\text{ and }\; \xi = x/L$$

The nonconservative loading vector can be expressed as:

$$\boldsymbol{q}_{nc}(\boldsymbol{\rho}) = \bar{T}(\boldsymbol{\rho})\boldsymbol{q}_{nc}^0$$

where $\bar{T}$ a nonlinear function of the displacement. It is proven in [AS81] that the current load vector can be written as:

$$\boldsymbol{q}_{nc} = \boldsymbol{q}_{nc}^0 + [\bar{C}_0 \;\; \bar{C}_N] \begin{bmatrix} \boldsymbol{\rho}_0 \\ \boldsymbol{\rho}_N \end{bmatrix}$$

where

$$\bar{C}_0 = \begin{bmatrix} 0 & 0 & p_y \\ 0 & 0 & 0 \\ 0 & 0 & -p_y \end{bmatrix} \text{ and } \bar{C}_N = \begin{bmatrix} 0 & \xi p_y & (\frac{1}{4} - 3\xi)p_y \\ 0 & 0 & 0 \\ 0 & -\xi p_y & (\frac{1}{4} - 3\xi)p_y \end{bmatrix}$$

The equivalent nodal forces are expressed as:

$$\boldsymbol{P}_{nc} = \underbrace{\left(L \int_{L/2}^{L/2} \bar{H}^T(\xi)[\bar{C}_0 \;\; \bar{C}_N] d\xi \right)}_{\bar{k}_{NC}} \boldsymbol{\rho}$$

with

$$\bar{H}(\xi) = \begin{bmatrix} 1 & 0 & 0 & x/L & 0 & 0 \\ 0 & 1 & -1 & 0 & -(x^2/2L - L/8) & (x^3/L^2 - x/4) \\ 0 & 0 & 1 & 0 & x/L & -(3x^2/L^2 - 1/4) \end{bmatrix}$$

It can be deduced that:

$$\bar{k}_{NC} = \frac{\partial \boldsymbol{P}_{nc}}{\partial \boldsymbol{\rho}} = \begin{bmatrix} \bar{k}_{00} & \bar{k}_{0N} \\ \bar{k}_{N0} & \bar{k}_{NN} \end{bmatrix}$$

with:

$$\bar{k}_{00} = \begin{bmatrix} 0 & 0 & p_{ym}L \\ 0 & 0 & -p_{xm}L \\ 0 & 0 & p_{xd}L^2/12 \end{bmatrix} \;,\; \bar{k}_{0N} = \begin{bmatrix} 0 & p_{yd}L/12 & 0 \\ 0 & -p_{xd}L/12 & 0 \\ 0 & p_{xm}L^2/12 & -p_{xd}L^2/60 \end{bmatrix}$$

$$\bar{k}_{N0} = \begin{bmatrix} 0 & 0 & p_{yd}L/12 \\ 0 & 0 & -p_{xm}L^2/12 \\ 0 & 0 & p_{xd}L^2/120 \end{bmatrix} \;,\; \bar{k}_{0N} = \begin{bmatrix} 0 & p_{ym}L/12 & -p_{zd}L/60 \\ 0 & -p_{xd}L^2/240 & -p_{xm}L^2/120 \\ 0 & p_{xm}L^2/120 & -p_{xd}L^2/1680 \end{bmatrix}$$

Finally, to move from the generalized back to the local Cartesian displacement vector, it suffices that:

$$\bar{K}_{NC} = \bar{a}^T \bar{k}_{NC} \bar{a}$$

2.2.6 Contact condition

The contact between two or more bodies manifests a boundary nonlinearity where both the displacement and the forces developed at an interface are unknown. A detailed analysis determines: (a) the region of contact, (b) the pressure developed between the bodies, and (c) whether the contact interface moves. The slave-master concept is introduced for the implementation of the contact solution. The deformable body is set as a slave body to the master rigid body. For a flexible-flexible contact interface[8], since both bodies can deform, this choice is made arbitrarily. In the

[8]No rigid bodies are involved.

general case, the contact algorithm determines for each slave node the contacting master segments. The contact condition imposed that the slave body cannot penetrate into the master body.

This procedure is examined Fig. 2.5. The contact pair $\{\boldsymbol{x}_S, \boldsymbol{x}_1, \boldsymbol{x}_2\}$ involves a slave node and its closest master segment i.e. the segment that includes its normal projection $\boldsymbol{x}_C$. The impenetrability condition states that:

$$g_N = (\boldsymbol{x}_S - \boldsymbol{x}_1)\boldsymbol{n} = \boldsymbol{g} \cdot \boldsymbol{n} \geq 0$$

with $\boldsymbol{n}$ the normal unit vector of the master segment. If $g_N < 0$ a contact condition should be imposed. Penalty-based contact forces $F_c = K_N g_N$ are applied at the contact pairs for every violated segment. The penalty parameter K_N controls the allowed penetration.

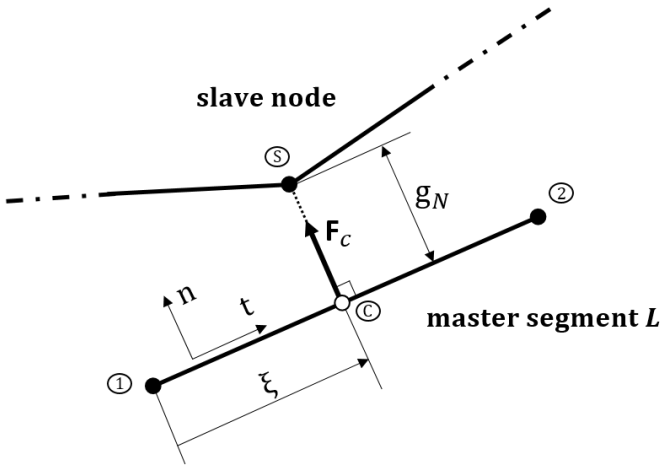

Figure 2.5: *Contact schematic.*

Formulation of contact problems

In this section we will follow Zavarise et al. [ZDLT12] in deriving the contact contribution to the stiffness and the residual forces. We will only examine frictionless (slip) contact constrains. The contact constraints can be imposed through a penalization of the potential energy. The penalty functional added takes the form:

$$\Pi_c = \frac{1}{2} \int_{S_c} K_N g_N^2 d\S_c$$

where S_c the contact boundary. For active contacts, the variation of this potential yields:

$$\delta\Pi_c = \int_{S_c} \underbrace{K_N g_N}_{F_c} \delta g_N dS_c \tag{2.39}$$

This expression is nonlinear with respect to the deformation vector:

$$\boldsymbol{U} = (u_s \;\; v_s \;\; u_1 \;\; v_1 \;\; u_2 \;\; v_2)^T$$

The linearization of Eq. 2.39 gives:

$$\Delta\delta\Pi_c = \int_{S_c} K_N \Delta g_N \delta g_N dS_c + \int_{S_c} K_N g_N \Delta\delta g_N dS_c$$

As the linearization introduces an error in the estimation, Newton-Raphson iterations are introduced to solve the set of equations:

$$\int_{S_c} K_N \Delta g_N \delta g_N dS_c + \int_{S_c} K_N g_N \Delta\delta g_N dS_c = -\int_{S_c} F_c \delta g_N dS_c \tag{2.40}$$

where we can further expand the terms:

$$\delta g_N = \delta \boldsymbol{g} \cdot \boldsymbol{n} + \boldsymbol{g} \cdot \delta \boldsymbol{n} \tag{2.41}$$

$$\Delta g_N = \Delta \boldsymbol{g} \cdot \boldsymbol{n} + \boldsymbol{g} \cdot \Delta \boldsymbol{n} \tag{2.42}$$

$$\Delta\delta g_N = \cancelto{0}{\Delta\delta \boldsymbol{g}} \cdot \boldsymbol{n} + \delta \boldsymbol{g} \cdot \Delta \boldsymbol{n} + \Delta \boldsymbol{g} \cdot \delta \boldsymbol{n} + \boldsymbol{g} \cdot \Delta\delta \boldsymbol{n} \tag{2.43}$$

where higher-order terms are cancelled out.

Finite element formulation

IN 2D, the unit tangent and normal vectors of the master segment of length L are defined as:

$$\boldsymbol{t} = \frac{\boldsymbol{x}_2 - \boldsymbol{x}_1}{L} \;\text{ and }\; \boldsymbol{n} = \boldsymbol{t} \times \boldsymbol{k}$$

where $\boldsymbol{k}$ the unit vector orthogonal to the plane. The non-dimensional position of the projection $\boldsymbol{x}_c$ of the slave point $\boldsymbol{x}_S$ (see Fig. 2.5) is defined as:

$$\xi = \frac{(\boldsymbol{x}_S - \boldsymbol{x}_1)^T}{L} \boldsymbol{t}$$

with $0 \leq \xi \leq 1$. It can be proven [ZDL09] after some detailed derivation that we can rewrite Eqs. 2.41-2.43 in a matrix form as:

$$\delta g_N = \delta \boldsymbol{U}^T \boldsymbol{N}_S$$

$$\Delta g_N = \boldsymbol{N}_S^T \Delta \boldsymbol{U}$$

$$\Delta\delta g_N = -\frac{1}{L} \delta \boldsymbol{U}^T \left(\boldsymbol{N}_0 \boldsymbol{T}_S^T + \boldsymbol{T}_S \boldsymbol{N}_0^T + \frac{g_N}{L} \boldsymbol{N}_0 \boldsymbol{N}_0^T \right) \Delta \boldsymbol{U}$$

with:

$$\boldsymbol{N}_s = \begin{Bmatrix} \boldsymbol{n} \\ -(1-\xi)\boldsymbol{n} \\ -\xi \boldsymbol{n} \end{Bmatrix}, \; \boldsymbol{N}_0 = \begin{Bmatrix} 0 \\ -\boldsymbol{n} \\ \boldsymbol{n} \end{Bmatrix}, \; \boldsymbol{T}_s = \begin{Bmatrix} \boldsymbol{t} \\ -(1-\xi)\boldsymbol{t} \\ -\xi \boldsymbol{t} \end{Bmatrix}$$

This allows us to rewrite Eq. 2.40 as:

$$\delta \boldsymbol{U}^T \underbrace{(\bar{K}_M + \bar{K}_G)}_{\bar{K}_c} \Delta \boldsymbol{U} = -\delta \boldsymbol{u}^T \boldsymbol{R}_c$$

where we set:

$$\bar{K}_M = K_N \boldsymbol{N}_S \boldsymbol{N}_S^T$$

$$\bar{K}_G = -\frac{F_c}{L}\left(\boldsymbol{N}_0 \boldsymbol{T}_S^T + \boldsymbol{T}_S \boldsymbol{N}_0^T + \frac{g_N}{L}\boldsymbol{N}_0 \boldsymbol{N}_0^T\right)$$

and

$$\boldsymbol{R}_c = F_c \boldsymbol{N}_S$$

This leads in adding the following terms in the Newton-Raphson procedure given by Eq. 2.32:

$$(\bar{K}_t + \bar{K}_c)_{i+1}^{n-1} \Delta \boldsymbol{U}^n = \boldsymbol{R}_{i+1} - \boldsymbol{P}_{i+1}^{n-1} - (\boldsymbol{R}_c)_{i+1}^{n-1} \tag{2.44}$$

Equation 2.44 is the final complete Newton-Raphson formulation for large strain deformation of structures under nonconservative forces and includes cocntact non-linearities.

Bibliography

[AS81] J. H. Argyris and Sp. Symeonidis. Nonlinear finite element analysis of elastic systems under nonconservative loading-natural formulation. part I. Quasistatic problems. *Computer Methods in Applied Mechanics and Engineering*, 26(1):75–123, April 1981.

[Bat96] K. J. Bathe. *Finite Element Procedures*. Prentice-Hall, Englewood Cliffs, 1996.

[BBH+07] S. Bourdet, M. Braza, Y. Hoarau, R. El Akoury, A. Ashraf, G. Harran, P. Chassaing, and H. Djeridi. Prediction and physical analysis of unsteady flows around a pitching airfoil with the dynamic mesh approah. *European Journal of Computational Mechanics*, 16(3-4):451–476, January 2007.

[BBHEA08] R. Bourguet, M. Braza, G. Harran, and R. El Akoury. Anisotropic Organised Eddy Simulation for the prediction of non-equilibrium turbulent flows around bodies. *Journal of Fluids and Structures*, 24(8):1240–1251, November 2008.

[BBPH07] R. Bourguet, M. Braza, R. Perrin, and G. Harran. Anisotropic eddy-viscosity concept for strongly detached unsteady flows. *AIAA Journal*, 45(5):1145–1149, 2007.

[BCRV12] R. Borst, M. Crisfield, J. Remmers, and C. Verhoosel. *Non-Linear Finite Element Analysis of Solids and Structures: Second Edition*. John Wiley & Sons, Ltd, 2012.

[Bla01] J. Blazek. *Computational Fluid Dynamics: Principles and Applications*. Elsevier Butterworth-Heinemann, third edition edition, 2001.

[BPH06] M. Braza, R. Perrin, and Y. Hoarau. Turbulence properties in the cylinder wake at high Reynolds numbers. *Journal of Fluids and Structures*, 22(6):757–771, August 2006.

[Chi82] K.-Y. Chien. Predictions of channel and boundary-layer flows with a low-Reynolds-number turbulence model. *AIAA Journal*, 20(1):33–38, 1982.

[CS88] I. J. D. Craig and A. D. Sneyd. An alternating-direction implicit scheme for parabolic equations with mixed derivatives. *Computers & Mathematics with Applications*, 16(4):341–350, January 1988.

[Har83] A. Harten. High resolution schemes for hyperbolic conservation laws. *Journal of Computational Physics*, 49(3):357–393, March 1983.

[HBR09a] W. Haase, M. Braza, and A. Revell. II presentation of modelling approaches. In *DESider – A European Effort on Hybrid RANS-LES Modelling. Notes on Numerical Fluid Mechanics and Multidisciplinary Design*, volume 103. Springer, Berlin, Heidelberg, 2009.

[HBR09b] W. Haase, M. Braza, and A. Revell. IV applications - test cases. In *DESider – A European Effort on Hybrid RANS-LES Modelling. Notes on Numerical Fluid Mechanics and Multidisciplinary Design*, volume 103. Springer, Berlin, Heidelberg, 2009.

[Hir07] C. Hirsch. *Numerical Computation of Internal and External Flows: The Fundamentals of Computational Fluid Dynamics*. Butterworth-Heinemann, Amsterdam, 2 edition, June 2007.

[Hoa02] Y. Hoarau. *Analyse physique par simulation numérique et modélisation des écoulements décollés instationnaires autour de surfaces portantes*. Phd thesis, INPT, 2002.

[HPV+16] Y. Hoarau, D. Pena, J. B. Vos, D. Charbonier, A. Gehri, M. Braza, T. Deloze, and E. Laurendeau. *Recent Developments of the Navier Stokes Multi Block (NSMB) CFD solver*. American Institute of Aeronautics and Astronautics, 2016.

[JB94] G. Jin and M. Braza. Two-equation turbulence model for unsteady separated flows around airfoils. *AIAA Journal*, 32(11):2316–2320, 1994.

[JST81] A. Jameson, W. Schmidt, and E. Turkel. Numerical solution of the Euler equations by finite volume methods using Runge Kutta time stepping schemes. In *14th Fluid and Plasma Dynamics Conference*. American Institute of Aeronautics and Astronautics, 1981.

[PCC+07] R. Perrin, E. Cid, S. Cazin, A. Sevrain, M. Braza, F. Moradei, and G. Harran. Phase-averaged measurements of the turbulence properties in the near wake of a circular cylinder at high Reynolds number by 2c-PIV and 3c-PIV. *Experiments in Fluids*, 42(1):93–109, January 2007.

[RS14] J. Reiss and J. Sesterhenn. A conservative, skew-symmetric finite difference scheme for the compressible Navier–Stokes equations. *Computers & Fluids*, 101:208–219, September 2014.

[SDS+06] P. R. Spalart, S. Deck, M. L. Shur, K. D. Squires, M. Kh. Strelets, and A. Travin. A New Version of Detached-eddy Simulation, Resistant to Ambiguous Grid Densities. *Theoretical and Computational Fluid Dynamics*, 20(3):181, May 2006.

[SGJG+15] D. Szubert, F. Grossi, A. Jimenez Garcia, Y. Hoarau, J. C. R. Hunt, and M. Braza. Shock-vortex shear-layer interaction in the transonic flow around a supercritical airfoil at high Reynolds number in buffet conditions. *Journal of Fluids and Structures*, 55:276–302, May 2015.

[SJSA97] P. Spalart, W.-H. Jou, M. Strelets, and S. Allmaras. Comments on the Feasibility of LES for Wings, and on a Hybrid RANS/LES Approach. In *Advances in DNS/LES: Direct numerical simulation and large eddy simulation*. Greyden Press, Louisiana Tech University, 1997.

[Spe98a] C. G. Speziale. A Combined Large-Eddy Simulation and Time-Dependent RANS Capability for High-Speed Compressible Flows. *Journal of Scientific Computing*, 13(3):253–274, September 1998.

[Spe98b] C. G. Speziale. Turbulence modeling for time-dependent rans and vles: A review. *AIAA Journal*, 36(2):173–184, 1998.

[SSST08] M. L. Shur, P. R. Spalart, M. Kh. Strelets, and A. K. Travin. A hybrid RANS-LES approach with delayed-DES and wall-modelled LES capabilities. *International Journal of Heat and Fluid Flow*, 29(6):1638–1649, 2008.

[ST87] R. Swanson and E. Turkel. Artificial dissipation and central difference schemes for the Euler and Navier-Stokes equations. In *8th Computational Fluid Dynamics Conference*. American Institute of Aeronautics and Astronautics, 1987.

[Wil06] D. Wilcox. *Turbulence Modeling for CFD*. DCW Industries, Inc., third edition edition, 2006.

[Yee97] H. C. Yee. Explicit and Implicit Multidimensional Compact High-Resolution Shock-Capturing Methods:Formulation. *Journal of Computational Physics*, 131(1):216–232, February 1997.

[YJ86] S. Yoon and A. Jameson. A multigrid LU-SSOR scheme for approximate newton iteration applied to the euler equations. *NASA-CR-179524*, 1986.

[ZDL09] G. Zavarise and L. De Lorenzis. The node-to-segment algorithm for 2d frictionless contact: Classical formulation and special cases. *Computer Methods in Applied Mechanics and Engineering*, 198(41):3428 – 3451, 2009.

[ZDLT12] G. Zavarise, L. De Lorenzis, and R. L. Taylor. A non-consistent start-up procedure for contact problems with large load-steps. *Computer Methods in Applied Mechanics and Engineering*, 205-208:91–109, January 2012.

[ZRTC93] H. Zhang, M. Reggio, J. Y. Trépanier, and R. Camarero. Discrete form of the GCL for moving meshes and its implementation in CFD schemes. *Computers & Fluids*, 22(1):9–23, January 1993.

[ZTF05] O.C. Zienkiewicz, R. Taylor, and D. Fox. *The Finite Element Method for Solid and Structural Mechanics*. Elsevier Butterworth-Heinemann, 2005.

Chapter 3

Turbulence modelling with stochastic forcing

Thin moving interfaces developed in high-Reynolds number flows significantly affect the large scale dynamics by locally sheltering sheared regions. Advanced turbulence modelling approaches should account for these interactions in order to accurately simulate high-Reynolds turbulent flows. The stochastic forcing approach examined in the present work consists of a re-injection of turbulence in sheared flow regions to account for upscale energy transfers. The addition of source terms in the turbulent transport equations causes local variations of the eddy viscosity and effectively reduces the excessive rate of turbulent diffusion which occurs in turbulence modelling apporaches assuming a downscale cascade. The method is extended here for three-dimensional flows and employed for a transonic flow to investigate the buffet instability. An enhanced prediction of the aerodynamic forces is demonstrated and the effect of the state (laminar/turbulent) of the incoming boundary layer is discussed.

3.1 Introduction

A great deal of fully developed inhomogeneous turbulent flows have been found to be bounded by thin layer-like structures that separate the turbulent and non-turbulent (or weakly turbulent) regions of the flow. Boundary layers, turbulent wakes and jets, all exhibit these type of interfaces and have been studied extensively by means of numerical simulations and experimental measurements. Furthermore, coherent interfacial layers have been identified inside turbulent homogeneous jets and wakes or in near-wall regions (wall-bounded turbulence). The dynamics of these

moving interfaces significantly affect the large scale flow dynamics and vortical interactions [HEW08] acting as barriers between the different flow regions, blocking individual perturbations and sheltering locally the sheared regions. It is important for advanced turbulence modelling approaches to account for these interactions in order to accurately predict high Reynolds turbulent sheared flows where these interfaces become too thin to be resolved at a realistic computational time.

3.1.1 Interfacial dynamics

The concept of shear sheltering is examined in [JD98]. The authors demonstrated that this procedure is indeed an intrinsic property of the linearized Navier-Stokes equations in high-shear regions. In these regions, the freestream turbulent disturbances are blocked, remain confined outside the shear layers, unable to penetrate them. As a result, boundary layers and wakes are shielded from external disturbances and the authors found a correlation between the penetration depth, the Reynolds number and the frequency of the disturbance. The authors in [HD99] examined sheltering phenomena in shear layers through some simplified mathematical models. They studied various cases of interactions between disturbances in external flows and adjacent vortical flows. They established the conditions (e.g. travelling speed, length scales) for which the blocking of turbulent perturbations takes place across the interface of the different flow regions. The authors demonstrated a stretching of the perturbations which was attributed to the creation of thin vortical interfacial layers at the edges of the shielded flow regions.

These interfaces were experimentally studied by Westerweel et al. [WFPH09]. The authors performed combined Particle Image Velocimetry/Laser Induced Fluorescence (PIV/LIF) measurements and validated the existence of thin interfacial shear layers on the boundaries of jets. These turbulent/non-turbulent (TNT) interfaces between rotational and irrotational parts of the flow presented small peaks of conditionally averaged vorticity on the rotational part of the interface. The length of this thin region was of the order of Taylor microscale and was found to produce local mixing phenomena at a small scale and interact with the turbulent large scales. The TNT interfaces have been identified also in [WZN18] through Direct Numerical Simulations (DNS). In this work, the characteristics and conditional statistics of interfaces developed at the edges of boundary layers and planar jets were examined.

However, thin interfacial shear layers have been found inside turbulent flows as well. At high Reynolds number turbulent flows, Ishihara et al. [IGK09], [IKH13] observed sharp velocity jumps across thin internal layers. Through DNS of homogeneous isotropic turbulence, the authors identified coherent layer-like structures containing vortices ten times larger than the Kolmogorov micro-scale with spanwise widths of the order of the integral length scale. In these regions the turbulent flow was found to be strongly anisotropic and significant inertial energy transfers (both forward and backward) took place. In addition, these turbulent/turbulent (TT) interfaces produced intense energy dissipation, much larger than the mean dissipation rate, and acted partly as (decorrelation) barriers to the outer fluctuations,

much like the TNT interfaces.

An important review of interfacial processes has been published in [HESW11]. It includes an extensive literature review concerning TT and TNT interfaces and an important discussion around interfacial dynamics and applications in practical problems. The authors note that conventional turbulence modelling approache fail to accurately predict flows where interfacial shear layers appear as they do not represent correctly the internal small scale dynamics and their interactions with larger scale (coherent) structures. They introduced a new concept in which an intermediate scale velocity field could be added in computations close to the interfaces through an inhomogeneous stochastic field. This addition assists the numerical analysis to predict thin turbulent regions for high Reynolds numbers by reproducing shear sheltering effects and mimic the upscale energy transfers (i.e. energy transfers from small to large structures) with the generation of local intermediate eddies. Even though various upscale (backscatter) models have been developed over the previous years, they lack this explicit connection with the interfacial dynamics involved.

3.1.2 Backscatter phenomena

Small scale and interfacial dynamics that act in a non-resolved (for a calculation) scale, even though not strictly random in nature, they are motions with a large number of degrees of freedom. As a result, they cause mean flow effects that can appear stochastic in nature. Traditional turbulence modelling approaches relate the unresolved turbulent stresses to the large scale velocity deformations through an eddy viscosity. It has been proven however that these stresses only weakly correlate with the local strain rates at best. Zones in the flow where misalignments between the stresses and the strain rates appear [BBHEA08], indicating that the small scale fluctuation effect cannot be purely dissipative.

As a matter of fact, the energy exchange between large and small scale structures in the flow is bidirectional. Contrary to the direct cascade assumption where energy only cascades from larger eddies to smaller ones, energy is also transferred in the opposite direction. This reverse flow of energy, namely backscatter [LQ79], has been clearly demonstrated by J. R. Chasnov [Cha91] in the study of freely decaying turbulence. Through DNS, he linked the rate of the evolution of the turbulent kinetic energy in time in smallest resolved wave-numbers with a backward energy transfer. The Partcile Image Velocimetry wind tunnel measurements of Perrin et al. [PCC$^+$07] for a strongly detached unsteady flow past a circular cylinder showed flow regions with negative tuebulence production which illustrated how inverse turbulence cascade is linked to relaminarisation processes.

There is a plethora of studies dedicated on the introduction of backscattering in numerical models to enhance the predictive capabilities of Large Eddy Simulations (LES) and hybrid (see Section 2.1.7) turbulence approaches. The dynamic extension of the Smagorinksy Sub-Grid Scale (SGS) model by Germano et al. [GPMC91] is considered able to account for part of the backscatter phenomena in regions where the eddy viscosity is reduced, provided that the grid is designed accordingly. Even

then however, strong backscatter events could lead into regions of negative eddy viscosity, endangering the numerical stability of the solution. In general, deterministic approaches do not mimic directly the random nature of the backscattering and lack the stochastic character of these events [SL95].

Stochastic modelling seems to be a more physical approach based on the nature of backscatter processes. J. P. Bertoglio [Ber85] was the first to introduce stochastic force terms via a spectral model in the analysis of isotropic turbulence to simulate backscatter effects. A simpler methodology was later proposed by C. E. Leith [Lei90], applicable in flows of higher complexity. It comprised the introduction of random accelerations in the momentum equations - in addition to the Smagorinsky SGS model - in the form of spatially and temporally uncorrelated divergent-free turbulent stresses. His method was then extended in [MT92]. Both of these studies demonstrated that the stochastic excitation not only assisted the transition into turbulence but also predicted solutions in better agreement with the experimental observations, especially in regions close to the wall boundaries. A similar approach was followed also in [SL95] where stochastic fluctuations with appropriate time-scale correlations were added directly in an eddy-viscosity model and significantly improved predictions when tested in computations of isotropic turbulence.

A stochastic SGS model with reduced computational cost from the ones mentioned above has been proposed in [MBJ07]. The authors applied stochastic variations of the eddy viscosity and compared the approach against DNS results. This approach however led to the appearance of regions with negative viscosity due to the forcing, that could lead to instabilities at large time scales. Based on a scale-similarity model, L. Davidson created a SGS model in which he included only the terms corresponding to the backscatter procedures in the momentum equation [Dav09]. In this mixed-model, Davidson's formulation resulted in a counter-gradient diffusion term that was acting opposing the dissipative counterparts of the equations. The methodology was tested in the context of hybrid turbulence approaches and was found capable of forcing the generation of instabilities when passing from an LES to a URANS mode. A similar direction was followed in [Kok17] where the stochastic backscattering of energy was employed to generate 3D instabilities and enable the grey-area mitigation in the context of Detached Eddy Simulation (DES).

The stochastic forcing approach examined in the present work was tested for the first time in [SGJG$^+$15] for 2D high-Reynolds transonic flows, in combination with the Organized Eddy Simulation (OES) approach. The method developed (IOES) consists of a re-injection of chaotic turbulence in sheared flow regions through the addition of forcing terms in the transport equations of turbulent kinetic energy and dissipation rate. The forcing yields variations of the eddy viscosity which result in fluctuations of the turbulent stresses in the momentum equations and inhibit excessive turbulence diffusion effects. The re-injection of turbulence reproduces the generation of intermediate eddies caused from upscale energy transfers. The forcing is calculated (see Section 2.1.7) based on the turbulent kinetic energy of the smaller resolved motions that are expected to be self-similar to the largest unresolved ones

[Dav09]. The flow is predicted first by an initial, unforced simulation. The small scale motions are identified and reconstructed from high-order low-energy modes educted via a Proper Orthogonal Decomposition (POD - see Appendix A) of the velocity flow field of the unforced simulation. Based on these small scale turbulent motions, the forcing terms are built. A random number generator provides a decorrelation of the forcing in time, imitating the stochastic nature of the backscattering due to the small scale motions.

With the proposed approach, the spatial non-uniformity of the forcing field is physically appropriate as it is contained well inside sheared regions identified from the POD, modelling small scale interfacial dynamics and without affecting irrotational areas of the flow. Using a reconstructed turbulent kinetic energy ensures that spots of negative turbulent eddy viscosity do not appear to endanger the numerical stability of the methodology. No filtering of the fluctuations is required as these remain independent of the computational grid and the dissipation rate towards the wall remains valid. The POD procedure requires the solution of an initial - unforced - flow field which can increase the cost of the method. It is possible however to apply a lower fidelity approach (e.g. URANS) for the initial estimation of the solution and the POD approach remains valid even for small variations of the initial and boundary conditions. During the forcing simulations, no additional fields are computed, and as a result the computational cost does not increase. The method is extended in the present work for three-dimensional flows and examined along the OES and a hybrid turbulence approach. Nevertheless, this method can be applied in any turbulence modelling approach (e.g. URANS, LES, hybrid RANS-LES). In the present work, the novel turbulence modelling approach developed will be examined in the context of high-Reynolds transonic flows for high angles of attack. The prediction of the buffet instability is studied here; the buffet causes large regions of separation and zones of significant shearing, governed by small scale dynamics. The study will be focused on the laminar supercritical V2C wing, designed and tested in the TFAST project.

3.1.3 The TFAST project

The TFAST[1] project (Transition Location Effect on Shock Wave Boundary Layer Interaction) was a four-year (2012-2016) European project on propulsion and flight physics, focusing especially on the shock wave/boundary layer interaction (SWBLI) and its control for laminar wings. The demands for emission reduction and more efficient air transport systems puts a continuous challenge for aircraft manufacturers. These demands require increased loads on wings and engine components while greener designs call for a reduction of drag and losses. Under this context, the main objective of the TFAST project was to study the effect of transition location on the shock wave appearing due to transonic flow conditions, which is inherently connected to increased loads. Wing drag reduction is directly related to fuel con-

[1] http://tfast.eu/

sumption and can be obtained by keeping the boundary layers of lifting parts of the airplane laminar. The laminar boundary layer in return interacts with the shock wave and can lead to significant flow separation, which is detrimental to aircraft performance and can cause safety issues. It is important, therefore, to maintain the turbulent character of the SWBLI in order to diminish the shock induced separation.

The TFAST experimental and numerical investigations were focused on this type of interaction in the wing design process. A significant part of the project was also focused on numerical models aiming at the accurate prediction of the flow phenomena. Basic flow configurations and appropriate flow control methods were investigated and characterized in controlling the location, interaction, the induced separation and the flow unsteadiness. A supercritical laminar wing profile - the V2C wing - was designed by Dassault Aviation and was set as the principal case study. Experimental measurements of the flow field and the transition mechanics were carried out by the department of engineering of Cambridge University and the Institute of Aviation of Warsaw. The profile allows the boundary layer to remain laminar up to the shock foot even for increased angles of attack. The TFAST project contributed in providing reliable methods applicable to unsteady compressible flows and in extending the expertise around the buffet instability, and the transition location effect and the control of the SWBLI.

3.1.4 Buffet instability

Under specific flight conditions in the transonic regime and due to aerodynamic excitation caused by random loading variations on the wing, the interactions between the shock front and the separated shear layer can lead to large amplitude, low frequency, self-sustained oscillations of the shock [MLD76]. This instability, known as transonic buffet, is the origin of large pressure fluctuations that can render the aircraft uncontrollable and be detrimental to its structural integrity as it occurs in frequencies close to the structural ones. As a result, the flight envelope of airplanes is limited in order to avoid conditions that could provoke shock buffeting and an important amount of research has been focused on studying the underlying mechanics of this complex phenomenon.

It has been observed that the appearance of the shock causes a separation over supercritical wing profiles that increases the width of the effective obstacle that the flow encounters, and consequently the width of the wake. This - initially - steady flow field gradually develops unsteadiness as it was demonstrated experimentally in [JMD$^+$09]. The authors described through measurements the periodic oscillation of the velocity field; the coupled interaction and phase-locked motion of the shock and the boundary layer were visualized during the whole buffeting motion. A detailed physical analysis of the buffet onset and the related interactions between shock and vortices was carried out numerically in [BB03a], [BB03b]. The authors identified four successive stages in the transition of the unsteady viscous transonic flow around a symmetric airfoil by solving the 2D time-dependent Navier–Stokes equations for a compressible fluid. A buffet instability emerged in a specific Mach

number range ($M = 0.7 - 0.8$) due to unsteady wake dynamics acting as a global oscillator for the flow. The authors analyzed the interaction between the buffet mode and the wake dynamics, governed by the von Kármán mode and the near-wake unsteadiness. Furthermore, the three-dimensional transition to turbulence in this transonic range was studied by DNS and stability analysis in [BBBT03]. The onset of the buffet instability was also studied in depth by Crouch et al. in [CGM07]. Using stability theory to enhance the physical understanding of the underlying mechanisms involved, they focused on the transition of a marginally stable flow towards an unsteady solution. Their findings around the buffet boundaries were in good agreement with previous experimental studies. The same authors provided further evidence connecting the buffet phenomenon to a global instability emerging in the flow in [CGMT09]. The buffeting was found to be consistent with a supercritical Hopf bifurcation and the whole global-instability approach was deemed capable of providing an accurate prediction of the buffet onset.

Grossi et al. [GBH14] carried out numerical simulation of the transonic buffet over a supercritical profile utilizing both URANS and hybrid turbulence approaches. The authors provided a detailed description of the flow statistical properties and the buffet limit cycle, based on the interactions of the shock with the unsteady wake. These interactions and the importance of feedback effects, arising from shear layers and vortex dynamics in the wake and in the near-trailing edge region of a suprecritical profile, have been analyzed by Szubert et al. [SGJG$^+$15]. The same aerodynamic profile and the unsteady interactions were also studied in great detail in [SMS15]. The authors remarked that the buffet frequency depended only on the Mach number characterizing the flow, signifying that the size of the separation region was not of key importance to the phenomenon. This was also suggested in [KYTK20] where the authors performed a resolvent analysis of the flow to identify the origin of two-dimensional transonic buffet. They suggested that the buffet amplification mechanism is present in the global dynamics and the origin of the forcing causing the instability comes from the shock foot. Perturbations from inside the boundary layer and close to the trailing edge were amplified to produce low amplitude oscillations. This study suggested that trailing edge buffet control mechanisms could be proven effective to this end. This is supported by the findings in [TSM$^+$19]. This numerical investigation, carried out in the context of the SMS European project, examined the actuation in the near-trailing edge region in order to exploit the importance of feedback mechanics. It was shown that vibrations and low-amplitude deformation of the trailing edge region were able to considerably modify the SWBLI. Based on this study, a "Transonic Reduced Scale Prototype" was constructed and investigated through a detailed experimental campaign carried out by IMP-PAN[2], partner of the SMS project.

Detailed RANS and DDES calculation were also on carried by F. Sartor and S. Timme [ST15], [ST17]. They studied the emerging instability on a half wing aircraft configuration were additional parameters guide the flow mechanics. In

[2]Institute of Fluid-Flow Machinery, Polish Academy of Sciences, Gdańsk,

the present work however, we will only focus on the governing dynamics of the buffet instability of 2D-like bodies, i.e. for wings for which the chord does not vary along the span. For constant chord wings, the studies of [Dec05] and [GD10] proved that scale-resolving simulations significantly affect the flow prediction and the shock properties, as it was also supported by Grossi et al. [GBH14]. Hybrid and scale-resolve approaches tend to overpredict the pressure fluctuations and the shock travelling distance at high incidence angles. Nevertheless, these approaches still offer a deep insight on the turbulence properties of such flows and it is important to find ways to aplly them properly. Small scale dynamics play an important role in high Reynolds numbers flows. Interfacial turbulent regions that appear in parts of the flow where shearing is important, become considerably thin and they cannot be - still - realistically resolved in the context of industrial applications. Their effect and modifications on the large scale dynamics should be adequately modelled in order to be taken into account. The re-injection of turbulence by stochastic forcing presented here and in Chapter 2 will be evaluated to this end.

3.2 Numerical approach for transonic simulations

The compressible time-dependent Navier-Stokes equations, within the OES and DES framework, have been solved under for the transonic flow in a 3D finite-volume structured grid formulation, using the NSMB (Navier-Stokes Multi-Block) code [HPV$^+$16]. The computational domain is subdivided into hexahedral grid cells of constant size in time and the multi-block strategy is followed in accordance to the parallelization procedure of the code. A third-order upwind Roe scheme with a MUSCL interpolation and slope limiters was used for the spatial discretization of the convection terms; a second-order central scheme was employed for the diffusion terms. For the temporal discretization, a dual time-stepping with a second order implicit backward difference scheme is utilized[3]. The physical time-step was kept constant in all the computations at 10^{-6} giving a CFL ranging between 10 and 30. A total of 100 inner iterations were carried out for each time-step to reach convergence. An additional 50 inner iterations were added to achieve convergence for the stochastic forcing calculations, without affecting the rest of the numerical parameters. The increased number of iterations was mainly due to the stiffness of the turbulent equations, especially when the stochastic terms were included. Only a few sweeps were carried out per iteration.

The C-type mesh around the V2C laminar wing profile illustrated in Fig. 3.1, used in [SAG$^+$16] in the context of the TFAST European project, is adopted in this study. The mesh was constructed by adding in the streamwise direction 426 points on the wing surface (including both the upper and the lower surface) and 192 points in the wake. Along the spanwise direction 59 points were added resulting in a total mesh size close to 9.65 million finite volume cells. The average y^+ value, corresponding to the height of the first cell (order of 10^{-7}) above the wall

[3] See Chapter 2 for an explicit presentation of the schemes used.

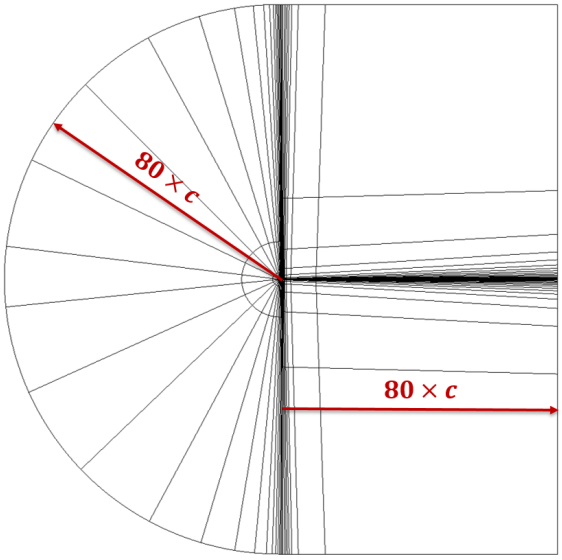

(a) *Multi-block description of the computational domain.*

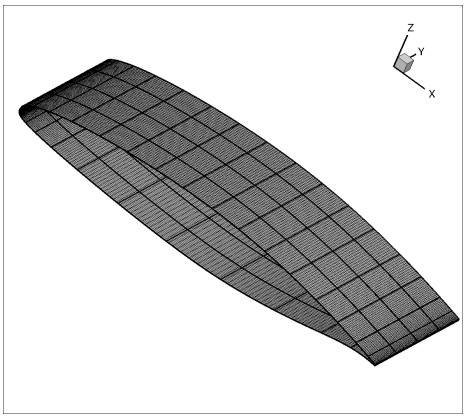

(b) *3D surface meshing of the wing.*

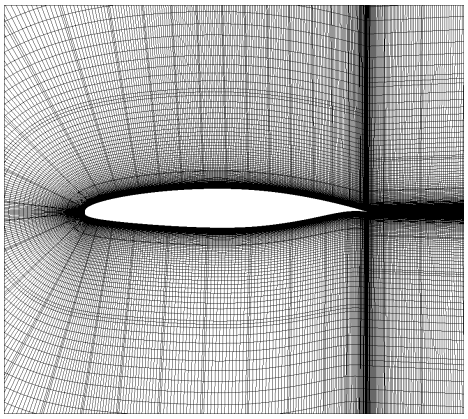

(c) *2D slice of the mesh.*

Figure 3.1: *Meshing of the computational domain around the V2C wing.*

surface, was around 0.3 over the whole wing. Freestream boundary conditions have been chosen for both the inlet and the outlet of the computational domain as the boundaries had been placed sufficiently far ($80 \times c$). A no-slip condition (zero velocity at the wall) has been given to the wing's surface and a symmetry condition on the planes perpendicular to the span direction. The block connectivity was updated between every sweep of the solution procedure.

The present study will be focused only on a single flow configuration of the V2C wing for which various turbulent modelling approaches will be examined. The $K-\varepsilon-$OES approach has been employed for the turbulent flow (see Section 2.1.7) as it allows coherent structures and their related instabilities to develop in the high

Reynolds numbers and is well adapted for highly detached flows [Hoa02]. In addition, the DES approach, in combination with OES (DOES), is also employed. Both of these modelling approaches are also examined with the addition of the stochastic forcing (OES+F and DOES+F). The stochastic source terms are treated explicitly in the computations. Ambient terms [SR07] have been added in all four case with a freestream turbulence intensity $T_u < 0.1\%$. A Delayed Detached Eddy Simulation (DDES) approach has been also carried out, employing the OES approach for the RANS part.

3.3 Highly detached transonic flow

In the present section, the V2C laminar wing is studied at a Mach number $M = 0.7$ and a 7° angle of attack. The specific configuration for a $Re/c \approx 13 \cdot 10^6$ per meter - where $c = 0.25m$ the chord of the profile - was inside the region where the buffet phenomenon is fully established. A constant wing section was tested with spanwise length$b = c/3$. The total temperature at the inlet was set at $290K$ and total pressure at $10^5 Pa$ in order to achieve the specific flow conditions. The viscosity was calculated from Sutherland's law. For the simulations, the streamwise direction is that of the x axis and the vertical direction (with respect to the wing's chord) is that of the z axis, leaving y axis along the span of the wing. The $X/c = Z/c = 0$ correspond to the position of the leading edge of the wing's profile.

Due to the transonic flow conditions, the acceleration over the wing leads to the apparition of a shock. At such a high angle of attack and in this specific M and Re number range [SML78], this marginally stable global flow mode gradually becomes unstable [CGMT09]. The interaction of the shock with the detached boundary layer and the unstable wake region results in a buffet instability. The buffet cycle describes the self-sustained phase-locked motion of the shock and the separated boundary layer, characterized by a low frequency (buffet frequency $f_b = 1/T_b$). The shock travels over the wing around and moves around a fixed position periodically. The shock movement during a buffet period is illustrated from the surface pressure distribution on the wing in Fig. 3.2, calculated with OES. The shock starts from its most downstream position (Fig. 3.2b)towards its most upstream position (Fig. 3.2f) and then moves backwards again (Fig. 3.2h). The shock almost reaches the leading edge of the profile which is surprising even at this high incidence angle. A visualization of the 3D flow structures are shown in the same figure (Fig. 3.2 - left). The spanwise vorticity ω_y iso-surface depicts the turbulent vortical structures generated due to the separated boundary layer, starting from the foot of the shock; this is clearly illustrated by the M coloring of the surface. This iso-vorticity layer presents spanwise undulations that give birth to smaller scale chaotic-like structures further downstream.

The 2D slice at the mid-span section $y = b/2$ in Fig. 3.3 is used to demonstrate the shock movement via the visualization of the M field, calculated from OES. The movement of the shock front is associated with the progressive thickenning of the

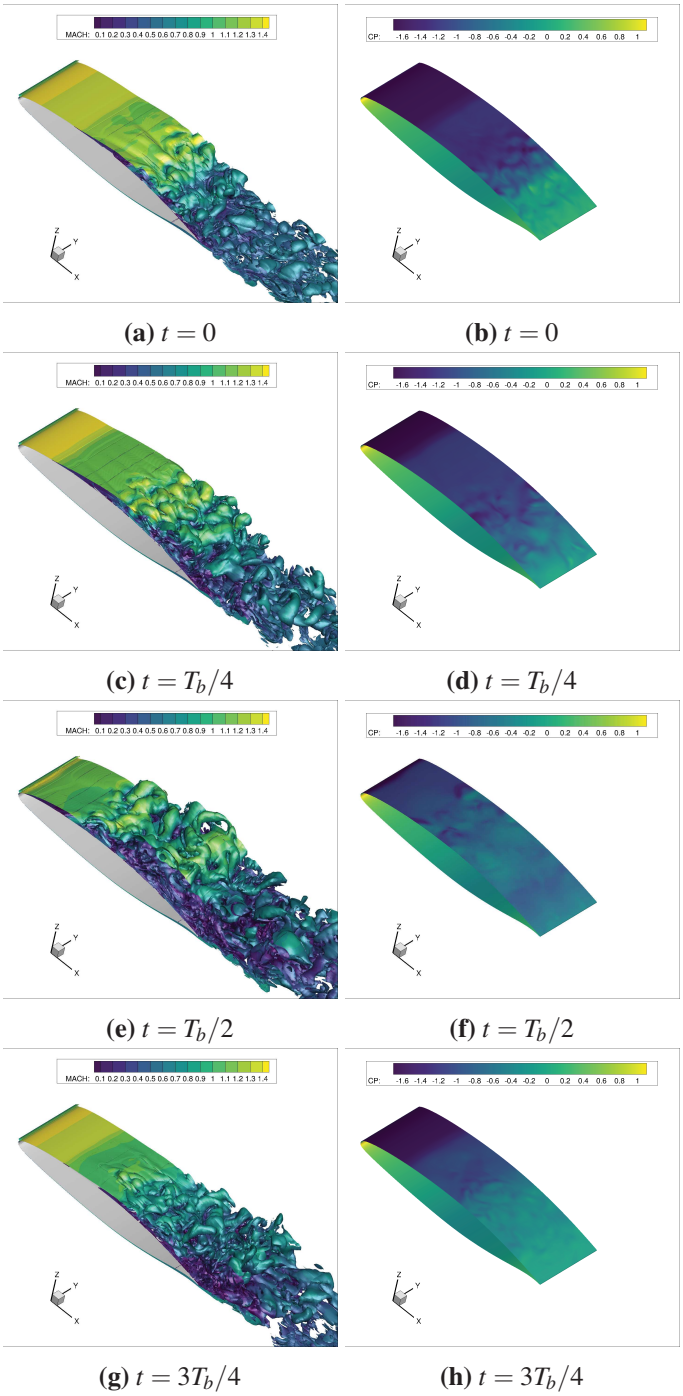

(a) $t = 0$ **(b)** $t = 0$

(c) $t = T_b/4$ **(d)** $t = T_b/4$

(e) $t = T_b/2$ **(f)** $t = T_b/2$

(g) $t = 3T_b/4$ **(h)** $t = 3T_b/4$

Figure 3.2: *Variation of the flow field over one buffet period T_b with OES. Left, the $y-$wise vorticity iso-surfaces for $\omega_y c/U_\infty = \pm 5.5$, colored by M; on the right, the surface pressure coefficient distribution.*

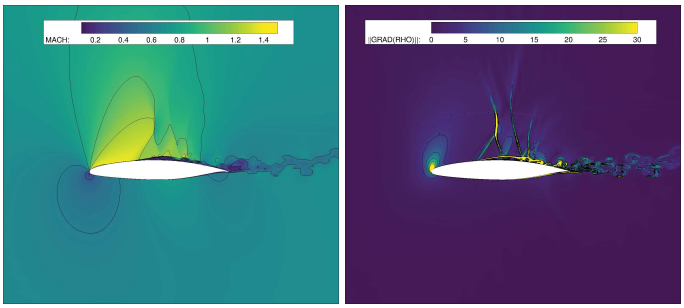

(a) $t = 0$ **(b)** $t = 0$

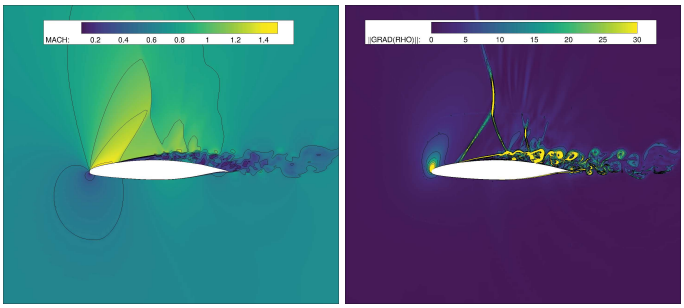

(c) $t = T_b/4$ **(d)** $t = T_b/4$

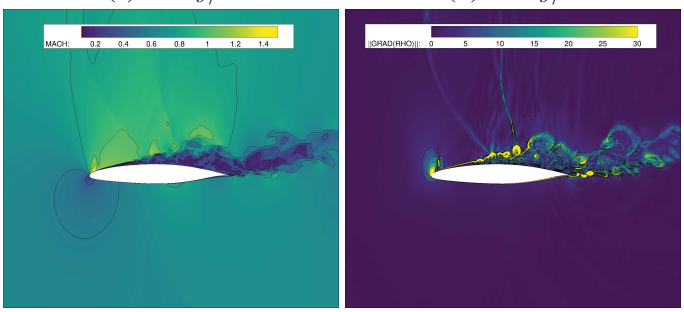

(e) $t = T_b/2$ **(f)** $t = T_b/2$

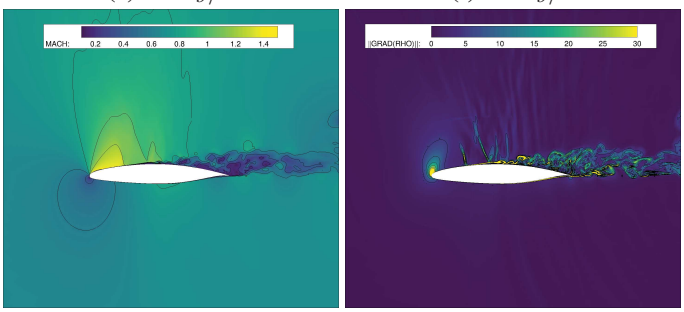

(g) $t = 3T_b/4$ **(h)** $t = 3T_b/4$

Figure 3.3: *Variation of the M number (left) and the gradient density magnitude (right) over one buffet period T_b on the mid-span xz section with OES.*

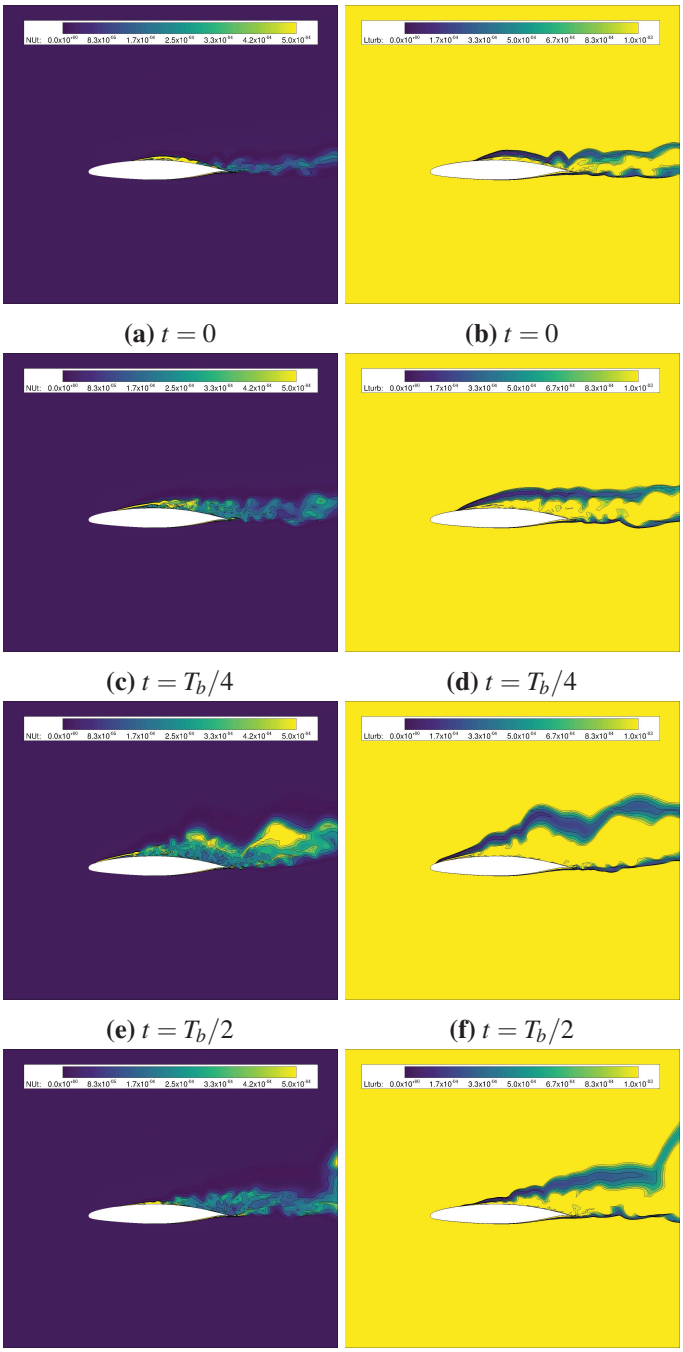

(a) $t = 0$ **(b)** $t = 0$

(c) $t = T_b/4$ **(d)** $t = T_b/4$

(e) $t = T_b/2$ **(f)** $t = T_b/2$

(g) $t = 3T_b/4$ **(h)** $t = 3T_b/4$

Figure 3.4: *Variation of the turbulence eddy viscosity ν_t (left) and the turbulent length scale $l_t = k^{3/2}/\varepsilon$ (right) over one buffet period T_b on the mid-span xz section with OES.*

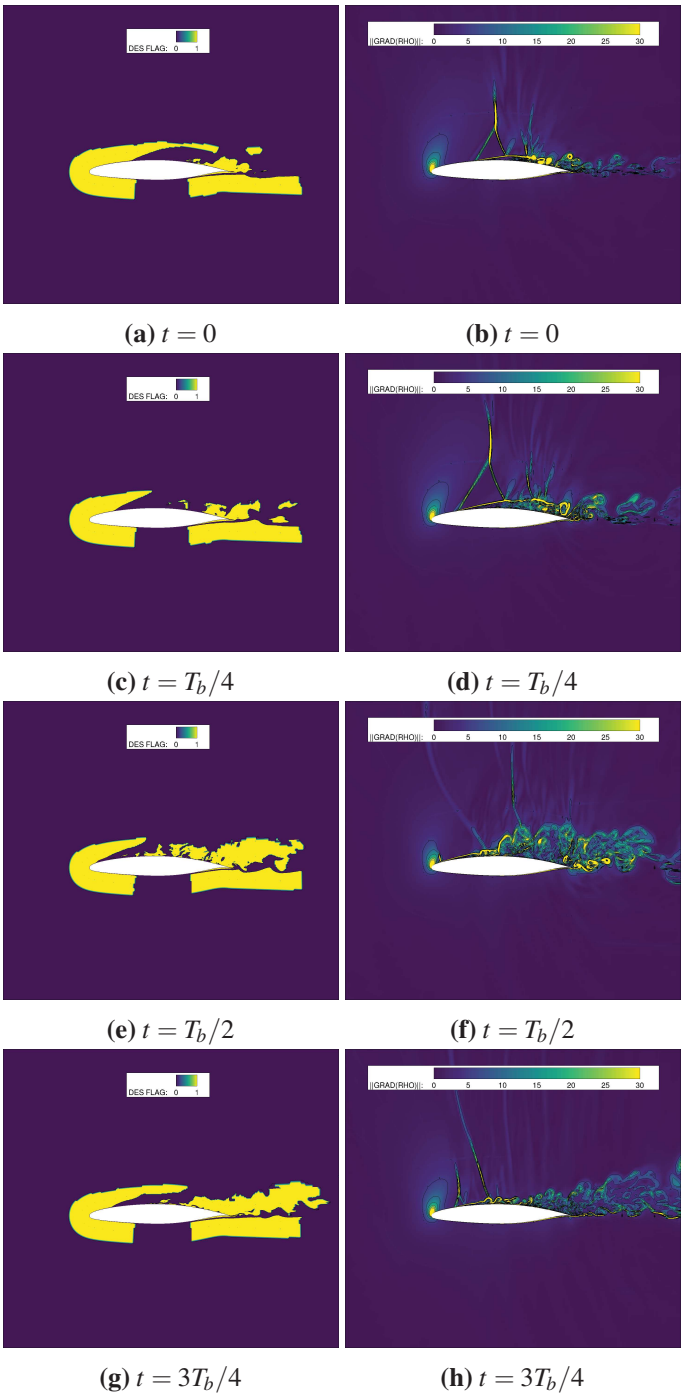

(a) $t = 0$ **(b)** $t = 0$

(c) $t = T_b/4$ **(d)** $t = T_b/4$

(e) $t = T_b/2$ **(f)** $t = T_b/2$

(g) $t = 3T_b/4$ **(h)** $t = 3T_b/4$

Figure 3.5: *Variation of the DES flag (left) and the gradient density magnitude (right) over one buffet period T_b on the mid-span xz section with DOES; DES mode for $flag = 1$ and OES mode for $flag = 0$.*

separated shear layer and follows the periodic movement described before. The detached zone increases in size as the shock (and the separation position) moves upstream and reduces as the shock moves backwards. Consequently, the thickness of the wake region is phase locked with the whole process. During the buffet period the separated boundary layer never reattaches to the wing's surface. The SWBLI can be efficiently visualized through the magnitude of the density gradient, illustrated also in Fig. 3.3 (right) for a buffet period. This type of visualization (equivalent to Schlieren's visualization) reveals the $\lambda-$shock (bifurcated) structure. The Mach compression waves collapse on the front leg of the shock (oblique shock) causing the initial separation of the boundary layer. Over the detached zone and due to the acceleration of the flow, the rear shock leg appears. The two legs meet with the normal shock at a higher position (triple-point). Due to the continuous expansion and acceleration of the flow, the detached zone increases in size and a secondary weaker $\lambda-$shock appears further downstream, relatively close to the first one. The shock structure prevails up until the shock reaches the leading edge where it collapses, then progressively redevelops as the separation point moves downstream and becomes fully established before a new cycle begins. The density variations also highlight the Kelvin-Helmholtz vortices of the detached shear layer, both on the suction and the pressure side of the wing.

The turbulent properties of the flow are included in Fig. 3.4 on the mid-span section, calculated with OES. The turbulence eddy viscosity $\nu_t = C_\mu K^2/\varepsilon$ (left) and the modelled turbulent length scale $l_t = K^{3/2}/\varepsilon$ (right) contours are plotted over one buffet period. The turbulence eddy viscosity field is contained well inside the separation region and the wake, following the dynamics of these two regions. The flow presents an apparent laminar character in the upstream region up to the shock foot. The turbulent motion is generated due to the SWBLI further downstream, where turbulent interactions are prevalent. The whole turbulent region is contained inside two thin layers of reduced turbulent length scale l_t, indicating strong dissipation layers that highlight rotational/irrotational (turbulent/non-turbulent) interactions. Detached organized eddy simulations (DOES) have been also carried out the current case study. The DES flag illustrated in Fig. 3.5 (left) underlines the regions where the calculation enters a DES mode ($flag = 1 \rightarrow C_{DES}\Delta < l_t$) and an OES mode ($flag = 1 \rightarrow C_{DES}\Delta > l_t$) respectively. The calculation presents multiple regions where it retains the OES mode due to the grid spacing and the reduced turbulent viscosity produced by the OES approach. The OES mode is activated in the outer region and close to the wall boundaries (viscous region), but also in the region just after the shock where the flow is detached. In the latter, the turbulent length scale is reduced implying that the mesh could be refined for a more efficient DES mode calculation. The DES mode is well activated both upstream of the shock (Euler region) and well inside the separation zone (LES region). The shock structure (Fig. 3.5 on the right) is similar to the one predicted by the OES and the turbulent interactions in the separation zone are slightly enhanced.

The difference between the two approaches is examined through Fig. 3.6 where the temporal variation of the aerodynamic force (lift and drag) coefficients is

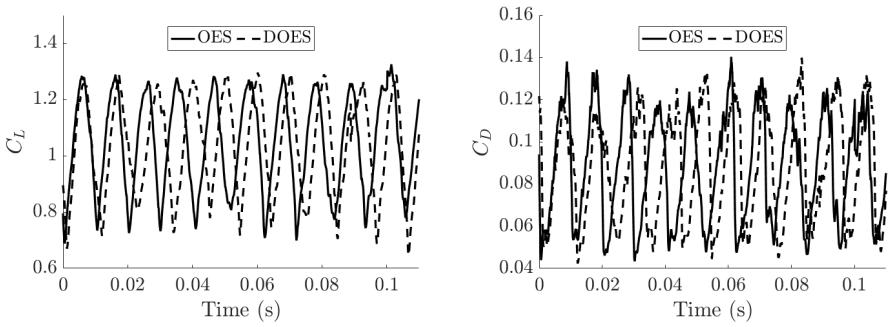

(a) *Lift coefficient.* **(b)** *Drag coefficient.*

Figure 3.6: *Temporal variation of aerodynamic force coefficients; comparison between the OES and the DOES solution.*

plotted. Both approaches predict a "saw tooth" shaped oscillatory behavior with sharp peaks. The time averaged values are quite close and slightly higher for the OES approach, while the *rms* (root-mean-squared) values match completely. This behavior has also been reported from DDES calculations carried out in the TFAST project [SAG+16]. The evaluation of the buffet frequency f_b from the aerodynamic coefficients is quite close for the two approaches as well. The pure OES predicts an $f_b \approx 92Hz \rightarrow St = 0.1$ based on the chord ($c = 0.125m$), while the DOES approach gives an $f_b \approx 95Hz$.

The averaged longitudinal velocity profiles calculated by both turbulent approaches are compared in Fig. 3.8. The non-dimensional extracted positions are illustrated in Fig. 3.7. Figures 3.8a-3.8c include the boundary layers on the second half of the wing. The two approaches predict almost similar profiles, especially in Fig. 3.8a where the DOES calculation runs in an OES mode. In this region, the boundary layer are detached and a shear layer develops above the suction side of the wing. In Figs. 3.8d-3.8e the wake velocity profiles are presented. The two approaches predict profiles that are close but present some slight differences in terms of their maximum deficit and slope.

3.3.1 POD-based turbulent kinetic energy

The POD [BHL93] is applied on the results of a URANS computation, available from the studies in the TFAST project [SAS+18]. The URANS ($K-\omega$ *SST*) simulation had provided relatively accurate results in terms of force prediction and shock dynamics. The Snapshot POD (see Appendix A) is applied here on the velocity field and therefore, the total energy represented by the eigenvalues corresponds to the turbulent kinetic energy of the flow, integrated over the computational domain. The sampling rate was constant ($10^{-3}sec$ - an order of magnitude higher than the time step used in the computation) and a series of successive snapshots (597 in total) was used to construct the POD data matrix. The total time duration of the

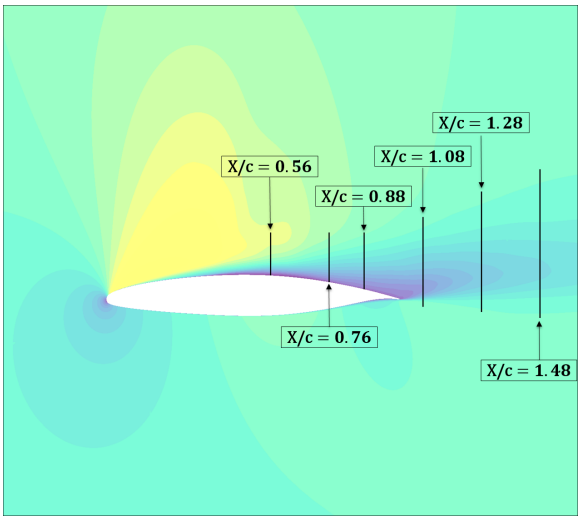

Figure 3.7: *Contour of averaged longitudinal velocity and positions of the extracted velocity profiles.*

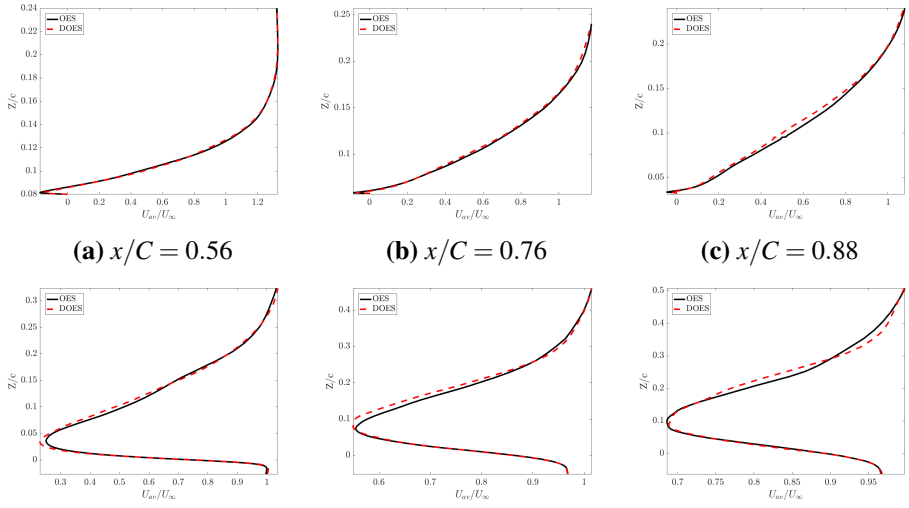

(a) $x/C = 0.56$ **(b)** $x/C = 0.76$ **(c)** $x/C = 0.88$

(d) $x/C = 1.08$ **(e)** $x/C = 1.28$ **(f)** $x/C = 1.48$

Figure 3.8: *Averaged longitudinal velocity profiles; comparison between the OES and the DOES solution.*

sampling covered about six periods of the buffet phenomenon. The flow field is split in spatial modes and temporal coefficients sorted by their relative energy in the flow; the higher the order of the mode, the lower its energy content. The tempo-spatial evolution of the flow velocity $\boldsymbol{u}(\mathbf{x},t) = (u,v,w)$ is approximated as:

$$\boldsymbol{u}(\boldsymbol{x},t) = \boldsymbol{U}_1(\boldsymbol{x}) + \sum_{n=2}^{N_{POD}} \alpha_n(t)\boldsymbol{U}_n(\boldsymbol{x}) \tag{3.1}$$

i.e. as the summation of the decoupled temporal coefficients a_n and spatial modes $\boldsymbol{U}_n = (U_n, V_n, W_n)$ over a finite number of N_{POD} modes. The first POD mode represents the time averaged (mean) velocity field. This is illustrated in Fig. 3.9 where the longitudinal and vertical components of the first POD mode are included. The remaining terms (i.e. the summation) correspond to the fluctuating part of the flow variable.

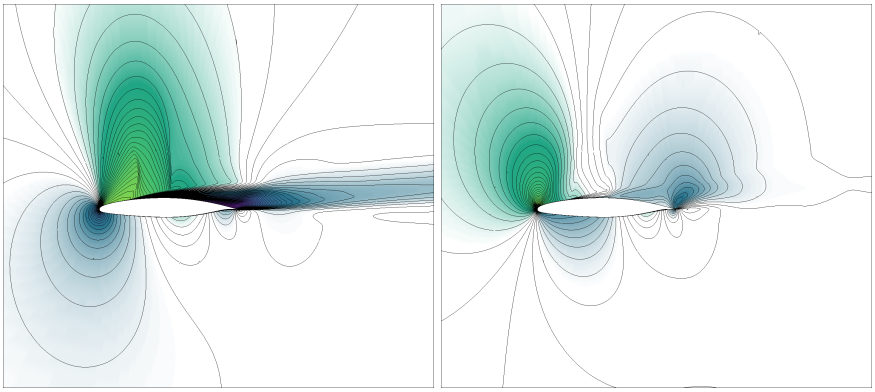

(a) U_1 **(b)** W_1

Figure 3.9: *First POD spatial mode for the longitudinal (left) and vertical (right) velocity components, computed from URANS simulations; the first mode corresponds to the mean (time averaged) flow.*

Selected lower and higher order fluctuating spatial modes are presented in Figs. 3.10 and 3.11 respectively. Different contour levels are used in these figures to account for the decreasing flow energy as the order increases. The second mode (Figs.3.10a-3.10b) corresponds to the buffet instability and highlights the shock movement and the detachment of the boundary layer. The fourth POD mode (Figs.3.10c-3.10d) underlines the unsteady wake region through a von-Kármá alternating vortex pattern. The modes that follow (Figs.3.10e-3.10f and Figs.3.10g-3.10h) present increased intensity close to the shock's foot, providing a link between the unsteadiness of the shock with the instabilities appearing in the wake. *The buffet limit cycle is sustained through this interaction between these two regions*. As the order of the modes increases, the flow structures become increasingly less coherent and smaller. Layer-like [IKH13], irregular vortex patterns appear inside regions of intense shearing. These small scale low-energy vortices are associated with turbulent-turbulent (TT) interactions which take the form of thin interfaces [IOH15]. In turbulent flows, these interfaces have been found to act as decorrelation barriers between the different flow regions, shielding the individual structures on either side. In the energy spectrum this translates to an upscale energy transfer (backscatter), moving energy from lower scales to larger ones, thus altering the direct energy cascade.

The velocity field can be approximated from Eq. 3.1. Based on this equation, we

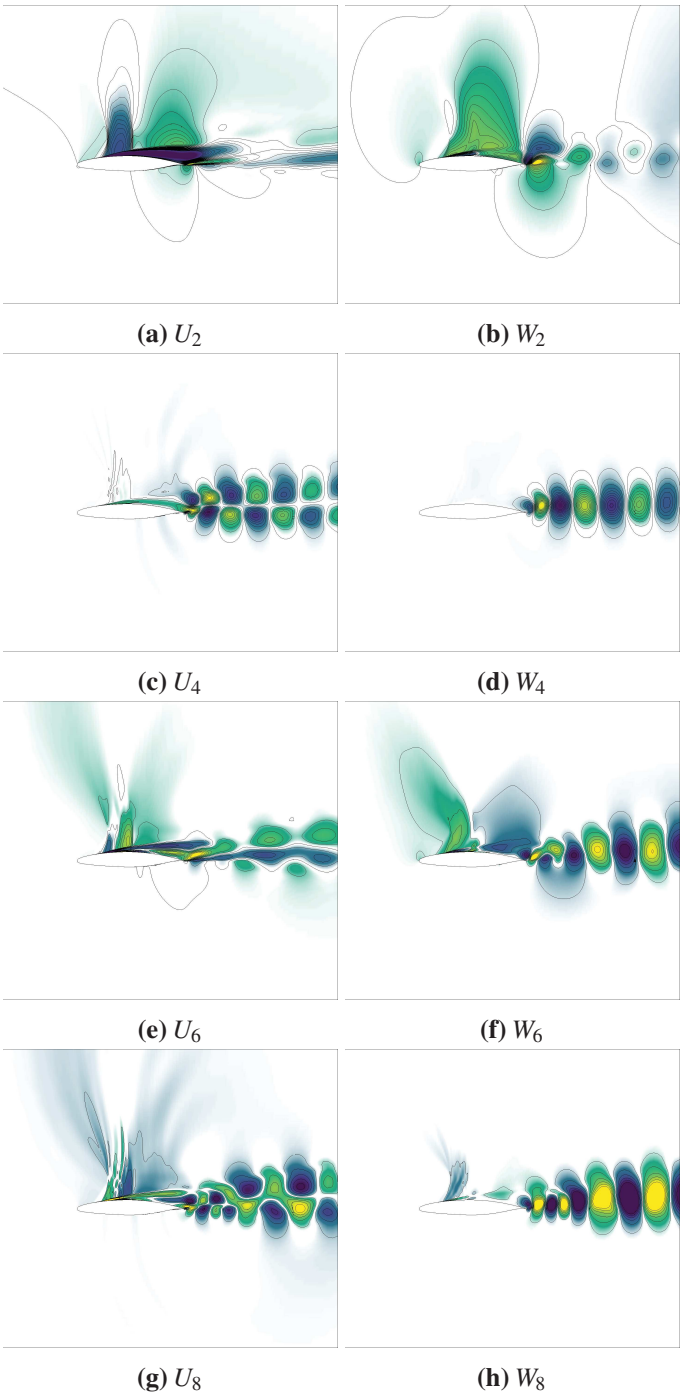

(a) U_2 **(b)** W_2

(c) U_4 **(d)** W_4

(e) U_6 **(f)** W_6

(g) U_8 **(h)** W_8

Figure 3.10: *Lower POD spatial modes for the longitudinal (left) and vertical (right) velocity components, computed from URANS simulations; indices refer to the order of the mode.*

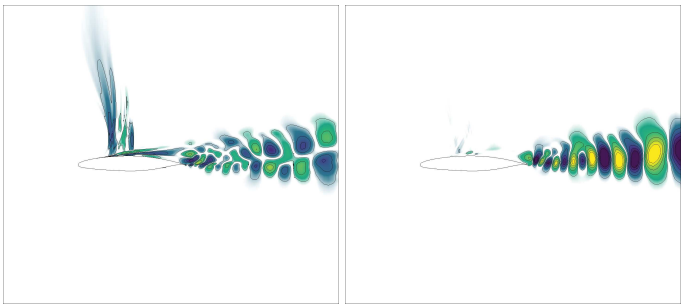

(a) U_{16} **(b)** W_{16}

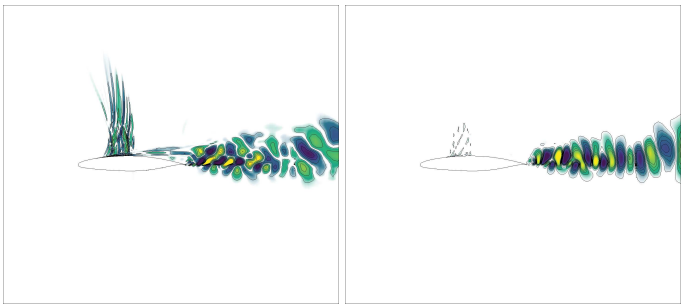

(c) U_{32} **(d)** W_{32}

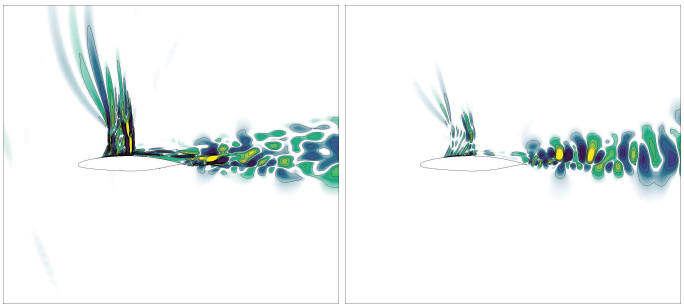

(e) U_{48} **(f)** W_{48}

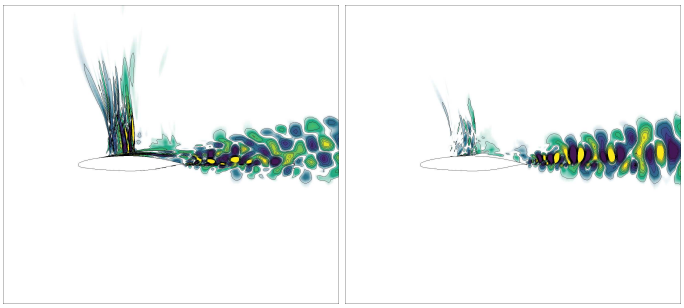

(g) U_{64} **(h)** W_{64}

Figure 3.11: *Higher POD spatial modes for the longitudinal (left) and vertical (right) velocity components, computed from URANS simulations; indices refer to the order of the mode.*

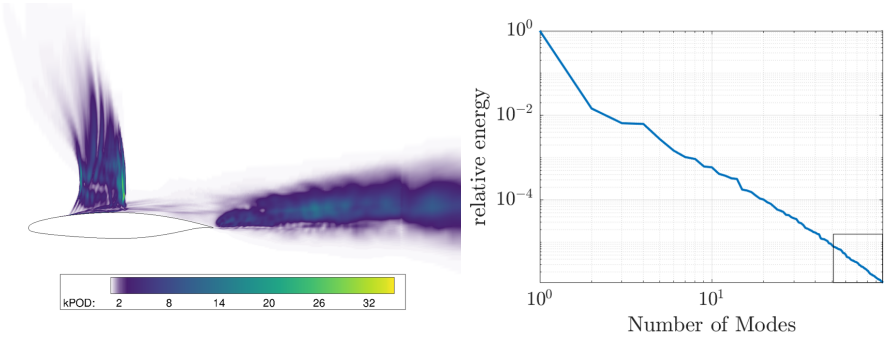

(a) **(b)**

Figure 3.12: *Turbulent kinetic energy (a) reconstructed from (b) high-order low-energy POD modes, enclosed in the rectangle.*

can build the fluctuating velocity field from:

$$\boldsymbol{u'}(\boldsymbol{x},t) = \boldsymbol{u}(\boldsymbol{x},t) - \boldsymbol{U}_1(\boldsymbol{x}) = \sum_{n=2}^{N_{POD}} \alpha_n(t)\boldsymbol{U}_n(\boldsymbol{x})$$

To build the stochastic forcing term, we need to calculate a kinetic energy distribution. The low-energy turbulent kinetic energy can be built after separating the high-order POD modes from:

$$K_{POD} = \frac{1}{2}(\overline{u'^2}_{recon} + \overline{v'^2}_{recon} + \overline{w'^2}_{recon})$$

where the $\overline{*}$ denotes a time-averaging procedure and only higher ($N_{POD} \geq 60$) modes were chosen for the reconstructed fluctuating velocity field:

$$\boldsymbol{u'}_{recon} = \sum_{n=60}^{N_{POD}} \alpha_n(t)\boldsymbol{U}_n(\boldsymbol{x})$$

The limits used for the reconstruction (see Fig. 3.12b) were chosen qualitatively in order for the highlighted zone to remain localized within the shock region and the wake (see Fig. 3.12a) and retain small values with respect to the mean flow. In addition, the temporal coefficients that corresponds to modes higher than 60 present an incoherent, chaotic-like spectral content. These small resolved motions should be self-similar to the largest unresolved [Dav09] ones and provide a good representation of the small scale dynamics.

3.3.2 Effects of the stochastic forcing

The inhomogeneous stochastic forcing term is built from the reconstructed turbulent kinetic energy K_{POD} (see Section 2.1.7). This enables the approach to stay within the shear layers where small scale dynamics take place without affecting the irrotational

regions. The forcing term will act as an energy transfer from the smaller scales to larger ones and limit the turbulent diffusion effect due to the direct energy cascade modelling assumptions. The stochastic character of these interactions will be considered through the random number generator that guides the dynamic evolution of the forcing within the regions of interest.

The introduction of the stochastic forcing increases locally the dissipation rate. In Fig. 3.13, the OES calculations with and without stochastic forcing are compared over one buffet period. The dissipation ε of the turbulent kinetic energy is increased within the regions where the inhomogeneous forcing is applied. The detachment zone is contained in a less wide region signifying a reduced shock movement and production of ε downstream of the shock. The distribution of the turbulent kinetic energy does not present any significant change. The forcing terms in the transport equations of K seems to balance the increase of turbulent dissipation and leaves the production of kinetic energy unaffected. Consequently, the effects of turbulent diffusion are reduced as expected resulting at fluctuating turbulent stresses in the momentum equations. The eddy turnover time $t_s = K/\varepsilon$ is consequently reduced signifying an acceleration of the direct energy cascading procedure.

In Fig. 3.14, the calculated turbulent viscosity ν_t (left) and the variation of the turbulent length scale l_t (right) are presented for the OES+F calculation. The turbulent viscosity is contained inside the detachment zone close to the wing. The regions were the forcing is applied present reduced turbulent viscosity which is coherent with the dynamics in such a high Reynolds number. The altered (reduced) turbulent stresses is equivalent to local accelerations added in the momentum conservation equations. The predicted turbulent length scale is also reduced for the whole area downstream of the shock. Due to the ambient terms added in the forcing terms (see Section 2.1.7) and the shearing caused by the presence of the shock, the layered zones of low turbulent length scale originally predicted without the stochastic forcing (see Fig.3.4) disappear. From the turbulent viscosity prediction, a few isolated zones where turbulent interactions take place are identified. The decrease of the modelled length scale significantly affects the DOES+F approach. The regions were the DES mode is activated become smaller (see DES flag on Fig. 3.15); the simulation operates in OES mode inside the wake and over a significant area of the suction side of the wing. As a result, the two approaches do not present large differences when the stochastic forcing terms are activated.

The dynamic behavior of the flow is altered as well due to the stochastic forcing. The general shock structure remains unchanged as it is illustrated in Fig. 3.16 (right). The shock movement however is significantly affected by the modifications associated with the turbulence variables: (i) The travelling length that the shock covers is reduced along with the intensity of the pressure fluctuations, (ii) the point around which the shock oscillates is moved downstream, (iii) the detachment of the flow becomes less pronounced as the shock never reaches the leading edge, (iv) the width of the wake is consequently reduced, and (v) the whole buffet limit cycle is slightly more stable. The DOES+F approach (see Fig. 3.15) predicts a similar behavior, supporting the results discussed for the OES+F approach.

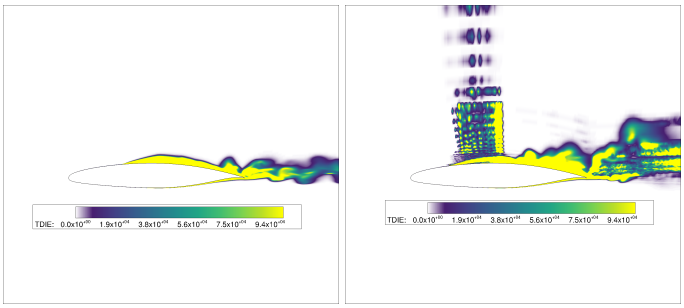

(a) $t = 0$ **(b)** $t = 0$

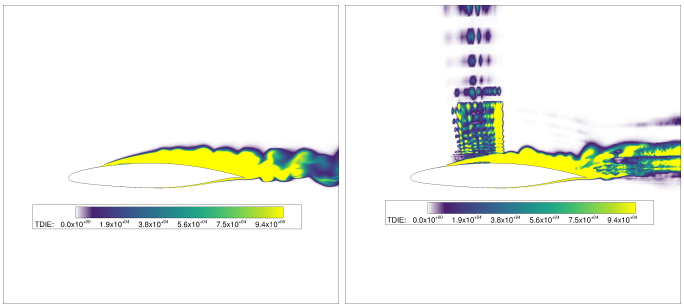

(c) $t = T_b/4$ **(d)** $t = T_b/4$

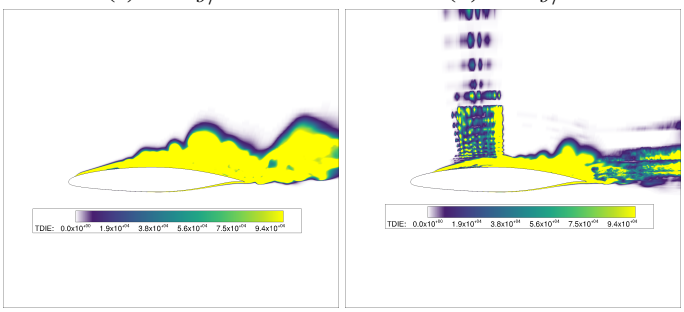

(e) $t = T_b/2$ **(f)** $t = T_b/2$

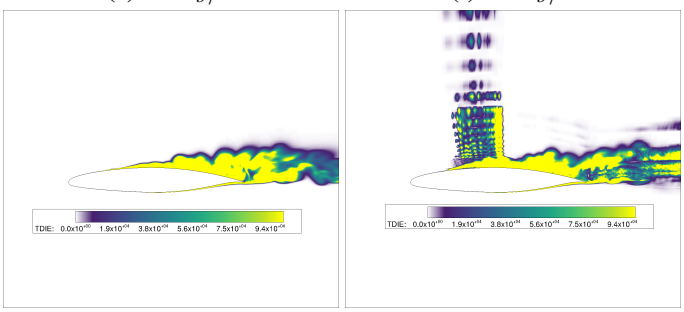

(g) $t = 3T_b/4$ **(h)** $t = 3T_b/4$

Figure 3.13: *Variation of turbulence dissipation ε over one buffet period T_b on the mid-span xz section; comparison of OES (left) and OES+F (right), i.e. without and with stochastic forcing.*

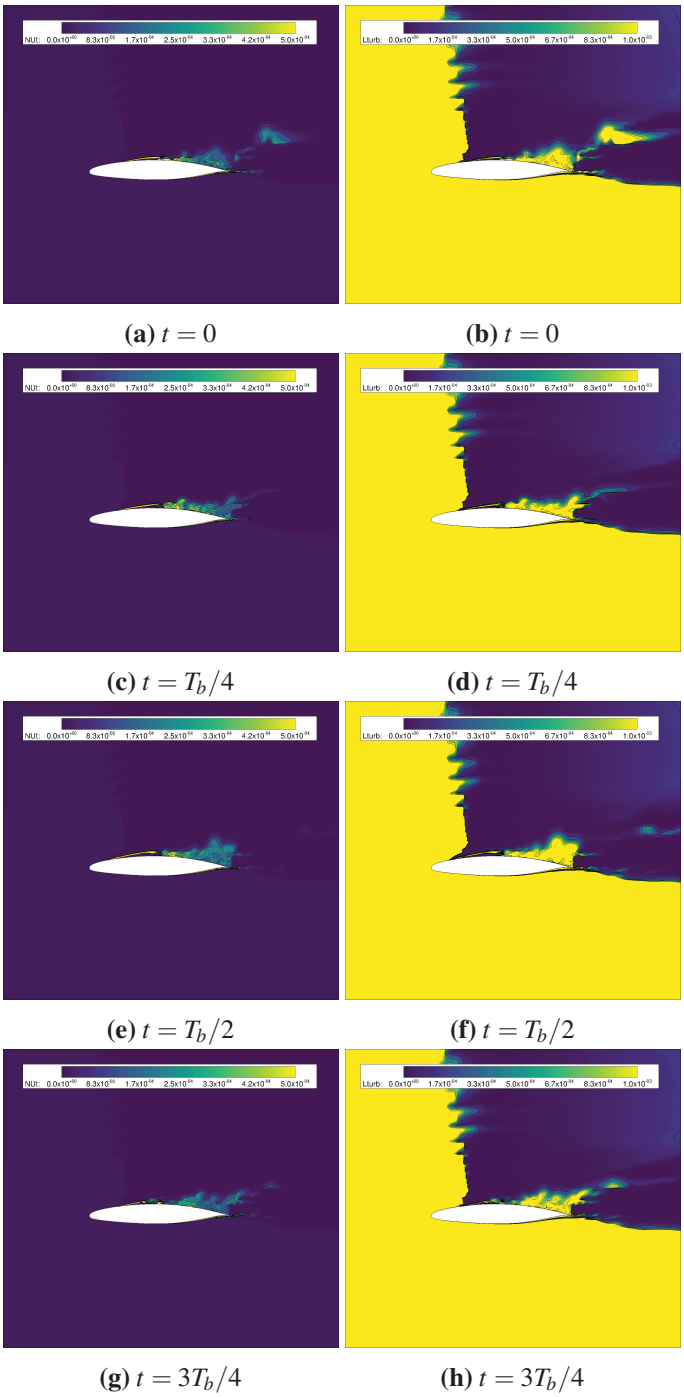

(a) $t = 0$ **(b)** $t = 0$

(c) $t = T_b/4$ **(d)** $t = T_b/4$

(e) $t = T_b/2$ **(f)** $t = T_b/2$

(g) $t = 3T_b/4$ **(h)** $t = 3T_b/4$

Figure 3.14: *Variation of turbulence eddy viscosity* ν_t *(left) and the turbulent length scale* $l_t = k^{3/2}/\varepsilon$ *(right) over one buffet period* T_b *on the mid-span xz section with OES+F.*

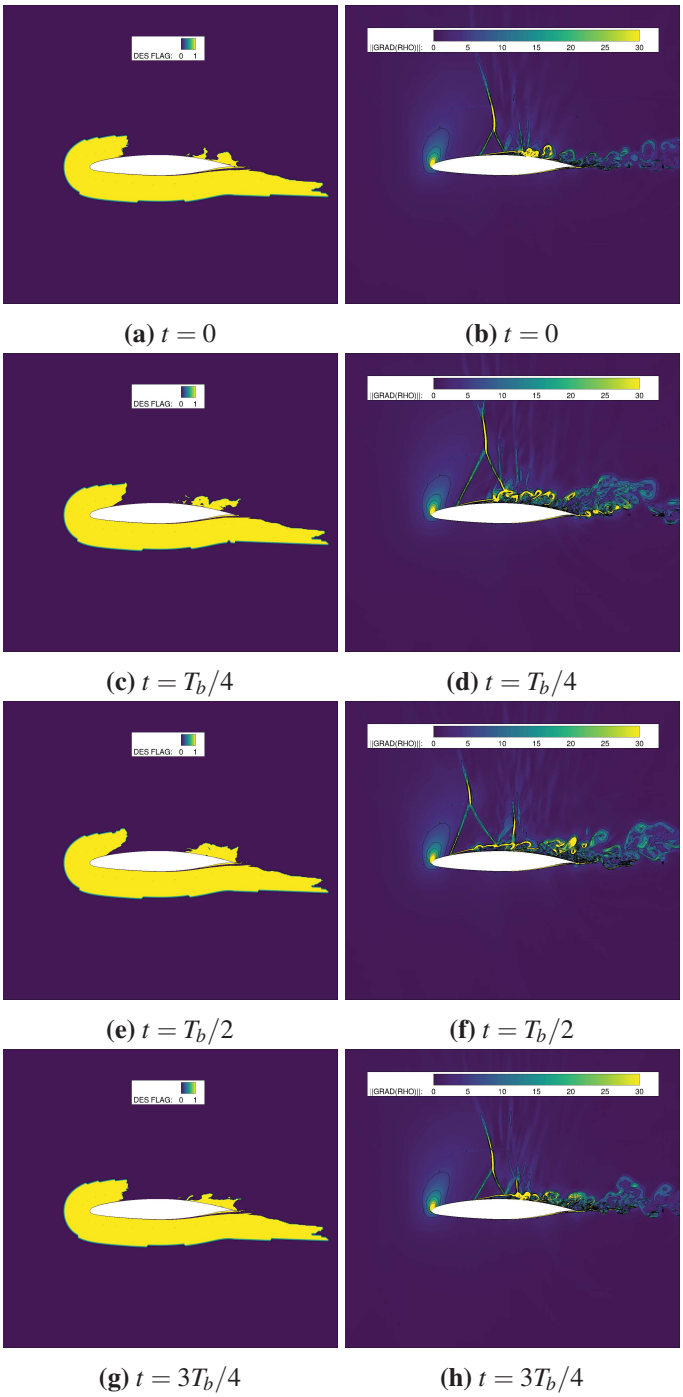

(a) $t = 0$ **(b)** $t = 0$

(c) $t = T_b/4$ **(d)** $t = T_b/4$

(e) $t = T_b/2$ **(f)** $t = T_b/2$

(g) $t = 3T_b/4$ **(h)** $t = 3T_b/4$

Figure 3.15: *Variation of the DES flag (left) and the gradient density magnitude (right) over one buffet period T_b on the mid-span xz section with DOES+F; DES mode for $flag = 1$ and OES mode for $flag = 0$.*

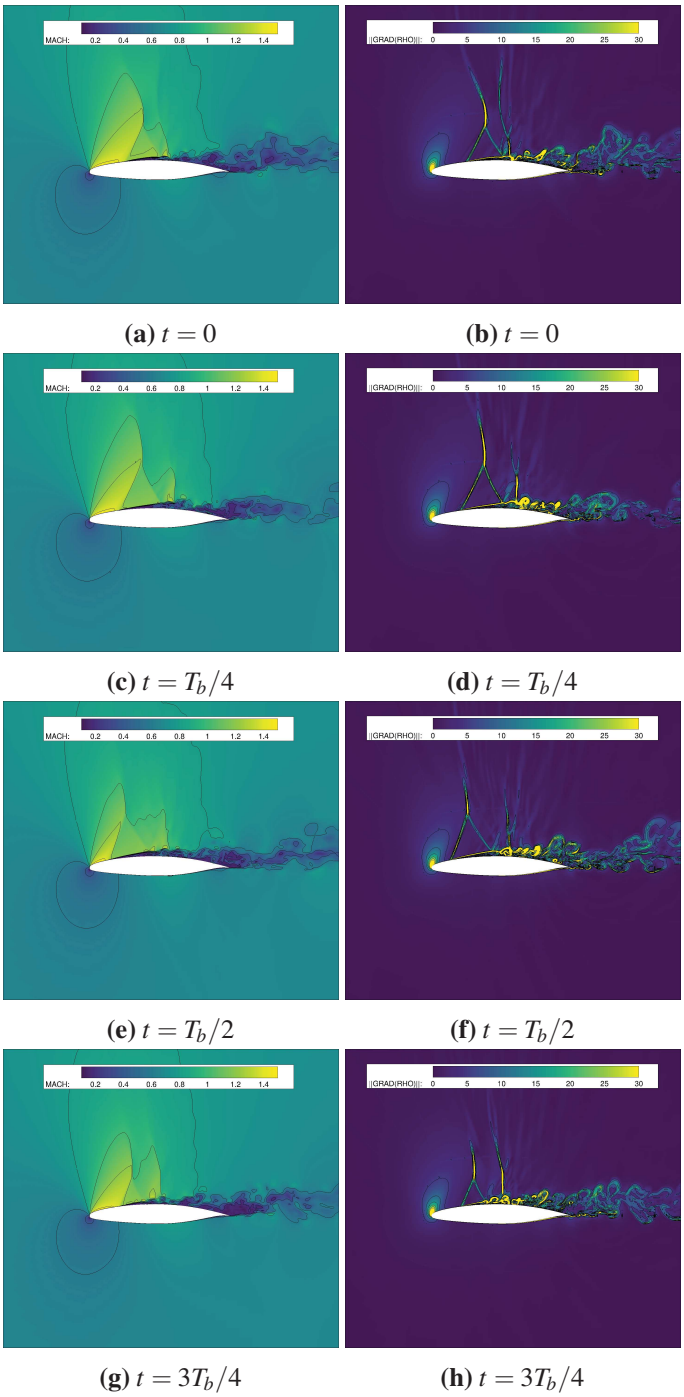

(a) $t = 0$ **(b)** $t = 0$

(c) $t = T_b/4$ **(d)** $t = T_b/4$

(e) $t = T_b/2$ **(f)** $t = T_b/2$

(g) $t = 3T_b/4$ **(h)** $t = 3T_b/4$

Figure 3.16: *Variation of the M number (left) and the gradient density magnitude (right) over one buffet period T_b on the mid-span xz section with OES+F.*

3.3.3 Modification of the coherent dynamics

Various monitoring points were placed along the surface of the wing to record the pressure variation in time. The points illustrated in Fig. 3.17 are selected to be presented here as they cover the chord length and are sufficiently spaced between them. The signals for the pressure difference with respect to the freestream pressure and the power spectral density (PSD) of the signals are included in Fig. 3.18. The signals from the OES and OES+F calculations are examined together for comparison; the DOES and DOES+F provide almost identical results. The periodic oscillations of the signal clearly indicate the buffeting motion along the suction side. The peak values correspond to the phase where the shock moves to its most upstream position while the valleys correspond to the shock's most downstream position. The superimposed higher-frequency oscillations at the crests of the signal correspond to the boundary layer detachment and transition (*St* number order of 1). This underlines the interaction of the shock with the boundary layer.

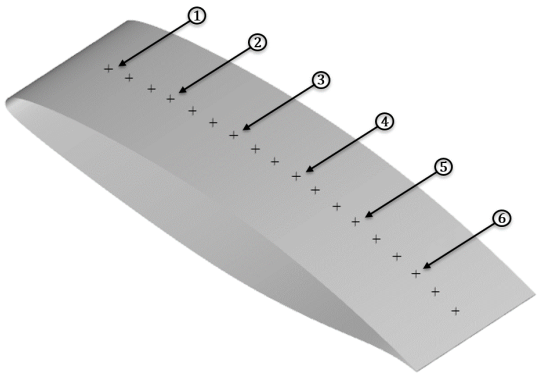

Figure 3.17: *Positioning of surface pressure monitors on the wing.*

The first point (Point 1) examined shows that the stochastic forcing prevents the shock from reaching the leading edge of the wing. For the position further donwstream and inside the area of the buffeting motion, the frequency is modulated (slightly reduced). The extreme peaks occuring in the case of standard OES are significantly reduced as well. The buffeting motion is contained in a narrower area (see Points 1 and 6) and the intensity of pressure fluctuations is weakened. Consequently, the mean pressure values are slightly reduced and an increase of the aerodynamic lift is to be expected. In the more downstream positions (Points 4-6) the time duration of the crests is longer, and the nonlinear interactions and smaller-scale effects are enriched. These remarks are supported by the PSD of the pressure signals as well. The buffet frequency is moved to a slightly lower value and the nonlinear interactions between its harmonics and higher frequencies are modified.

These modulations are directly affect the temporal evolution of the aerodynamic forces. The time variation of the lift and drag coefficients is shown in Fig.3.19

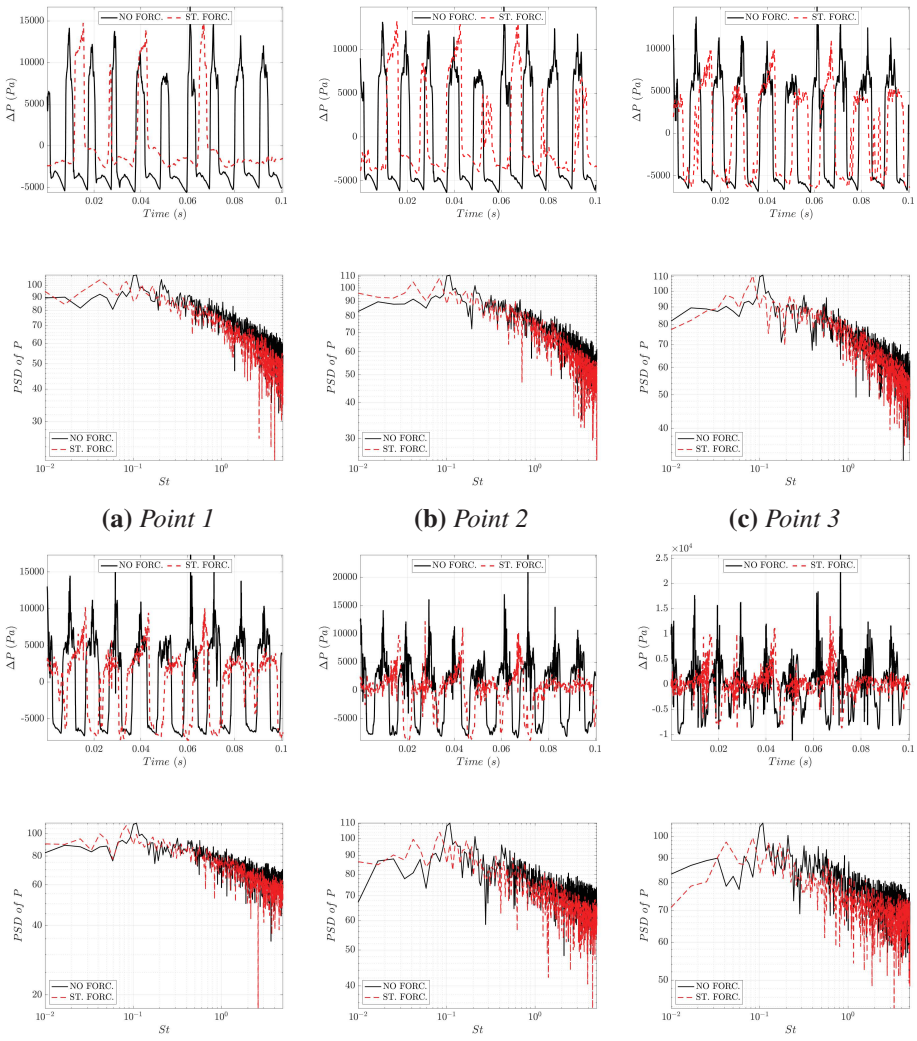

(a) *Point 1* **(b)** *Point 2* **(c)** *Point 3*

(d) *Point 4* **(e)** *Point 5* **(f)** *Point 6*

Figure 3.18: *Comparison of surface pressure temporal variation with OES and OES+F.*

for the OES/OES+F (Figs. 3.19a-3.19b) and the DOES/DOES+F (Figs. 3.19c-3.19d) approach. Both methods present qualitatively identical results. The regular "saw tooth" shaped oscillations, that were predicted without forcing due to the strong suction effects, are replaced by a more irregular pattern with less sharp - more physical - variations. The modulations are even more prominent in the drag evolution which displays lower amplitudes and rms levels, and could be attributed to the stochastic local acceleration of the flow due to the forcing. The mean values are also modified as expected. A slight increase of the lift coefficient and a simultaneous decrease of the drag is predicted with the stochastic forcing. The statistics of the evolution of

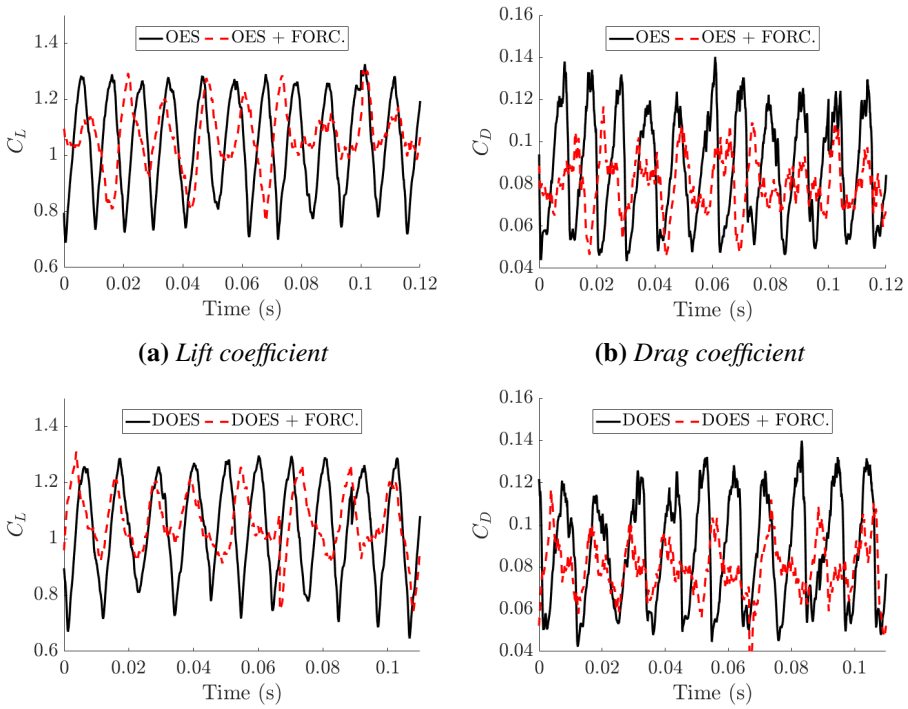

(a) *Lift coefficient* **(b)** *Drag coefficient*

(c) *Lift coefficient* **(d)** *Drag coefficient*

Figure 3.19: *Temporal variation of aerodynamic force coefficients with OES(+F) (top) and DOES(+F) (bottom).*

the forces are summarized in Table 3.1 along with the experimental measurements (EXPE) [IoA20]. The experiments were carried out by the Institute of Aviation (IoA), Warsaw, partner of the TFAST project. The mean values calculated with the stochastic forcing are closer to the experimentally measured values. A significant decrease of the excessive root-mean-square value of the force variation is achieved with the new approach. Finally, the frequency modulations reduce the Strouhal number (based on the chord) which also correlates well with the one estimated by experimental unsteady pressure measurements.

3.3.4 Mean flow field

The time averaged boundary layers and velocity profiles in the wake are illustrated in Fig. 3.20 for the longitudinal (U_{av}) and in Fig. 3.21 for the vertical (W_{av}) velocity component. The comparison is made for the OES/OES+F calculations but the same trends have been observed from the DOES/OES+F. The reader can refer to Fig. 3.7 for the X/c streamwise positions used for the extraction of the velocity profiles.

Moderate modifications are present in the velocity profiles in the sections above the wing surface (Figs.3.20a-3.20c and 3.21a-3.21c). The profiles reach the upstream value more abruptly; the boundary layer thickness is slightly reduced

	$\overline{C}_L$	$\sqrt{\overline{(C_L-\overline{C}_L)^2}}$	$\overline{C}_D$	$\sqrt{\overline{(C_D-\overline{C}_D)^2}}$	St_b
EXPE	1.077	–	0.0748	–	0.09
OES	1.046	0.171	0.0885	0.0259	0.10
OES+F	1.067	0.105	0.0802	0.0128	0.08
DOES	1.036	0.171	0.0884	0.0256	0.11
DOES+F	1.057	0.105	0.0795	0.0128	0.09

Table 3.1: *Comparison of force prediction; the experimentally measured values (EXPE) for final (v2) polished clean prototype. Strouhal number based on the chord.*

and the turbulent flow does not contaminate (upper) regions where the flow should stay irrotational. The detached zone is slightly thinner and the vertical velocity component is reduced as the recirculation zone becomes smaller. In the wake (Figs.3.20d-3.20f and 3.21d-3.21f), the velocity profiles are significantly affected. The shearing mechanism is intensified, resulting in a sharper slope for the longitudinal velocity profiles and a higher velocity deficit due to the fluctuating turbulent stresses. The velocity profiles reach the upstream values more abruptly and the wake thickness is reduced signifying a consequent reduction of the entrainment velocity. The wake seems to be shielded from the outside perturbations and, at the same time, the irrotational regions are less contaminated. Therefore, the reinjection of turbulence meets the objectives of shear sheltering processes mentioned in the beginning of this chapter.

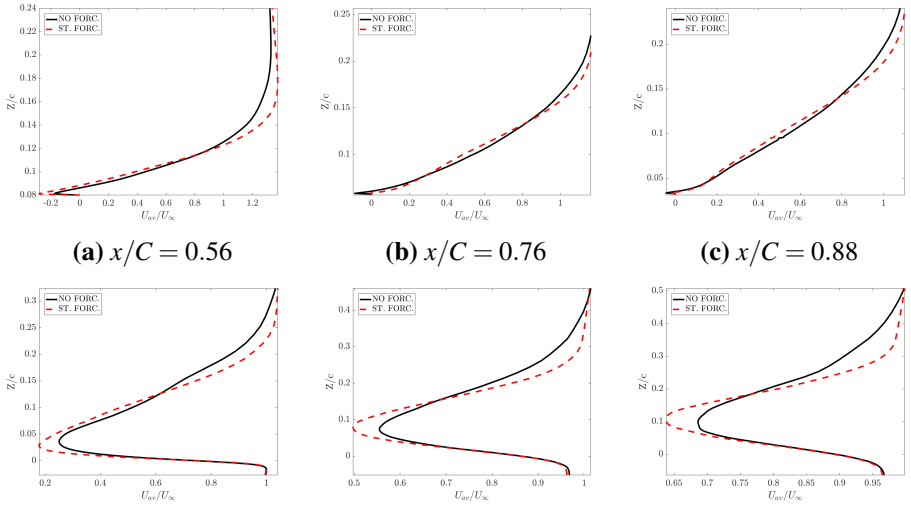

(a) $x/C = 0.56$ **(b)** $x/C = 0.76$ **(c)** $x/C = 0.88$

(d) $x/C = 1.08$ **(e)** $x/C = 1.28$ **(f)** $x/C = 1.48$

Figure 3.20: *Averaged longitudinal velocity profiles; comparison between OES and OES+F.*

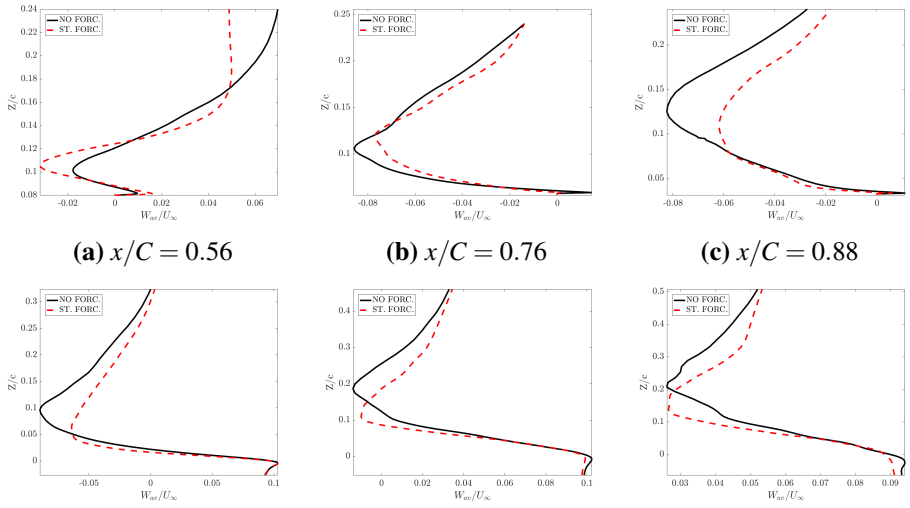

(a) $x/C = 0.56$ **(b)** $x/C = 0.76$ **(c)** $x/C = 0.88$

(d) $x/C = 1.08$ **(e)** $x/C = 1.28$ **(f)** $x/C = 1.48$

Figure 3.21: *Averaged vertical velocity profiles; comparison between OES and OES+F.*

3.3.5 Tripped transition

The OES+F and DOES+F approaches yield an improved prediction of the experimentally measured aerodynamic forces as it was discussed in a previous section. However, the intensity of the pressure fluctuations - even if reduced with the forcing - is still quite large due to the long distance that the shock covers as it travels along the wing's surface. Whether this is physical needs to be investigated. In this section we will examine the physical procedures that strongly affect the prediction and are responsible for the dynamics captured. In terms of numerical parameters, we will evaluate the effects of the turbulence transition of the boundary profile on the suction side of the wing, which was found to greatly alter the the flow prediction. In the present simulations, we account for the 3D transition with the addition of a plane (2D) that numerically suppresses the generation of turbulence by replacing the turbulent source terms with a zero matrix, imposing a zero eddy viscosity on the domain that precedes the plane. The stochastic forcing terms are only activated inside the domain downstream of the transition plane. The discussion here included is based on the average pressure profiles over the wing's surface. The time averaged pressure distribution on the wing's surface (Fig. 3.23) is examined on the mid-span section illustrated in Fig. 3.22.

The (non-dimensional) pressure coefficient is plotted for several of the cases examined. The studies carried out in the present work are completed by experimental measurements carried out by the Institute of Aviation (IoA) and DNS by the University of Rome *La Sapienza* (URMLS), both partners in the TFAST project. The measurements for the final (v2) version of the wing without tripping (CLEAN)

are examined here. A second prototype of the final wing was constructed with better geometry accuracy that resulted in reduced surface roughness (POLISHED) and is also investigated. Two cases for the DNS calculations are presented here as well, both carried out on a fine mesh with $N_x \cdot N_y \cdot N_z = 2560 \cdot 512 \cdot 768$ grid points. The first one (DNS) examines the purely laminar interaction on the V2C airfoil where the term laminar refers to the state of the incoming boundary layer until it reaches in the proximity of the shock foot. In this case, the transition to turbulence takes place due to the strong pressure gradient in this region. In the second case (DNS TRIP) a numerical tripping of the boundary layer was added at $X/c = 0.1$ on the suction side of the wing in order to initiate the transition to turbulence. The tripping was achieved by a roughness element placed along the span and resolved with an immersed boundary approach.

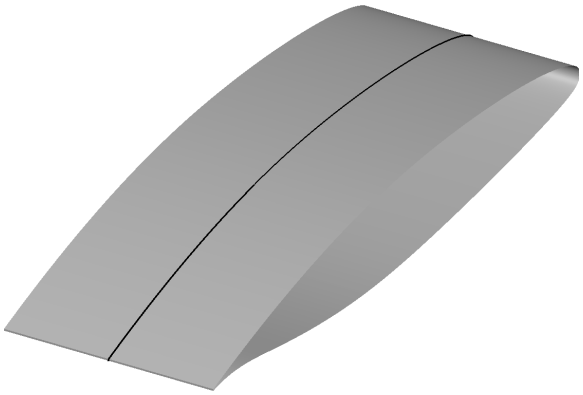

Figure 3.22: *Mid-span section on the wing's surface.*

In Fig. 3.23a, a comparison is made between the experimental pressure measurements and the DNS. There is an apparent qualitative agreement overall between the two investigations. The "laminar" DNS predicts a shock position at $X/c \approx 0.4$ which is really close to the one measured on the polished profile. The polished V2C design is able to sustain a laminar boundary layer up until the shock foot, in accordance with the laminar wing concept. Downstream of the shock, the sudden decrease of the pressure coefficient marks the transition to turbulence and the steep slope signifies that the shock remains quasi-steady. On the contrary, the shock position moves upstream when the non-polished profile (CLEAN) is examined. Due to the increased roughness, the transition to turbulence is hastened and the decrease in the slope of the pressure coefficient illustrates a shock unsteadiness. The buffeting motion covers a long distance over the surface and the tripped simulation (DNS TRIP) predicts an almost identical behavior. The tripping initiates the turbulent transition which takes place at $X/c \approx 0.3$ and consequently the shock

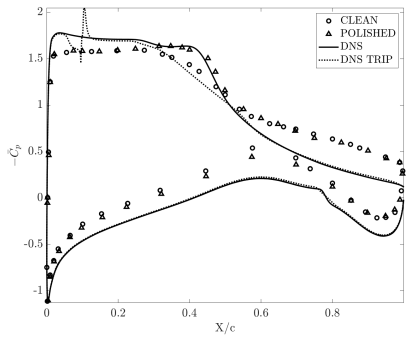

(a) *Comparison of DNS with experiments.*

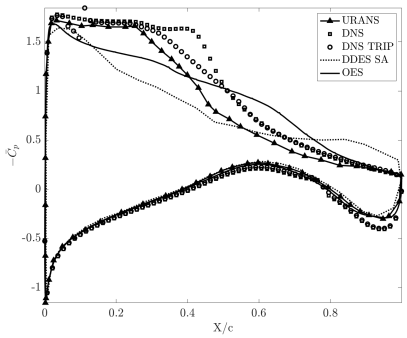

(b) *Various modelling approaches.*

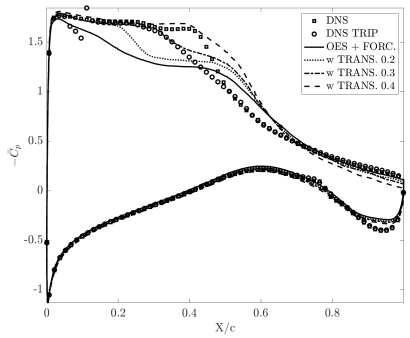

(c) *Effect of the transition planes.*

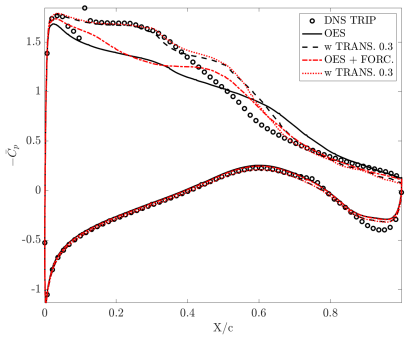

(d) *With and without stochastic forcing.*

Figure 3.23: *Averaged surface C_p distribution on the mid-span section; experimental measurements on the final (v2) clean and polished clean prototype by IoA, URANS carried out by IMFT and DNS, DDES by URMLS during the TFAST project.*

movement reaches this point. Additional experimental measurements with tripping of the boundary layer on the suction side support these remarks; when the transition to turbulence is initiated through tripping, the shock becomes more unstable and its travelling reaches more upstream positions. It should be mentioned that, even though the DNS predicts a dynamic response for the shock in agreement with the experimental measurements, the two investigations produce differences in the pressure distribution on the pressure side of the wing and downstream on the suction side.

Various turbulence modelling approaches are compared in Fig. 3.23b. The pressure distribution predicted with the OES approach in the current work is shown along with the previously mentioned DNS results. In the same figure, the DDES studies carried out by URMLS are also included. The Spalart-Allmaras (SA) model was employed for the RANS-mode calculations of the DDES approach. Finally, past URANS simulations carried out by IMFT, utilizing the $k-\omega$ model, were added [SAG+16]. All the approaches present identical results on the pressure side

of the wing and on the downstream part of the suction side. The OES and DDES approaches predict a similar behavior with the OES yielding a higher pressure coefficient in the shock travelling region. The shock presents intense unsteadiness and covers a wide distance over the surface of the wing reaching up until the leading edge. It had been demonstrated by subsequent studies of URMLS that the spanwise length does not contribute to this prediction. This large shock travelling area was also observed in the contours presented in previous section for the OES approach. As it has been demonstrated (Fig. 3.4), turbulence is generated at the vicinity of the shock foot. Close to the surface, due to the low-Mach number in the boundary layer region, the turbulent field contaminates upstream regions. The adverse pressure gradient pushes the detachment forward until it reaches the trailing edge. The URANS approach presents a more stable solution compared to the OES and the DDES. This was expected since statistical approaches provides a higher disspipation rate level than the OES and the DDES. The stochastic forcing (OES+F) based on the URANS modes leads to an improved behavior (see Fig. 3.23d). The $\bar{C}_p$ moves towards the DNS tripped simulation and presents an overall better tendency. However, it can be seen that the stochastic forcing on its own does not alleviate the intense shock unsteadiness.

Subsequent studies have been carried out with the addition of the aforementioned transition planes. In Fig. 3.23c, the pressure distribution is illustrated for the OES+F computations without and with transition planes (w TRANS) at three positions $X/c = 0.2/0.3/0.4$ based on the chord of the wing. It is demonstrated that the suppression of turbulence source terms upstream of the transition plane, blocks the shock from moving towards upstream regions, supporting the previous analysis. The pressure plateau is established and the pressure levels are in very good agreement with the DNS with and without tripping with the plane placed at $X/c = 0.3$ and $X/c = 0.4$ respectively. In the shock travelling region, the current approach predicts a small acceleration zone that corresponds to the secondary shock previously observed and is responsible for a slight bump in the $\bar{C}_p$ distribution. These regions do not appear in the DNS predictions and according to the author's understanding it can be attributed to an insufficient mesh refinement for the present simulations. This is also supported by the remark made for the DOES calculation in which the simulation worked in an OES mode in the region downstream of the shock. Nevertheless, the current investigation mainly examines the parameters that affect the prediction of the shock position and studies on a finer mesh could be the subject of a future study. To conclude this analysis, it should be mentioned that the use of transition planes reduces the apparent effects of the stochastic forcing in the pressure distribution. This is shown in Fig. 3.23d where the two approaches are - as expected - identical in the region upstream of the plane where no turbulent source terms are accounted for. In addition, minor differences in the region downstream of the shock are observed and the stochastic forcing does produce improvements on the flow prediction since the pressure distribution approaches the DNS results slightly better.

3.4 Conclusion

In the present chapter we examined a stochastic forcing turbulence modelling approach. The method was first examined in [SGJG+15] for a 2D transonic flow in combination with the OES approach. It consists of turbulence re-injection which models upscale energy transfers causing the generation of intermediate eddies. The forcing terms are built from turbulence kinetic energy reconstructed from low-energy POD modes and a random number generator that accounts for the stochastic nature of the backscattering. In the present work, the method was extended for three-dimensional flows to be used in the investigations on the transonic flow around the laminar V2C wing designed and studied by in the context of the TFAST European project.

The methodology was examined along the OES and a DES approach and applied for the prediction of the buffet instability. The forcing increased the dissipation rate locally, inside the sheared regions identified from the POD, reducing the turbulence eddy viscosity. The flow field, the SWBLI and the buffet limit cycle prediction have been analyzed with the stochastic forcing. The general shock structure was not affected but the travelling length of the shock was reduced and the buffet cycle was slightly more stable. The detachment of the flow became less pronounced and consequently the width of the wake was also reduced.

The evaluations of the dynamics showed a reduced buffet frequency which correlated better with the experiments, and higher-frequency modulations of the pressure signals. The extreme peaks and the mean pressure values were reduced and the intensity of pressure fluctuations was attenuated. These modifications resulted in a force prediction that was closer to the experimentally measured values. The effects of the turbulence transition of the boundary profile on the suction side of the wing were also considered. We demonstrated that the suppression of turbulence source terms upstream of the shock stabilized the flow, prevented the shock from reaching the leading edge and a pressure plateau was established in very good agreement with the past DNS results. Subsequent studies on a refined mesh in the region after the shock front should follow. This investigation will be focused mainly in the region right after the shock front in order to evaluate the prediction of the narrow acceleration zone due to the secondary shock. This will also allow to perform DDES-OES calculations which were not examined in the present study since the simulations perfomed in an OES mode for this specific grid.

Overall, the proposed methodology succeeds in representing the TNT and TT interfaces and the effects that the modelled small scale dynamics were expected to cause by predicting a sharper slope for the axial velocity profiles. The wake was shielded from the outside perturbations; a thinner wake was predicted suggesting reduced entrainment velocity. The addition of the stochastic forcing also yielded an increase of the lift and simultaneously decrease of the drag. It is of interest to investigate whether the same type of effects can be achieved by employing electroactive morphing strategies targeting the control of the TT and TNT interfaces. In the following chapter, we will examine a morphing application in which we enhance

the aerodynamic performance via a high-frequency low-amplitude actuation near the trailing edge region of a wing, introducing in the flow small scale fluctuations that actively modify the wake dynamics.

Bibliography

[BB03a] A. Bouhadji and M. Braza. Organised modes and shock–vortex interaction in unsteady viscous transonic flows around an aerofoil: Part I: Mach number effect. *Computers & Fluids*, 32(9):1233 – 1260, 2003.

[BB03b] A. Bouhadji and M. Braza. Organised modes and shock–vortex interaction in unsteady viscous transonic flows around an aerofoil: Part II: Reynolds number effect. *Computers & Fluids*, 32(9):1261 – 1281, 2003.

[BBBT03] S. Bourdet, A. Bouhadji, M. Braza, and F. Thiele. Direct Numerical Simulation of the Three-Dimensional Transition to Turbulence in the Transonic Flow around a Wing. *Flow, Turbulence and Combustion*, 71(1):203–220, March 2003.

[BBHEA08] R. Bourguet, M. Braza, G. Harran, and R. El Akoury. Anisotropic Organised Eddy Simulation for the prediction of non-equilibrium turbulent flows around bodies. *Journal of Fluids and Structures*, 24(8):1240–1251, November 2008.

[Ber85] J. P. Bertoglio. A stochastic subgrid model for sheared turbulence. In U. Frisch, J. B. Keller, G. C. Papanicolaou, and O. Pironneau, editors, *Macroscopic Modelling of Turbulent Flows*, pages 100–119, Berlin, Heidelberg, 1985. Springer Berlin Heidelberg.

[BHL93] G. Berkooz, P. Holmes, and J. L. Lumley. The Proper Orthogonal Decomposition in the Analysis of Turbulent Flows. *Annual Review of Fluid Mechanics*, 25(1):539–575, 1993.

[CGM07] J. Crouch, A. Garbaruk, and D. Magidov. Predicting the onset of flow unsteadiness based on global instability. *Journal of Computational Physics*, 224:924–940, 2007.

[CGMT09] J. D. Crouch, A. Garbaruk, D. Magidov, and A. Travin. Origin of transonic buffet on aerofoils. *Journal of Fluid Mechanics*, 628:357–369, June 2009.

[Cha91] J. R. Chasnov. Simulation of the Kolmogorov inertial subrange using an improved subgrid model. *Physics of Fluids A: Fluid Dynamics*, 3(1):188–200, January 1991.

[Dav09] L. Davidson. Hybrid LES-RANS: back scatter from a scale-similarity model used as forcing. *Philosophical Transactions of the Royal Society A: Mathematical, Physical and Engineering Sciences*, 367(1899):2905–2915, 2009.

[Dec05] S. Deck. Numerical simulation of transonic buffet over a supercritical airfoil. *AIAA Journal*, 43(7):1556–1566, July 2005.

[GBH14] F. Grossi, M. Braza, and Y. Hoarau. Prediction of transonic buffet by delayed detached-eddy simulation. *AIAA Journal*, 52(10):2300–2312, 2014.

[GD10] E. Garnier and S. Deck. Large-eddy simulation of transonic buffet over a supercritical airfoil. In V. Armenio, Be. Geurts, and J. Fröhlich, editors, *Direct and Large-Eddy Simulation VII*, pages 549–554, Dordrecht, 2010. Springer Netherlands.

[GPMC91] M. Germano, U. Piomelli, P. Moin, and W. H. Cabot. A dynamic subgrid-scale eddy viscosity model. *Physics of Fluids A: Fluid Dynamics*, 3(7):1760–1765, July 1991.

[HD99] J. C. R. Hunt and P. A. Durbin. Perturbed vortical layers and shear sheltering. *Fluid Dynamics Research*, 24(6):375–404, June 1999.

[HESW11] J. C. R. Hunt, I. Eames, C. B. da Silva, and J. Westerweel. Interfaces and inhomogeneous turbulence. *Philosophical Transactions of the Royal Society of London A: Mathematical, Physical and Engineering Sciences*, 369(1937):811–832, February 2011.

[HEW08] J. C. R. Hunt, I. Eames, and J. Westerweel. Vortical Interactions with Interfacial Shear Layers. In *IUTAM Symposium on Computational Physics and New Perspectives in Turbulence*, IUTAM Bookseries, pages 331–338. Springer, Dordrecht, 2008.

[Hoa02] Y. Hoarau. *Analyse physique par simulation numérique et modélisation des écoulements décollés instationnaires autour de surfaces portantes*. Phd thesis, INPT, 2002.

[HPV+16] Y. Hoarau, D. Pena, J. B. Vos, D. Charbonier, A. Gehri, M. Braza, T. Deloze, and E. Laurendeau. *Recent Developments of the Navier Stokes Multi Block (NSMB) CFD solver*. American Institute of Aeronautics and Astronautics, 2016.

[IGK09] T. Ishihara, T. Gotoh, and Y. Kaneda. Study of High–Reynolds Number Isotropic Turbulence by Direct Numerical Simulation. *Annual Review of Fluid Mechanics*, 41(1):165–180, 2009.

[IKH13] T. Ishihara, Y. Kaneda, and J. C. R. Hunt. Thin Shear Layers in High Reynolds Number Turbulence—DNS Results. *Flow, Turbulence and Combustion*, 91(4):895–929, December 2013.

[IoA20] Transition location effects on shock wave boundary layer interaction. In P. Doerffer, P. Flaszynski, J.-P. Dussauge, H. Babinsky, P. Grothe, A. Petersen, and F. Billard, editors, *Notes on Numerical Fluid Mechanics and Multidisciplinary Design*, volume in print, pages 135–147. Springer, 2020.

[IOH15] T. Ishihara, H. Ogasawara, and J. C. R. Hunt. Analysis of conditional statistics obtained near the turbulent/non-turbulent interface of turbulent boundary layers. *Journal of Fluids and Structures*, 53:50–57, February 2015.

[JD98] R. G. Jacobs and P. A. Durbin. Shear sheltering and the continuous spectrum of the Orr–Sommerfeld equation. *Physics of Fluids*, 10(8):2006–2011, 1998.

[JMD+09] L. Jacquin, P. Molton, S. Deck, B. Maury, and D. Soulevant. Experimental study of shock oscillation over a transonic supercritical profile. *AIAA Journal*, 47(9):1985–1994, 2009.

[Kok17] J. Kok. A Stochastic Backscatter Model for Grey-Area Mitigation in Detached Eddy Simulations. *Flow, Turbulence and Combustion*, 99, 2017.

[KYTK20] Y. Kojima, C.-An Yeh, K. Taira, and M. Kameda. Resolvent analysis on the origin of two-dimensional transonic buffet. *Journal of Fluid Mechanics*, 885, 2020.

[Lei90] C. E. Leith. Stochastic backscatter in a subgrid-scale model: Plane shear mixing layer. *Physics of Fluids A: Fluid Dynamics*, 2(3):297–299, March 1990.

[LQ79] D. C. Leslie and G. L. Quarini. The application of turbulence theory to the formulation of subgrid modelling procedures. *Journal of Fluid Mechanics*, 91(1):65–91, 1979.

[MBJ07] L. Marstorp, G. Brethouwer, and A. V. Johansson. A stochastic subgrid model with application to turbulent flow and scalar mixing. *Physics of Fluids*, 19(3):035107, 2007.

[MLD76] J. B. McDevitt, L. L. Levy, and G. S. Deiwert. Transonic flow about a thick circular-arc airfoil. *AIAA Journal*, 14(5):606–613, 1976.

[MT92] P. J. Mason and D. J. Thomson. Stochastic backscatter in large-eddy simulations of boundary layers. *Journal of Fluid Mechanics*, 242:51–78, 1992.

[PCC+07] R. Perrin, E. Cid, S. Cazin, A. Sevrain, M. Braza, F. Moradei, and G. Harran. Phase-averaged measurements of the turbulence properties in the near wake of a circular cylinder at high Reynolds number by 2c-PIV and 3c-PIV. *Experiments in Fluids*, 42(1):93–109, January 2007.

[SAG+16] D. Szubert, I. Asproulias, F. Grossi, R. Duvigneau, Y. Hoarau, and M Braza. Numerical study of the turbulent transonic interaction and transition location effect involving optimisation around a supercritical aerofoil. *European Journal of Mechanics - B/Fluids*, 55:380 – 393, 2016. Vortical Structures and Wall Turbulence.

[SAS+18] D. Szubert, I. Asproulias, N. Simiriotis, Y. Hoarau, and M. Braza. Numerical simulation of a 3-d laminar wing in transonic regime. In *Notes on Numerical Fluid Mechanics and Multidisciplinary Design*, volume 137, pages 277–290. Springer, 03 2018.

[SGJG+15] D. Szubert, F. Grossi, A. Jimenez Garcia, Y. Hoarau, J. C. R. Hunt, and M. Braza. Shock-vortex shear-layer interaction in the transonic flow around a supercritical airfoil at high Reynolds number in buffet conditions. *Journal of Fluids and Structures*, 55:276–302, May 2015.

[SL95] U. Schumann and B. E. Launder. Stochastic backscatter of turbulence energy and scalar variance by random subgrid-scale fluxes. *Proceedings of the Royal Society of London. Series A: Mathematical and Physical Sciences*, 451(1941):293–318, 1995.

[SML78] H. L. Seegmiller, J. G. Marvin, and L. L. Levy. Steady and unsteady transonic flow. *AIAA Journal*, 16(12):1262–1270, 1978.

[SMS15] F. Sartor, C. Mettot, and D. Sipp. Stability, receptivity, and sensitivity analyses of buffeting transonic flow over a profile. *AIAA Journal*, 53(7):1980–1993, 2015.

[SR07] Philippe R. Spalart and Christopher L. Rumsey. Effective inflow conditions for turbulence models in aerodynamic calculations. *AIAA Journal*, 45(10):2544–2553, 2007.

[ST15] F. Sartor and S. Timme. Reynolds-averaged navier-stokes simulations of shock buffet on half wing-body configuration. *53rd AIAA Aerospace Sciences Meeting*, 2015.

[ST17] F. Sartor and S. Timme. Delayed detached–eddy simulation of shock buffet on half wing–body configuration. *AIAA Journal*, 55(4):1230–1240, 2017.

[TSM+19] J. B. Tô, N. Simiriotis, A. Marouf, D. Szubert, I. Asproulias, D. M. Zilli, Y. Hoarau, J. C. R. Hunt, and M. Braza. Effects of vibrating and deformed trailing edge of a morphing supercritical airfoil in transonic regime by numerical simulation at high Reynolds number. *Journal of Fluids and Structures*, 91:102595, November 2019.

[WFPH09] J. Westerweel, C. Fukushima, J. M. Pedersen, and J. C. R. Hunt. Momentum and scalar transport at the turbulent/non-turbulent interface of a jet. *Journal of Fluid Mechanics*, 631:199–230, 2009.

[WZN18] T. Watanabe, X. Zhang, and K. Nagata. Turbulent/non-turbulent interfaces detected in DNS of incompressible turbulent boundary layers. *Physics of Fluids*, 30(3):035102, 2018.

Chapter 4

Wing morphing via near-trailing edge actuation[1]

This chapter examines the morphing effects due to the trailing-edge low-strain vibration on the aerodynamic forces and the turbulent structures in the wake of a supercritical wing. The actuation is produced with piezoactuators placed in the trailing edge region of the wing. The study is carried out in the low subsonic regime (Reynolds number ~ 1 Million) corresponding to take-off/landing flight phases. It is shown that the electroactive morphing has the capacity to produce an enhanced aerodynamic performance. Optimal frequency/amplitude ranges for the vibrations are quantified.

4.1 Introduction

The state and the governing dynamics of wake regions downstream of hydrodynamic bodies has been the subject of multiple investigations. The instabilities emerging in the wake provoke the generation of vortices that significantly affect the flow and performance of aerodynamic surfaces through feedback mechanisms. The characteristic flow patterns developed around a symmetric airfoil at a low Reynolds number have been experimentally studied in [HL95]. The boundary layer on the suctions side of the wing was found to be strongly correlated to the unstable shear layers developed in the flow around the wing. The authors examined the relation between shear layer instabilities and the emerging vortex shedding behind the airfoil

[1] The work presented in this chapter has led to a journal [SJM+19] and a conference [SDJ+19] publication

and analyzed the shedding characteristics as a function of the Reynolds number and the angle of attack.

The work of Hoarau et al. [HFB$^+$03] further analyzed the three-dimensional transition of the flow around the same symmetric geometry. The authors performed Direct Numerical Simulations (DNS) at a low Reynolds number as well. Besides the interaction between the shear layer and the shedding modes appearing in the wake, the authors emphasized the importance of three-dimensional modes in the spanwise direction that were found to guide the passage towards turbulence. The coherent structures developed around airfoils was also the subject of the experimental study in [YSK06] and [YSK09] for higher Reynolds number (order of $10^4 - 10^5$). This investigation examined flow characteristics such as separation bubbles, separated boundary layers and turbulent vortex shedding in the wake. The authors analyzed the amplification and growth of disturbances inside the boundary layers along with the roll-up and vortex merging mechanisms, all of which govern the transitional wake dynamics in the respective Reynolds number range.

All the above studies were focused on the governing dynamics of flows around wings and demonstrated the importance of vortex interactions and flow conditions. They created a solid background on which flow control techniques that manipulate the emerging instabilities could be developed based on the physical processes involved.

4.1.1 Forced wakes & shear layers

D. Oster and I. Wygnanski [OW82] investigated the sensitivity of turbulent shear layers to small amplitude two-dimensional perturbations. A moving flap was set at the trailing edge of a splitter plate in order to introduce sinusoidal oscillations at the origin of the shear layer. The oscillations were found to cause significant modifications of the development of the shear layer by reinforcing existing natural flow instabilities, without greatly affecting the initial velocity profiles. They attributed the energy transfer from the natural modes to the actuating ones to a collective interaction of shedding vortices that coalesce (pair) together to form larger structures. In that way, the forcing only redistributed the flow energy. Later, Kourta et al. [KBCH87] numerically studied the successive zones of transitioning shear layers. The authors applied a forcing to study the pairing mechanics and the nonlinear interactions caused from actuation at an incommensurate frequency. The observations were in agreement with previous studies and experimental measurements. These transitional zones of shear layers were also analyzed in more detail in [WW88] through experimental measurements and numerical tools. Flow visualizations, a stability and a spectral analysis were employed to investigate the amplification of phase-locked perturbations added in a shear layer.

The effect of sinusoidal oscillations, introduced on the wake of a flat plate via a trailing edge flap, on the growth of a turbulent wake was examined by [MCW92]. They introduced in the flow travelling waves of various amplitudes and frequencies and demonstrated important variations of the spreading rate of the wake, linked to

the turbulent stresses. They observed that the perturbations added to the flow were initially amplified by draining energy from the mean flow. At a second stage, and after the development of larger coherent structures, the energy of the flow is mainly distributed towards the mean turbulent flow at the expense of the motions linked to the perturbations. N. Reau and A. Tumin developed a numerical model based on the triple decomposition of the flow field [RT02] in order to analyze the introduction of harmonic perturbations in a turbulent mixing layer. Their numerical approach was found to be in good agreement with previous experimental measurements. They examined the nonlinear interactions between coherent and turbulent stresses and proposed a new approach for the accurate prediction of the shear layer spreading. The authors observed the thinning of the shear layer when the perturbations were introduced, and concluded that the same mechanics could guide the development of active flow control strategies.

Forced nonlinear interactions have been also analyzed in the wakes of aerodynamic profiles. The authors in [WCM86] have expanded their previous studies; they investigated the forced development of instabilities in small deficit turbulent wakes of bluff bodies. n this study, they examined the two-dimensional development of turbulent structures due to the interaction of shear layers of opposite vorticity. The work of [Koo89] examined experimentally the vortex patterns generated in the wake of a pitching airfoil. The authors investigated harmonic and stochastic oscillations of the symmetric airfoil profile and analyzed the vortex interactions and wake patterns for various actuation frequencies and amplitudes. They concluded that this type of excitation was able to produce larger scale modifications when compared with traditional flow control techniques. Experimental measurements were also carried out by M. Gharib and K. Williams-Stuber [GWS89] on the forced wake of airfoils . The authors equipped the examined wing geometry with strip-heaters in order to locally alter the flow and effectively change the wake development. They demonstrated that the flow was more receptive to actuations close to the natural frequencies while for larger amplitudes the receptivity range - namely locking range - was expanded. The authors achieved the cancellation of the wake unsteadiness by symmetrically actuating the strip-heaters on both sides of the airfoil and attributed the changes in the aerodynamic performance to the additional thrust generated from the actuation. Through a stability analysis they demonstrated the amplification of the natural frequencies due to the forcing as the wake was found to be adjusting through variations of the mean profiles. The same authors expanded their studies in [WSG90] where they examined the actuation with multiple frequencies. The wake was find to pass into a chaotic state after three different frequencies were applied simultaneously due to the nonlinear dynamics involved. Both studies however were carried out at low Reynolds numbers.

4.1.2 Electroactive morphing

The effect on the wake dynamics and the aerodynamic forces due to an electroactive actuation close to the trailing edge of a wing was studied in great detail in

[SCR+15]. The authors developed and tested a morphing prototype where the actuation was introuced with a piezoelectric push-push mechanism that imposed low-amplitude, high-frequency vibrations of the trailing edge. The system was integrated in a symmetric airfoil and the flow was examined through Particle Image Velocimetry (PIV) measurements. The authors demonstrated that the actuation had a considerable impact on the shear-layer vortices and suggested that through the same mechanisms it is possible to attenuate structures that are detrimental to the aerodynamic performance. Via a Proper Orthogonal Decomposition (POD) analysis they highlighted the influence of the low-amplitude piezoelectric actuation on the temporal and spatial modes and achieved a reduction of the predominant shear-layer frequencies.

The experimental study of Jodin et al. [JMS+17] examined a hybrid morphing wing prototype where the trailing edge actuation was achieved directly from piezoelectric patches incorporated into a silicon trailing edge (see Section 1.2.2). This article presented a first analysis of the morphing effects due to the high-frequency actuation applied close to the trailing edge of an A320 wing at a high Reynolds number and angle of incidence. In the present work, the study of [JMS+17] is extended; we examine the morphing effects on the aerodynamic performance by means of both numerical simulation and experimental investigation, an original element in the state of the art. Both the Reynolds range and the angle of attack for the configuration examined here correspond to take-off/landing flight phases. The flow in the supercritical Reynolds range presents complex vortex dynamics and interactions with the solid structure, calling for specific attention in order to produce successful morphing effects. As a result, high Reynolds dynamics change the general flow behavior and both the morphing practices and targets. In this context, the electroactive morphing is a more general strategy than standard flow control techniques as it creates interactions among the structural dynamics and turbulent flow field.

4.2 Experimental procedure

The hybrid morphing wing prototype embeds both camber control and Higher-Frequency Vibrating Trailing Edge (HFVTE) actuators. In this chapter, only the electroactive morphing effects of the HFVTE actuation are examined. This will highlight the effects coming from the actuated trailing edge in the context of the hybrid morphing. The large-scale deformation at low frequencies achieved with the Shape Memory Alloy (SMA) actuators will be studied in a following chapter of the thesis (see Chapter 5).

The present study follows the experimental work of G. Jodin et al. [Jod17] for a Reynolds number of 1 million. The measurements and the numerical studies will be compared against each other in order to validate both approaches. The wing prototype with a chord $c = 0.7m$ is examined at an incidence angle of 10°. Time Resolved Particle Image Velocimetry (TRPIV) measurements were carried

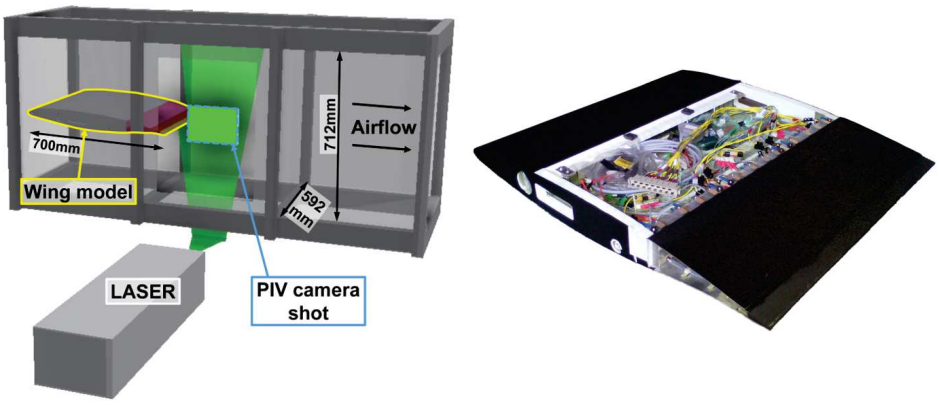

Figure 4.1: *Schematic representation of the experimental test section of the S4 wind tunnel of IMFT (left) with the A320 wing (right) mounted on [JMS$^+$17]; the prototype bears the HFVTE actuators on the trailing edge along the span.*

out in the subsonic wind tunnel S4 of IMFT. The test section has width $w = 592mm$ and height $h = 712mm$ (see Fig. 4.1). The measurement of the unsteady velocity fields has been realized with the contribution of the Signal and Image processing service of IMFT. The post-processing of the raw PIV results was carried out with the CPIV-IMFT open-source software, developed by the Software Services of IMFT, for parallel (MPI) post-treatment of the results in supercomputing architectures. CPIV-IMFT is a multiplatform (Windows/Linux) software, based on a multi-grid iterative algorithm with image distortion [TTS$^+$10]. It is capable of computing large sets of images efficiently in terms of computational time, significantly shortening the post-treatment duration for large-size results. For a more detailed presentation of the software the reader can refer to the CPIV Software description online [2]. In the present study, the CALMIP supercomputing center has been used for the data analysis.

The measurements were carried out at an ambient temperature $(295K)$. For the TRPIV, smoke particles of $3.4\mu m$ diameter were introduced in the airflow, giving a Stokes number $Stk = 5 \cdot 10^{-4}$; $Stk << 1$ indicates that the particles follow consistently the motion of the fluid. Particle images are recorded during the experiments using the digital high-speed camera Phantom V1210. Regarding the depth of the field, the camera was focused in the mid-section. The sampling rate was about $10KHz$. The laser sheet representation in the mid-span region is shown in Fig. 4.1, placed in the stream-wise direction. Each image is divided into interrogation windows of $16X16pixel^2$ size, which corresponds to $3.4X3.4mm^2$, with an overlap of 75%. The thickness of the laser sheet was 2.5 mm. The laser pulsations are generated by a two cavity Nd:YLF (527 nm) laser (Photonics Industries International Inc. DS-527-60) and they were redirected using mirrors to light the wake

[2] http://www.smartwing.org/SMS/EU/CPIV_description

region downstream of the wing. For a more detailed description of the experimental equipment and procedure the reader should refer to [Jod17].

Acquisitions of 50000 images has been proven sufficient to obtain a statistical convergence of the results. The most probable displacement of the particles between two consecutive images is obtained from the cross-correlation of consecutive images. The velocity variation evaluated over multiple experiments was estimated to be below 1.5% while the blockage ratio was found to be acceptable as long as the focus is the relative effects of the morphing application. The experimental benchmark was also equipped with an aerodynamic balance in order to measure the lift and drag forces. However, the quantification of lift and drag was far from trivial in this study since the measurements were significantly affected by the trailing edge vibration. As a result, only qualitative comparisons concerning the morphing effects will be included in this chapter.

4.3 Numerical approach for subsonic flow

The time dependent Navier-Stokes equations have been solved under the conservative form in a finite-volume structured grid formulation, using the NSMB (Navier-Stokes MultiBlock) code [HPV$^+$16], in two and three dimensions. The computational domain is subdivided into a number of quadrilateral (2D) and hexahedral (3D) grid cells resulting in a structured mesh. The multi-block strategy is followed in accordance to the parallelization procedure of the code. A separate discretization of the equations in space and time is applied. Finite volume cells of constant size in time are considered for the discretization in space. A fourth order central skew-symmetric spatial scheme with second and fourth-order artificial dissipation terms is used for the convection terms and a second-order central scheme for the diffusion terms. For the temporal discretization, dual time-stepping with a second-order implicit backward difference scheme is performed (see Chapter 2). The artificial compressibility method for the preconditioning of the flow was chosen after various numerical investigations, in order to enhance the convergence of the computations in the low subsonic regime.

Following the experimental studies, computational grids were constructed depicting faithfully the geometry of test section (see Fig. 4.1). Two meshes (M1 and M2) have been used for the 2D computations. The grid sizes were selected after thorough numerical studies. The M1 includes 300000 finite volume cells. Its refined version, M2 grid, contains 500000 finite volume cells. The additional points were added in the streamwise direction, both on the wing surface and in the wake region. For the 3D computations, the M1 grid was extruded in the spanwise direction leading to a total mesh size slightly higher than 10 million (M3). The y^+ values, corresponding to the first grid spacing above the wall, were below 1 for all the grids considered. The three grids are summarized in Table 4.1.

The physical time-step was kept constant in all the computations at 10^{-5}, giving a CFL number around 50. Additional simulations with a Courant number

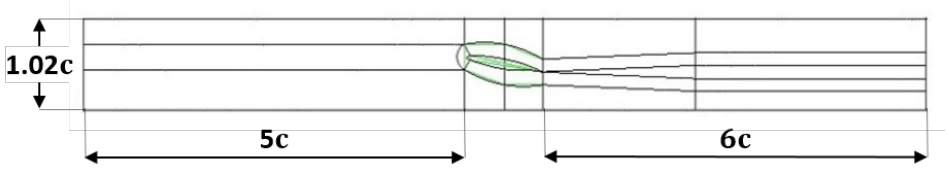

(a) *Multi-block description of the computational domain.*

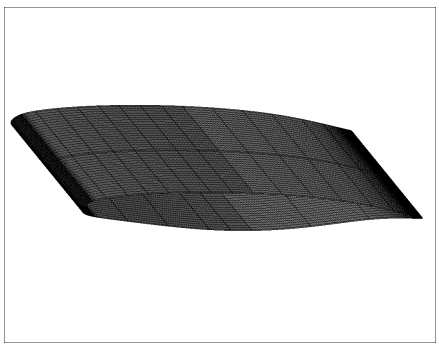

(b) *M3 surface mesh of the A320 wing.*

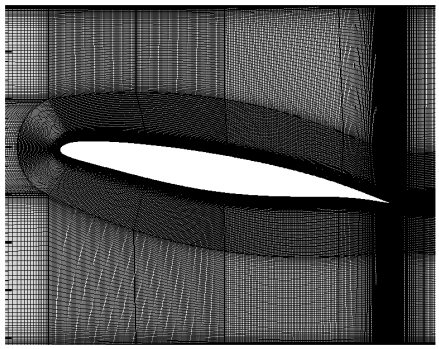

(c) *M1 mesh around the A320 wing.*

Figure 4.2: *Meshing of the computational domain.*

around 5 ($\Delta t = 10^{-6}$) have been also performed and the results compared well with the present studies. About $60-80$ inner iterations were carried out at each time-step. The increased number of iterations is justified from the low-Mach aerodynamics simulated in the cases following. For the upper and lower walls of the tunnel, both non-slip (zero velocity at the wall) and slip (velocity tangent to the surface) boundary conditions were considered; after numerical tests that indicated no considerable effect on the wake development due to the respective boundary condition, the simulations were carried out assuming slip boundary conditions which provided a slightly better agreement with the experimental results. A velocity inlet and a pressure outlet were used in the respective boundaries of the domain. The boundary conditions and the computational parameter has been chosen after various numerical tests. In the present work the Organized Eddy Simulation (OES) approach (Section 2.1.7) has been employed for the turbulent flow.

Grid	Simulation	Cells
M1	2D	300K
M2	2D	500K
M3	3D	10M

Table 4.1: *Grids developed for the numerical analysis.*

For the morphing cases studies, the unsteady Arbitrary Lagrangian-Eulerian methodology [DGH82] is utilized for the calculations in the moving grid. The displacement of the trailing edge region follows exactly the second-order polyno-

mial deformation applied on the reduced scale prototype with the actuation. The frequency of the vibration f_a and the amplitude A_o of the sinusoidal time variation are imposed in each case. The time-dependent vertical deformation dz for every surface point along the streamwise x direction, is given in Eq. 4.1.

$$dz = A_o[\frac{2}{3{L_p}^2}(x-x_o)^2 + \frac{1}{3L_p}(x-x_o)]sin(2\pi f_a) \tag{4.1}$$

for every $x > x_o$, where $x_o = c - L_p$ with c the chord of the airfoil and L_p the piezoelectric patch length. The amplitude A_o corresponds to the displacement of the trailing edge tip end. In the tests following, the feedback effect of the aerodynamic forces on the vibrational behavior of the piezoactuators has not been taken into account (i.e. one-way fluid-structure interaction) as it had been evaluated as negligible in [GSR+15].

4.4 Aerodynamic evaluation without morphing

In this section, both numerical and experimental results for the non-morphed wing are examined. For all the results following, the wing is mounted at an incidence angle of 10°. The chord of the prototype was constant and equal to $0.7m$. The incoming velocity was held constant $(21.5m/s)$; for the reference temperature $(293K)$ and pressure $(101325Pa)$ values, the Reynolds number is $Re \approx 1 \cdot 10^6$. The turbulence intensity of the inlet section of the wind tunnel was estimated at about 0.1% of the free stream velocity; for the numerical simulations, a higher value (1%) was used. Due to the turbulence dissipation, a significant decay of turbulent kinetic energy occurs from the inlet towards the computational domain. Increasing the freestream turbulence intensity ensures comparable - with the experiments - turbulent intensities around the body, and a significant distance between the inlet boundary and the body. This allows for a more faithful representation of the experimental test section.

4.4.1 Time Resolved PIV results

The instantaneous velocity field measured by means of TRPIV is presented in Fig. 4.3. The plane presented in this figure is the one downstream of the wing, as shown in 4.1. The streamwise direction for the measurements is that of x axis and the vertical direction is that of y axis. The $x/c = 1$, $y/c = 0$ position corresponds to the trailing edge. Points were added numerically in post-processing to follow the velocity vector measured at each time-step, allowing for a streakline visualization. The color of each "particle" represents its initial position. With the streakline visualization, the coherent and chaotic turbulent structures developed in the wake are highlighted, providing a view of the dynamic behavior of the wake. The turbulent wake is restrained in between two thin shear layers, the Turbulent/Non-Turbulent (TNT) interfaces [HESW11], examined in more detail in Chapter 3. Inside the

wake region, additional Turbulent/Turbulent (TT) interfaces develop [IOH15]. The interfaces are illustrated clearly in Fig. 4.3, captured by TRPIV measurements, and indicated with the respective notation. The time-averaged longitudinal velocity field from TRPIV measurements is shown in Fig. 4.4a.

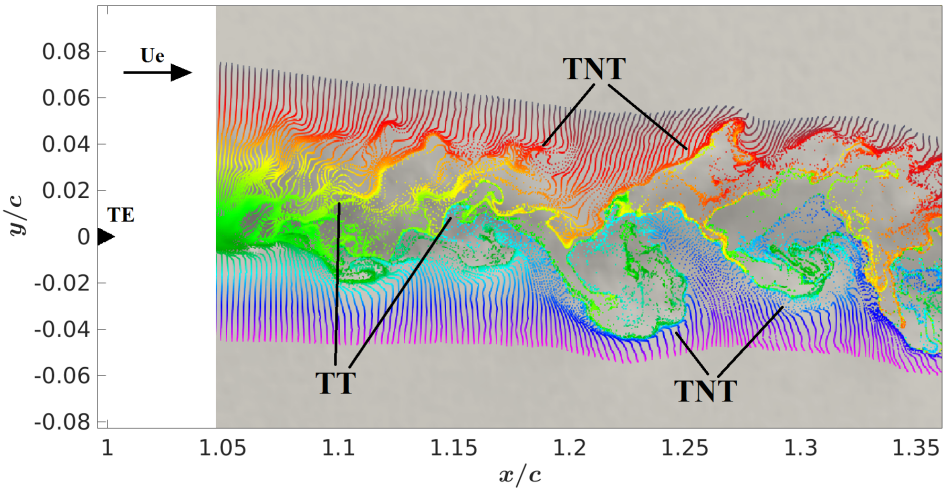

Figure 4.3: *Instantaneous velocity field from the TRPIV measurements, streakline visualization for Re* $= 1M$*, angle of attack* $a_o = 10°$*; the color of each particle represents its initial positions. Trailing edge marked with a triangle.*

To investigate the dynamics in the static configuration case (i.e. when no morphing is applied), time signals of the vertical velocity component have been extracted in selected positions downstream of the trailing edge; the corresponding Fast Fourier Transform (FFT) for these signals has been calculated. Plots of the Power Spectral Density (PSD) are presented in Fig. 4.4b and Fig. 4.4c for two points selected in the near wake region (see Fig. 4.4a). The predominant frequency bump shown in these spectra corresponds to an alternating shedding mode developed downstream. The existence of this bump is representative of a coherent pattern smeared by chaotic turbulence motion due to non-linear interactions between the coherent vortex shedding and the finer-scale chaotic turbulent motion. This irregular formation of large scale structures is characteristic of the supercritical flow developed in this Reynolds range.

The characteristic frequency of the Kármán instability is found to be around 254 Hz as indicated by the signal acquired from monitor points 2 and 3. This frequency corresponds to a Strouhal ($St = fL/U_\infty$) number between $0.4 - 0.5$, for a characteristic length equal to the initial wake's width. This estimation is in agreement with measurements for circular cylinders close to the same Reynolds number [Ros61]. The instability is a result of the interactions between the lower and upper shear layers, developed from the respective unstable boundary layers. Traces of these shear layer instabilities are seen in the spectra. The lower shear

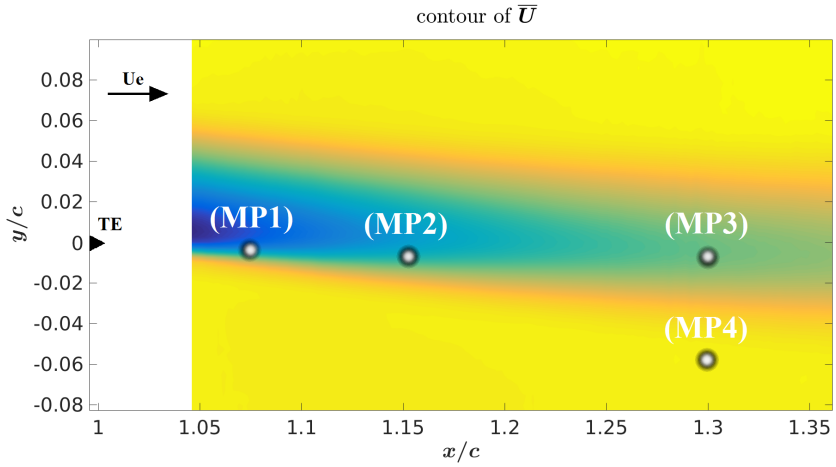

(a) *Contour of time-averaged longitudinal velocity from TRPIV measurements; position of the monitor points along the wake; the trailing edge is marked with a symbol.*

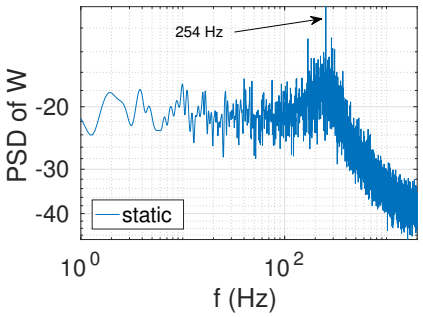

(b) *Spectrum from monitor point 2.*

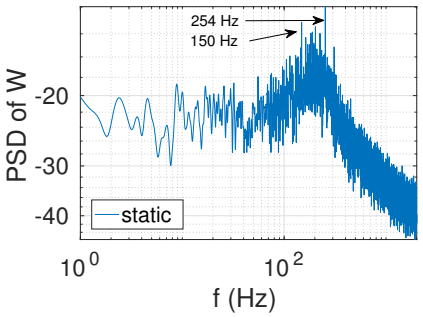

(c) *Spectrum from monitor point 3.*

Figure 4.4: *Spectral content of the vertical velocity component in the near wake region; TRPIV results for the static case.*

layer instability is placed in a higher frequency range ($> 330Hz$) while the upper shear layer seems to be placed around $150-170Hz$. A detailed analysis of the PIV measurements by a Proper Orthogonal Decomposition (POD) is included in [JMS+17].

4.4.2 Numerical study

Numerical simulations have been carried out respecting the aforementioned experimental conditions. For the numerical simulations, the streamwise direction is on the x axis and the vertical direction is that of the z axis, leaving y axis along the spanwise direction. This is the reference system that will be used for the comparison of the computations with the experimental results. Unlike the experimental reference system, the $x/c = 0$, $z/c = 0$ position corresponds to the leading edge.

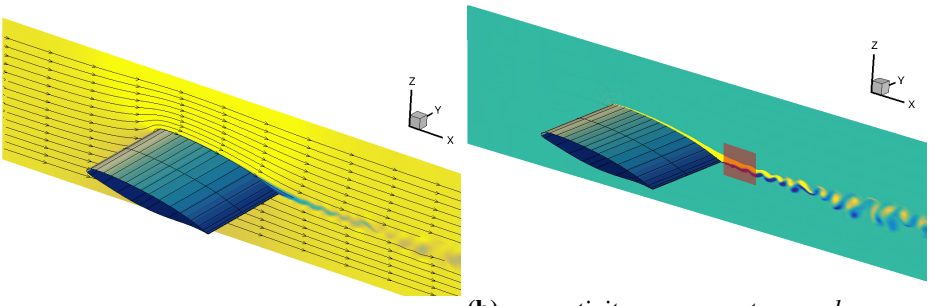

(a) *Velocity magnitude on a plane section.* **(b)** *y−vorticity component on a plane section.*

Figure 4.5: *3D simulation for Re* $= 1M$*, angle of attack* $a_o = 10°$*; wing is colored by time-averaged surface pressure.*

Figure 4.5 provides a global view of the solution over the computational domain, acquired by means of numerical simulation with the M3. The flow coming from the inlet moves downstream from left to right. In Fig 4.5b the plane used for the PIV measurements is noted with a rectangular box and is used for all comparisons between computed and measured data. A small detachment at the trailing edge of the wing is shown through streamlines in Figs. 4.6 and 4.8b. The detachment causes the unstable wake region following downstream and results to a thicker effective body. The upper and lower shear layer instabilities interact with each other giving an irregular alternating shedding further downstream. This gives birth to secondary three-dimensional instabilities by mechanisms examined in low Reynolds numbers around a wing in [HFB$^+$03]. Figure 4.6 illustrates the formation of undulated vortex rows along the span, displaying large-scale wavelengths. The coherent vortices develop spanwisely counter-rotating cells according to a secondary instability amplification [BFP01] and become undulated displaying predominant wavelengths that are fractions of the chord. This can be seen from the spanwise velocity fluctuations shown in Fig. 4.7 in the region downstream of the wing. The velocity is plotted along lines in the spanwise direction drawn for constant x/c values. Despite this three-dimensionnality, the initial development of vortices, i.e. near-wake region close to the trailing edge of the wing, presents a quasi-2D behavior.

Contours of the time-averaged velocity magnitude and the instantaneous (ensemble-averaged) turbulent kinetic energy K calculated by means of numerical simulation with M1, are presented in Fig. 4.8. The regions close to the leading (Figs. 4.8a and 4.8c) and trailing edge (Figs. 4.8b and 4.8d) are zoomed respectively. The quasi-steady detachment begins after $x = 0.55$ which corresponds to an $x/c \approx 79\%$. Close to the leading edge, the appearance of a laminar separation bubble causes the local detachment and then re-attachment of the flow; this mechanism guides the transition to turbulence as depicted in Fig. 4.8c. The production of turbulent kinetic energy starts at $x = 0.03$, i.e. where the bubble ends, which corresponds to an $x/c = 4.3\%$ and as a result, the boundary layer is turbulent when

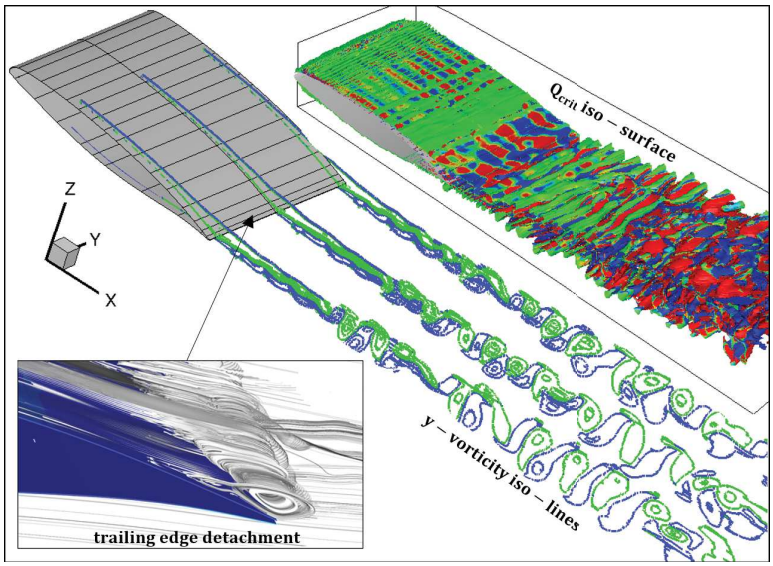

Figure 4.6: *Results from the 3D simulation for* $Re = 1M$*, angle of attack* $a_o = 10°$*; birth and evolution of primary and secondary instabilities in the wake. Iso-lines of span-wise* (y) *vorticity along (middle), Q criterion iso-surfaces (top-right) colored by longitudinal vorticity ranging from* $[-2]$ *(blue) to* $[+2]$ $1/s$ *(red).*

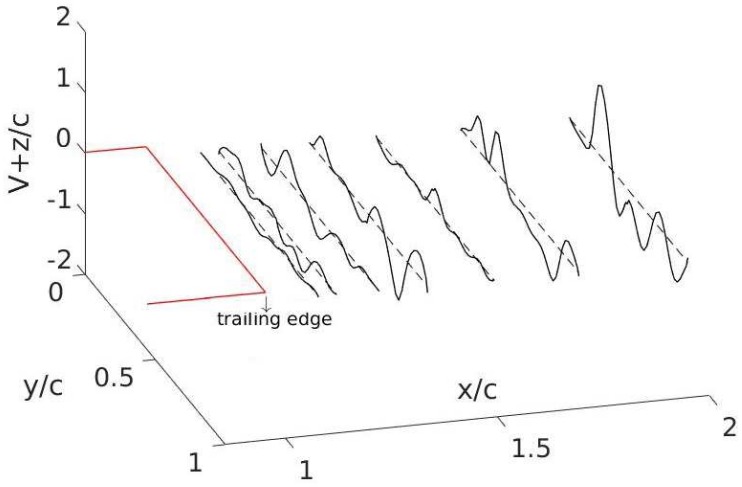

Figure 4.7: *Spanwise velocity component along the wake by means of numerical simulation; the 3D effects result to spanwise predominant wavelengths that are fractions of the chord.*

it reaches trailing edge and separates. Furthermore, the unstable upper and lower boundary layers can be seen in Fig. 4.8d. The undulations of the turbulent kinetic energy suggest that the two shear layers present instabilities with different length

scale and are prone to interact with each other.

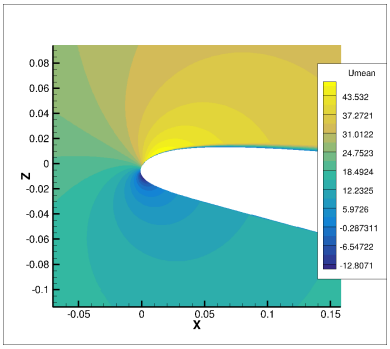

(a) *Time averaged velocity magnitude close to the leading edge.*

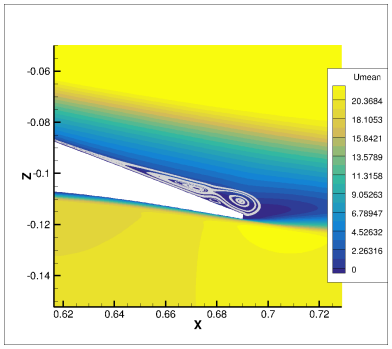

(b) *Time averaged velocity magnitude close to the trailing edge.*

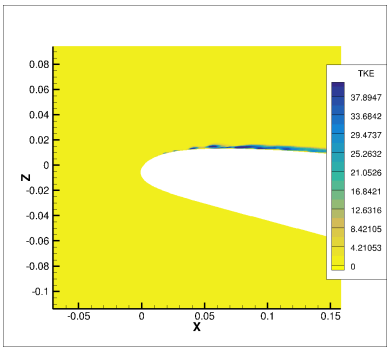

(c) *Ensemble-averaged turbulent kinetic energy close to the leading edge.*

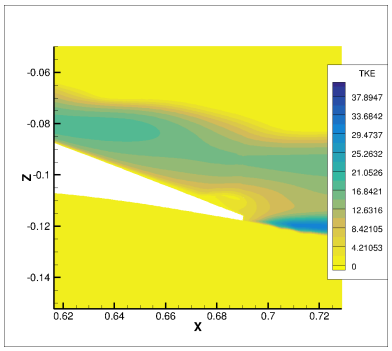

(d) *Ensemble-averaged turbulent kinetic energy close to the trailing edge.*

Figure 4.8: *Contours of velocity and turbulent kinetic energy, 2D simulation with M1 grid for* $Re = 1M$*, angle of attack* $a_o = 10°$*. The detachment is shown by streamlines close to the trailing edge.*

It has been shown (Fig. 4.6) that the flow has a pronounced 3D character. It was mentioned however, that the initial development of the vortical patterns in the wake has a strong apparent two-dimensional behavior. As a result, the main large scale coherent flow dynamics involved in the near-wake development can be accurately captured even by the standard 2D mesh (M1) and are in good agreement with the experimental ones. Figure 4.9 attests to this. The PSD of the vertical velocity signals are superimposed with the experimentally measured signals, for two positions in the wake shown in Fig. 4.9a. The frequency range of the spectral bump is well captured by the numerical simulation, both close to the trailing edge and further downstream in the wake where the alternating shedding is fully developed. Spectral peaks underline the main instabilities in the wake and present larger amlitudes in the simulations.

The vortex structure dynamics and their non-linear interactions are visualized

using streaklines in the wake, pictured in Fig.4.9a. The unstable shear layers develop predominant frequencies close to the trailing edge. As seen in the experiments, the lower and upper shear layers interact with each other yielding a von Kármán vortex street further downstream. The vortex shedding is placed around 214 Hz, which compares well with the value obtained from the experiments. The unstable upper shear layer seems to present oscillation around 170 Hz while the lower shear layer is characterized by a higher frequency (above 370 Hz), also in relatively good agreement with the PIV measurements. All the above mentioned frequencies will be referred to from hereby and after as natural frequencies as they correspond to instabilities that appear naturally in the flow. These mechanisms are also highlighted by the POD performed on the computational results and presented in a later section of this chapter.

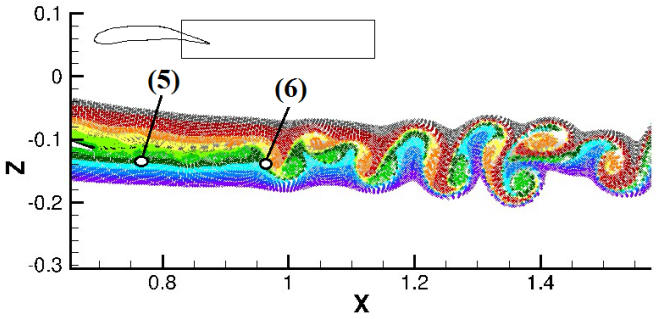

(a) *Position of the monitor points in the computational domain; streaklines where the color of each particle represents its initial positions. Trailing edge tip at* $x = 0.69$, $z = -0.12$*;*

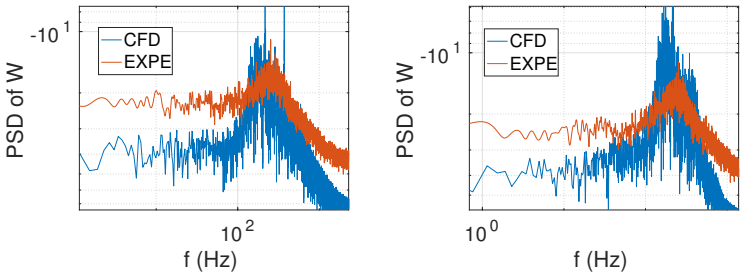

(b) *Spectrum from monitor point 5.* **(c)** *Spectrum from monitor point 6.*

Figure 4.9: *Spectral content of the near wake region, comparison between computational results for the M1 grid and experiments,* $Re = 1M$*, angle of attack* $a_o = 10°$.

Comparisons of the time-averaged velocity profiles along the wake are shown in Fig. 4.10; here, only the longitudinal velocity component is shown for comparison. The velocity profiles are extracted from the simulations in various x/c streamwise locations illustrated in Fig. 4.11a. Comparisons between the 2D and the 3D simulations with the experimentally measured velocity profiles are carried

out. It is recalled here that the reference system used for the comparisons is the one adopted in the simulations. It is demonstrated that the agreement between the measured and computed profiles is quite satisfactory for all the grids tested. Despite the aparent three-dimensional character of the flow, the 2D simulations accurately predict the flow field. The wake expansion is well captured and only at the latest position the velocity deficit is slightly overestimated. With this comparison it is evidenced that besides the dynamic flow behavior, the mean flow is well captured even with the M1 grid.

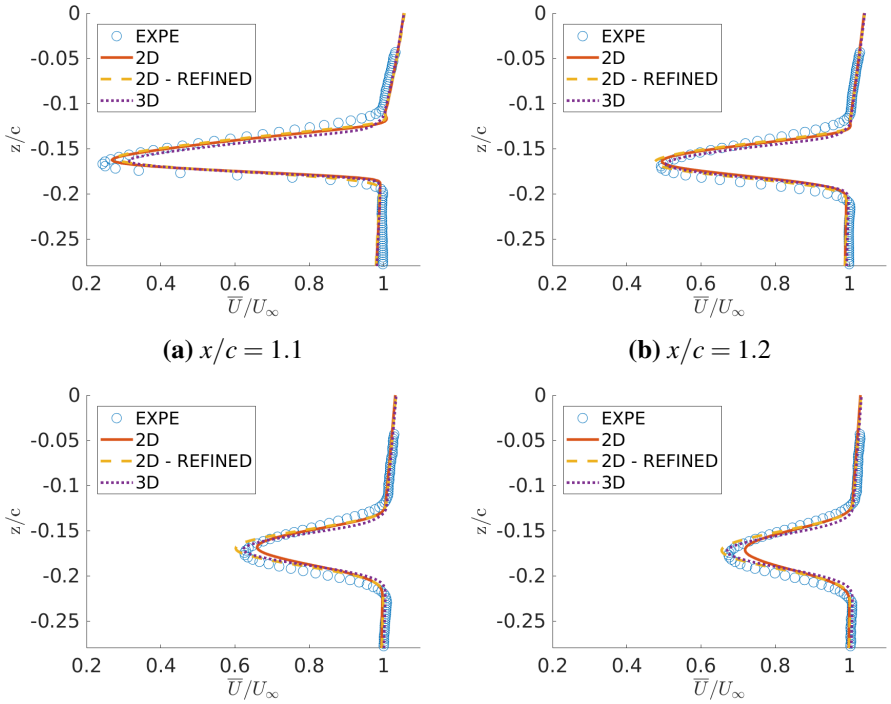

(a) $x/c = 1.1$ **(b)** $x/c = 1.2$

(c) $x/c = 1.3$ **(d)** $x/c = 1.35$

Figure 4.10: *Comparison of longitudinal time-averaged velocity profiles along the wake for Re = 1M, angle of attack $a_o = 10°$; computations with the M1 mesh (2D), the refined M2 mesh (2D-REFINED) and the M3 mesh (3D) are compared with the TRPIV results (EXPE).*

In Figs. 4.11b and 4.11c, characteristic wake values are compared for the various numerical tests and the experiments. The calculation for the displacement δ^* and momentum thickness θ in the wake are calculated from:

$$\delta^* = \int_{z_{99\%}^{low}}^{z_{99\%}^{up}} (1 - \frac{u}{u_{99\%}}) dz \tag{4.2}$$

and:

$$\theta = \int_{z_{99\%}^{low}}^{z_{99\%}^{up}} \frac{u}{u_{99\%}} (1 - \frac{u}{u_{99\%}}) dz \tag{4.3}$$

where $u_{99\%} = 0.99 \cdot U_{inlet}$ and $z^*_{99\%}$ the vertical positions along the wake where $u_{99\%}$ is found. The superscript low and up refer to the lower and upper shear layer position respectively. The displacement thickness δ is accurately predicted with the three different grids as shown in Fig. 4.11b. The momentum thickness which is closely related to the forces is shown in Fig. 4.11c. A better agreement is observed for the refined mesh M2 but overall all the computations present a reasonable agreement.

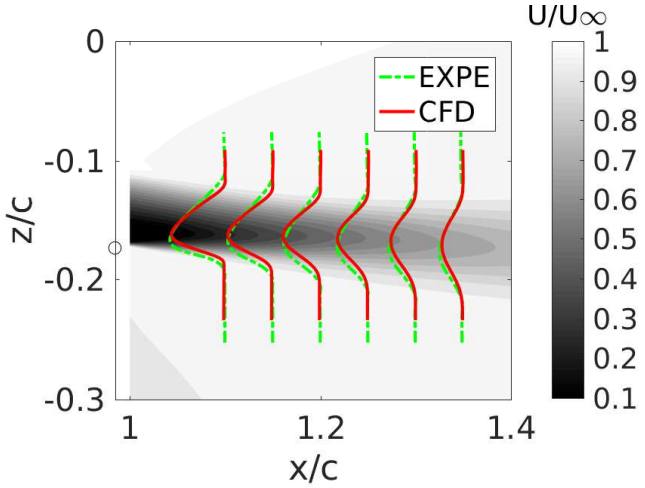

(a) *Time-averaged longitudinal velocity profiles; comparison between the computations for the M1 grid and the experimental results. Trailing edge marked with a hollow circle.*

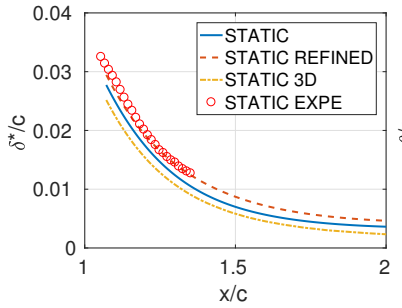

(b) *Displacement thickness.*

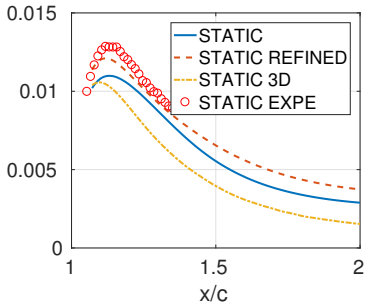

(c) *Momentum thickness.*

Figure 4.11: *Quantitative comparison of the computations for the M1 mesh (STATIC), the refined M2 mesh (STATIC-REFINED) and the M3 mesh (STATIC 3D) with the TRPIV results (STATIC EXPE).*

For the validation of the static case (i.e. when no morphing is applied), 2D and 3D simulations were carried out with the M1, M2 and M3 grids. In the sections that follow, morphing tests are carried out. The HFVTE actuation is examined in this chapter of the thesis. A two-dimensional multi-parametric study is carried out, in order to assess the optimal frequency and amplitude ranges - with respect to

the aerodynamic performance - at a moderate CPU time. As it was demonstrated, the comparison between 3D and 2D simulations justify using a two-dimensional parametric study in order to describe the morphing effects. The 3D morphing effects are also discussed.

At a given camber, the vibrating trailing edge is expected to create small-scale turbulent eddies and add kinetic energy in the wake, which in return causes interactions in the upper and lower shear layer. This aims at enhancing the supercritical character of the flow and produce an eddy-blocking effect constricting and strengthening (shielding) the shear layers in order to achieve narrower wakes [JMS+17]. This eddy-blocking concept was first put into evidence experimentally in [SCR+15]. This shear sheltering effect produced, leads to a considerable thinning of the separated shear layers, as shown in [SGJG+15]. The thinning of the wake region as well as feedback effects through vorticity, enable an increase of lift and the attenuation of noise sources. In the present study the same phenomena will be examined, achieved by the HFVTE morphing actuation.

4.5 Electroactive actuation of the trailing edge

The HFVTE system on the prototype is designed to reach amplitudes up to one millimeter. The technical characteristics for the electro-active hybrid morphing actuation are extensively described in [SCR+15] and [GSR+15]. For more details the reader can also refer to Section 1.2.2. The motion and low-strain deformation of the near-trailing edge region due to the $L_p = 35mm$ long MFC piezo-actuators vibrating is also applied in the numerical simulations. This section includes both experimental and computational results in that order, following a similar organization to the previous section.

4.5.1 Experimental analysis of the morphing

For the investigation of the morphing results, a different window for the TRPIV measurements will be studied. The image acquisition takes place at a more upstream area, in a region that includes the trailing edge. The morphing frequency is increased progressively and the modifications in the dynamics are then qualitatively compared with the numerical investigations that follow. Visualizations by steaklines are examined in Fig. 4.12 to highlight the different flow structures witnessed due to the high-frequency vibration applied on the trailing edge. As mentioned in a previous section, the streaklines are produced by numerically adding points in post-processing; this time, blue seeds are emitted from the pressure side while red ones from the suction side covering the respective boundary and shear layers. Black colored seeds used in the first and last figure are placed close to the separation point in order to highlight possible sharp TT interfaces. The results presented in Fig. 4.12 correspond to a $Re = 500000$ allowing only for a qualitative comparison with the numerical computations which are carried out for a higher Reynolds number.

The non-actuated case (Fig. 4.12a) serves as a reference; then the morphing frequency is varied taking increasingly larger values (i.e. $0 < f_1 < f_2 < f_3$). The frequencies presented in Figs. 4.12b-4.12d are sufficiently spaced and each one of them is specifically selected as it prompts different effects in the wake. Starting at a low actuation frequency $f_1 = 55Hz$, no apparent effects in the coherent wake dynamics are visible. A higher frequency $f_2 = 110Hz$ leads to a change in the modes in the wake (Fig. 4.12c) as the natural shedding frequency is approached. An alternating pattern is formed and a von Kármán sheet is shaped downstream of the wing, tracking the actuation frequency. Finally, applying an even higher frequency $f_3 = 220Hz$, the dynamics change once more. The lower shear layer instability gets reinforced as its natural frequency is approached by f_3 and is locked to the actuation frequency as it can be seen in Fig. 4.12d. Smaller energetic vortices are convected downstream and the upper shear layer instability seems to be blocked from the lower shear layer as they no longer strongly interact with each other. The wake remains thin as it depends on the size of the newly created turbulent structures. These mechanics will be observed also in the simulation in the following sections; the actuation frequencies will be shifted however to higher values, conformal to the increase of the natural frequency due to the higher Reynolds number (1 million in the simulations).

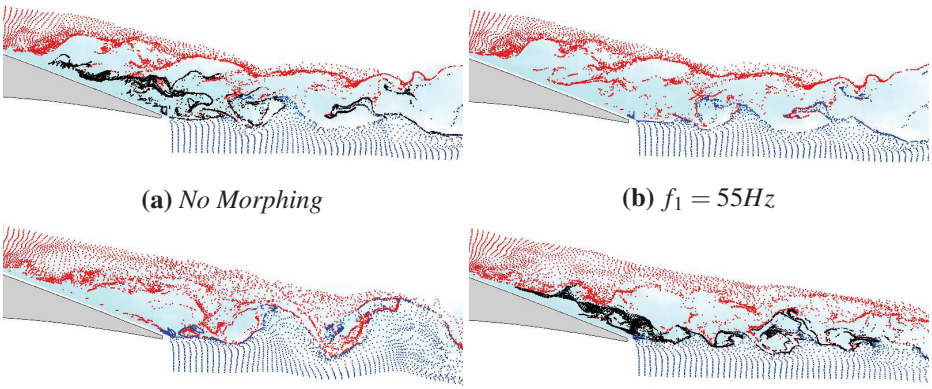

(a) *No Morphing* **(b)** $f_1 = 55Hz$

(c) $f_2 = 110Hz$ **(d)** $f_3 = 220Hz$

Figure 4.12: *Development of vortices in the wake, visualization with streaklines, TRPIV measurements for various actuation frequencies.*

Black color seeding has been added in Fig. 4.12a for the non-morphed and in Fig. 4.12d for last actuation case in order to suport the explanation of the mechanisms involved. As the upper and lower seeding highlight the TNT interfaces, the black seeding seems to follow an existing TT interface developed between the two. The latter interface is created due to the shear caused by the detachment of the flow. This interface is manipulated by the morphing applied on the trailing edge and could possibly act as a thin layer that de-correlates the two TNT interfaces. It has been proven in [IOH15] that interfacial shear layers tend to act in this way.

It is also hypothesized that this interface strengthens the low shear layer with which it correlates since the actuation frequency is high enough. As a result, it blocks the interactions and perturbations coming from the upper shear, it shields the lower-shear vortices which are reinforced and keeps them unaltered as they propagate downstream. This could as well be a clear manifestation of eddy blocking phenomena taking place and preventing the generation of larger turbulent structures in the wake, as seen for example in the static case.

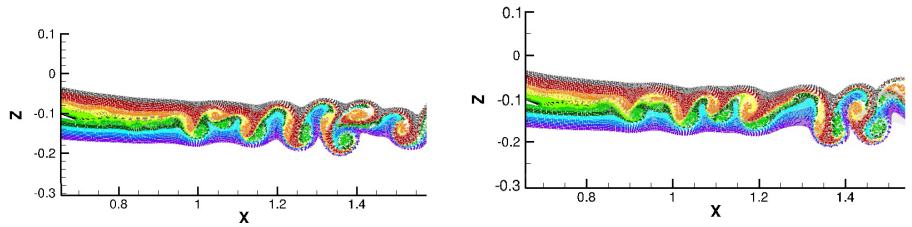

(a) *No Morphing*

(b) $f_a = 60Hz$

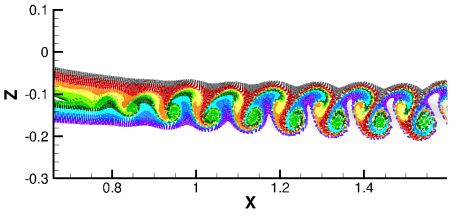

(c) $f_a = 200Hz$

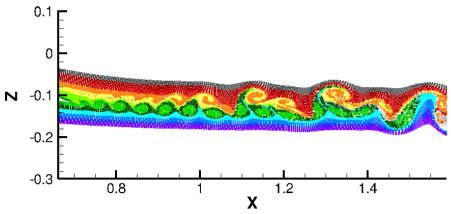

(d) $f_a = 300Hz$

Figure 4.13: *Development of vortices in the wake by means of numerical simulation, visualization with streaklines; the color of each particle represents its initial positions. The amplitude is* $0.35mm$ *for every actuating frequency.*

4.5.2 Numerical investigation of wake dynamics

The same analysis is carried out here for the numerical simulations. Morphing has prominent effects on the development of vortices in the wake. In this first part of the analysis, the amplitude of the vibration was held constant at $0.35mm$ while different values for the actuation frequency f_a were tested. This amplitude value was chosen as it was the largest one to be tested during the first series of experiments with this specific morphing implementation. The actuation patch length was also held constant at $L_p = 35mm$, equal to the length of the actual piezoelectric patches used in the experiments. A complete parametric study of the morphing effects that these characteristic length scales (i.e. amplitude and patch length) have will be examined in a following section. In this section, only the M1 grid is examined as it has been proven to provide results that compare well with the experimental data. This will enable a multi-parametric study with reduced computational cost and provide a complete image over the morphing effects achieved with the HFVTE system. The

Reynolds number for the numerical investigation of the morphing effects was 1 million.

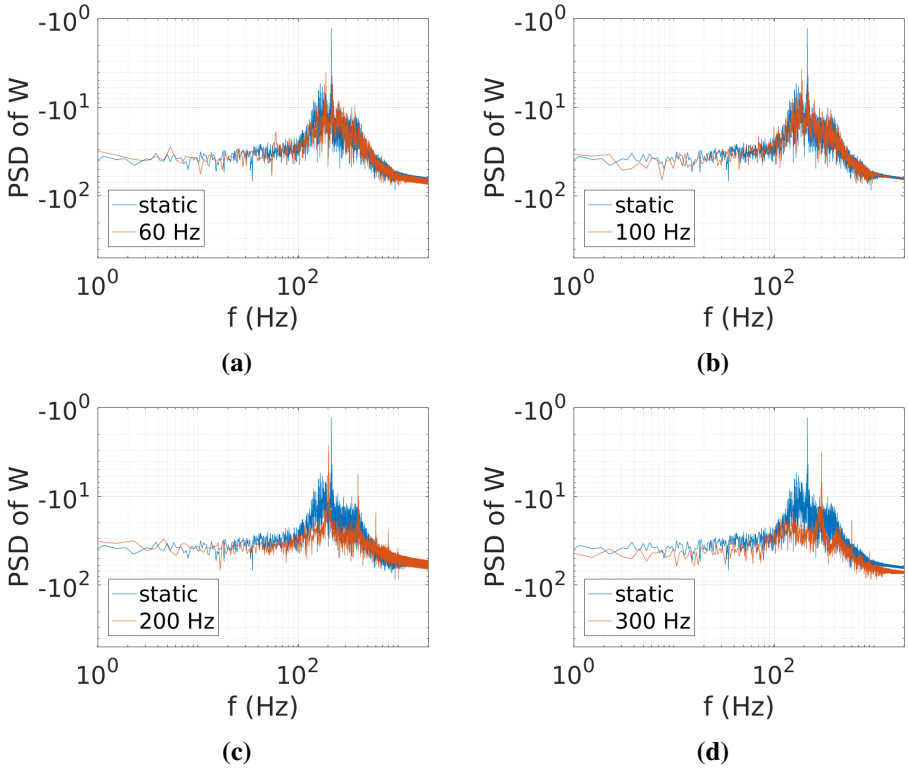

Figure 4.14: *Spectra of the vertical velocity profile in the wake by means of numerical simulation; the case where no morphing is applied (STATIC) is plotted versus various actuating frequencies.*

Visualizations by streaklines, created in the same manner with the experiments, are presented in Fig. 4.13. The effects due to the sinusoidal actuation (figures 4.13b- 4.13d) are compared with the (static) case where no morphing was applied (Fig. 4.13a). Respectively, in Fig. 4.15 contours of the ensemble-averaged $y-$vorticity (axis vertical on the illustrated plane) show the morphing the modifications of the wake dynamics for various frequencies. For frequencies lower than the ones related to the shear layer instabilities and the alternating shedding (e.g. for $f_a = 60Hz$ in Fig. 4.13b, for $f_a = 100Hz$ in Fig. 4.15b), the flow coherent dynamics seem unaffected by the perturbation travelling at a much lower propagation speed, in accordance with the experimental investigation. The irregular character of the flow is still prevailing. For an actuation close to the von Kármán shedding frequency $(f_a = 200Hz)$, resonance phenomena take place. As seen also in Fig. 4.12c, the alternating vortex shedding "locks" onto the morphing frequency, non-linear interactions are suppressed and large, coherent, highly energetic structures are developed creating a vortex sheet. This was first suggested in [GWS89] where the receptivity

of the flow in the wake of an airfoil was studied. It was proven that for a frequency range (namely the "locking range") close to the natural frequency, the measured velocity signals presented a uniform time series, a suppression of irregularities and an energy increase of the fluctuations. The width of this range was dependent on the amplitude of the input power for the forcing. In our numerical experiments, this dependency was not observed. By further increasing the actiation frequency $(f_a = 300Hz)$, smaller vortices are generated in the lower shear region and are convected further downstream. These high-momentum vortices are reinforced and shielded due to the morphing and as a result they tend to remain intact ignoring the influence of the upper shear layer. The interaction with the latter is downgraded resulting to the suppression of the alternating sheading until way further downstream, in accordance with the TRPIV results. The forced lower shear layer undergoes a merging process that leads to the halving of its frequency and an alternating pattern is emitted at this halved frequency after $x = 1.4m$. As a result, the wake regions remains much thinner for a longer distance downstream of the wing.

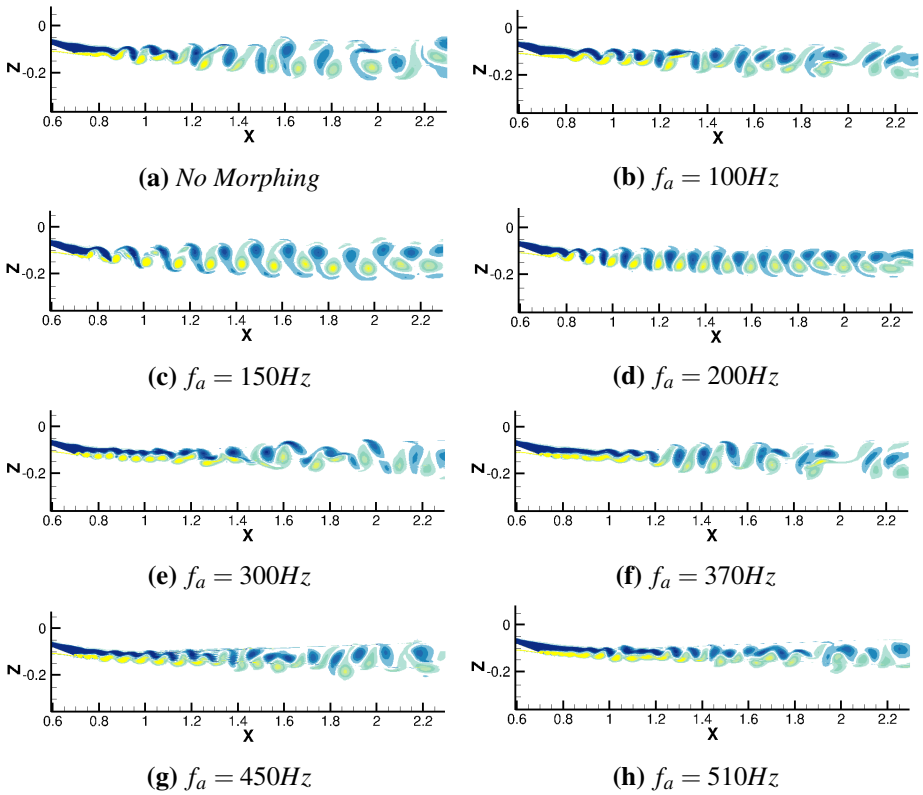

(a) *No Morphing* **(b)** $f_a = 100Hz$

(c) $f_a = 150Hz$ **(d)** $f_a = 200Hz$

(e) $f_a = 300Hz$ **(f)** $f_a = 370Hz$

(g) $f_a = 450Hz$ **(h)** $f_a = 510Hz$

Figure 4.15: *Development of vortices in the wake by means of numerical simulation, visualization with the ensemble-averaged $y-$vorticity. The amplitude is set at* $0.35mm$ *for every actuating frequency.*

This behavior is highlighted in the spectra plotted in Fig. 4.14 where the Fast

Fourier Transformation (FFT) of the vertical velocity signals is computed. The signals are acquired for the same point in the wake for various morphing cases and are compared to the signal acquired for the static case. For lower actuating frequencies (figures 4.14a and 4.14b) the spectral content of the non-morphed case seems almost unaffected. The frequencies naturally existing in the flow continue to guide the formation of vortices. The energy of the actuation is not receipted by the flow and the power of the morphing frequency remains in low levels. In contrast, for the higher frequencies tested (figures 4.14c and 4.14d) the wide bump seen in the static case is replaced by a redistribution of the energy of the flow in the harmonics of the actuation frequency. The natural frequencies are suppresed and replaced by these harmonics.

A complete image on the morphing affects with respect to the wake dynamics is deducted considering Fig. 4.15. Snapshots of the ensemble-averaged $y-$vorticity contours are extracted to highlight the vortex interactions in the wake. Due to the nature of the turbulent spectrum, it is interesting to go over the morphing effects by sweeping over a wide range of frequencies. For $f_a = 100Hz$ no apparent effect in the dynamics is visible. Supporting the remarks previously made, the irregular character of the flow is prevailing. Applying the morphing at $f_a = 150Hz$ (see Fig. 4.15c) and approaching the spectral bump (i.e. the upper shear layer instability), the actuation frequency becomes enhanced and takes over the shear layer development, leading to a regular alternating pattern immediately after in the wake. The flow dynamics track the forcing frequency, irregularities are suppressed and the upper shear layer is reinforced. Increasing the f_a further, and moving away from the spectral bump of natural frequencies, weakens the "locking mechanism" and irregularities start to reappear closer to the wing (see Fig. 4.15f). Actuating at $f_a = 450Hz$ brings back the "lock-in" phenomena since it acts as the harmonic of a natural frequency. For this frequency however, the wake region remains thinner as smaller, faster structures are developed. Further increasing the frequency once again leads to a change in the flow mode, the low shear layer gets mainly affected and guides the wake development.

POD analysis

The Snapshot POD (see Appendix A) is applied here on the computational results for the two components (longitudinal and vertical) of the velocity field. By using the velocity field for the POD, there is a direct correspondence between the eigenvalues provided by the method and the kinetic energy of the flow. Two cases are examined here: the static one where no morphing is applied and the actuation at $300Hz$ where prominent effects in the wake development were observed and a change in the nature of the flow modes. In both cases the sampling rate was taken constant ($10^{-4}sec$) and a series with the same number of successive snapshots (619) was used to construct the POD data matrix, providing a time duration that covers multiple periods of the principal flow phenomena.

In Fig. 4.16a the eigenvalues of the respective modes are plotted for the two

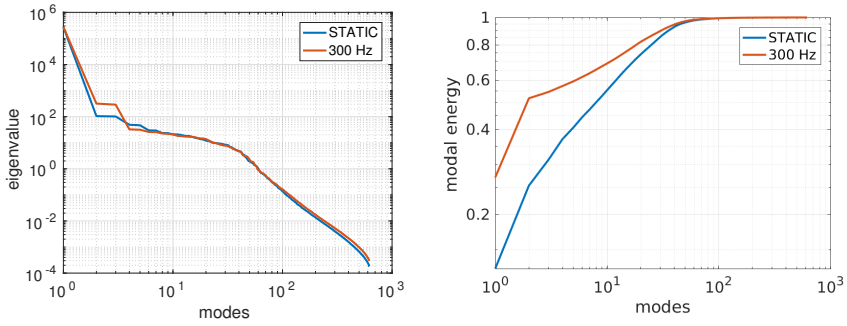

(a) *Sorting of eigenvalues.* **(b)** *Cumulative fluctuating energy.*

Figure 4.16: *Eigenvalues of the modes sorted by the method (left) and relative cumulative energy (right) corresponding only to the fluctuating part of the flow, predicted by means of numerical simulation.*

cases. The first mode corresponds to the mean flow and exhibits the highest values since it represents the biggest portion of the flow's kinetic energy. Higher-order modes have smaller relative importance and they represent an increasingly diminishing part of the energy of the flow. Taking into account the modes corresponding only to the fluctuating part of the flow, Fig. 4.16b is recreated. It can be deduced that less than 60 modes cover 98% of the fluctuating energy. Due to the high Reynolds number and the irregular flow dynamics, the energy is spred over multiple modes. The energy levels of the first few fluctuating modes are increased with the morphing and the slope of the cumulative fluctuating energy is reduced, attesting to the weakening of flow irregularities and the reinforcement of the first modes. While the energy of the mean modes is in the same level (less than 1% difference) between the two cases, the total fluctuating energy is significantly increased with the morphing since highly energetic modes are developed due to the receptivity of the flow to the morphing.

The spatial as well as the temporal behavior of the modes is significantly different between the two cases as it was expected from previously discussed results. This is exhibited in figures 4.17 and 4.18 where the spatial distribution of selected modes is plotted in the wake region. The modes coming from the horizontal and the vertical velocity components are noted as U_n and W_n respectively, where n denotes the order of the mode. Alongside, the FFT of the respective temporal coefficient a_n is also presented of each mode to provide a correspondence to the frequency analysis that preceded. For the case where no morphing is applied (Fig. 4.17), the modes 2 (coupled with mode 3) and 4 (coupled with mode 5) correspond to the initial instability and the alternating shedding respectively, as they have been evaluated in the spectral analysis. The coupling of the modes in pairs is due to the use of both velocity components in the POD calculation. Mode 6 presents modulations of the shedding due to non-linear interactions and irregularities. Higher modes (ommitted here) also correlate with modulations and low frequency feedback effects. Mode

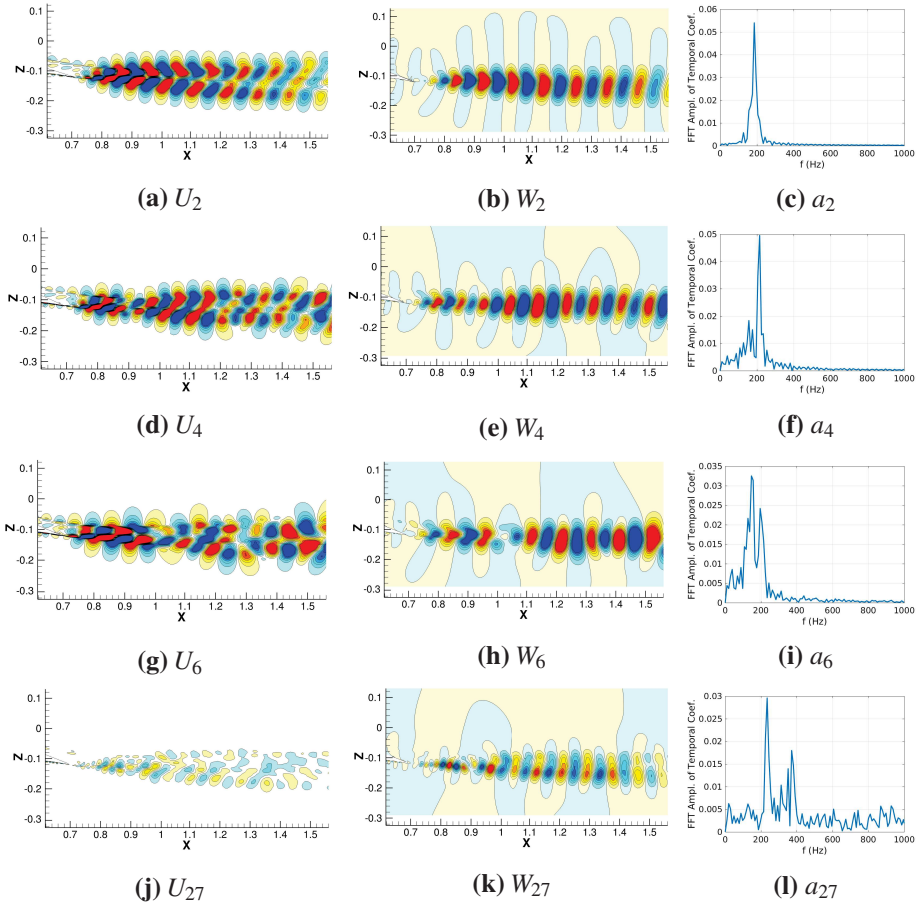

(a) U_2 **(b)** W_2 **(c)** a_2

(d) U_4 **(e)** W_4 **(f)** a_4

(g) U_6 **(h)** W_6 **(i)** a_6

(j) U_{27} **(k)** W_{27} **(l)** a_{27}

Figure 4.17: *Spatial modes computed with the POD of the two velocity components and FFT of the respective temporal coefficients. Indices provide the order of the mode. Case without morphing by means of numerical simulation.*

27 indicates the low shear layer instability pattern. A frequency close to $350Hz$ is prominent in this region and interacts with the shedding frequency also visible in the spectrum. This instability could be related to a separation bubble created on the pressure side, close to the trailing edge, due to the (supercritical) shape of the A320 wing. Modes of even higher order (above 50) are related to smaller scale fluctuations in the wake that present a more chaotic - less coherent - nature.

Considering the morphing case (Fig. 4.18), modifications are present. Mode 2 (coupled with mode 3) corresponds to the reinforced shear layer close to the trailing edge. The temporal coefficient presents a variation locked to the actuating frequency ($300Hz$) while the spectrum of mode 4 (coupled with mode 5) relates to the secondary instability (after merging) that takes place at a frequency with half of this value. In this case, the von Kármán shedding takes over further downstream and is contained to a less wide region as the whole wake becomes thinner. This change

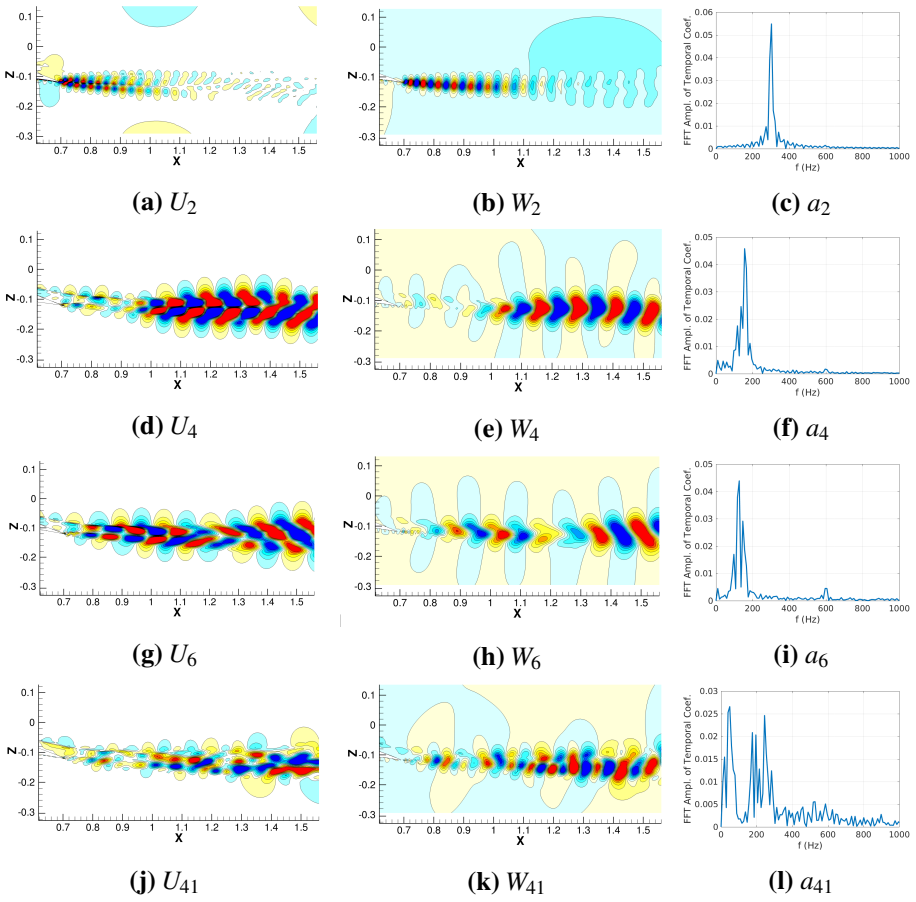

(a) U_2 **(b)** W_2 **(c)** a_2

(d) U_4 **(e)** W_4 **(f)** a_4

(g) U_6 **(h)** W_6 **(i)** a_6

(j) U_{41} **(k)** W_{41} **(l)** a_{41}

Figure 4.18: *Spatial modes computed with the POD of the two velocity components and FFT of the respective temporal coefficients. Indices provide the order of the mode. Morphing case at* $300Hz$ *by means of numerical simulation.*

in the wake form is directly associated with the enhancement of the aerodynamic performance analysed in a following section. Modulations of the instabilities occur, indicating however a move to different and narrower frequency range (Mode 6) while harmonics of the actuation frequency appear as well in higher modes (ommitted here) causing further interactions. In mode 41, a structure resembling the one of mode 27 of the non-morphed case appears, attesting to the displacement of irregularities to lower energy ranks. As the energy of the fluctuations increases, previous modes are shifted in regions of relatively lower order. The predominant frequency at $350Hz$ appearing previously has vanished as it was replaced by the actuation that has moved to a higher modal rank.

Using the modal shapes and the temporal coefficients it is possible to reconstruct portions of the flow corresponding to different instabilities (see Eq. A.1 in the Appendix). This will assist this study as it provides a direct correspondence

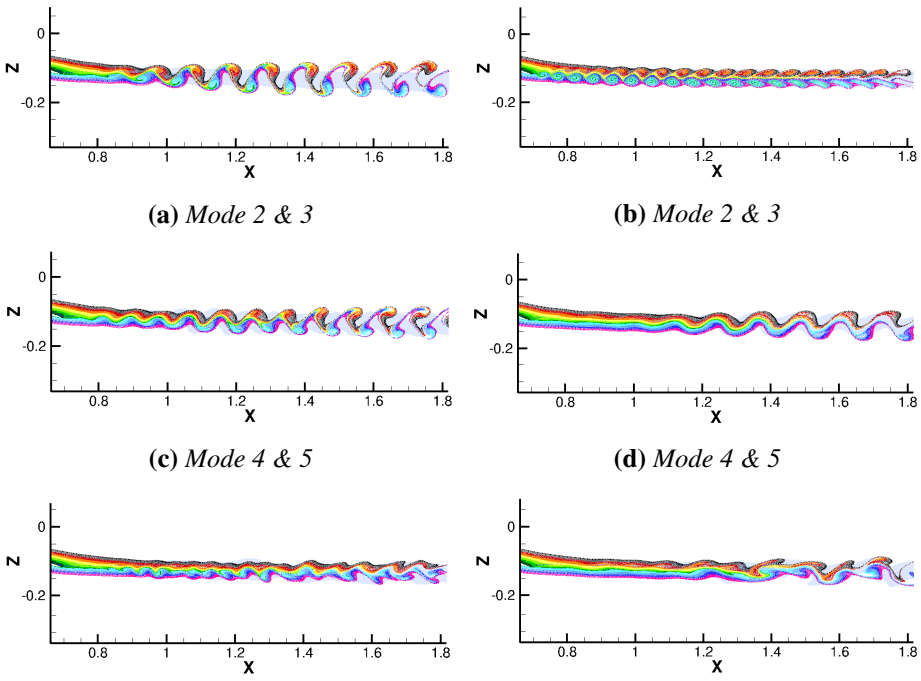

(a) *Mode 2 & 3* **(b)** *Mode 2 & 3*

(c) *Mode 4 & 5* **(d)** *Mode 4 & 5*

(e) *Higher Modes* **(f)** *Higher Modes*

Figure 4.19: *Development of vortical structures in the wake by means of numerical simulation, visualization with streaklines; the color of each particle represents its initial positions. Reconstruction from POD modes along with mean for STATIC (left) and* 300 *Hz (right).*

between the modes and the nature of the vortical structures in the wake, supporting the previous remarks. The eddy blocking procedure can be highlighted through the change in the modal dynamics. It will also provide an overview of how flow instabilities are born and develop in space and time. In Fig. 4.19 a reconstruction was carried out using specific modes added to the first one representing the mean flow. This recreates the flow development in the wake. The static flow case (left column) is examined along with the morphing case (right column). In Fig. 4.20, a cumulative reconstruction is presented where the addition of more high-order modes, i.e. additional irregular flow phenomena, results in a more accurate representation of the flow .

In figures 4.19a and 4.19c the reconstruction of the modes provides a representation of the von Kármán and the upper shear layer instability respectively for the case where no morphing is applied. The signature of the von Kármán is prominent close to the wing. Undulations resulting from the unstable upper layer are convected downstream and influence the alternating pattern. Higher-order modes (above 20) are presented in Fig. 4.19e; they recreate the low shear layer instability. Applying morphing at an actuation frequency $300Hz$ changes completely the first pair of

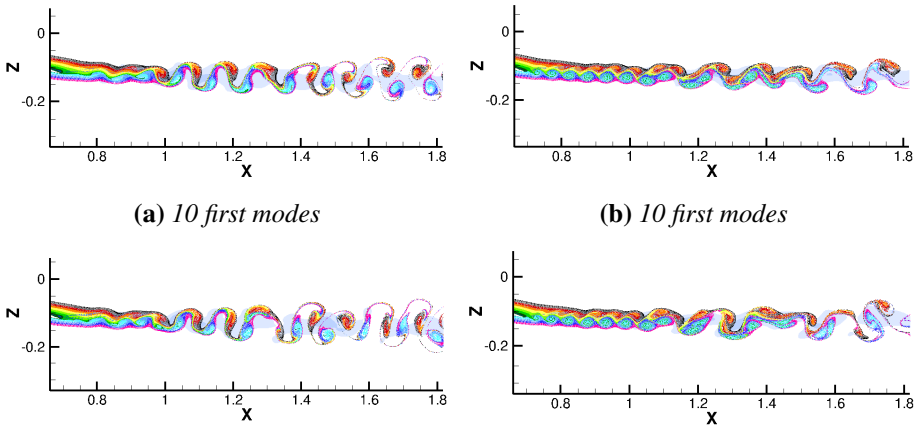

(a) *10 first modes* **(b)** *10 first modes*

(c) *40 first modes* **(d)** *40 first modes*

Figure 4.20: *Development of vortical structures in the wake by means of numerical simulation, visualization with streaklines; the color of each particle represents its initial positions. Reconstruction from POD modes for STATIC (left) and* 300 Hz *(right).*

modes. A low shear layer develops (Fig. 4.19b) and is convected downstream. The wake regions remains thin. The instability tracks perfectly the actuation frequency, something that can also be evidenced in Fig. 4.19f from the disappearance of the low shear layer previously disposed in higher modes. The vortex pairing mechanism seems to take place after $x = 1.2m$ as it can be seen in Fig. 4.19d where the halving of the frequency takes place. This results to an alternating pattern that develops further away from the wing and is absolutely locked to the half of the actuation frequency. The effects of the modal changes and the mechanisms described are highlighted in the collective reconstructions presented in Figs.4.20a and 4.20b. Figures 4.20c and 4.20d add the high-order irregular phenomena in the flow. As it was mentioned reviously, the flow dynamics are represented effectively even with a reduced number of modes.

Mean wake analysis

In this section, a comparison through time-averaged results is carried out. In Fig. 4.21 the mean longitudinal velocity profiles are plotted along the wake for various x/c streamwise positions (previously illustrated in Fig. 4.11a). It it recalled here that the $z/c = x/c = 0$ position corresponds to the leading edge of the wing. It is observed that for frequencies lower than the ones naturally existing in the flow (e.g. for $60Hz$ and $100Hz$), only minor changes are visible in the profiles and mostly at early x/c stages, i.e. really close to the trailing edge. For an actuation frequency close to the natural one ($200Hz$), the wake is slightly displaced downwards and becomes wider. For a higher frequency ($300Hz$), a much thinner wake is visible. As

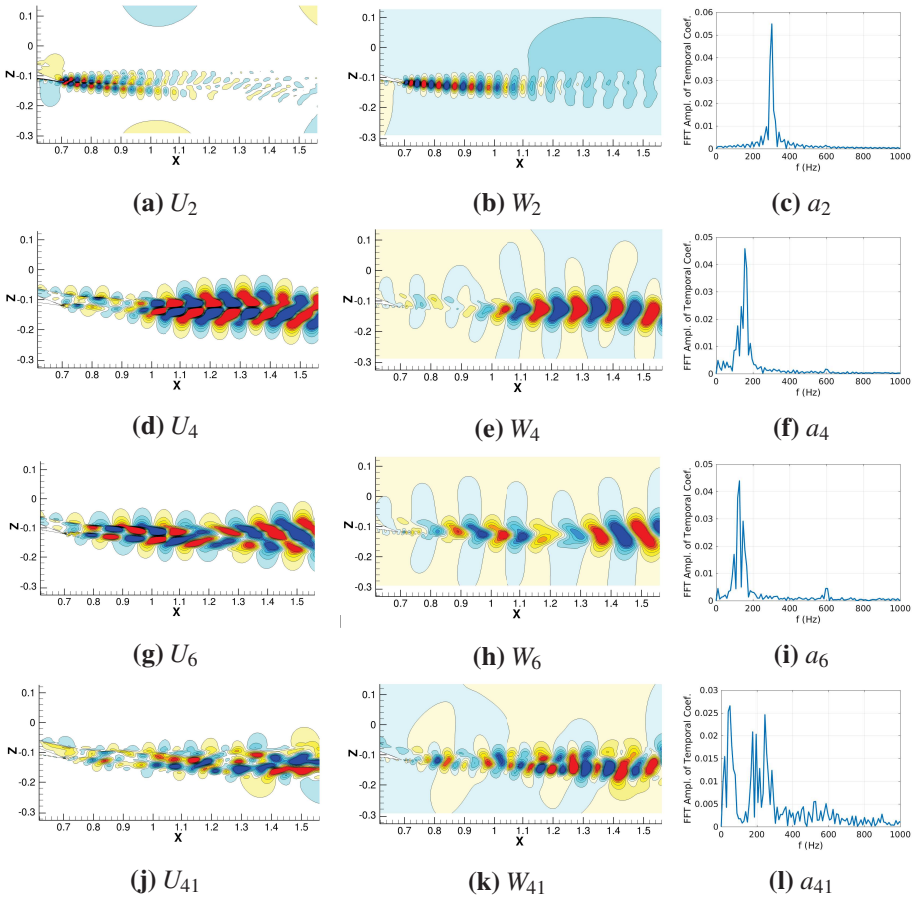

(a) U_2 **(b)** W_2 **(c)** a_2

(d) U_4 **(e)** W_4 **(f)** a_4

(g) U_6 **(h)** W_6 **(i)** a_6

(j) U_{41} **(k)** W_{41} **(l)** a_{41}

Figure 4.18: *Spatial modes computed with the POD of the two velocity components and FFT of the respective temporal coefficients. Indices provide the order of the mode. Morphing case at* $300Hz$ *by means of numerical simulation.*

in the wake form is directly associated with the enhancement of the aerodynamic performance analysed in a following section. Modulations of the instabilities occur, indicating however a move to different and narrower frequency range (Mode 6) while harmonics of the actuation frequency appear as well in higher modes (ommitted here) causing further interactions. In mode 41, a structure resembling the one of mode 27 of the non-morphed case appears, attesting to the displacement of irregularities to lower energy ranks. As the energy of the fluctuations increases, previous modes are shifted in regions of relatively lower order. The predominant frequency at $350Hz$ appearing previously has vanished as it was replaced by the actuation that has moved to a higher modal rank.

Using the modal shapes and the temporal coefficients it is possible to reconstruct portions of the flow corresponding to different instabilities (see Eq. A.1 in the Appendix). This will assist this study as it provides a direct correspondence

The wake width is calculated from:

$$b_{95\%} = z^{up}_{95\%} - z^{low}_{95\%} \tag{4.4}$$

where $z^*_{95\%}$ the position for which the $u^*_{95\%} = 0.95 \cdot U_{inlet}$ in the upper and lower shear layers respectively. The spreading rate is defined here as the distance from the position where the halving of the inlet velocity is achieved $(z^*_{50\%})$ for each shear layer as well. The momentum thickness θ is computed using eq. 4.22c presented previously while the shearing coefficient r for each shear layer is calculated according to:

$$r_* = \frac{u^*_{95\%} - u^*_{50\%}}{z^*_{95\%} - z^*_{50\%}} \tag{4.5}$$

where as before, $z^*_{95\%}$ and $z^*_{50\%}$ the positions for which $u^*_{95\%} = 0.95 \cdot U_{inlet}$ and $u^*_{50\%} = 0.50 \cdot U_{inlet}$ respectively.

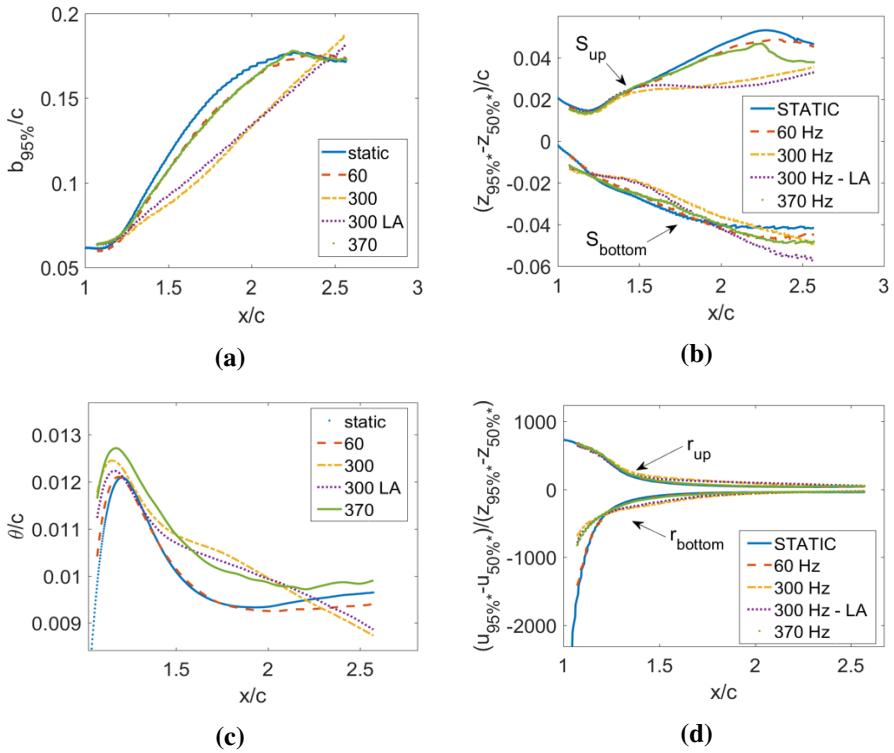

Figure 4.22: *Comparison of the wake characteristics for various actuating frequencies; numerical simulation. (a) Width of the wake (b) Spreading of upper (S_{up}) and lower (S_{bottom}) shear layer (c) momentum thickness and (d) shearing coefficient r; the amplitude is set at 0.35mm for every morphing application besides the 300Hz-LA (lower amplitude) where a value of 0.15 mm was used.*

In Fig. 4.22a the thinning of the wake is observed and it is attributed to the suppression of the shedding. Only minor variations are present for the actuation

frequency of $60Hz$. A linear expansion of the wake is achieved for the $300Hz$ actuation frequency, for both amplitudes tested; this linear expansion suggests more self-similar profiles. Increasing the frequency to even higher values (i.e. $370Hz$) weakens this shedding delay and the expansion returns to what has been seen for lower frequencies. This was expected from examining the dynamic response of the flow in this morphing actuation. Figure 4.22b shows the decrease of the spreading of the upper shear layer for $300Hz$. The upper shear gets overpowered by the strengthened lower one and the interactions between them are suppressed. The resulting shedding mechanism is delayed as it has been previously shown. Same as before, this mechanism does not exist for the lower frequencies tested and is weakened for the $370Hz$. The results for each shear layer are in good agreement with the investigations in [WW88]. Finallt, the r coefficient presented in Fig. 4.22d exhibits only slight changes while the momentum thickness is always increased since more energy is introduced in the flow.

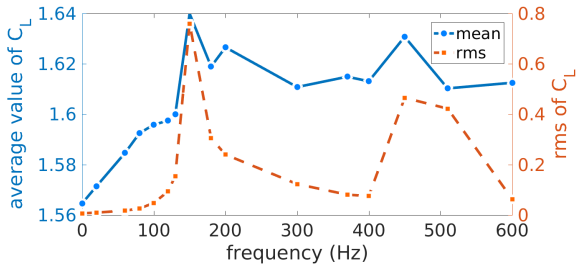

(a) *Lift coefficient*

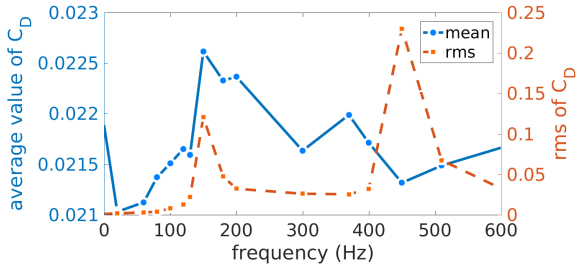

(b) *Drag Coefficient*

Figure 4.23: *Effect on the aerodynamic forces. Frequency variations with a constant amplitude of 0.35mm; zero values for frequency imply absence of morphing.*

4.5.3 Morphing benefits

The effect on the aerodynamic forces is evaluated in this section. The lift and drag coefficients are compared in Fig. 4.23. In Fig. 4.23a and 4.23b the effect of the actuation frequency is presented for a constant amplitude of $0.35mm$. Actuating in the region around the natural shedding frequency and the upper layer instability (i.e. $150Hz - 200Hz$) presents a prominent increase in both lift and drag mean

values. This is accompanied by a significant increase in the fluctuations if the forces as indicated by the root-mean-squared (*rms*) values. This attests to the resonance observed in the previous section and is also in agreement with the experimental studies included in [GWS89]. Acting with frequencies outside this region still provides an increase in lift and in some cases a decrease in drag. More importantly however, it retains the *rms* in low - acceptable - levels.

Approaching the region of the first harmonic of the shedding frequency, the resonance phenomena reappear. The increase of the *rms* values can be exhibited through distinct peaks that are especially prominent in the drag evolution and clearly indicate the regions where reasonance takes place. The aerodynamic efficiency, expressed by the c_L/c_D ratio is always increases with the morphing. The flapping of the trailing edge increases the energy attributed to the flow and produces a higher-incidence effect resuling to the lift increase. These frequency ranges are related to the Re number of the flow; the morphing range should take into account the flow regime and adapt accordingly. Finally it should be mentioned that in all morphing cases, the increased aerodynamic performance could not be achieved with a static deformation of the trailing edge at the maximum displacements, attesting to the fact that the dynamic nature of the morphing application is responsible for the effects on the forces.

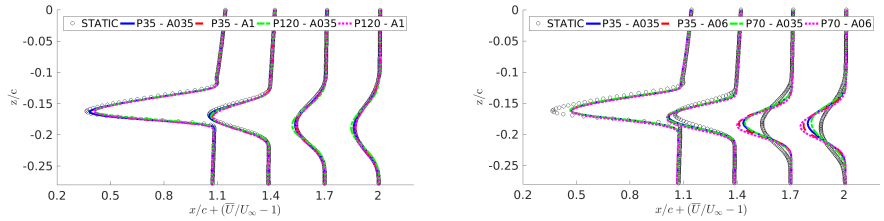

(a) $100Hz$ **(b)** $300Hz$

Figure 4.24: *Comparison of mean longitudinal velocity profiles along the wake for patch lengths $L_p = 35mm$ (P35), $L_p = 70mm$ (P70) and $L_p = 120mm$ (P120); the amplitude effect is also examined with $A_o = 0.35mm$ (A035), $A_o = 0.6mm$ (A06) and $A_o = 1mm$ (A1).*

4.5.4 Morphing Length Scales

In this section, the effects of the characteristic length scales involved in the morphing are analyzed. The amplitude A_o and the length of the actuating patch L_p were examined separately and in combination in regards to the effects they produced at specific actuation frequencies. It is reminded that the amplitude corresponds to the maximum displacement, i.e. the displacement of the end tip of the trailing edge. Two frequencies are examined here, at values both below ($100Hz$) and above ($300Hz$) the natural shedding frequency. The reference case P35, for which $L_p = 35mm$ as in the experiments, was compared with cases where the patch length was increased.

For $f_a = 100Hz$, an $L_p = 120mm$ is tested (P120). Two amplitudes $A_o = 0.35mm$ (A035) and $A_o = 1mm$ (A1) are considered. A lower value of $70mm$ (P70) for the patch length is examined for the frequency $f_a = 300Hz$. The effect of the amplitude is also examined with $A_o = 0.35mm$ (A035) and $A_o = 0.6mm$ (A06).

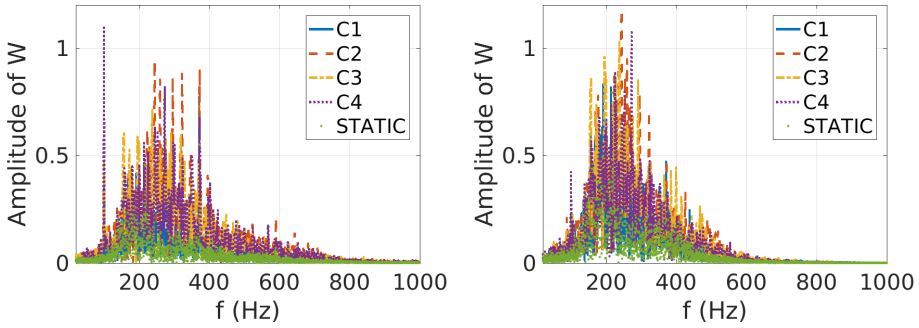

(a) *Spectrum from point 5.* **(b)** *Spectrum from point 6.*

Figure 4.25: *Spectral content of vertical velocity, actuation at* $100Hz$ *for* $Re = 1M$*, angle of attack* $a_o = 10°$*, M1 grid; comparing P35 with A035 (C1), P120 with A035 (C2), P120 with A06 (C3) and P120 with A1 (C4) and no morphing (STATIC).*

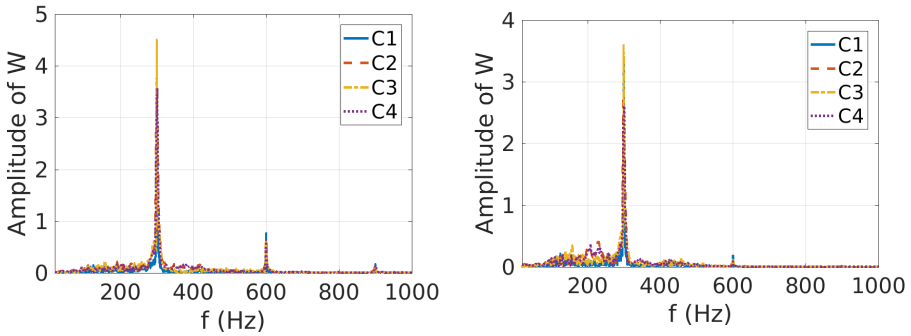

(a) *Spectrum from point 5.* **(b)** *Spectrum from point 6.*

Figure 4.26: *Spectral content of vertical velocity, actuation at* $300Hz$ *for* $Re = 1M$*, angle of attack* $a_o = 10°$*, M1 grid; comparing P35 with* $A_o = 0.35mm$ *(C1), P35 with* $A_o = 0.35mm$ *(C2), P70 with* $A_o = 0.6mm$ *(C3) and P70 with* $A_o = 0.6mm$ *(C4).*

As it is observed in Fig. 4.24, the effect that the patch length has on the mean velocity profiles in the wake region is minimal. Only minor changes are exhibited as the dynamics remain mainly unaffected by the change in the patch length, at least when the actuation amplitude remains the same. Higher actuation amplitudes cause an increased velocity deficit in more downstream positions. In Figs. 4.25 and 4.26 the spectral content in the wake region is examined. An FFT was performed on

the vertical velocity component in the two points mentioned in Fig. 4.9a and the amplitude of the fourier modes is presented. For the lower frequency, the combined patch - amplitude increase seems to intensify the chaotic nature of the flow which receives the whole amount of energy added with the actuation. The amplitude of the frequency bump is increased while the frequency range is not modified. The static case where no morphing was applied is also included in Fig. 4.25 as a reference. The coherent picks identified in the static case are always present in the spectrum for $100Hz$. For the higher actuation frequency, practically no effect is exhibited in the wake dynamics due to the change of the patch - amplitude length scales used in the morphing. The vortex dynamics and the changes examined in the previous section seem depend only on the actuation frequency. Similar to the analysis previously presented, the energy of the flow reorganises in harmonics of the actuation frequency.

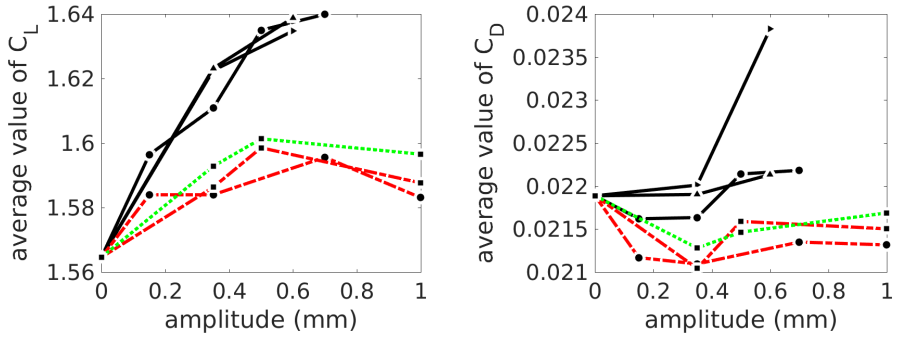

(a) *Lift coefficient* **(b)** *Drag coefficient*

Figure 4.27: *Effect on the mean aerodynamic forces versus amplitude variations for 60Hz (dashed line), 100Hz (dotted line) and* $300Hz$ *(solid line) with P35* (●)*, P120* (■)*, P45* (▲) *and P70* (►)*; zero values amplitudes imply absence of morphing.*

The effect of the patch length and the amplitude variation on the aerodynamic forces is examined in Fig. 4.27. The patch length seems to provide only minor changes for each frequency while the actuation amplitude is increased. The evolution of the forces presents a non-linear behavior with the increase of the amplitude. The lift coefficient increases up to a point and then starts decreasing again. The maximum lift value depends on the actuation frequency and this value gets a higher as the frequency increases. The drag coefficient initially decreases for the lower frequencies and then starts to increase again. After a specific amplitude, the value of the drag seems to be practically constant for the amplitudes examined in this investigation. It is expected however to continue increasing if even higher amplitude values are examined. Whether this plateau is higher or lower than the initial drag value without morphing correlates with the frequency of the actuation. Consequently, it seems as an optimal frequency-amplitude combination exists for

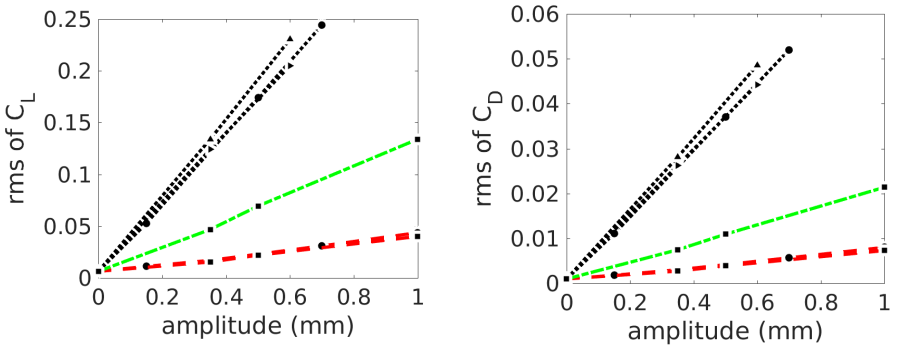

(a) *Lift rms* **(b)** *Drag rms*

Figure 4.28: *Effect on the aerodynamic forces fluctuation versus amplitude variations for 60Hz (dashed line), 100Hz (dash-dot line) and* $300Hz$ *(dotted line) with P35 (●), P120 (■), P45 (▲) and P70 (►); zero values amplitudes imply absence of morphing.*

which a maximum lift - minimum drag ratio can be identified. The fluctuation of the forces is shown in Fig. 4.28. No effect on the *rms* values is exhibited from the variation of the patch length. The amplitude causes a linear response: the *rms* values increase with the amplitude at a constant rate. The slope of the *rms* variation increases with the actuation frequency.

4.5.5 3D Morphing Effects

In this final section the three-dimensional effects of the morphing are analyzed. Only the case with $f_a = 300Hz$ is examined here as it presents prominent modal changes in the wake region. The deformation of the surface due to the electroactive morphing application was uniform along the span of the wing. A 3D view of the morphing effects on the wake can be seen in Fig. 4.29. The Q criterion iso-surface, colored by Mach, is shown along the wing and in the wake region for the identification of the vortices. In the same figure, the vortical structures are also highlighted from streaklines computed on a mid-span slice section.

With the identification of the vortical patterns in the wake it is evidenced that the two-dimensional behavior of the flow is enhanced. Until way further downstream, the vortical tubes generated in the flow remain uniform along the span. The undulated patterns exhibited in the static (non-morphed case) cease to exist and secondary three-dimensional instabilities are suppressed due to the re-orientation of the axes of the vortical structures that naturally emerged in the unforced case. The streamwise vortex tubes - associated with the spanwise velocity fluctuations and the undulations on the iso-surface - are weakened. As a result, the chaotic wake image caused by these interactions is eliminated, at least until further downstream. The new modes emerging in the wake correlate with smaller sized vortices that - as

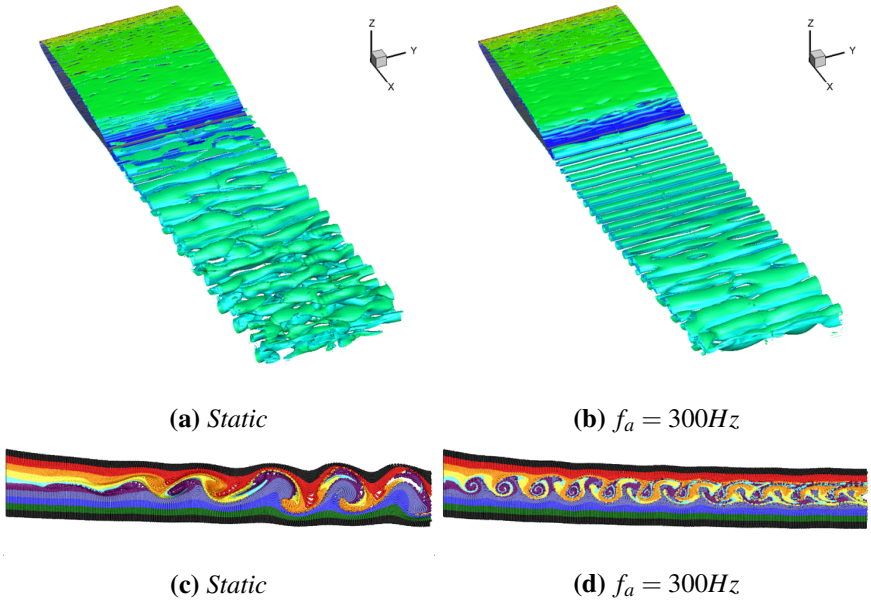

(a) *Static* **(b)** $f_a = 300Hz$

(c) *Static* **(d)** $f_a = 300Hz$

Figure 4.29: *Q criterion iso-surface (top) for* $Q = 1000$ *colored by the Mach value along with streaklines (bottom) in the mid-span section; results for the non-morphing (Static) and the* $300Hz$ *cases.*

evidenced also in the 2D simulations - keep the wake region thinner (see Figs. 4.29c and 4.29d). With the application of the morphing, the velocity fluctuations are suppressed attesting to the two-dimensional behavior witnessed in Fig. 4.29. This is in aggrement with the observations in [OW82]. The authors noted that the turbulent intensity due to the actuation was not significantly affected under the infuelnce of the forcing. On the contrary, the shear layers examined were found to be more orderly than they were naturally and 2D-like due to the redistribution of energy from the whole flow to the modes actuated by the forcing.

4.6 Conclusion

In this chapter, the electroactive morphing effects created by Macro-Fiber Composite piezoelectric patches disposed along the span of an A320 wing have been studied by means of TRPIV and high-fidelity numerical simulations. These actuators introduce optimal vibrations and low-amplitude deformations of the trailing-edge region. Through detailed experimental database and newly acquired computational results, a combined examination of high Reynolds dynamics in the wake of this supercritical wing has been carried out, in respect to the aerodynamic performance. The main flow characteristics have been underlined. Various frequencies and amplitude combinations have been studied numerically to evaluate the morphing effects in order to enable future experiments around the same prototype, focusing on the most

optimal morphing actuations. The actuation frequency has been identified as the main driving factor for the manipulation of the dynamics in the wake.

The wake dynamics are significantly affected by the application of morphing when acting in frequencies close or above the natural frequencies of the separated shear layers. This has been emphasized by the POD analysis. New modes emerge and take the place of naturally existing ones in positions of higher relative energy. It was assessed possible to manipulate the interactions between the different instabilities and control the generation of turbulent structures in the wake. The investigation of mean wake properties has shown a thinning of the far wake region and a suppression of the alternating pattern until later downstream regions. At a given camber, the vibrating trailing edge creates smaller-scale turbulent eddies and adds kinetic energy in the wake which in turn causes interactions in the upper and lower shear layer. This enhances blocking effects, constricts and strengthens the shear layers (shielding), resulting in narrower wakes. The application of the morphing has be proven to suppress three-dimensional secondary instabilities and enhance the two-dimensional behavior of the flow. Thanks to proper high-frequency actuation, suppression of pre-existing predominant instability modes was achieved.

An increase in the aerodynamic performance was achieved through overall surface pressure modifications. The thinning of the wake region as well as feedback effects through the vorticity, enables mainly a lift increase. The aerodynamic performance gets enhanced as the mean value of the lift versus drag is found to be increased in every morphing case examined. By the present electroactive morphing concept, an order of 3.2% increase in lift has been achieved and at the same time a 1% decrease in the drag. The actuations at $60Hz$ and $300Hz$ have both achieved an increase of lift-to-drag ratio of 4%. Optimal frequency ranges were identified suggesting that morphing can be adapted to the flow conditions and the chord of the wing. Similar to the actuation produced by the small feathers at the edges of the wings of the hunting birds, the electroactive morphing is proven capable to achieve similar effects, inspired from the nature and targeting the design of the future wings. As in nature however, the aerodynamic performance can be further enhanced by fully exploiting the hybrid morphing capacities. This entails the combined actuation of different classes of electroactive actuators that, when realized simultaneously, yield modifications of turbulence at multiple scales. To this end, in the following chapter we examine the use of Shape Memory Alloys (SMA) to achieve high deformations at low frequencies imitating the camber effect of large-span birds.

Bibliography

[BFP01] M. Braza, D. Faghani, and H. Persillon. Successive stages and the role of natural vortex dislocations in three-dimensional wake transition. *Journal of Fluid Mechanics*, 439:1–41, July 2001.

[DGH82] J. Donea, S. Giuliani, and J. P. Halleux. An arbitrary lagrangian-eulerian finite element method for transient dynamic fluid-structure

interactions. *Computer Methods in Applied Mechanics and Engineering*, 33(1):689–723, September 1982.

[GSR+15] J. Gurvan, J. Scheller, K. J. Rizzo, E. Duhayon, J. F. Rouchon, and M. Braza. Dimensionnement d'une maquette pour l'investigation du morphing électroactif hybride en soufflerie subsonique. In *22e Congrès Français de Mécanique*, pages 1–13, Lyon, France, 2015. Thanks to the AFM, Association Française de Mécanique.

[GWS89] M. Gharib and K. Williams-Stuber. Experiments on the forced wake of an airfoil. *Journal of Fluid Mechanics*, 208:225–255, November 1989.

[HESW11] J. C. R. Hunt, I. Eames, C. B. da Silva, and J. Westerweel. Interfaces and inhomogeneous turbulence. *Philosophical Transactions of the Royal Society of London A: Mathematical, Physical and Engineering Sciences*, 369(1937):811–832, February 2011.

[HEW08] J. C. R. Hunt, I. Eames, and J. Westerweel. Vortical Interactions with Interfacial Shear Layers. In *IUTAM Symposium on Computational Physics and New Perspectives in Turbulence*, IUTAM Bookseries, pages 331–338. Springer, Dordrecht, 2008.

[HFB+03] Y. Hoarau, D. Faghani, M. Braza, R. Perrin, D. Anne-Archard, and D. Ruiz. Direct Numerical Simulation of the Three-Dimensional Transition to Turbulence in the Incompressible Flow around a Wing. *Flow, Turbulence and Combustion*, 71(1):119–132, March 2003.

[HL95] R. F. Huang and C. L. Lin. Vortex shedding and shear-layer instability of wing at low-Reynolds numbers. *AIAA Journal*, 33(8):1398–1403, 1995.

[HPV+16] Y. Hoarau, D. Pena, J. B. Vos, D. Charbonier, A. Gehri, M. Braza, T. Deloze, and E. Laurendeau. *Recent Developments of the Navier Stokes Multi Block (NSMB) CFD solver*. American Institute of Aeronautics and Astronautics, 2016.

[IOH15] T. Ishihara, H. Ogasawara, and J. C. R. Hunt. Analysis of conditional statistics obtained near the turbulent/non-turbulent interface of turbulent boundary layers. *Journal of Fluids and Structures*, 53:50–57, February 2015.

[JMS+17] G. Jodin, V. Motta, J. Scheller, E. Duhayon, C. Döll, J.F. Rouchon, and M. Braza. Dynamics of a hybrid morphing wing with active open loop vibrating trailing edge by time-resolved PIV and force measures. *Journal of Fluids and Structures*, 74(Supplement C):263–290, October 2017.

[Jod17] G. Jodin. *Hybrid electroactive morphing at real scale - application to Airbus A320 wings*. Phd thesis, Toulouse, INPT, October 2017.

[KBCH87] A. Kourta, M. Braza, P. Chassaing, and H. Haminh. Numerical analysis of a natural and excited two-dimensional mixing layer. *AIAA Journal*, 25(2):279–286, 1987.

[Koo89] M. M. Koochesfahani. Vortical patterns in the wake of an oscillating airfoil. *AIAA Journal*, 27(9):1200–1205, 1989.

[MCW92] B. Marasli, F. H. Champagne, and I. Wygnanski. Effect of travelling waves on the growth of a plane turbulent wake. *Journal of Fluid Mechanics*, 235:511–528, 1992.

[OW82] D. Oster and I. Wygnanski. The forced mixing layer between parallel streams. *Journal of Fluid Mechanics*, 123:91–130, 1982.

[Ros61] A. Roshko. Experiments on the flow past a circular cylinder at very high Reynolds number. *Journal of Fluid Mechanics*, 10(3):345–356, May 1961.

[RT02] N. Reau and A. Tumin. On harmonic perturbations in a turbulent mixing layer. *European Journal of Mechanics - B/Fluids*, 21(2):143–155, January 2002.

[SCR+15] J. Scheller, M. Chinaud, J.F. Rouchon, E. Duhayon, S. Cazin, M. Marchal, and M. Braza. Trailing-edge dynamics of a morphing NACA0012 aileron at high Reynolds number by high-speed PIV. *Journal of Fluids and Structures*, 55(Supplement C):42–51, May 2015.

[SDJ+19] N. Simiriotis, K. Diakakis, G. Jodin, F. Kramer, A. Marouf, Y. Hoarau, J.F. Rouchon, G. Tzabiras, and M. Braza. Synthesis on high-fidelity numerical simulation of a morphing a320 wing in subsonic speeds and sensitivity evaluation. *AIAA Aviation 2019 Forum*, 2019.

[SGJG+15] D. Szubert, F. Grossi, A. Jimenez Garcia, Y. Hoarau, J. C. R. Hunt, and M. Braza. Shock-vortex shear-layer interaction in the transonic flow around a supercritical airfoil at high Reynolds number in buffet conditions. *Journal of Fluids and Structures*, 55:276–302, May 2015.

[SJM+19] N. Simiriotis, G. Jodin, A. Marouf, P. Elyakime, Y. Hoarau, J. C. R. Hunt, J. F. Rouchon, and M. Braza. Morphing of a supercritical wing by means of trailing edge deformation and vibration at high Reynolds numbers: Experimental and numerical investigation. *Journal of Fluids and Structures*, July 2019.

[TTS+10] S. Tarashima, M. Tange, S. Someya, K. Okamoto, and GPU.AIV deformaion. Gpu accelerated direct cross-correlation piv with window

deformation. In *15th Int Symp on Applications of Laser Techniques to Fluid Mechanic*, 2010.

[WCM86] I. Wygnanski, F. Champagne, and B. Marasli. On the large-scale structures in two-dimensional, small-deficit, turbulent wakes. *Journal of Fluid Mechanics*, 168:31–71, 1986.

[WSG90] K. Williams-Stuber and M. Gharib. Transition from order to chaos in the wake of an airfoil. *Journal of Fluid Mechanics*, 213:29–57, 1990.

[WW88] I. Weisbrot and I. Wygnanski. On coherent structures in a highly excited mixing layer. *Journal of Fluid Mechanics*, 195:137–159, 1988.

[YSK06] S. Yarusevych, P. E. Sullivan, and J. G. Kawall. Coherent structures in an airfoil boundary layer and wake at low Reynolds numbers. *Physics of Fluids*, 18(4):044101, 2006.

[YSK09] S. Yarusevych, P. E. Sullivan, and J. G. Kawall. On vortex shedding from an airfoil in low-Reynolds-number flows. *Journal of Fluid Mechanics*, 632:245–271, August 2009.

Chapter 5

Optimal shape control using Shape Memory Alloys

A novel approach for determining optimal configurations for the shape control using Shape Memory Alloy (SMA) actuators is proposed. A robust algorithm is developed and successfully validated to deal with nonlinear structural problems. The proposed methodology is coupled with an optimization code to solve the design problems for smart controllable structures. This problem finds a special application in the morphing of aeronautical structures that are the focus of the present chapter.

5.1 Introduction

The needs of aircraft manufacturers continuously grow along with the interest on the design of innovative smart configurations with multiple actuators. To this end, morphing architectures are widely adopted to maximize the aerodynamic efficiency by introducing smart material into shape control applications. The use of Shape Memory Alloys (SMA) will soon be realistic at an industrial level for aircraft manufacturers as they propose a valid solution coherent with morphing applications and the concept of a green, more electric aircraft. SMAs are material of high power effectiveness (i.e. a modest number of actuators is needed) and reduced volume/weight. There has been a plethora of published works devoted on SMA constitutive models that describe accurately the thermomechanical behavior of the material. A quite extensive review of SMA structures published in [Bir97] includes various model describing the material laws in different levels of fidelity. As a result, SMAs have already been used in various aspects of engineer applications.

The working principle of an aeronautical morphing configuration that employs SMA actuators is illustrated in Fig. 5.1. An airfoil is cambered with the aid of SMA actuators placed on ribs that are connected through hinges with each other. The SMA "tendons" provide the torgue necessary to rotate the platelets in order to deform the flexible skin covering the wing, providing the final deformed shape. Since the SMAs are positioned in pairs in respect to the neutral axis of the structure, the cambered shape can be moved both upwards and downwards and recover its neutral shape fast. The SMA actuating systems can be smartly integrated inside the structure in order to have a minimal impact on the shape of the aircraft and avoid aerodynamic penalties. It is deduced however that the sizing, the positioning of the SMAs and the available space are key issues directly related to the overall cost and the feasibility of the solution. If correctly designed, the SMA actuation results into efficient and cheap concepts.

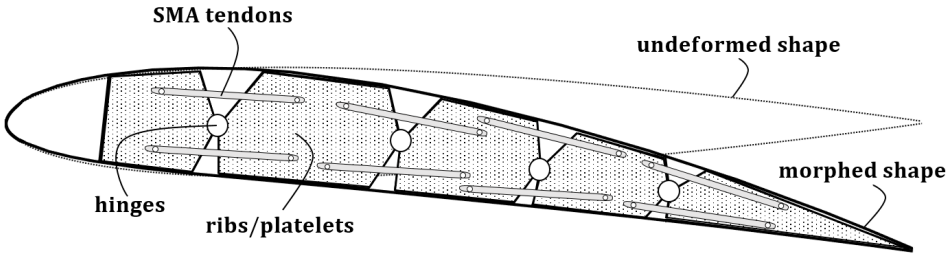

Figure 5.1: *An airfoil architecture with SMAs: placement of the hinges and of pairs of SMA tendons to adjust the aerodynamic shape.*

In the field of aeronautics however, the SMAs are stil not used at an indurtrial level, mainly due to the fact that the design of an SMA actuation system is hambered by conflicting requirements that should be met. For this reason, numerical tools should be devoted to the optimal preliminary design of such actuating morphing systems. The design process should be able to attest that the SMA actuators are able to sustain the external aerodynamic loading and the internal forces developed and adapt the flexible morphing structures to the different flight phases. This entails to accurately predict the nonlinear thermomechanical response of the SMAs and their interaction with the structure. In addition, the limited space constraints, the number of actuators needed, operational parameters (e.g. available power supply) and the complexity of the aeronautical geometries should be taken into account.

One of the first works that studied numerically the SMA-structure interaction problem is the work of Brinson et al. [BHBB97]. The authors present an analytic nonlinear beam formulation coupled with an SMA actuator. This problem was also addressed in [SLHW97] using a different SMA constitutive model. Both studies focus on demonstrating the control efficiency of the SMAs and the predictive capabilities of the constitutive models used, but are limited to simple academic structures. The coupling with a Finite Element (FE) code for solving more complicated geome-

tries was discussed in [BSMN06]. The SMAs were modeled as adaptive trusses and a solution procedure was developed and introduced to a commercial software code. The authors of [GTBB05] also performed a FE analysis, focused in designing SMA hybrid composites that could be actuated and adaptively stiffen or change their shape. These studies however, did not examine the shape control application of the SMAs.

One of the first works on the latter, is that of Barbarino et al. [BPL$^+$09] who presented numerical results from a FE analysis for the displacement of a morphing trailing edge, induced by SMA actuation. Experimental and numerical studies were also carried out in [BPL$^+$11] for the design of a flap architecture with a variable-camber trailing edge. The authors considered the reference geometry of a full-scale wing of a regional aircraft and their approach took into account the SMA phenomenology, the aerodynamic loading and the structural properties of the wing. A preliminary design study with finite element simulations is presented by Icardi and Ferrero [IF11] who have verified that an adaptive wing for a small unmanned air vehicle (UAV), which is totally driven by SMA devices, could sustain the aerodynamic pressure under any flight conditions, without weight increase or stiffness loss compared to other conventional actuators. Solomou et al. in [SMS14] developed a beam element that incorporates the thermomechanical properties of SMA wire actuators. The study of [MKK$^+$18] followed these developments, coupled them with a lower-fidelity fluid solver and performed a fluid-structure interaction (FSI) study of a hinged-flap configuration and a segmented airfoil to be used in with turbine applications.

The above works focus on the development of solution strategies for the numerical prediction of the static/dynamic response of morphed aeronautical configurations. What it is not explicitely addressed, however, is a way to translate these strategies into numerical methods that are devoted in the upstream design of configurations able to achieve a specific target shapes. Model-based methods for the optimal control of smart structures are extensively examined in the review of [SM04]. The authors discuss various aspects of modeling and deduct optimal feedback control methods that account for the nonlinear hysteretic behavior of the SMAs and can be used in real-time. Experimental and numerical studies in [BBM10] were devoted in optimizing selectively the offset distance used in controlling a beam, depending on its flexural rigidity. The work of [ABT$^+$12] was also devoted in optimizing an SMA system to be integrated within a morphing flap. The authors performed detailed parametric studies and a heuristic optimization procedure, using however a simplified model for the latter. A global optimization of the flapping kinematics applied with a morphing wing was carried out in [GHM$^+$12]. This interesting publication was focused on parametrizing the morphing deformation and optimizing the response with respect to the propulsive efficiency.

The aforementioned studies are problem-specific and it is difficult to transpose the formulations proposed in systems of higher complexity. The present study is dedicated on the systematic design of optimally controlled configurations. We discuss the use of SMA-based actuators for the shape control of flexible deformable

structures with focus on aircraft wings. A numerical method is proposed for the prediction of optimal smart configurations that are able to achieve pre-described shapes using SMA actuators. This procedure takes into account constraints imposed by the limited space, the rigidity of the controllable structure and the necessary external loading capacity. In order to produce optimally controlled configurations, the overall cost related to the number of the SMA actuators used and the operational specifications when calculating the actuation temperature are also considered. The proposed algorithm can be used in that regard to produce optimal configurations and greener (in terms of power consumption) solutions.

A properly fast and accurate design solver is developed The approach developed consists of two parts: (a) a robust algorithm that solves the "control of a structure by SMAs" problem in the context of a FE analysis, and (b) the coupling of the whole procedure with an optimization code. The structure is modeled with the FE approach which allow integrating the various components included in a complex aeronautical structure. The nonlinear thermomechanical behavior of SMA actuators is then coupled with the (large) response of the controlled deformable configuration in order to calculate the internal stresses due the heating and/or cooling of the material. The optimization process is introduced to determine specific design variables (structural or operational) leading to optimally functioning configurations, able to achieve the desired target shapes. This procedure takes into account any structural, geometric (e.g. limited space) and/or operational (e.g. maximum power supply) constraints and the external aerodynamic loading specifications. The proposed technique can be also used in training systems or reduced order models in order to obtain control laws for controlled cambering in real-time. The latter can be used in determining according to the working conditions and the operational needs the functioning of the SMAs included in the smart morphing system.

5.2 Thermo-Mechanical behavior of SMAs

The thermo-mechanical behavior of SMA materials is already well-document. However, it is here briefly summarized for the sake of completeness, in relation to the parameters and the assumptions adopted in the examined implementation. SMAs operate in two states: austenite and martensite; depending on the stress condition, the martensite phase can be either twinned or detwinned. Austenite is called the parent phase from which a transformation process occurs into the martensite phase (product phase). The state of the material depends on its temperature and the applied mechanical load. In a *stress-free* state, the SMAs are characterized by four phase-changing temperatures: A_s, A_f which control respectively the starting and ending of the austenitic transformation, and M_s, M_f for the martensitic transformation. For temperatures between M_f and A_s no phase changes take place and the material can exist both in an austenite or a martensite phase. Austenite phase is characterized by *pseudo-elasticity*, which refers to the non-existence of residual strains after a cycle of loading and unloading, at a temperature higher than A_f. The *shape memory*

effect is linked to the recovery of large residual strains of multi-variant martensite. After being turned into single-variant martensite due to the application of stress, the SMA has to be heated at a temperature beyond A_f for the residual strain to be fully recovered. The limit in the maximum recoverable strain ranges from 6% to 10% [Bir97]. The various transformations that SMAs undergo are summarized in Fig. 5.2.

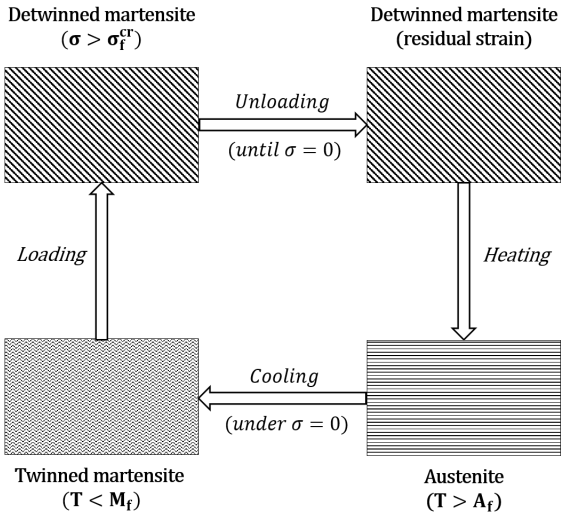

Figure 5.2: *Schematic of the phase-transformation cycle for SMAs.*

5.3 SMA constitutive modelling

A number of constitutional relationships have been proposed. Phenomenological models relate stress, strain and martensite fraction through a kinetic law that governs the martensitic transformation as a function of temperature and stress. These type of models are both robust and easily incorporated into a finite element software producing accurate results for the applications examined in this chapter. The one-dimensional (1D) models are able to account for every significant feature of the SMA's thermomechanical behavior while retaining a simpler formulation and introducing a modest number of material parameters [LA14]. Various uniaxial material models for SMAs have been proposed by different research groups. They can be distinguished to three different families: (a) those based on the Tanaka model [TKS86] (e.g. Liang-Rogers [LR90], Brinson [Bri93]), (b) models based on the work of Auricchio and his coworkers [AS97], [ATL97], and (c) models based on the work of Lagoudas and his co-workers [BL96]. In the present study, we adopted the Brinson model which is, essentially, an extension of the Liang-Rogers model that accounts for multi-variant martensite.

All of the Tanaka-based models utilize the same well-known constitutive

equation that couples the mechanical stress, the thermo-plastic stress and the stress due to the phase transformation:

$$\sigma - \sigma_0 = E(\xi)(\varepsilon - \varepsilon_0) + \Theta(T - T_0) + \Omega(\xi)(\xi - \xi_0) \tag{5.1}$$

where σ the stress in the material, ε the reduced strain, T the temperature, E the modulus of elasticity while Θ and Ω are respectively the thermal elasticity measure and the phase change factor. The latter are material characteristics that are measured experimentally at a zero stress state. The subscript 0 refers to quantities in their initial state. T_0 is the temperature for which the thermal strain is zero. The non-dimensional quantity $\xi(\sigma, T)$ expresses the martensitic fraction of the material, i.e. for $\xi = 1$ the material is in a full martensitic state and for $\xi = 0$ the material is austenitic. Both the elastic modulus and the phase change coefficient are functions of ξ:

$$E(\xi) = E_A + (E_M - E_A)\xi \ , \ \ \Omega(\xi) = -\varepsilon_L E(\xi)$$

where ε_L is the maximum deformation that can be removed by heating, i.e. the maximum residual strain that the SMA can support, and is considered constant for the whole range of temperatures below A_f. E_A, E_M are the austenitic and the martensitic moduli of elasticity respectively. Brinson introduced a separation of the volume fraction: $\xi = \xi_T + \xi_s$. The ξ_T accounts for the temperature-induced martensite while ξ_s accounts for the stress-induced percentage. In this way, the model is able to account for the detwinning of the martensite that is responsible for the shape memory effect at lower temperatures. It was shown in [Bri93] that Eq. 5.1 can be reduced to a simplified form:

$$\sigma = E(\xi)(\varepsilon - \varepsilon_L \xi_s) + \Theta(T - T_0) \tag{5.2}$$

The transformation equations were modified in [Bri93] to accommondate the separation of the volume fraction. Below the M_s temperature, critical stress limits (σ_s^{cr} and σ_f^{cr}) apply, guiding the conversion between martensite variants. For higher temperatures, the stress influence coefficients C_M and C_A express the dependence of the transformation temperature on the stress. The phase change equations contain cosine functions; their arguments are constrained so that a phase change occurs when the temperature and the stress ranges are within the proper transformation regions.

When moving from Austenite to detwinned Martensite with cooling or after a stress increase:

- for $T > M_s$ and $\sigma_s^{cr} + C_M(T - M_s) < \sigma < \sigma_f^{cr} + C_M(T - M_s)$

$$\xi_s = \frac{1 - \xi_{s0}}{2} cos\left\{ \frac{\pi}{\sigma_s^{cr} - \sigma_f^{cr}} \left[\sigma - \sigma_f^{cr} - C_M(T - M_s) \right] \right\} + \frac{1 + \xi_{s0}}{2}$$

$$\xi_T = \xi_{T0} - \frac{\xi_{T0}}{1 - \xi_{s0}} (\xi_s - \xi_{s0})$$

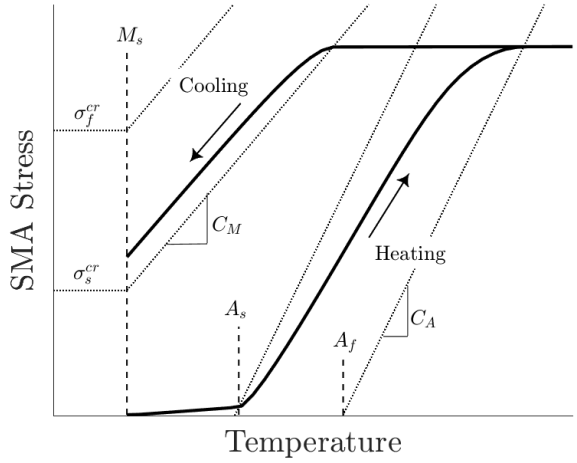

Figure 5.3: *Stress-temperature diagram as modeled by Brinson; austenite to detwinned martensite conersion for $T > M_s$ and $\sigma_s^{cr} + C_M(T - M_s) < \sigma < \sigma_f^{cr} + C_M(T - M_s)$; twinned to detwinned martensite conversion for $T < M_s$ and $\sigma_s^{cr} < \sigma < \sigma_f^{cr}$; martensite to austenite conversion for $T > A_s$ and $C_A(T - Af) < \sigma < C_A(T - A_s)$.*

When moving from twinned Martensite to detwinned Martensite with stress increase:

- for $T < M_s$ and $\sigma_s^{cr} < \sigma < \sigma_f^{cr}$

$$\xi_s = \frac{1-\xi_{s0}}{2} cos\left[\frac{\pi}{\sigma_s^{cr} - \sigma_f^{cr}}\left(\sigma - \sigma_f^{cr}\right)\right] + \frac{1+\xi_{s0}}{2}$$

$$\xi_T = \Delta_{T\varepsilon} - \frac{\Delta_{T\varepsilon}}{1-\xi_{s0}}(\xi_s - \xi_{s0})$$

where if $M_f < T < M_s$ and $T < T_0$

$$\Delta_{T\varepsilon} = \frac{1-\xi_{s0}-\xi_{T0}}{2} cos\left[\alpha_M(T - M_f)\right] + \frac{1-\xi_{s0}-\xi_{T0}}{2}$$

else

$$\Delta_{T\varepsilon} = \xi_{T0}$$

In the previous, the modification developed in [CHL06] is applied as well. In this way, regardless of the initial conditions, it is assured that the following conditions are always satisfied: (i) $\xi(\sigma, T) <= 1$, (ii) $\xi_s = 1$ if $\sigma = \sigma_f^{cr}$ and (iii) $\xi = 1$ if $T = M_f$. Finally, when moving from Martensite to Austenite with the increase of temperature:

- for $T > A_s$ and $C_A(T - Af) < \sigma < C_A(T - A_s)$

$$\xi = \frac{\xi_0}{2} cos\left[\alpha_A(T - A_s) + b_A\sigma\right] + \frac{\xi_0}{2}$$

$$\xi_s = \xi_{s0} - \frac{\xi_{s0}}{\xi_0}(\xi_0 - \xi)\ ,\ \ \xi_T = \xi_{T0} - \frac{\xi_{T0}}{\xi_0}(\xi_0 - \xi)$$

where the constants α_A, b_A are obtained from

$$\alpha_A = \frac{\pi}{A_s - A_f},\ \ b_A = -\frac{\alpha_A}{C_A}$$

A synopsis of the predicted thermomechanical behavior of the model is presented in Fig. 5.3. The imposed constraints are also included in the caption of the Fig. 5.3.

5.4 Structural control using SMAs

The shape control of an aeronautical configuration equipped with SMAs manifests a complicated problem. The shape control refers to the identification of equilibrium points between the deformation capacity of the structure and the working range of the SMA actuator. The working range of the actuators depends on the thermomechanical properties of the material. The solution requires the coupling of the thermomechanical behavior of the SMAs with the structure's response to any temperature change in the actuators. The coupling is accomplished through an iterative solving procedure since the complete system is material nonlinear due to the presence of SMAs and geometrically nonlinear due to the large displacements that the morphing structure typically undergoes. It is important for a shape control algorithm to accurately predict the points that determine the working capabilities of the whole controlled configuration.

If the controlled structure is expected to reach specified target shapes (e.g. various wing shapes adapted at the different flight phases) the whole configration should be optimally designed to meet the specified necessities. The design should be able to produce configurations that can achieve desirable shapes. The procedure should respect the (a) geometric and structural constraints posed by the controlled structure and the (b) external loading specifications. Referring back to Fig. 5.1, the preliminary design should predict the operational temperatures and the positioning for each actuator that results in a best-fitted shape with respect to the target. For optimally designed configurations, the available power supply should be also taken into account when solving for the design variables. As the number of SMA actuators and the degrees of freedom of the structure increase, so does the complexity of the design problem.

The solution of the preliminary design problem follows a two-step procedure. The first step necessitates the accurate prediction of the structural response under the control of SMAs. To this end, the NonLinear-Builds (NLB) code has been developed to introduce the SMAs in a FE framework. The second step adresses the

coupling of the shape-control solver to an optimization tool in order to predict the design that best produces the desired shape. These two steps are discussed in the sections that follow.

5.4.1 Structure-SMA interaction

Aeronautical configurations are often complicated geometries with various structural parts to be modeled. To this end, it is important to develop any methodology in a FE analysis framework to be able to predict accurately the strucural response. This allows to take into account the specified structural rigidity, boundary conditions and the inclusion of composite materials that usually coincide with flexible deformable structures (e.g. skin of the aerodynamic surface). The non-conservativity of the aerodynamic loading is also taken into account by the solver. In this context, appropriate constitutive relations of the thermomechnical SMA behavior are coupled with the structural response.

The proposed methodology is nested in an iterative algorithm that determines for a given temperature history and initial conditions the displacement of a structure and the stresses developed inside the SMA actuators, induced by the structure's reaction to any temperature variation of the actuator. The SMA properties are adjusted through temperature and calculated by the constitutive material law. The coupling of the two is achieved by considering the forces acting on either side: (a) the structure "sees" the SMA actuators only through equivalent "external" following forces, and (b) the actuators receive the reactive stresses in the opposite direction. The reactive forces alter the SMA thermomechanical behavior of the actuator and this necessitates the adjustment of the forces on the structure. Hence the iterative procedure. The fulfillment of the deformation compliance criterion is required for the identidfication of an equilibrium point and for the iterative process to end. The NLB algorithm is outlined below step-by-step:

Initialization of the problem

- The FE model of the structure is built. The nodes to which the SMA wire elements are connected are defined for the coupling.

- The SMA actuators are introduced in the FE model as tension-only trusses; each SMA element denoted as $k = 1\ ,\ 2\ ,\ \ldots\ ,\ m\ ,\ \ldots$ is connected to one common node.

- For the m^{th} actuator, the strain ε^m_{str} is calculated from the nodal displacement of the structure and the strain ε^m_{SMA} is calculated by the constitutive relationship (see Section 5.3).

- For the m^{th} SMA actuator, the initial states ξ^m_{s0}, ξ^m_{T0} and the temperature T_0 are derived from the intial stress/strain conditions; the SMAs can be pretrained and/or under stressed due to their connection to the structure.

- For each m SMA actuator a starting length $L^m_{SMA,0}$ is defined corresponding to the initial phase for which no prestrain/prestress has been imposed and zero residual strain is accounted for. This length $L^m_{SMA,0}$ differs from L^m_0 since the latter is the initial element length after it has been mounted on the structure.

Temperature increment ΔT^m_i in the i^{th} pseudo time-step:

- For the m^{th} SMA actuator, the thermal loading $\Delta\theta^m = \Theta(T^m_i - T_0)$ is applied with the variation of the temperature.
- Stresses $\sigma^{m,o}_i$ are taken from the previous pseudo time-step $\sigma^{m,n}_{i-1}$; the exponents o, n refer to "old" or "new" values respectively.
- An iterative procedure follows until convergence, i.e. until the strains converge:
  - The states ξ^m_s, ξ^m_T, ξ^m are calculated from the phase changing model.
  - The strains ε^m_{SMA} are derived with ξ^m_s, $\sigma^{m,o}_i$ and the thermal loading $\Delta\theta^m$.
  - The norm of the force $F^m = \sigma^{m,o}_i A_{SMA}$ is calculated, where A^m_{SMA} is the cross section area of the truss element.
  - The equivalent nodal forces for the structure are calculated from F^m after they are transformed from the local SMA coordinate system to the global system. The nodal displacements are updated with a new FE analysis applying the equivalent nodal forces.
  - From the updated displacements of the SMA (common) nodes, the new effective length $L^{m,n}_{SMA}$ is calculated for each SMA actuator.
  - The strain ε^m_{str} is updated for the m^{th} SMA actuator from:
$$\varepsilon^m_{str} = \frac{L^{m,n}_{SMA} - L^m_{SMA,0}}{L^m_{SMA,0}}$$
  - The derivative $\frac{\partial\sigma}{\partial\varepsilon}\Big|^m_{T_i}$ is analytically derived from the constitutive law and the transformation equations and calculated for a specific temperature.
  - The stresses in the m^{th} SMA actuator are updated as:
$$\sigma^{m,n}_i = \sigma^{m,o}_i - (\varepsilon^m_{SMA} - \varepsilon^m_{str})\frac{\partial\sigma}{\partial\varepsilon}\Big|^m_{T_i}$$
    Note that if $\sigma^{m,n}_i < 0$ we set $\sigma^{m,n}_i = 0$ since tension-only trusses cannot react to compression and yield after they reach a zero residual strain.
  - The stress values are updated with $\sigma^{m,o}_i = \sigma^{m,n}_i$ and the error is calculated:
$$error \approx \frac{|\varepsilon^m_{SMA} - \varepsilon^m_{str}|}{\varepsilon^m_{SMA}}$$

  - Return.

- After the convergence for an increment, the same procedure is repeated for every pseudo time-step until the desired temperature history is applied; the exact same procedure can be followed for the reverse (cooling) procedure where a thermal unloading takes place.

5.4.2 Design of an optimized morphed configuration

The second part of the preliminary design consists of coupling the NLB solver to an optimization tool. The efficiency and robustness of NLB render the code adaptable to any optimization technique for the pre-design of controlled configurations. The optimization procedure is used to calculate the design variables for a controlled configuration that is able to achieve a pre-defined shape target. In the present work, the code is evaluated coupled with a stochastic optimization algorithm, appropriate for strongly nonlinear structural optimization problems where the number of design parameters is modest.

The Genetic Algorithms (GA) are probably the most widely used category of Evolutionary Algorithms (EA). The GA begins by creating a first set of random candidates. At each step (generation), the method uses the current individuals (population) in order to create the next set of candidates. To create a new population, each member of the current iteration is evaluated on its fitness value from an objective function (to be minimized) and is attributed a score. Based on this score, few of the best members (elites) are directly passed down to the next generation. From the remaining members, some are selected to be used as parents from which new candidates (offsprings) will be produced. The offsprings are generated either by mutation i.e. from stochastic changes over a single parent, or by crossover, where two parents are combined to produce two children. The procedure is repeated for the whole sequence of evolving populations that have a progressively better fitness and from which an optimal solution will be identified.

The formulation of the problem requires first to define the objective function and chose the design variables.

Design algorithm for shape control through temperature

- For a pre-defined number of SMA actuators, the design variables are chosen; they could be combination of working parameters (e.g. actuation temperature in each actuator), geometric (e.g. placement of SMAs, attachment positions to the structure) or even SMA properties (e.g. size, material properties).

- Any given constraint is included; usually this corresponds to geometric limitation (available space) the structure imposes or working limitations posed by the actuators (e.g. maximum temperature that can achieved by a system).

- At least one target is specified; if this is a desired shape, the objective is the minimization of the difference between the target and the deformation

achieved by the controlled configuration. The objective function can be defined to account for multiple target shape or the electric energy consumption.

- The (stochastic) optimization procedure starts:
  - NLB solves the coupling problem (previously described procedure) for the current values of the design variables
  - The objective function(s) are evaluated (e.g. comparing the deformed and the target shape).
  - New values of the design variables are derived by the optimization method (this step depends on the optimization technique).
  - The loop continues until the objective is achieved or the optimization is stalled, i.e. a better evaluation for the objective function has not be reached for multiple iterations.
- The final values for the design variables are evaluated.

The optimum design can lead to a solution where some of the SMAs are not actuated, implying that they are redundant to the specific design. On the other hand, it is also possible that the distance from the target shape is sufficiently small but can be further reduced only with the addition of more actuators. More implementations details are discussed in the cases that follow.

5.5 Case studies

The proposed algorithm is examined through two numerical examples. The flexible structures considered are geometrically nonlinear and hence, the methodology is developed within a nonlinear FE analysis framework (see Section 2.2.3) that allows to capture the significantly higher stresses compared to the linear case. To this end, NLB is developed to solve for elastic nonlinear truss and frame elements. The implicit (Newton-Raphson) algorithm developed follows the corotational formulation presented in [FF04] and [Yaw08]. An incremental-loading variation of the algorithm is also available. The code can also solve for problems with nonconservative nodal forces and distributed loads (i.e. following force problems). This aspect is essential for the problems considered as the SMA actuators change orientation with the deformation of the controlled structure and the forces should account for this. In addition, when dealing with aeronautical structures specifically, the effect of the aerodynamic pressure is a clear manifestation of a circulatory distributed nonuniform loading. Following the work of Argyris et al. [ADS78], [AS81], a pertinent correction of the tangent stiffness matrix is implemented. The resulting non-symmetric stiffness formulation slightly increases the computational cost but stabilizes the the solution and assures convergence.

The FE code has been successfully validated for two flexible structures undergoing large deflection due to nonconservative loading. The cantilever (Figure 5.4a)

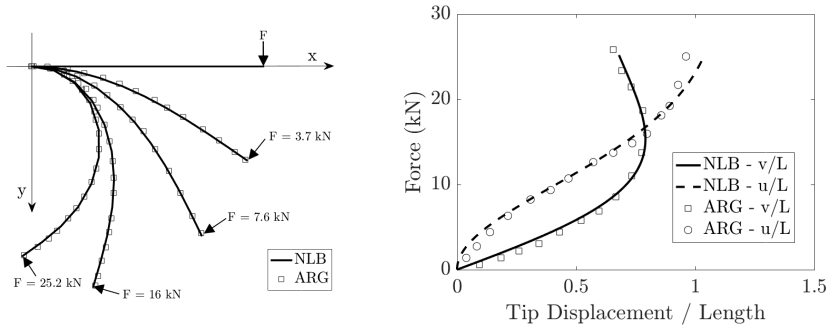

(a) *Deformed geometry of beam mid-axis.* **(b)** *Load-displacement diagram of end point.*

Figure 5.4: *Large deflection of cantilever under nonconservative transverse tip load; comparison of the NLB code with numerical results (ARG) from [AS81].*

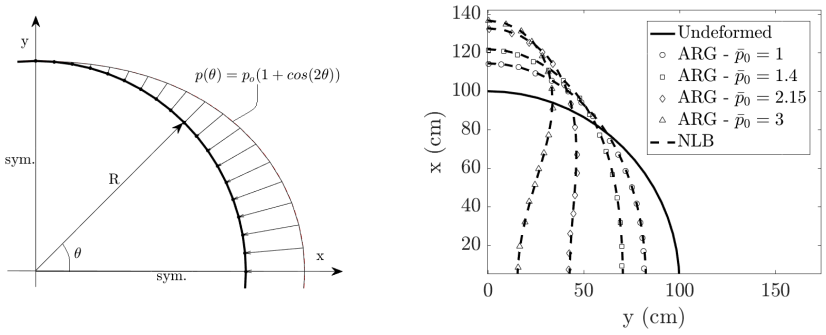

(a) *Test case configuration:* $1/4$ *ring.* **(b)** *Deformed geometry of ring centerline.*

Figure 5.5: *Large deflection of circular ring under nonconservative nonuniform normal pressure (left); comparison of the NLB code with numerical results (ARG) from [AS81] for different loading amplitudes* $\bar{p}_o = p_0 r^3/EI$.

of length $L_b = 100mm$ undergoes large deflection due to a nonconservative point force that acts at its free end. The ring (Figure 5.5a) of radius $R = 100mm$ is subjected to a inward pressure load that is given by the expression $p = p_0(1 + cos2\theta)$, where p_0 is the maximum load amplitude and θ the angular coordinate of the ring geometry. Since the ring is doubly symmetric, only one quarter is considered. The properties assumed for the two examples are $E = 210GPa$, $I_b = 1.6667cm^4$ and $A = 20cm^2$. Ten (10) and eighteen (18) elements have been used for the cantilever and for the ring problem, respectively.

The deformation and the load-displacement diagrams for the cantilever case are presented in Fig. 5.4a and 5.4b respectively. It is worth noting that NLB is capable of predicting deformations up until the stability limit of the elastic beam, granted that the structure is flexible enough. The calculations are in excellent agreement

with the results included in [AS81] and denoted as "ARG". Figure 5.5b presents the displacement diagram for the $1/4$ ring geometry. Same goes for the circular $1/4$ ring test case. The code provides results that are in very good agreement with the reference for all the loading magnitudes examined. It is also demonstrated that NLB remains robust even for large enough deformations.

5.5.1 Cantilever shape control

In this section, the implementation of the SMA constitutive modelling is evaluated. The controlled configuration adopted here and shown in Fig.5.6 was first examined in [BHBB97]. A cantilever of length L_b is equipped with a single SMA actuator is considered; the actuator is connected under an angle to an offset device d through which it can regulate and control the beam displacement, without causing any buckling issues. A rectangular cross-section $A_b = T_b \times W_b$ is assumed for the beam. When the SMA actuator is subjected to a temperature variation, its length changes and thus imposes a force that deforms the cantilever. This connection results to a force following the beam as it deforms; due to the displacement, the orientation of the force vector changes significantly.

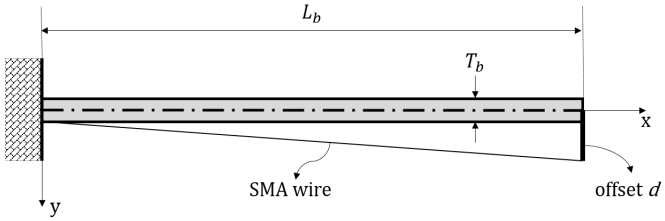

Figure 5.6: *The elastic beam controlled with an SMA wire; configuration examined in [BHBB97].*

BEAM	**E (GPa)**	**L_b (mm)**	**T_b (mm)**	**W_b (mm)**	**d (mm)**
A	69	400	1	50	5
B	69	400	1	25	5
C	69	300	2	100	5

Table 5.1: *Geometric and material properties; d the offset distance.*

Three beams are examined in total; the material and geometric properties for all the beams considered can be found in Table 5.1. For the first two (BEAM A & B), calculations were carried out without taking into consideration the SMA actuation as in [BHBB97]. The loading was applied with a weight fixed at the lower end of a steel wire. The deformation of the beam geometry is illustrated in Fig. 5.7a for BEAM A. As the weight (i.e. the loading) increases, the wire gets shorter and deforms the cantilever. In Fig. 5.7b the load-displacement diagrams calculated

with NLB are presented for both beams. For higher values of loading, a strongly nonlinear behavior for the beams is observed and is attributed to the nonlinear kinematics and to the nonconservativity of the applied force. The aggreement with the results included in [BHBB97] is remarkable.

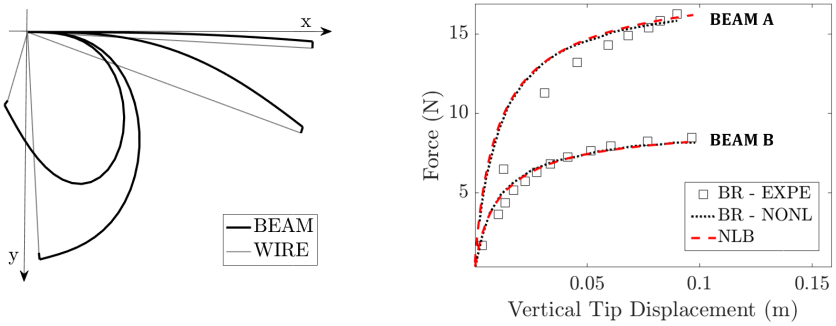

(a) *Deformed geometry of BEAM A mid-axis.* **(b)** *Load-displacement diagram of end point.*

Figure 5.7: *Large deflection of cantilever under nonconservative tension through a steel wire; comparison of the NLB code with experimental (BR-EXPE) and numerical (BR-NONL) results from [BHBB97].*

BEAM C is then examined under the effect of the SMA actuation; the properties of BEAM C are also included in Table 5.1. The SMA actuator has diameter $D_{SMA} = 1.3mm$ and is initially prestrained with strain $\varepsilon_0 = 3\%$ and stress $\sigma_0 = 0$. The material properties assumed for the SMA are shown in Table 5.2. A full heating and cooling cycle for the SMA actuator is computed. The temperature of the actuator begins from $20°C$, then linearly increases up to $80°C$ and is cooled back down to $20°C$. The results obtained are shown in Fig. 5.8; for comparison, the results of the reference [BHBB97] are also shown with a hollow square marker.

$\mathbf{M_f}$ (°C)	$\mathbf{M_s}$ (°C)	$\mathbf{A_s}$ (°C)	$\mathbf{A_f}$ (°C)
9	18.4	34.5	49
$\mathbf{E_A}$ (GPa)	$\mathbf{E_M}$ (GPa)	$\mathbf{C_A}$ (MPa/°C)	$\mathbf{C_M}$ (MPa/°C)
67	26.3	13.8	8
ε_L	Θ (MPa/°C)	σ_s^{cr} (MPa)	σ_f^{cr} (MPa)
6.7%	0.55	100	170

Table 5.2: *SMA material properties [BHBB97] used in the controlled cantilever example.*

In Fig. 5.8a the stress-strain values for the SMA wire are presented. The predicted working points are placed along the permissible by the structure deformation line and shown with filled circular markers. The points are contained within the

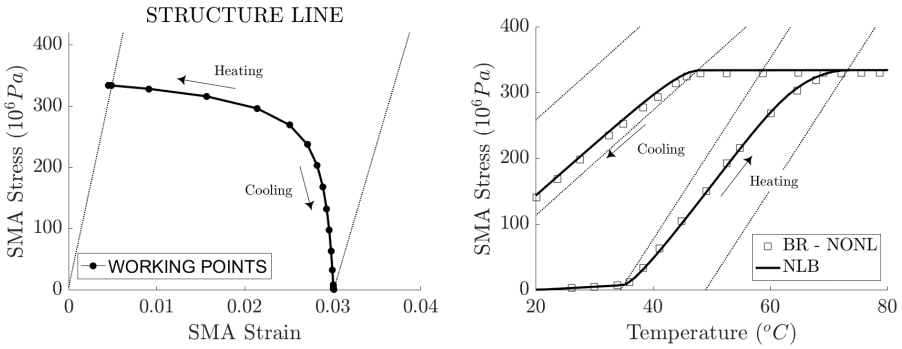

(a) *Stress-strain diagram for the SMA wire.* **(b)** *Stress in the SMA wire with temperature.*

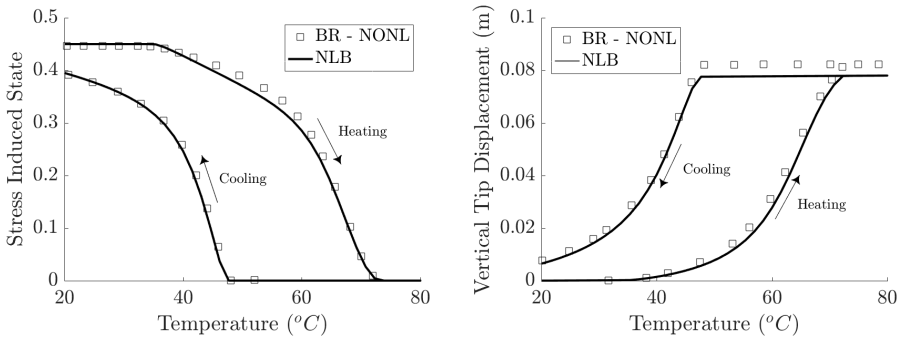

(c) *Stress induced martensite fraction of the SMA wire with temperature.* **(d)** *End point vertical deflection of the cantilever with temperature.*

Figure 5.8: *Large deflection of cantilever as controlled by temperature in the SMA actuator; comparison of the proposed methodology (NLB) with numerical results (BR-NONL) from [BHBB97].*

working range of the actuators which can be observed in Fig. 5.8a with dotted lines. Each of these points is produced from identifying an equilibrium between (a) the reactive forces induced from the cantilever to the SMA and (b) the stress-strain-temperature state of the actuator. The ensemble of points determines the working capabilities of the controlled configuration. As the temperature increases, the SMA wire tends to recover the initial strain ε_0. Since it remains connected to the structure, it deforms the cantilever and high levels of stress are produced as observed in the stress-temperature diagram in Fig. 5.8b. The stress reaches a plateau at a temperature close to $70°C$ and the prestrain is almost completely recovered (Fig. 5.8a). After this temperature, the wire reaches its complete transformation to an austenitic phase as zero martensitic fraction remains. This is illustrated in Fig. 5.8c where the variation of stress-induced fraction ξ_s is shown as function of the temperature. Further increase of the temperature cannot lead to any additional transformation and the actuator is not able to retrieve its residual strain completely (Fig. 5.8a). As a result, the controlled beam reaches its maximum displacement as observed in Fig. 5.8d, where the end point vertical deflection of the cantilever is

shown as function of the temperature.

When the temperature is reduced, the displacement is reversed. After a temperature, martensitic fraction develops inside the SMA wire and the stress decreases along with the beam's deformation. The martensitic fraction is generated purely due to the structure which "pulls" back the actuator as it tends to recover its initial undeformed shape. At 20°C, the whole configuration reaches an equilibrium state which differs from the initial one (Fig. 5.8d). The whole system balances under a residual stress (Fig. 5.8b) as a lower martensitic fraction is produced. In conclusion, the hysteretic behavior of the SMA actuator is well captured by the NLB FE code and the proposed methodology produced results in remarkable agreement with those of Brinson et al. [BHBB97].

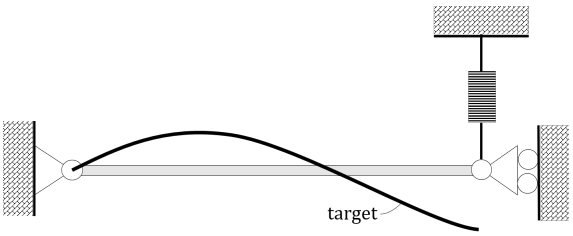

(a) *Controlled configuration and target shape.*

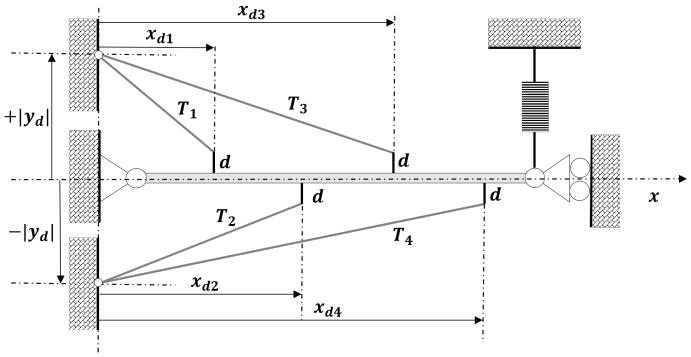

(b) *Design parameters for the control.*

Figure 5.9: *Problem definition for the optimization procedure.*

5.5.2 Optimal shape control

The second case study demonstrates the capacity of the proposed algorithm to design a controlled configuration that is able to achieve a pre-defined target shape by adjusting the temperature of the SMA actuators. One of the main motivations for the development of the proposed algorithm was the applicability to optimization problems. A fast and accurate solver coupled with an optimization methodology provides with a strong preliminary design tool capable of determining optimal configurations for the control of structures by SMAs. In this context, NLB was used

along with the genetic algorithm (GA) solver available in the optimization toolbox of MATLAB® [TM19].

The controlled configuration to be studied is shown in Fig. 5.9a. The structure is pinned at its left side, while the right end is free to move vertically. For numerical stability purposes, a low-stiffness spring ($k_{spr} = 1000N/m$) has been inserted at the free end. The properties of the beam are: $E = 69GPa$, $L_b = 300mm$, $T_b = 2mm$ and $W_b = 100mm$. A desirable aerodynamic shape is set as the target shape. The target shape was produced by a third-order polynomial function in order to create a realistic convex aerodynamic shape (Fig. 5.9a). This shape which will be obtained by adjusting the temperature of the four (4) SMA-based actuators, as shown in Fig. 5.9b. The optimization procedure will be set to determine the actuation temperatures and an optimal placement of the SMA wires in order to produce this shape as closely as possible.

The nonlinear optimization problem can be solved through the stochastic minimization of an objective function. The objective function is the normalized norm of the distance of each point of the beam structure from the target shape, i.e.:

$$F_{obj} = \frac{||\mathbf{x}_{str} - \mathbf{x}_{tar}||_2}{||\mathbf{x}_{und} - \mathbf{x}_{tar}||_2}$$

where $\mathbf{x}_{str} = (x_{str}, y_{str})$ and $\mathbf{x}_{und} = (x_{und}, y_{und})$ the vectors containing all the nodal coordinates for the deformed and undeformed configuration respectively; $\mathbf{x}_{tar} = (x_{tar}, y_{tar})$ the target geometry. The design variables to be identified by the optimization process are:

(a) the actuation temperature T_i for each SMA wire with $i = 1, \ldots, 4$, and

(b) the beam node N_i at which each SMA wire should be attached, with $i = 1, \ldots, 4$.

The design variables are bounded:

$$T_i \in [40, 250] \subset \mathbb{Z}$$

$$N_i \in [2, N_p] \subset \mathbb{Z}$$

where $N_P = number\ of\ elements + 1$, the total number of FE nodes which only admit integer values. The attachment positions could only be fixed at the available nodes of the structure. Hence, the integer condition. The temperature was set as an integer to speed-up the optimization process by limiting the available candidates. No additional constraints were taken into account for the optimization.

For this morphing example, the total number (here four) of the SMA actuators was constant. Two of them were placed above the frame (see Figure 5.9b) and two below. The SMA actuators were pinned on their left side ($x = 0$) at a fixed vertical distance $\pm|y_d|$ from the neutral axis of the frame. For the problem examined, $|y_d|/L_b = 0.125$. The actuators were attached to the structure with the same offset distance $d = 5mm$ which was also fixed. All the SMA-based actuators were assumed

to have the same material properties, included in Table 5.3, and a constant diameter $D_{SMA} = 1mm$. The actuators start from a fully martensitic state with a stress-induced fraction $\xi_s = 66\%$ due to a prestrain $\varepsilon_0 = 4\%$ at $T_0 = 20°C$.

$\mathbf{M_f}$ (°C)	$\mathbf{M_s}$ (°C)	$\mathbf{A_s}$ (°C)	$\mathbf{A_f}$ (°C)
43.9	48.4	68	73.75
$\mathbf{E_A}$ (GPa)	$\mathbf{E_M}$ (GPa)	$\mathbf{C_A}$ (MPa/°C)	$\mathbf{C_M}$ (MPa/°C)
31.5	20	6.73	6.32
ε_L	$\mathbf{\Theta}$ (MPa/°C)	σ_s^{cr} (MPa)	σ_f^{cr} (MPa)
6.1%	0.5	25	78

Table 5.3: *SMA properties for the optimization problem.*

Various realizations were carried out to establish the existence of a global minimum. Both a linear (Linear16) and a nonlinear (NLB16) beam were tested for 16 elements along the structure. An additional calculation was carried for a nonlinear beam with a double number of elements (NLB32) to evaluate the sensitivity of the prediction to the number of the available attachment nodes. Finally, the $x-wise$ symmetric target shape case (see Fig. 5.11b) was also examined (NLB16R) for 16 finite elements. The calculations presented hereafter, were carried out for a population size of 60 for each generation. A Gaussian mutation function was used for the results following and the elite count was 3 members to be passed down to the next generation. The rank (position) of each individual, in terms of sorted evaluations, was used for the scaling of the raw scores since this method removes the effect of their spread. Due to the integer constraints given to the design variables, no crossover functions are used by the GA solver of MATLAB®. In every case study, the optimization procedure terminated after the maximum number of 80 stalled generations was reached.

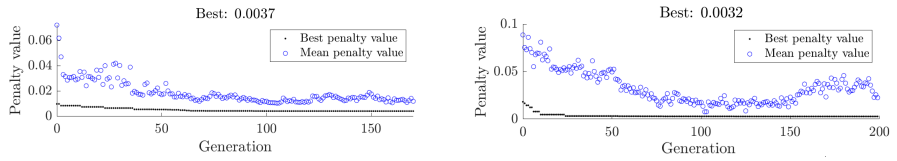

(a) *Linear16.* **(b)** *NLB16.*

Figure 5.10: *Optimization procedure of the GA coupled with the NLB code; the F_{obj} is noted as Best.*

In Fig. 5.10, the optimization procedure is presented for the Linear16 and the NLB16 studies. The dots in this figure monitor the best solution identified from the optimization procedure while the hollow circular marker the mean solution predicted at each generation, produced from an average of all the evaluations that take place. As the evaluation of the mean solution decreases during the optimization,

the chances to find a better candidate increase with time. Since no better solution is predicted after 80 consecutive generations, the optimization stops. The linear structure case terminated after 178 generations predicting an $F_{obj} = 4.7\%$. A few more generations (≈ 200) were necessary for the nonlinear case to be terminated. However, a solution with a slightly lower value for the objective function $F_{obj} = 4.1\%$ is predicted for the nonlinear case. For the NLB32 case study, the calculation was terminated after 320 generations with an $F_{obj} = 6.9\%$ and for the NLB16R, after 193 generations with an $F_{obj} = 4.2\%$. All the deformed shapes produced by the predicted optimal configurations are illustrated in Fig. 5.11 along with the respective target shapes. The target is well captured in every case examined as expected from the low values produced by the evaluations of the objective function. The NLB32 gives a slight upward deformation on the second half of the frame which explains the higher value for the objective function.

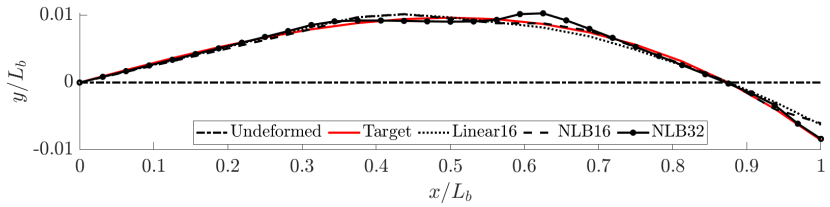

(a) *Convex aerodynamic target shape.*

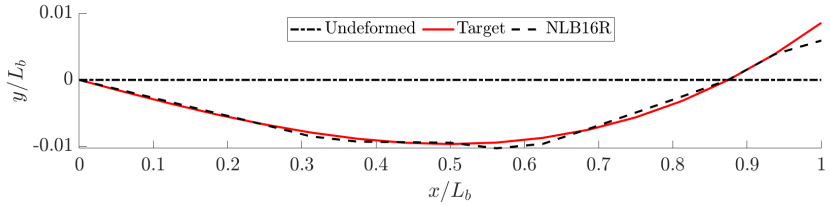

(b) *Symmetric aerodynamic target shape.*

Figure 5.11: *Deformed controlled shape after the optimization procedure.*

The results of the optimization along with the respective evaluation of the objective function are regrouped in Table 5.4 for all the cases. The normalized positions of the attachments $x_{di}/L_b = x_d(N_i)/L_b$ and the actuating temperature T_i identified are listed for each SMA wire. The martensitic fraction ξ and its stress-induced component ξ_s predicted at the deformed configuration for each actuator are also included. The Linear16 and the NLB16 cases predict the exact same optimal attachment points (see Table 5.4). However, the temperature prediction is significantly different. The actuation temperatures for all wires in the linear case (Linear16) are significantly higher as, for the same deformation to be achieved, large stresses are developed in the structure. This comes to highlight the importance of the nonlinear effects in the design process. As a matter of fact, with the nonlinear approach NLB16, the first SMA which is placed below the structure is not actuated at all. Examining the ξ and ξ_s values for this wire, it can be observed that due to

its temperature and positioning it ends up receiving zero stress (it yields) and does not partake in the actuation. The design produced a simplified solution that ends up using less actuators than what was originally conceived for the shape control.

Table 5.4: *Optimization results for the different cases;* $\xi_0 = 1.00$, $\xi_{s0} = 0.66$ *and* $\varepsilon_0 = 4\%$ *at* $T_0 = 20°C$, *the initial conditions for all the actuators.*

NoSMA	**1**	**2**	**3**	**4**	**1**	**2**	**3**	**4**
Case	*Linear*16				*NLB*16			
T (°**C**)	211	250	234	229	67	102	136	89
$\mathbf{x_d/L_b}$ (%)	94	63	100	38	100	63	94	38
$\boldsymbol{\xi}$ (%)	0	0	0	0	100	73	56	69
$\boldsymbol{\xi_s}$ (%)	0	0	0	0	66	48	37	45
F_{obj}	0.0471				0.0408			
Case	*NLB*32				*NLB*16*R*			
T (°**C**)	50	140	178	86	81	144	107	132
$\mathbf{x_d/L_b}$ (%)	62.50	59.38	96.88	31.25	31.25	56.25	56.25	93.75
$\boldsymbol{\xi}$ (%)	100	50	35	67	70	65	67	58
$\boldsymbol{\xi_s}$ (%)	68	33	23	44	46	43	44	38
F_{obj}	0.0688				0.0420			

In the NLB32, almost identical attachment positions are identified even though the range of available candidates had been doubled. The same wire (first one) is not actuated but in this case it receives a small amount of stress that produces a slightly higher stress-induced martensitic fraction. Slight variations in the actuating temperatures are observed due to the marginal differences between the NLB16 and NLB32. However, the two cases present reasonable agreement. As expected, the NLB16R optimization case provided a positioning that was symmetric to the ones previously examined. The resulting configuration was closer to the one predicted in the NLB32 case. However, contrary to the previous studies, all the wires are actuated and end up receiving some portion of the stresses developed. Finally, in all the nonlinear cases, none of the wires went through a complete transformation to Austenite as $\xi > 0$ indicates. As a result, the configurations are able to achieve even higher deformations and should be tested to this. The solution of the *NLB*16 case is identified as the optimal one since it produces the target accurately (lowest F_{obj}), at lower actuation temperature (reduced energy consumption) and with the less active actuators than what was initially resulting in a simpler design.

5.6 Wing shape control

This final study examines the application of the proposed algorithm for the shape control and re-design of an aeronautical configuration. The present study will be split into two parts. First, in Section 5.6.1 NLB will be used to solve the structure-SMA interaction problem for the shape control of the Morphing Wing Prototype (MWP). The results from this calculation will be compared to past investigations on the constructed wing [JMS$^+$17]. It will be demonstrated that the solver accurately predicts the deformation of the electroactive wing and estimates the actuation temperature. Then, in Section 5.6.2 the proposed algorithm will be adopted in order to re-design/optimize the actuation system inside the wing. For the given wing geometry and a desirable target shape, it is examined whether the existing system can be reconsidered. The target will be to achieve the same pre-described displacement that the current actuation system is able to produce while consuming less energy, i.e. at a lower actuation temperature.

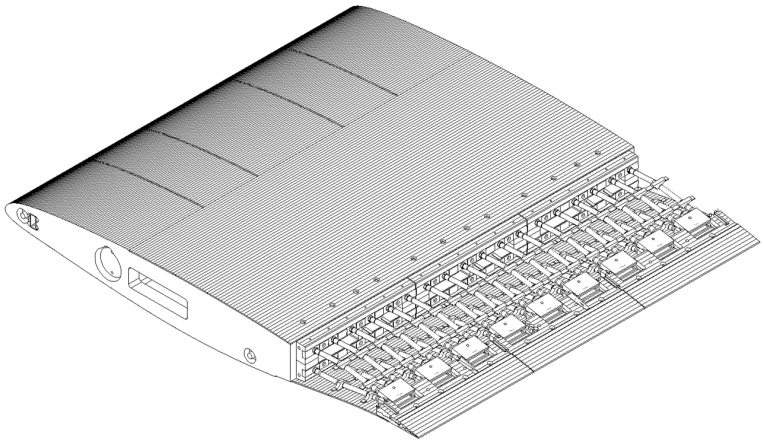

Figure 5.12: *3D CAD representation of the MWP constructed by LAPLACE/IMFT; upper skin removed on the rear/deformable part to reveal the SMA-based actuation system.*

The considered MWP is a reduced-scale design of an electroactive hybrid morphing wing, equipped with both a camber control system and trailing edge (HFVTE) actuators [JMS$^+$17, SJM$^+$19]. The morphed wing prototype is shown in Fig. 5.12 in 3D. A side view of the wing section is illustrated in Fig. 5.13a. The baseline airfoil for the MWP has a chord $c_w = 700mm$ and a span $S_w = 590mm$. The camber control system employs SMA actuators that were designed to be inserted on a length covering the last 30% of the chord (Fig. 5.13) which corresponds to the deformable part of the wing. Eighteen (18) equidistant pairs of SMA-based actuators cover the whole span of the wing, acting both on the suction (upper) and the pressure (lower) side of the wing. The actuators are pinned on their left side to the fixed (non-deformable) part of the wing and attached either on the upper or the

lower skin side. When the top actuator from each pair is heated, the wing deforms downwards, towards higher camber angles. Respectively, when the bottom actuator is heated, the wing moves upwards. Through this "agonist-antagonist" configuration, the wing is able to move efficiently in both directions and more importantly, recover its neutral shape fast if needed. The deformation between the upper and lower skin side is transmitted through a rigid body part (see Fig. 5.13a) which is attached on the suction side of the wing and is free to slide along the pressure side of the wing. Additional information about the construction and the aerodynamic performance of the MWP can be found in [JMS$^+$17, SJM$^+$19, GSR$^+$15].

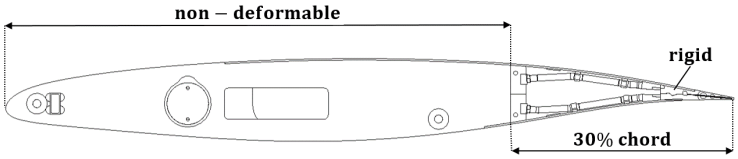

(a) *Side-view; one of the 18 pairs of the actuator.*

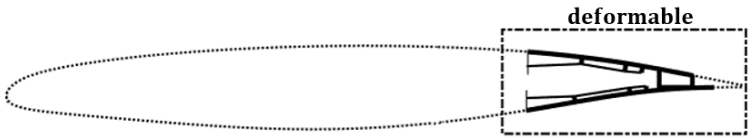

(b) *FE model on the deformable part of the wing.*

Figure 5.13: *CAD of the MWP and FE model with respect to the wing geometry.*

For the studies following, a two-dimensional finite element model is developed for the deformable part of the wing, as shown in Fig. 5.13b. The FE model illustrated in Fig. 5.14 represents only one of the 18 equidistant actuation pairs, acting on a narrow (spanwise) region corresponding to $1/18$ of the total span. Elastic beam elements clamped on their left side were chosen to represent this narrow aluminum ($E = 69GPa$) skin region with thickness $T_b = 1.5mm$ and width $W_b = 1/18 \times S_w$. For the suction and pressure side of the wing, 30 and 34 finite elements have been used respectively in order to accurately reproduce the curvature of the geometry. SMA wires made of Nickel-Titanium (Ni-Ti) alloys with diameter $D_{SMA} = 1mm$ were used in the MWP; the material constants assumed in the modeling are included in Table 5.5. The SMAs were in a fully martensitic phase and were prestrained by $\varepsilon_0 = 3\%$. As in the prototype, the wires are pinned on their left side and are attached to the wing skin via multiple offsets (Figures 5.13a and 5.14). The intermediate attachments were modeled to behave like pulley/wire-type of joints, pulling the respective surface as the wire tends to straighten itself. In order to model the transmission of the deformation between the upper and lower skin, NLB has been developed to deal with contact problems based on the work of Zavarise et al.

[ZDLT12]. The rigid body remains connected to the suction side and slides along the pressure side of the wing without penetrating it. Frictional and gravitational forces were not taken into account in the model.

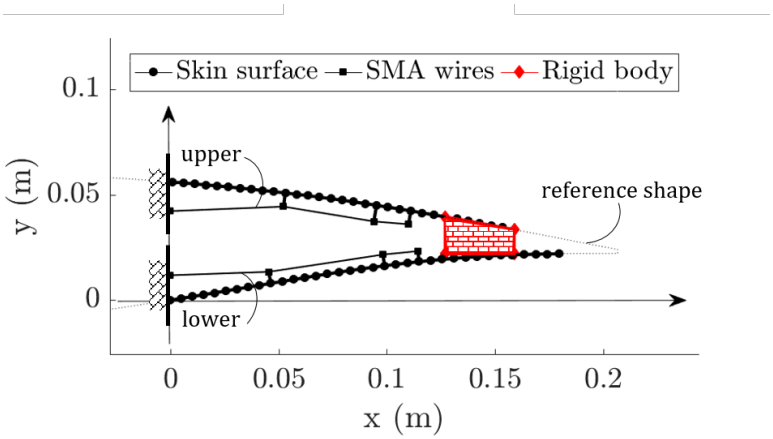

Figure 5.14: *FE model and boundary conditions for the SMA actuation on the deformable part of the MWP.*

$\mathbf{M_f}$ (°C)	$\mathbf{M_s}$ (°C)	$\mathbf{A_s}$ (°C)	$\mathbf{A_f}$ (°C)
25	65	30	75
$\mathbf{E_A}$ (GPa)	$\mathbf{E_M}$ (GPa)	$\mathbf{C_A}$ (MPa/°C)	$\mathbf{C_M}$ (MPa/°C)
75	28	10.3	10.3
ε_L	Θ (MPa/°C)	σ_s^{cr} (MPa)	σ_f^{cr} (MPa)
6.7%	0.55	100	170

Table 5.5: *Ni-Ti SMA properties as included in [Jod17];* $\sigma_0 = 0$ *and* $\varepsilon_0 = 3\%$ *the initial conditions for the wire.*

5.6.1 Simulations for the existing design

Two calculations were carried out for the current actuation system previously presented. The temperature for the upper and the lower SMA cables was respectively linearly varied, starting from 26°C up to 154°C. When each wire is heated, its pair (supporting wire) remains at a constant ambient temperature (26°C). In total, 32 (pseudo) time-steps ($t_s = 1, \ldots, 32$) were used for the calculations with a temperature increase $\Delta T_i = 4°C$ applied in each one. In Fig. 5.15 the results for the two calculations are regrouped. The left column (Figs. 5.15a, 5.15c) presents the calculation carried out with heating the upper (top) actuator, while the right column (Figs. 5.15b, 5.15d) the results from heating the lower (bottom) actuator.

Figure 5.15c shows the stress variation in both wires due to heating of the upper actuator while the lower one remains at a constant temperature. The temperature increases in time resulting in the development of high levels of stress in the upper wire, which reach a plateau after $t_s = 24$. The wing deforms downwards and the actuator that is connected on the lower side resists to this shape change. As a result, stresses develop to the bottom actuator as well. The inverse procedure is shown in Fig. 5.15d where heating the bottom actuator deforms the wing upwards and produces large stresses inside the actuating SMA and resulting stresses on the supporting wire. For the upward movement, larger stresses develope inside both the actuating wire and its pair in comparison with the downward deformation.

The temperature variation and the increase of the stress prompt changes in the stress-induced component ξ_s of the martensitic fraction in each actuator. Both wires begin at $\xi_{s0} \approx 45\%$ due to the initial prestrain ($\varepsilon_0 = 3\%$). Figure 5.15e illustrates the ξ_s variation in both wires due to heating of the upper actuator. Due to the temperature increase, the upper SMA undergoes an *austenitic* transformation which is concluded at $T \approx 122°C$ (i.e. for $t_s = 24$) for which $\xi_s = 0$. After this point, the actuator is no longer able to recover more length and consequently cannot deform the wing further, justifying the plateau observed in the stress diagram. With stress developed in the lower actuator, the stress-induced component increases as the material undergoes a $twinned \rightarrow detwinned$ martensitic transformation. After the complete transformation of the upper actuator, the wing will not be further cambered and both the stress and the stress-induced fraction computed for the lower actuator stabilize as well. The inverse procedure is shown in Fig. 5.15f where heating the bottom actuator is examined. The complete austenitic transformation of the actuating (here lower) wire takes place at a much higher temperature ($T \approx 150°C$) due to the increased stresses which tend to strengthen the martensitic behavior. Finally, the ξ_s for the supporting wire (here upper) stabilizes around a higher value when compared to the downward deformation, due to the increased forces previously observed (Fig. 5.15d).

Finally, in Figures 5.15a and 5.15b the deformed wing is presented, calculated with $T = 118°C$ for the upper and $T = 98°C$ for the lower actuation respectively. In the same figures, the maximum upward and downward deflection that the real actuation system is able to achieve are superimposed with dotted lines. These reference shapes were evaluated during the design process and the construction of the morphing wing (private communication with Dr. G. Jodin). The temperature value in each case has been evaluated from the working point for which the calculation arrives at each reference shape. For the cambering of the wing, the reference shape is reproduced exactly in the simulation (Fig. 5.15a) for an actuation temperature $T = 118°C$ for the upper wire. This working point is also noted in Figures 5.15c and 5.15e with a hexagram marker. For this temperature, NLB predicts only a small reminiscent martensitic fraction ($\xi = 0.04$), suggesting that the transformation is almost complete and that the actuator approaches its (lower) working limit. This is in complete agreement with the working capacities of the real constructed prototype. Respectively, for the upward deformation, the reference shape is reproduced by

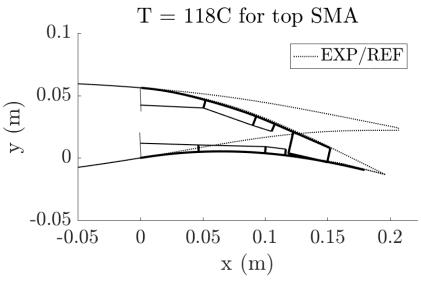

(a) *Deformation with upper actuator, superimposed with the reference shape.*

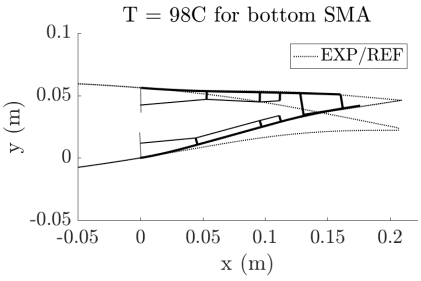

(b) *Deformation with lower actuator, superimposed with the reference shape.*

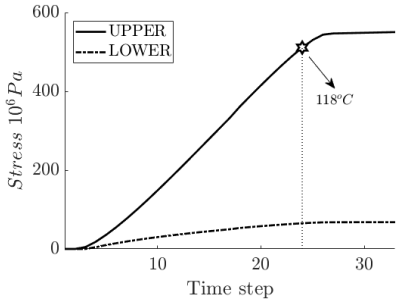

(c) *Stress variation for both actuators.*

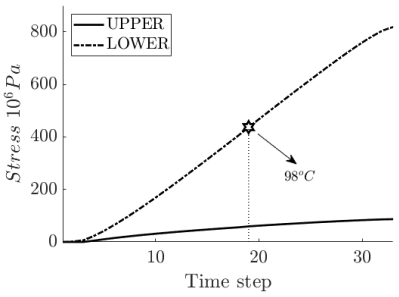

(d) *Stress variation for both actuators.*

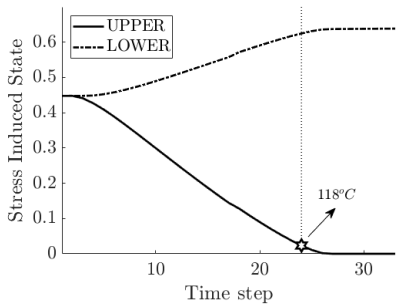

(e) ξ_s *variation for both actuators.*

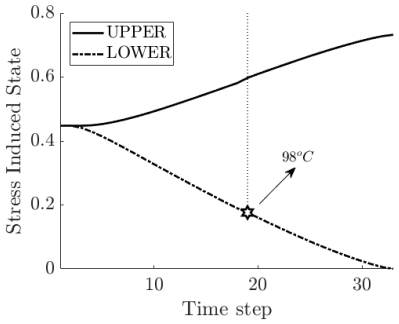

(f) ξ_s *variation for both actuators.*

Figure 5.15: *Control of the aerodynamic shape of the MWP with NLB; calculation heating* ***(a)****,* ***(c)****,* ***(e)*** *the upper and* ***(b)****,* ***(d)****,* ***(f)*** *the lower actuator respectively.*

heating the lower actuator at $T = 98°C$ (Fig. 5.15b). Same as before, the working point is also noted in Figures 5.15d and 5.15f with a hexagram marker. For this temperature, a higher reminiscent martensitic fraction is predicted ($\xi = 0.13$) by NLB, revealing that the actuator has a slightly wider upper working range. However, as the stresses significantly increase in the actuator after surpassing this temperature, it is possible that this upward deflection limit was defined in the design process in order to protect the constructed prototype from any fracture. Finally, some overall

differences could be attributed to the modeling hypotheses (e.g. gravity ignored, 2D wing).

5.6.2 Optimization of the actuation system

In the previous section, the working capabilities of the existing MWP design were examined. The temperatures, for which the reference downward and upward deflections are produced, were evaluated. In this section, it will be investigated whether the actuation system can be re-designed in order to achieve this reference deformation in a more efficient way. In the present application, the target is to identify an actuation system capable of producing the same pre-described shape while consuming less energy i.e. at a reduced actuation temperature. Modifications concerning only the design of the upper actuator will be discussed. The target shape is the deformed reference shape of maximum downward deflection examined in the previous section and illustrated in Fig. 5.16b. It is recalled here that the existing actuation system was able to produce this deflection for a temperature $T = 118°C$ in the upper actuator. It will be investigated whether a new design can produce the same deformed shape for an actuation temperature $T_u < T_{MAX} = 118°C$. To this end, the proposed design methodology examined in Section 5.4.2 is employed to revisit the actuation system.

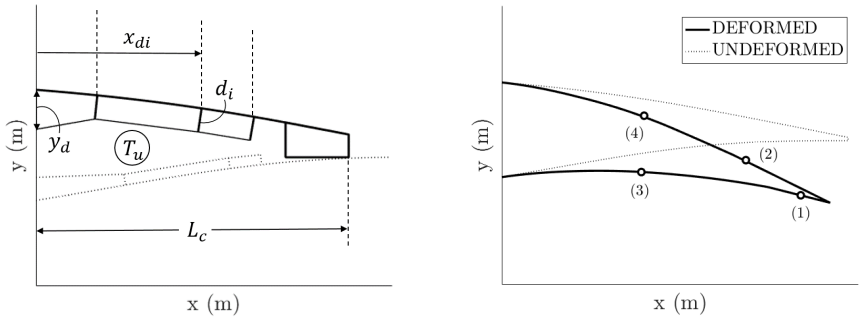

(a) *Design parameters for the upper actuator.* **(b)** *Target shape in descend and target points.*

Figure 5.16: *Revisiting the actuation system of the MWP; problem definition and parameters.*

The target deformed shape will be imposed in the design process through the minimization of the distance of selected control points placed on the upper and the lower skin of the wing from target points (Fig. 5.16b), i.e. the minimization of:

$$F_{dist} = \sum_{k=1}^{n_p} \sqrt{\left(y_{str}^k - y_{tar}^k\right)^2}$$

where n_p the total number of selected control points, y_{str}^k the vertical coordinate of the selected structural control points and y_{tar}^k the vertical target coordinate. In

order account for the contribution of the temperature, the objective function for the optimization process is calculated from:

$$F_{obj} = F_{dist} + w_g \cdot \log\left(10^{T_u/T_{MAX}}\right)$$

where a weight parameter w_g and scaling have been employed in order to keep the contribution of the design variable T_u in a range comparable to F_{dist}. The weight parameter has been evaluated through numerical investigations. The design parameters examined in this application are illustrated in Fig. 5.16a. The same number (3) of attachments was assumed in the re-design. Besides the actuation temperature T_u, the design variables to be identified by the optimization process are:

(a) the positions $x_{di} = x_d(N_i)$ of the attachments onto the skin, where N_i the upper skin beam node with $i = 1,2,3$,

(b) the offset distance d_i for each attachment, with $i = 1,2,3$, and

(c) the vertical distance y_d below the upper skin at which the actuator is pinned.

Three optimization cases will be discussed in total. The first two can be summarized as:

- **OPT1**: with $w_g = 1 \cdot 10^{-3}$ and $n_p = 2$
- **OPT2**: with $w_g = 1 \cdot 10^{-3}$ and $n_p = 4$

In OPT1, only points 1 and 2 from Fig. 5.16b were used for the evaluations of the F_{dis} and the objective function. For the OPT2 case, all four points illustrated in Fig. 5.16b were used in the evaluation of the objective function. In both cases, the same weight factor has been used. The design temperature was bounded as:

$$T_u \in [40, T_{MAX}] \subset \mathbb{Z}$$

with $T_{MAX} = 118°C$ as previously mentioned. Once again, the temperature was set as an integer to speed-up the optimization process. For the attachments:

$$N_i \in [2, N_{MAX}] \subset \mathbb{Z}$$

where $N_{MAX} = 24$,the latest acceptable FE node for the attachment of the actuator; after this node, the rigid body is attached. An additional constrain is set for the attachments:

$$N_1 < N_2 < N_3$$

as the order of the connections should be respected for a solution to be valid. The distance between the upper skin and the position where the actuator was pinned was bounded as:

$$y_d \in [0.005, 0.055] \subset \mathbb{R}$$

Finally, all the offset distances were set equal $d_1 = d_2 = d_3 = d$ and bounded as:

$$d \in [0.001, 0.015] \subset \mathbb{R}$$

The bounds for the y_d and the d were assumed after carefull considerations of the overall wing geometry. The third and final optimization case is:

- **OPT3**: for a fixed temperature $T_u = 110°C$ with $w_g = 0$ and $n_p = 4$

In OPT3, the actuation temperature is fixed. With a constant value for the T_u, only the geometric parameters remain to be identified. To negate the contribution of the temperature in the objective function, the weight factor was set $w_g = 0$ so that $F_{obj} = F_{dist}$. The same bounds stand for the design parameters except for the T_u which is no longer a variable. All four points illustrated in Fig. 5.16b were used in the evaluation of the objective function.

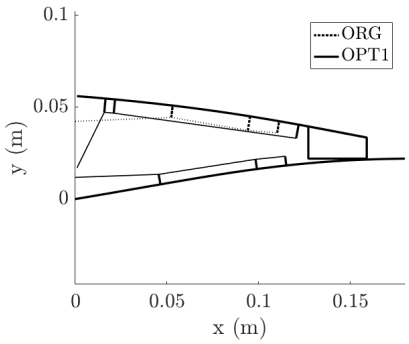

(a) *Undeformed configuration.*

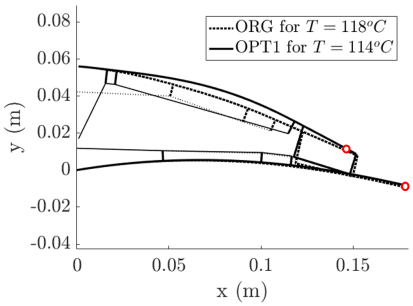

(b) *Deformed configuration.*

Figure 5.17: *Comparison between OPT1 and the original design (ORG); they arrive at the target position for different values of temperature. With circles, the y^k_{str} used in the evaluation of F_{obj}.*

For every calculation, the initial conditions were same with the ones examined in the previous section, i.e. $\varepsilon_0 = 3\%$, $\sigma_0 = 0$, $\xi_{s0} = 45\%$ and $T_0 = 26°C$. All the optimization cases were terminated after the maximum number of 60 stagnated generations was reached. For OPT1, a total of 255 generations were evaluated before the calculation was terminated. For OPT2 and OPT3, a total of 200 and 311 generations respectively were evaluated. All the re-designed configurations are illustrated in Figures 5.17-5.19, both at an undeformed and at a deformed position. The structural control points, from which the coordinates y^k_{str} are evaluated, are noted with the circular markers. As a reference, the original configuration examined in Section 5.6.1 is superimposed in all of these figures with dotted lines and will be referred to as ORG. The results for all the studies are regrouped in Table 5.6. The design parameters of the original configuration (ORG) examined in the previous section are also included for comparison. A characteristic length $L_c = 0.1589m$

(Fig. 5.16a) has been used for the normalization of the geometric values. The attachment positions are calculated as $x_{di} = x_d(N_i)$, where N_i the nodes of the upper skin beam.

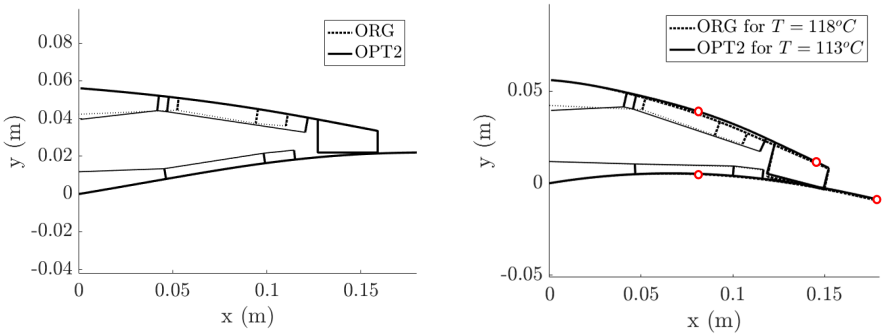

(a) *Undeformed configuration.* **(b)** *Deformed configuration.*

Figure 5.18: *Comparison between OPT2 and the original design (ORG); they arrive at the target position for different values of temperature. With circles, the* y^k_{str} *used in the evaluation of* F_{obj}.

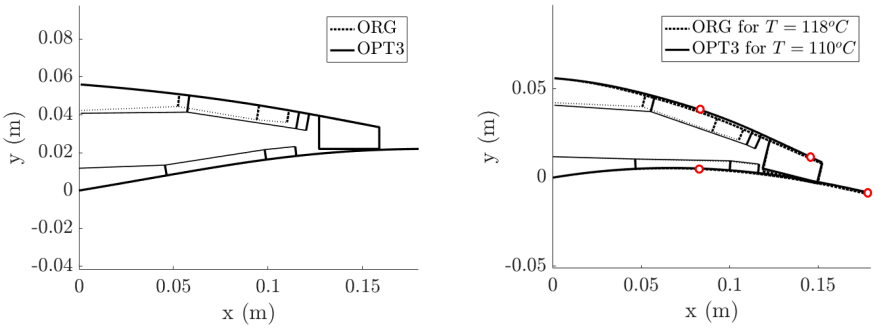

(a) *Undeformed configuration.* **(b)** *Deformed configuration.*

Figure 5.19: *Comparison between OPT3 and the original design (ORG); they arrive at the target position for different values of temperature. With circles, the* y^k_{str} *used in the evaluation of* F_{obj}.

In Fig. 5.17, the design produced by OPT1 is examined at an undeformed and at a deformed position. Compared to the original configuration, both of the first two attachments are moved to the left, towards the front part of the actuator (Fig. 5.17a). The calculation suggests that these two attachments could be replaced by one, simplifying the proposed design. The third and final attachment point is displaced towards the other end of the actuator, at the last acceptable FE node ($N_3 = 24$). To achieve the deformed shape, the vertical distance y_d is significantly increased while a slight increase for the offset distance is also observed (Table 5.6). Fig. 5.17b

presents the deformed OPT1 configuration in comparison to the deformed ORG. The target used in the evaluation of the objective function is sufficiently reached by the optimized configuration, resulting in a very low F_{dist} as presented in Table 5.6. The OPT1 produces the necessary deflection at a lower actuation temperature $T_u = 114°C$, compared to ORG ($T_u = 118°C$). However, the overall deformed aerodynamic profile presents some difference with the one produced by ORG. Due to the new attachment locations, an induced curvature is observed for the upper skin side. This is attributed to the fact that only two points were used in the evaluation of the F_{obj} and is expected to be alleviated in the following cases where four points have been used.

	ORG	**OPT1**	**OPT2**	**OPT3**
$\mathbf{T_u}$ $(°\mathbf{C})$	118	114	113	**110**
$\mathbf{x_{d1}/L_c}$ $(\%)$	33.4	10.4	26.8	36.7
$\mathbf{x_{d2}/L_c}$ $(\%)$	60.0	13.7	30.1	73.3
$\mathbf{x_{d3}/L_c}$ $(\%)$	70.0	76.6	76.6	76.6
$\mathbf{y_d/L_c}$ $(\%)$	8.7	24.6	10.4	9.6
$\mathbf{d/L_c}$ $(\%)$	≈ 4.5	4.7	5.0	5.6
$\mathbf{F_{dist}/L_c}$ $(\%)$	–	0.4	2.2	2.6

Table 5.6: *Optimization results for the different cases compared with the original design (ORG); the temperature T_u was fixed for OPT3. The initial conditions referenced in Section 5.6.1 have been assumed for the actuator.*

In Fig. 5.18, the design produced by OPT2 is shown. The first two attachments are moved towards the front (Fig. 5.18a), slightly to the left and really close to the first ORG attachment. Once again, the calculation suggests that these two attachments could be replaced by one. The third attachment point is also placed at the last acceptable FE node ($N_3 = 24$). The vertical distance y_d predicted is marginally higher than the value in ORG but the offset distance is further increased, when compared to OPT1 (Table 5.6). The target shape is sufficiently reached by the optimized deformed configuration (Fig. 5.18b). The OPT2 produces the necessary deflection at an actuation temperature $T_u = 113°C$ which is lower, even compared to OPT1. However, the F_{dist} is increased (Table 5.6) as the number of the points used for the evaluation of the objective function is doubled. Regardless, the overall deformed aerodynamic profile is almost identical to the one produced by ORG due to the fact that four control points were used in the evaluation of the objective function.

For the final case, the actuation temperature is fixed at $T_u = 110°C$ and only the geometric parameters are searched for. The design produced by OPT3 is illustrated in Figures 5.19a and 5.19b. The first attachment is slightly moved to the right compared to the ORG configuration, while the two remaining are displaced at $N_2 = 23$ and $N_3 = 24$ respectively. The calculation supports the previous

observations that only two attachments are sufficient in producing the deformed shape. The predicted vertical distance y_d is lower than in OPT1 and OPT2 and almost equal to the ORG (Table 5.6). However, higher offsets are predicted in OPT3 so that the design can achieve the downward deformation with the reduced actuation temperature. In general, there is great agreement between the OPT2 and OPT3 designs, besides the difference in offset values which is attributed to the different actuation temperature. In OPT3, the deformed wing (Fig. 5.19b) approaches closely the target giving a lower $F_{dist} = 4.2 \cdot 10^{-3}$ when compared to OPT2. No apparent differences are observed in the overall deformed aerodynamic shape between OPT3, OPT2 and ORG. Finally, it should be mentioned that the existing ORG architecture is well designed as OPT2 and OPT3 demonstrated. Only slight changes on the attachment connections are needed in order to produce an actuating system that will consume less energy.

5.7 Conclusion

In the present chapter of the thesis, the use of SMA actuators for the shape control of flexible deformable aeronautical structures was discussed. The study presented is dedicated on the design of optimally controlled configurations. A fast and robust numerical design approach has been developed to be used in the prediction of smart configurations, able to achieve pre-described shapes under the control of SMA actuators. The methodology developed has been based on the following steps: (a) a robust algorithm that solves the “coupled structure-SMA" problem in the context of a FE analysis by including a 1D constitutive model, and (b) the coupling of the whole procedure with an optimization code for the design of actuation architectures. In the context of morphing, the inclusion of flexible deformable structures is extremely relevant, rendering the inclusion of a nonlinear structural analysis essential.

A first series of simulations examined the control of cantilever beam with an SMA actuator. The physical processes taking place during one heating-cooling cycle were analyzed in detail. A strongly nonlinear behavior for the beams has been ontained, attributed to the thermo-mechanical SMA behavior, the large deformation of the structure and the non-conservativity of the force. The approach showed a very good agreement with a reference test case and the hysteretic behavior of the SMA actuator was accurately captured. The has been used used along with a stochastic optimization for the design of an actuation system controlling a simplified geometry. A target aerodynamic target shape was closely captured and there was a reasonable agreement between the predicted controlled configurations. A significant difference in the temperature prediction was observed when a linear structure was used for the FE modelling. The investigation highlighted the importance of nonlinear effects in the design process. Evaluating the results of the optimization, the design led to a solution were fewer actuators are needed and the configuration was found capable to achieve even larger deformation targets. The complete analysis attested to a fast and robust methodology that provides a design tool capable of determining optimal

configurations controlled by SMAs.

Finally, the proposed methodology has been also evaluated in the shape control and re-design of a realistic aeronautical configuration. It has been shown that the solver predicted the deformation and estimated the actuation temperature for a morphing prototype. The design methodology was adopted to revisit and optimize the architecture of the actuation system so that it consumes less energy. Only the upper actuator, responsible for the downward deformation of the wing was discussed. Three new designs have been evaluated in the current investigation, all able to produce the target deformation at a lower actuation temperature compared to the original actuation architecture. All the designs suggested that the number of attachments could be reduced and as a result, the proposed systems have had less complex and more robust architectures. The optimized actuation systems have provided lower energy consumption while maintaining their functioning capabilities, which is an important aspect of future "green" aircraft transport.

Bibliography

[ABT+12] S. Ameduri, A. Brindisi, B. Tiseo, A. Concilio, and R. Pecora. Optimization and integration of shape memory alloy (SMA)-based elastic actuators within a morphing flap architecture. *Journal of Intelligent Material Systems and Structures*, 23(4):381–396, March 2012.

[ADS78] J. H. Argyris, P. C. Dunne, and D. W. Scharpf. On large displacement-small strain analysis of structures with rotational degrees of freedom. *Computer Methods in Applied Mechanics and Engineering*, 14(3):401–451, June 1978.

[AS81] J. H. Argyris and Sp. Symeonidis. Nonlinear finite element analysis of elastic systems under nonconservative loading-natural formulation. part I. Quasistatic problems. *Computer Methods in Applied Mechanics and Engineering*, 26(1):75–123, April 1981.

[AS97] F. Auricchio and E. Sacco. A one-dimensional model for superelastic shape-memory alloys with different elastic properties between austenite and martensite. *International Journal of Non-Linear Mechanics*, 32(6):1101–1114, November 1997.

[ATL97] F. Auricchio, R. L. Taylor, and J. Lubliner. Shape-memory alloys: macromodelling and numerical simulations of the superelastic behavior. *Computer Methods in Applied Mechanics and Engineering*, 146(3):281–312, July 1997.

[BBM10] A. Banerjee, B. Bhattacharya, and A. K. Mallik. Optimum Discrete Location of Shape Memory Alloy Wire for Enhanced Actuation of

a Compliant Link. *Journal of Mechanical Design*, 132(2), February 2010.

[BHBB97] L. C. Brinson, M. S. Huang, C. Boller, and W. Brand. Analysis of Controlled Beam Deflections Using SMA Wires. *Journal of Intelligent Material Systems and Structures*, 8(1):12–25, January 1997.

[Bir97] V. Birman. Review of Mechanics of Shape Memory Alloy Structures. *Applied Mechanics Reviews*, January 1997.

[BL96] J. G. Boyd and D. C. Lagoudas. A thermodynamical constitutive model for shape memory materials. Part I. The monolithic shape memory alloy. *International Journal of Plasticity*, 12(6):805–842, January 1996.

[BPL+09] S. Barbarino, R. Pecora, L. Lecce, A. Concilio, S. Ameduri, and E. Calvi. A Novel SMA-based Concept for Airfoil Structural Morphing. *Journal of Materials Engineering and Performance*, 18(5):696–705, August 2009.

[BPL+11] S. Barbarino, R. Pecora, L. Lecce, A. Concilio, S. Ameduri, and L. De Rosa. Airfoil Structural Morphing Based on S.M.A. Actuator Series: Numerical and Experimental Studies. *Journal of Intelligent Material Systems and Structures*, 22(10):987–1004, July 2011.

[Bri93] L.C. Brinson. One-Dimensional Constitutive Behavior of Shape Memory Alloys: Thermomechanical Derivation with Non-Constant Material Functions and Redefined Martensite Internal Variable. *Journal of Intelligent Material Systems and Structures*, 4(2):229–242, April 1993.

[BSMN06] E. L. Bandeira, M. A. Savi, P. C. da Camara Monteiro, and T. A. Netto. Finite Element Analysis of Shape Memory Alloy Adaptive Trusses with Geometrical Nonlinearities. *Archive of Applied Mechanics*, 76(3):133, March 2006.

[CHL06] J.-H. Chung, J.-S. Heo, and J.-J. Lee. Implementation strategy for the dual transformation region in the Brinson SMA constitutive model. *Smart Materials and Structures*, 16(1):N1–N5, November 2006.

[CL18] A. Concilio and L. Lecce. Chapter 1 - Historical Background and Current Scenario. In A. Concilio, I. Dimino, L. Lecce, and R. Pecora, editors, *Morphing Wing Technologies*, pages 3–84. Butterworth-Heinemann, January 2018.

[FF04] F. Filippou and G.L. Fenves. Methods of analysis for earthquake - resistant structures. *Earthquake Engineering: From Engineering Seismology to Performance-Based Engineering*, 6:36–43, May 2004.

[GHM+12] M. Ghommem, M. R. Hajj, D. T. Mook, B. K. Stanford, P. S. Beran, R. D. Snyder, and L. T. Watson. Global optimization of actively morphing flapping wings. *Journal of Fluids and Structures*, 33:210–228, August 2012.

[GSR+15] J. Gurvan, J. Scheller, K. J. Rizzo, E. Duhayon, J. F. Rouchon, and M. Braza. Dimensionnement d'une maquette pour l'investigation du morphing électroactif hybride en soufflerie subsonique. In *22e Congrès Français de Mécanique*, pages 1–13, Lyon, France, 2015. Thanks to the AFM, Association Française de Mécanique.

[GTBB05] X. Gao, T. L. Turner, D. Burton, and L. C. Brinson. Finite element analysis of adaptive-stiffening and shape-control SMA hybrid composites. In *Smart Structures and Materials 2005: Active Materials: Behavior and Mechanics*, volume 5761, pages 406–416. International Society for Optics and Photonics, May 2005.

[IF11] U. Icardi and L. Ferrero. SMA Actuated Mechanism for an Adaptive Wing. *Journal of Aerospace Engineering*, 24(1):140–143, January 2011.

[JMS+17] G. Jodin, V. Motta, J. Scheller, E. Duhayon, C. Döll, J.F. Rouchon, and M. Braza. Dynamics of a hybrid morphing wing with active open loop vibrating trailing edge by time-resolved PIV and force measures. *Journal of Fluids and Structures*, 74(Supplement C):263–290, October 2017.

[Jod17] G. Jodin. *Hybrid electroactive morphing at real scale - application to Airbus A320 wings*. Phd thesis, Toulouse, INPT, October 2017.

[LA14] L. Leonardo and C. Antonio, editors. *Shape Memory Alloy Engineering: For Aerospace, Structural and Biomedical Applications*. Butterworth-Heinemann, Amsterdam, 1 edition edition, October 2014.

[LR90] C. Liang and C.A. Rogers. One-Dimensional Thermomechanical Constitutive Relations for Shape Memory Materials. *Journal of Intelligent Material Systems and Structures*, 1(2):207–234, April 1990.

[MKK+18] T. Machairas, A. Kontogiannis, A. Karakalas, A. Solomou, V. Riziotis, and D. Saravanos. Robust fluid-structure interaction analysis of an adaptive airfoil using shape memory alloy actuators. *Smart Materials and Structures*, 27(10):105035, sep 2018.

[SJM+19] N. Simiriotis, G. Jodin, A. Marouf, P. Elyakime, Y. Hoarau, J. C. R. Hunt, J. F. Rouchon, and M. Braza. Morphing of a supercritical wing by means of trailing edge deformation and vibration at high Reynolds numbers: Experimental and numerical investigation. *Journal of Fluids and Structures*, July 2019.

[SLHW97] S. G. Shu, D. C. Lagoudas, D. Hughes, and J. T. Wen. Modeling of a flexible beam actuated by shape memory alloy wires. *Smart Materials and Structures*, 6(3):265–277, jun 1997.

[SM04] S. Seelecke and I. Müller. Shape memory alloy actuators in smart structures: Modeling and simulation. *Applied Mechanics Reviews*, 57(1):23–46, January 2004.

[SMS14] A. G. Solomou, T. T. Machairas, and D. A. Saravanos. A coupled thermomechanical beam finite element for the simulation of shape memory alloy actuators. *Journal of Intelligent Material Systems and Structures*, 25(7):890–907, May 2014.

[TKS86] K. Tanaka, S. Kobayashi, and Y. Sato. Thermomechanics of transformation pseudoelasticity and shape memory effect in alloys. *International Journal of Plasticity*, 2(1):59–72, January 1986.

[TM19] Inc. The MathWorks. *Global Optimization Toolbox*. Natick, Massachusetts, United State, 2019.

[Yaw08] L. L. Yaw. *Co-rotational Meshfree Formulation for Large Deformation Inelastic Analysis of Two-dimensional Structural Systems*. University of California, Davis, 2008. Google-Books-ID: YXrJ86o74aoC.

[ZDLT12] G. Zavarise, L. De Lorenzis, and R. L. Taylor. A non-consistent start-up procedure for contact problems with large load-steps. *Computer Methods in Applied Mechanics and Engineering*, 205-208:91–109, January 2012.

Chapter 6

Conclusions & Outlook

This chapter presents an overview of the work performed in this thesis. Perspectives and future investigations are also discussed.

6.1 Conclusions

The present thesis investigated the physical mechanisms related to the flow dynamics around supercritical wings. The investigations were focused on the modifications caused by the application of morphing, targeting increased aerodynamic performance in the context of future wing designs. The numerical studies have been carried out in high Reynolds numbers employing efficient advanced turbulence modelling approaches. In this context, a novel approach, based on reinjection of turbulence in shear layers, has been extended to three-dimensional flows to account for small scale dynamics that cause energy backscatter. The physical mechanisms related to interfacial dynamics developed in high Reynolds number flows inside separated shear layers and wakes were addressed.

Based on this analysis, morphing concepts were employed for the manipulation of the turbulent flow and the enhancement of the aerodynamic efficiency. The electroactive morphing realized by Macro-Fiber Composite piezoelectric patches disposed along the span of an A320 wing was investigated. The actuators introduced higher-frequency vibrations and low-amplitude deformations of the trailing-edge region. The flow was studied by means of Particle Image Velocimetry measurements and high-fidelity numerical simulations. Finally, in the context of hybrid electroactive morphing, the use of SMA actuators was also discussed for the shape control of flexible deformable aeronautical structures. An electrostructural model has been developed to simulate an SMA-based actuation system able to impose

large deflections at low actuation frequencies for a morphing wing . A methodology that allows for the optimal design of configurations able to attain target shapes utilizing SMA actuators was presented. The main conclusions are outlined in the following parts; the thesis also led to a series of publications which are listed in page 189.

Turbulence modelling with stochastic forcing

In Chapter 3, a stochastic forcing turbulence modelling approach was examined. It consisted of forcing source terms, included in the turbulent transport equations, causing variations of the eddy viscosity. The forcing was based on the turbulent kinetic energy reconstructed from high-order low-energy POD modes. It was shown that this forcing is contained inside the sheared regions, identified from the POD, without affecting irrotational areas of the flow. The stochastic behavior of the forcing, linked to the nature of small scale motions, was imposed through a random number generator. The methodology was examined along the OES and the DOES approaches for the transonic flow on a supercritical wing.

It was shown that the source terms increased the dissipation rate locally and therefore, the sheared regions were modelled with reduced effective turbulent viscosity. This limited the excessive generation of turbulence diffusion which characterizes standard modelling approaches employing downscale assumptions. These terms produced fluctuations of the turbulent stresses that cause the generation of intermediate size vortices. The flow field and the buffet cycle prediction were examined with the stochastic forcing contribution. The shock structure remained practically unchanged and the buffet cycle was found to be more stable. The travelling length of the shock was reduced and consequently the intensity of the shearing in the separation zones was mitigated. The flow dynamics were evaluated from signals monitoring the surface pressure on the wing. The buffet frequency was slightly reduced and the Strouhal number was closer to the experimentally measured value. The root-mean-square and the mean pressure values were reduced and the intensity of pressure fluctuations was mitigated.

The flow detachment was attenuated and the width of the wake was reduced along with the entrainment velocity. Velocity profiles with sharp slopes demonstrated the thinning of the wake and stronger shearing on the edges of the profiles. The modelled chaotic dynamics directly affected the prediction of the aerodynamic forces. An increase of the lift and a decrease of the drag was obtained and the force predictions were closer to the experimental measurements. The temporal variation of the forces presented less sharp peaks and a significant decrease of the root-mean-square value.

Finally, the turbulence transition location was considered in order to examine the effects on the shock unsteadiness and the intense pressure fluctuations. The suppression of the turbulent source terms was employed to maintain a laminar incoming boundary layer profile on the suction side of the airfoil. It was demonstrated that the suppression of turbulence upstream of the shock stabilized the flow and prevented

the shock front from reaching the leading edge of the wing. A pressure plateau was established over the first half of the wing which was also in good agreement with the DNS carried out in the TFAST project. The stochastic forcing in combination with the transition location produced an improvement of the wall-pressure prediction.

The present study illustrated the influence of the turbulence reinjection on the shear-layer thinning and consequently on the SWBLI and its upstream regions. These feedback effects have been used for the design of a transonic morphing prototype used in the SMS project targeting increased aerodynamic performance in cruise.

High-frequency low-amplitude morphing near the trailing edge

The present thesis showed that the shear-sheltering effects of the turbulence reinjection through stochastic forcing can be materialized with a near-trailing edge actuation, experimentally realized by MFC piezoactuators. In Chapter 4, the investigation was focused on a morphing application in which the aerodynamic performance is enhanced by a high-frequency low-amplitude actuation which introduces small-scale fluctuations in the flow. A large experimental database in low subsonic regimes was employed to complete the numerical simulations performed for the analysis of the main flow characteristics and wake dynamics in $Re \approx 10^6$, corresponding to take-off and landing flight phases. A detailed parametric study of the vibration frequencies and amplitudes allowed evaluation of optimal ranges in respect of lift-to-drag ratio improvement.

It was shown that actuation frequencies close to the natural frequencies shortened the formation region of the shear layer and led to a reorganization of the wake through a "lock-in" mechanism. The vibrating trailing edge creates smaller-scale turbulent eddies and adds kinetic energy in the wake. These smaller-scale eddies interacted either with the upper or the lower shear layer, depending on the actuation frequency and the natural shedding frequency of the related instability. It was shown that this interaction strengthens the respective shear layer (shielding) and enhances blocking effects, limiting the wake expansion and the entrainment. The related natural instabilities were "locked-in" with the actuation frequency and as a result, a suppression of pre-existing predominant instability modes was achieved. A POD analysis showed that new modes replaced the natural ones in the shear layers and the velocity profiles showed a thinning of the wake region. The application of the morphing was also found to enhance the two-dimensional behavior of the flow. The spanwise velocity fluctuations were reduced implying the suppression of three-dimensional secondary instability modes. The streamwise vortex tubes were weakened and the wake became thinner. Uniform spanwise aligned vortex tubes were generated in the flow and the secondary instabilities associated with spanwise undulations was practically suppresed.

The effect of the vibration amplitude and the streamwise length of the actuators were also examined. For actuation frequencies lower than the natural ones, the combined increase of the patch-amplitude lengths, intensified the chaotic character

of the flow. The spectral content of the signals in the wake was increased due to the additional kinetic energy introduced in the flow due to the larger amplitudes/patches. No breakdown of the natural coherent structures was identified. For the higher actuation frequencies, neither the amplitude nor the patch length variation had any considerable effect on the wake dynamics; the frequency was found to be the main driving factor.

The thinning of the wake region as well as vorticity feedback effects, enabled a significant increase of the aerodynamic performance through surface pressure modification. The lift-to-drag was increased in every morphing case examined. By the present electroactive morphing concept, an order of 3% increase in lift has been achieved and at the same time a 1% decrease in the drag. Optimal frequency ranges were identified suggesting that the actuation frequency can be adapted to the incoming flow conditions and the chord of the wing. The patch length variation provided only minor changes in the forces but the actuation amplitude had significant effects. The aerodynamic forces presented a non-linear behavior with the variation of the amplitude. It was demonstrated that optimal frequency-amplitude combinations exist for which a maximum lift-to-drag ratio can be identified. The *rms* of the force signals was an increasing linear function of the amplitude and the slope of the *rms* variation depended on the actuation frequency.

Low-freqeuncy large-deflection morphing

The hybrid morphing concept entails the combined actuation of different classes of electroactive actuators. To this end, in Chapter 5 the use of SMAs for the shape control was discussed. The present study was dedicated on a fast and robust numerical design method of new actuation architectures and optimally controlled configurations. The physical processes and the hysteretic behavior of the SMA actuators were analyzed in detail and the approach was validated showing very good agreement with reference numerical studies.

The proposed method was coupled with an optimization solver for the design of controlled configurations able to achieve pre-described shapes. A simplified structure was given a desirable aerodynamic shape and optimal disposition of the SMA actuators and actuation temperatures were obtained. The analysis put in evidence that the nonlinear effects are extremely relevant and should always be accounted for during the design process. The design led to a solution where less actuators were active, producing a less complex architecture than what was originally assumed for the shape control. The configuration was also found capable to achieve even larger deformation targets.

Finally, the proposed methodology was also evaluated in the shape control and re-design of a realistic morphing wing. It was demonstrated that the solver was able to predict the deformation and estimate the actuation temperature for the existing actuation architecture. The proposed methodology was adopted to revisit the architecture of the actuation system in order to achieve reduced energy consumption. Three new designs were proposed and proven able to produce the target deformation

at a lower actuation temperature and utilizing fewer attachments resulting in a more robust architecture. Compared to the original design, the proposed systems were greener and safer while maintaining their working capabilities.

The present electrostructural model has been presented to *AIRBUS Emerging technologies and Concepts Toulouse - ETCT(XCT)*, for the wing morphing of a large UAV (THOR) to be tested in real flight in 2020.

6.2 Perspectives

After summarizing the main conclusions derived from the present work, future investigations are discussed in this section. The outlook is split in three parts, following the general outline of the thesis.

Regarding stochastic forcing turbulence model, a few further developments and investigations are suggested:

- The flow decomposition in the stochastic forcing approach splits the turbulent fluctuations in a the downscale $\hat{u}(x,t)$ (direct energy cascade) and an upscale $\check{u}(x,t)$ part (energy backscatter). This decomposition of the flow variables introduces additional correlation terms to be modelled in the turbulent transport equations. Further refined experiments and a subsequent analysis of the turbulence interfaces could model the respective correlation terms separately and according to their physical contribution to the flow dynamics.

Regarding the high-frequency low-amplitude morphing, the results presented offer the possibility for novel trailing edge actuation approaches and the design of future morphing prototypes, summarized as follows:

- For a swept wing, the variation of the chord yields a change of the local Reynolds number along the span. This should cause a shift in the local natural frequencies, even though in this Reynolds number range (order of millions) the modulations of the Strouhal number are moderate. It would be interesting to examine a variable morphing application along the span. Based on the analysis presented here for a constant actuation frequency, morphing can be adapted to be applied along the span with respect to the local modulations of the natural instability frequencies.

- From the investigations presented, new morphing concepts can emerge. The examined trailing-edge actuation introduced in the flow a sinusoidal oscillation and the dynamic response of the system mostly correlated with the frequency. Currently, we examine multiple frequencies and stochastic electric signals for the existing actuation system. By specifically steering the piezoactuators placed along the span to generate spatial undulations of the aerodynamic surface, the introduction of spatially travelling waves could also be examined. As a first step, a numerical analysis could be devoted to the

investigation and optimization of the parameters (e.g. length and time scales) of these travelling waves.

Shape control of aeronautical configurations continues to be in the center of interest of industrial research. Emerging technologies are employed to adapt the aerodynamic profiles to different flight phases and electroactive morphing is adopted since it proposes an efficient solution. To this end, SMAs will soon be realistic at an industrial level for aircraft manufacturers since they are coherent with the concept of future electric aircrafts. The method developed in the present thesis could be expanded as follows:

- The design procedure can be applied for 3D configurations were more design parameters are introduced and the number of actuators and degrees of freedom increase significantly. To this end, it is essential to couple the propose solver with a faster optimization method to handle the large size of the problem.

- The coupling of the electrostructural model developed in this thesis with the CFD solver NSMB is currently examined. Fluid-structure interaction simulations are essential in order to determine whether the controlled configuration is able to sustain the external aerodynamic loading variations and simultaneously maintain the target profiles. The methodology can be further expanded with models describing the electrothermal response of the SMA material. The complete multi-physical system will provide the framework for realistic electroactive fluid-structure interaction simulations.

- The methodology developed can be used in training control systems. Multiple scenarios under aerodynamic loading can be simulated in order to produce correlations between expected deformations and stress-strain measurements on the controlled configuration. In this way, control laws can be produced to be used on the constructed design. As developed in the SMS European project, the complete morphing approach, besides the use of electroactive material, also incorporates the sensor-actuation connection and the closed-loop control laws in order to adapt the smart structures to the response of the complete dynamic system.

List of publications

The present thesis has led to the following publications.

Journal Publications in Peer-Reviewed Journals

- **N. Simiriotis**, M. Fragiadakis, J.-F. Rouchon, M. Braza (2020). An efficient algorithm for the shape control and optimization of aeronautical configurations using shape memory alloy actuators. *Submitted*, Smart Materials and Structures.

- **N. Simiriotis**, G. Jodin, A. Marouf, P. Elyakime, Y. Hoarau, J.C.R. Hunt, J.-F. Rouchon, M. Braza (2019). Morphing of a supercritical wing by means of trailing edge deformation and vibration at high Reynolds numbers: Experimental and numerical investigation. Journal of Fluids and Structures, 91.
URL https://doi.org/10.1016/j.jfluidstructs.2019.06.016

- J.-B. Tô, **N. Simiriotis**, A. Marouf, D. Szubert, I. Asproulias, D.M. Zilli, Y. Hoarau, J.C.R. Hunt, M. Braza (2019). Effects of vibrating and deformed trailing edge of a morphing supercritical airfoil in transonic regime by numerical simulation at high Reynolds number. Journal of Fluids and Structures, 91.
URL https://doi.org/10.1016/j.jfluidstructs.2019.02.011

- A. Marouf, Y. Bmegaptche, **N. Simiriotis**, J.-B. Tô, J.-F. Rouchon, Y. Hoarau, M. Braza (2019). Numerical investigation of frequency-amplitude effects of dynamic morphing for a high-lift configuration at high Reynolds number. International Journal of Numerical Methods for Heat and Fluid Flow, Vol. ahead-of-print.
URL https://doi.org/10.1108/HFF-07-2019-0559.

Articles in books after international Conferences

- A. Marouf, **N. Simiriotis**, J.-B. Tô, Y. Bmegaptche, Y. Hoarau, M. Braza (2020) DDES and OES Simulations of a Morphing Airbus A320 Wing and Flap in Different Scales at High Reynolds. In: Hoarau Y., Peng SH.,

Schwamborn D., Revell A., Mockett C. (Sci. Eds.) Progress in Hybrid RANS-LES Modelling. Notes on Numerical Fluid Mechanics and Multidisciplinary Design, vol 143. Springer.

- G. Jodin, **N. Simiriotis**, A. Aalilija, A. Marouf, Y. Hoarau, G. Harran, J.-F. Rouchon, M. Braza (2019). Fluid-Structure Interaction and Control Around Vibrating and Morphing Configurations at High Reynolds Number. In: Zhou Y., Kimura M., Peng G., Lucey A., Huang L. (Sci. Eds.) Fluid-Structure-Sound Interactions and Control. FSSIC 2017. Lecture Notes in Mechanical Engineering. Springer. ISBN 978-981-10-7542-1.

- D. Szubert, I. Asproulias, **N. Simiriotis**, Y. Hoarau, M. Braza (2018). Numerical Simulation of a 3-D Laminar Wing in Transonic Regime. In: Hoarau Y., Peng SH., Schwamborn D., Revell A. (Sci. Eds.) Progress in Hybrid RANS-LES Modelling. HRLM 2016. Notes on Numerical Fluid Mechanics and Multidisciplinary Design, vol 137. Springer.

Articles in international Conferences/Symposia

- **N. Simiriotis**, G. Jodin, A. Marouf, Y. Hoarau, J.-F. Rouchon, M. Braza (2018). Electroactive morphing on a supercritical wing targeting improved aero-dynamic performance and flow control in high Reynolds numbers. In 53^{rd} 3AF International Conference on Applied Aerodynamics AERO 2018 - Congrès 3AF, Salon de Provence, France. *Best Communication Award*.

- **N. Simiriotis,** K. Diakakis, G. Jodin, F. Kramer, A. Marouf, Y. Hoarau, J.-F. Rouchon, G. Tzabiras, M. Braza (2019). Synthesis on High-Fidelity Numerical simulation of a morphing A320 wing in subsonic speeds and sensitivity evaluation. In AIAA Aviation 2019 Forum, Dallas-TX, USA.

- **N. Simiriotis**, A. Marouf, G. Jodin, Y. Hoarau, J.C.R. Hunt, J.-F. Rouchon, M. Braza (2019). High-Fidelity Numerical simulation of morphing and the suppression of the 3D instabilities. International Symposium FSSIC2019 on Flow Structure Sound Interactions and Control, Chania, Crete, Greece.

- **N. Simiriotis**, D. Szubert, I. Asproulias, J. Hunt, M. Braza (2018). Transonic buffet over a supercritical wing by means of Organized Eddy Simulation with stochastic forcing capturing detached flow dynamics. IUTAM Symposium on Critical flow dynamics around moving/deformable structures with design applications, Santorini, Greece.

Appendix

Appendix A. Proper Orthogonal Decomposition

The Proper Orthogonal Decomposition (POD) is a powerful method applied in the data analysis of nonlinear phenomena. In the context of fluid mechanics, it is used in the eduction and study of the coherent structures developed in the flow. The POD method was introduced first by Karhunen [Kar46] and Loéve [Loè45] and applied in the context of turbulent flows by Lumley [Lum67] and Berkooz et al. [BHL93]. The method is a linear procedure that creates an orhogonal basis from a collection of flow data. The decomposition is essentially a procedure that transforms the matrix that includes the data to be analysed into a canonical form in order to retrieve its eigenvectors.

The flow field solution can be split in spatial modes and temporal coefficients sorted by their importance (relative energy) in the flow. The tempo-spatial evolution of a flow variable $u(\mathbf{x},t)$ can be approximated as:

$$u(\boldsymbol{x},t) = \overline{u}(\boldsymbol{x}) + u'(\boldsymbol{x},t) = \overline{u}(\boldsymbol{x}) + \sum_{n=2}^{N} \alpha_n(t)\Phi_n(\boldsymbol{x}) \tag{A.1}$$

i.e. as the summation of the decoupled coefficients a_n and Φ_n varying only temporally (t) or spatially $\boldsymbol{x}$ respectively. This finite sum expression becomes exact as $n \to \infty$. The $\overline{u}(\boldsymbol{x})$ denotes the time averaged u while the $u'(\boldsymbol{x},t)$ corresponds to the fluctuating part of the flow variable. The POD method proceeds in determining the base functions $\Phi_n(\boldsymbol{x})$ from data corresponding to the nature of the variable u to be approximated. For orthonormal bases:

$$\int_{\Omega} \Phi_{n_1}(\boldsymbol{x})\Phi_{n_2}(\boldsymbol{x})d\boldsymbol{x} = \delta_{n_1 n_2}$$

with $\delta_{n_1 n_2}$ the Kronecker symbol, the calculation of the time functions then follows as:

$$\alpha_n(t) = \int_{\Omega} u(\boldsymbol{x},t)\Phi_n(\boldsymbol{x})d\boldsymbol{x}$$

Searching for optimal basis functions is equivalent to solving the minimization problem:

$$min \left[\sum_{m=1}^{M} \left(||u(\boldsymbol{x},t_m) - \overline{u}(\boldsymbol{x}) - \sum_{n=2}^{N} \alpha_n(t_m)\Phi_n(\boldsymbol{x})||_2 \right)^2 \right] \tag{A.2}$$

for $M \geq N$ time instants, were $||\boldsymbol{y}||_2 = \sqrt{\boldsymbol{y}^T \boldsymbol{y}}$. In practice, the minimization problem is solved by constructing the following data matrix including K measurable locations:

$$A = \begin{bmatrix} u(x_1,t_1) & u(x_1,t_2) & \cdots & u(x_1,t_M) \\ u(x_2,t_1) & u(x_2,t_2) & \cdots & u(x_2,t_M) \\ \vdots & \vdots & \vdots & \vdots \\ u(x_K,t_1) & u(x_K,t_2) & \cdots & u(x_K,t_M) \end{bmatrix}$$

and then applying the truncated Singular Value Decomposition (SVD) of length N on the $A_{K\times M}$ matrix. The SVD is a factorization method that lets us write:

$$A = U\Sigma V^+ \tag{A.3}$$

with $U_{K\times K}$, $V_{M\times M}$ unitary matrices, V^+ the conjugate transpose of V [1] and $\Sigma_{K\times M}$ a diagonal matrix with the nonzero singular values $(\sigma_1,\ \sigma_2,\ ...,\ \sigma_R) \in \mathbb{R}$ of A on its diagonal. With $R = min(K,\ M)$, the first r columns of U are the left singular vectors of A and V the right ones. From Eq. A.3 we can write:

$$A^+A = V\Sigma U^+ U\Sigma V^+ = V\Sigma^2 V^+ = V\Lambda V^{-1}$$

with $\Lambda = diag(\lambda_i,\ \lambda_i,\ ...,\ \lambda_M)$ the eigenvalues of A^+A, or even:

$$AA^+ = U\Sigma V^+ V\Sigma U^+ = U\Sigma^2 U^+ = U\Lambda U^{-1}$$

with $\Lambda = diag(\lambda_i,\ \lambda_i,\ ...,\ \lambda_K)$ the eigenvalues of AA^+. The correspondance between the SVD method and an eigenvalue decomposition is straightforward with $\lambda_i^2 = \sigma_i$. In practice, solving the eigenvalue problem is generally prefered when dealing with problem where there is a big difference between the available time instants M and the spatial positions of measurements K.

A.1 POD formulation

The minimization problem of Eq. A.2 can be expressed as follows:

$$max\left[\frac{<(\mathbf{u},\ \boldsymbol{\Psi})^2>}{|\boldsymbol{\Psi}|^2}\right] \quad \text{for } \boldsymbol{\Psi} \in L^2(D) \tag{A.4}$$

with the constraint:

$$|\boldsymbol{\Psi}|^2 = 1 \tag{A.5}$$

were we look for the function that maximizes the mean square projection on the observations, i.e. the function that best correlates with the measurements $\boldsymbol{u}(\boldsymbol{X})$ with $\boldsymbol{X} = (\boldsymbol{x},t) \in D = \mathbb{R}^3 \times \mathbb{R}^+$. The brackets $< . >$ denote a - case dependent -

[1] for $A \in \mathbb{R}$, unitary matrices are orthogonal matrices, i.e. $V^+ = V^{-1} = V^T$

averaging procedure. The space $L^2(D)$ is the collection of all square integrable functions[2] in D. For real functions, the L^2-inner product is defined as:

$$(\boldsymbol{u},\ \boldsymbol{v}) = \int_D \boldsymbol{u}(\boldsymbol{X}) \cdot \boldsymbol{v}(\boldsymbol{X}) d\boldsymbol{X}$$

and the L^2-norm as:

$$|\boldsymbol{u}|^2 = (\boldsymbol{u},\ \boldsymbol{u})$$

We introduce the operator $\mathscr{R} : L^2(D) \mapsto L^2(D)$ as:

$$\mathscr{R}\boldsymbol{\Psi} = \int_D \bar{R}(\boldsymbol{X},\boldsymbol{X'})\boldsymbol{\Psi}(\boldsymbol{X'}) d\boldsymbol{X'}$$

where

$$\bar{R}(\boldsymbol{X},\boldsymbol{X'}) =< \boldsymbol{u}(\boldsymbol{X})\boldsymbol{u}^T(\boldsymbol{X'}) >$$

We calculate:

$$\begin{aligned}
(\mathscr{R}\boldsymbol{\Psi},\ \boldsymbol{\Psi}) &= \left(\textstyle\int_D \bar{R}(\boldsymbol{X},\boldsymbol{X'})\boldsymbol{\Psi}(\boldsymbol{X'}) d\boldsymbol{X'},\ \boldsymbol{\Psi}(\boldsymbol{X})\right) \\
&= \textstyle\int_D < \boldsymbol{u}(\boldsymbol{X}) \int_D \boldsymbol{u}^T(\boldsymbol{X'})\boldsymbol{\Psi}(\boldsymbol{X'}) d\boldsymbol{X'} > \cdot \boldsymbol{\Psi}(\boldsymbol{X}) d\boldsymbol{X} \\
&= < \textstyle\int_D \boldsymbol{u}(\boldsymbol{X'}) \cdot \boldsymbol{\Psi}(\boldsymbol{X'}) d\boldsymbol{X'} \int_D \boldsymbol{u}(\boldsymbol{X}) \cdot \boldsymbol{\Psi}(\boldsymbol{X}) d\boldsymbol{X} > \\
&= < (\mathbf{u},\ \boldsymbol{\Psi})^2 >
\end{aligned}$$

were we suppode that the averaging and the integration are interchangeable. It is obvious that the maximation problem of Eq. A.4 can be rewritten as:

$$max \left[\frac{(\mathscr{R}\boldsymbol{\Psi},\ \boldsymbol{\Psi})}{|\boldsymbol{\Psi}|^2} \right] = \lambda$$

which can be solved via an equivalent eigenvalue problem:

$$\mathscr{R}\boldsymbol{\Psi} = \lambda \boldsymbol{\Psi}$$

or, as a discrete set of equations in 3D:

$$\sum_{j=1}^{3} \int_D R_{ij}(\boldsymbol{X},\boldsymbol{X'})\Psi_j^{(n)}(\boldsymbol{X'}) d\boldsymbol{X'} = \lambda^{(n)}\Psi_i^{(n)}(\boldsymbol{X}) \tag{A.6}$$

with $n = 1,\ 2,\ ...,\ N_{POD}$ the number of the POD eigenvalues/vectors. The eigenfunctions are orthogonal to one another but can be also chosen orthonormal:

$$\sum_{i=1}^{3} \int_D \Psi_i^{(n)}(\boldsymbol{X'})\Psi_i^{(m)}(\boldsymbol{X'}) d\boldsymbol{X'} = \delta_{nm}$$

[2]This is particularly interesting in the cntext of fluid mechanics as the kinetic energy should be finite.

Among all linear decompositions, the POD is the most efficient as it will always contain the most information for a given number of modes. The truncation error ε for using N_C out of the N_{POD} basis function, can be calculated as:

$$\varepsilon = ||\boldsymbol{u}(\boldsymbol{X}) - \sum_{n=1}^{N_C} (\boldsymbol{u}(\boldsymbol{X}),\, \boldsymbol{\Psi}^{(n)}(\boldsymbol{X}))\boldsymbol{\Psi}^{(n)}(\boldsymbol{X})||^2 = ||\sum_{n=N_C+1}^{N_{POD}} (\boldsymbol{u}(\boldsymbol{X}),\, \boldsymbol{\Psi}^{(n)}(\boldsymbol{X}))\boldsymbol{\Psi}^{(n)}(\boldsymbol{X})||^2$$

with $N_C < N_{POD}$. In practice, the accumulated error can be estimated from the percentage of the energy contained in the N_C modes from the ratio:

$$\frac{\sum_{n=1}^{N_C} \lambda^{(n)}}{\sum_{n=1}^{N_{POD}} \lambda^{(n)}}$$

As R is a self-adjoint non negative matrix, all its eigenvalues $\lambda^{(n)}$ are real and positive and the total energy is bounded:

$$\sum_{n=1}^{N_{POD}} \lambda^{(n)} < +\infty \tag{A.7}$$

A.1.1 Direct POD

We will apply a temporal averaging of the results. This will lead to a spatial correlation matrix. We will examine the procedure for a one-dimentional domain. Let us set in the previous $\boldsymbol{X} = (x,t)$ with $x \in \Omega = \mathbb{R}$. The two point spatial correlation tensor is defined as:

$$R(x,x') = \frac{1}{T}\int_T \bar{u}(x,t)\bar{u}^T(x',t)dt = \frac{\Delta t}{T}\sum_{m=1}^{M} \boldsymbol{u}(x,t_m)\boldsymbol{u}^T(x',t_m)$$

$$R_{ij} = \frac{1}{M}\sum_{m=1}^{M} u(x_i,t_m)u(x'_j,t_m) = \frac{1}{M}\sum_{m=1}^{M} u_i(t_m)u_j(t_m)$$

with M the total number of time steps and $\boldsymbol{u}^T(x,t_m) = [u_1(t_m)\ \ u_2(t_m)\ \ \ldots\ \ u_K(t_m)]$ the matrix containing the scalar value field u for the all domain points K at a time step. The system of equations A.6 can be written:

$$\frac{1}{K}\sum_{k=1}^{K} R_{ij}\Psi_j^{(n)} = \lambda^{(n)}\Psi_i^{(n)}$$

$$\bar{C}\boldsymbol{\Psi}^{(n)} = \lambda^{(n)}\boldsymbol{\Psi}^{(n)}$$

with $\boldsymbol{\Psi}^{(n)}$ the n^{th} eigenfunction, i.e. the n^{th} proper purely spatial mode, and $\bar{C}$ the tensor:

$$C_{ij} = \frac{1}{KM}\sum_{m=1}^{M} u_i(t_m)u_j(t_m)$$

The spatial eigenfunctions result from the complete set of eigenvectors of $\bar{C}$. If the velocity field is used to construct the spatial correlation matrix then the total energy given from Eq. A.7 corresponds to the turbulent kinetic energy integrated over the flow domain. This also justifies choosing to work in the L^2-space for the derivations presented up to now.

A.1.2 Snapshot POD

If we are working with a number of time steps $M << K$ that are however adequate in describing the process[3], we can alter the method presented in the previous section so as to work on an eigenvalue problem of size M. The snapshot POD method introduces a space averaging procedure over the domain Ω. Same as before, the two point spatial correlation is written:

$$R(x,x') = \frac{1}{M}\sum_{m=1}^{M} \boldsymbol{u}(x,t_m)\boldsymbol{u}^T(x',t_m)$$

Since:

$$\boldsymbol{\Psi}^{(n)}(x) = \bar{u}(x,t)\boldsymbol{a}^{(n)}(t)$$

$$\Psi_i^{(n)} = \sum_{m=1}^{M} a^{(n)}(t_m)u(x_i,t_m)$$

the set of equations A.6 can be expressed as:

$$\sum_{j=1}^{N}\left[\frac{1}{M}\sum_{m=1}^{M}\left(\int_\Omega \boldsymbol{u}(x,t_m)\boldsymbol{u}^T(x,t_j)dx\right)a(t_m)\right]u(x_i,t_j) = \lambda^{(n)}\sum_{m=1}^{M} a^{(n)}(t_m)u(x_i,t_m)$$

It suffices that for each coefficient it stands:

$$\frac{1}{M}\sum_{m=1}^{M}\left(\int_\Omega \boldsymbol{u}(x,t_m)\boldsymbol{u}^T(x,t_j)dx\right)a(t_m) = \lambda^{(n)}a^{(n)}(t_j)$$

$$\bar{C}\boldsymbol{V}^{(n)} = \lambda^{(n)}\boldsymbol{V}^{(n)}$$

with $\boldsymbol{V}^{(n)} = [a^{(n)}(t_1)\ \ a^{(n)}(t_2)\ \ \ldots\ \ a^{(n)}(t_M)]^T$ and $\bar{C}$ the tensor:

$$C_{ij} = \frac{1}{KM}\sum_{k=1}^{M} u_k(t_i)u_k(t_j)$$

Same as before, all the $\boldsymbol{V}^{(n)}$ vectors containing the temporal coefficients come from the eigenvectors of matrix $\bar{C}$. Due to the orthogonality of the vectors:

$$\frac{1}{M}\sum_{m=1}^{M} a^{(n)}(t_m)a^{(l)}(t_m) = \lambda^{(n)}\delta_{nl} \tag{A.8}$$

[3]This could be easily seen for a periodic phenomenon as enough points per period and sufficient number of periods captured.

The spatial eigenfunctions can be calculated from:

$$\boldsymbol{\Psi}^{(n)}(x) = \frac{1}{M\lambda^{(n)}} \sum_{m=1}^{M} a^{(n)}(t_m)\boldsymbol{u}(x,t_m) \tag{A.9}$$

that are also orthonormal.

Bibliography

[BHL93] G. Berkooz, P. Holmes, and J. L. Lumley. The Proper Orthogonal Decomposition in the Analysis of Turbulent Flows. *Annual Review of Fluid Mechanics*, 25(1):539–575, 1993.

[Kar46] K. Karhunen. Zur spektraltheorie stochastischer prozesse. In *Ann. Acad. Sci. Fennicae Ser. A1*, volume 34, 1946.

[Loè45] M. Loève. Fonctions aleatoires de second ordre. *Comptes Rendus De L'Académie Des Sciences*, 220:105035, 1945.

[Lum67] J. L. Lumley. The structure of inhomogeneous turbulence. In *Atmospheric Turbulence and Wave Propagation, Nauka, Moscow*, pages 166–178, 1967.

Appendix B. Jacobian matrices, eigenvalues and eigenvectors

B.1 Inviscid Jacobian

The three inviscid Jacobian matrices:

$$\tilde{A} = \frac{\partial f}{\partial W} \ , \ \tilde{B} = \frac{\partial g}{\partial W} \ , \ \tilde{C} = \frac{\partial h}{\partial W}$$

are given by:

$$\tilde{A} = \begin{bmatrix} 0 & 1 & 0 & 0 & 0 \\ -u^2 + \frac{\gamma-1}{2}\vec{u}^2 & (3-\gamma)u & -(\gamma-1)v & -(\gamma-1)w & \gamma-1 \\ -uv & v & u & 0 & 0 \\ -uw & w & 0 & u & 0 \\ -u[\gamma E - (\gamma-1)\vec{u}^2] & \gamma E - \frac{\gamma-1}{2}(\vec{u}^2 + 2u^2) & -(\gamma-1)uv & -(\gamma-1)uw & \gamma u \end{bmatrix}$$

$$\tilde{B} = \begin{bmatrix} 0 & 0 & 1 & 0 & 0 \\ -uv & v & u & 0 & 0 \\ -u^2 + \frac{\gamma-1}{2}\vec{u}^2 & -(\gamma-1)u & (3-\gamma)v & -(\gamma-1)w & \gamma-1 \\ -vw & 0 & w & v & 0 \\ -v[\gamma E - (\gamma-1)\vec{u}^2] & -(\gamma-1)uv & \gamma E - \frac{\gamma-1}{2}(\vec{u}^2 + 2v^2) & -(\gamma-1)vw & \gamma v \end{bmatrix}$$

$$\tilde{C} = \begin{bmatrix} 0 & 0 & 0 & 1 & 0 \\ -uw & w & 0 & u & 0 \\ -vw & 0 & w & v & 0 \\ -w^2 + \frac{\gamma-1}{2}\vec{u}^2 & -(\gamma-1)u & -(\gamma-1)v & (3-\gamma)w & \gamma-1 \\ -w[\gamma E - (\gamma-1)\vec{u}^2] & -(\gamma-1)uw & -(\gamma-1)vw & \gamma E - \frac{\gamma-1}{2}(\vec{u}^2 + 2w^2) & \gamma w \end{bmatrix}$$

The inviscid Jacobian matrix is then calculated at a cell face as: $A_c = \tilde{A}S_x + \tilde{B}S_y + \tilde{C}S_z$, with $\vec{S}$ the cell surface vector. The Jacobian can then be diagonalized as:

$\Lambda = T^{-1}AT$, where Λ the diagonal matrix of the eigenvalues:

$$\Lambda = \begin{bmatrix} \vec{u}\cdot\vec{S} & \cdot & \cdot & \cdot & \cdot \\ \cdot & \vec{u}\cdot\vec{S} & \cdot & \cdot & \cdot \\ \cdot & \cdot & \vec{u}\cdot\vec{S} & \cdot & \cdot \\ \cdot & \cdot & \cdot & \vec{u}\cdot\vec{S}+c||\vec{S}||_2 & \cdot \\ \cdot & \cdot & \cdot & \cdot & \vec{u}\cdot\vec{S}-c||\vec{S}||_2 \end{bmatrix}$$

with c the speed of sound. The left eigenvector with respect to the primitive variables is given from:

$$T_p^{-1} = \begin{bmatrix} 1 & 0 & 0 & 0 & -1/c^2 \\ 0 & h_x & h_y & h_z & 0 \\ 0 & t_x & t_y & t_z & 0 \\ 0 & n_x & n_y & n_z & 1/(\rho c) \\ 0 & -n_x & -n_y & -n_z & 1/(\rho c) \end{bmatrix}$$

and the right eigenvector:

$$T_p = \begin{bmatrix} 1 & 0 & 0 & \rho/(2c) & \rho/(2c) \\ 0 & h_x & t_x & n_x/2 & -n_x/2 \\ 0 & h_y & t_y & n_y/2 & -n_y/2 \\ 0 & h_z & t_z & n_z/2 & -n_z/2 \\ 0 & 0 & 0 & \rho c/2 & \rho c/2 \end{bmatrix}$$

The unit vectors $\vec{h}$ and $\vec{t}$ are chosen such as they form an orthonormal basis with the surface normal vector $\vec{n}$. They are given from:

$$\vec{h} = \frac{1}{\sqrt{n_y^2+n_z^2}} \begin{Bmatrix} 0 \\ -n_z \\ n_y \end{Bmatrix} \text{ and } \vec{t} = \frac{1}{\sqrt{n_y^2+n_z^2}} \begin{Bmatrix} n_y^2+n_z^2 \\ -n_x n_y \\ -n_x n_z \end{Bmatrix}$$

if $|n_z| > 0.7$, and from:

$$\vec{h} = \frac{1}{\sqrt{n_x^2+n_y^2}} \begin{Bmatrix} n_y \\ -n_z \\ 0 \end{Bmatrix} \text{ and } \vec{t} = \frac{1}{\sqrt{n_x^2+n_y^2}} \begin{Bmatrix} -n_x n_z \\ -n_z n_y \\ n_x^2+n_y^2 \end{Bmatrix}$$

if $|n_z| \leq 0.7$, to avoid division by zero. The left and right eigenvectors with respect to the conservative variables are obtained from:

$$T^{-1} = T_p^{-1}M^{-1} \text{ and } T^{-1} = MT_p$$

where the transformation matrices are given from:

$$M^{-1} = \begin{bmatrix} 1 & 0 & 0 & 0 & 0 \\ -u/\rho & 1/\rho & 0 & 0 & 0 \\ -v/\rho & 0 & 1/\rho & 0 & 0 \\ -w/\rho & 0 & 0 & 1/\rho & 0 \\ (\gamma-1)\vec{u}^2/2 & -(\gamma-1)u & -(\gamma-1)v & -(\gamma-1)w & \gamma-1 \end{bmatrix}$$

and

$$M = \begin{bmatrix} 1 & 0 & 0 & 0 & 0 \\ u & \rho & 0 & 0 & 0 \\ v & 0 & \rho & 0 & 0 \\ w & 0 & 0 & \rho & 0 \\ \vec{u}^2/2 & \rho u & \rho v & \rho w & 1/(\gamma-1) \end{bmatrix}$$

B.2 Viscous Jacobian

The three viscous Jacobian matrices with respect to the primitive variables:

$$\tilde{A}_v = \frac{\partial f_v}{\partial W_p} \ , \ \tilde{B}_v = \frac{\partial g_v}{\partial W_p} \ , \ \tilde{C}_v = \frac{\partial h_v}{\partial W_p}$$

are given by:

$$\tilde{A}_v = \begin{bmatrix} 0 & 0 & 0 & 0 & 0 \\ 0 & 4\mu S_x/3 & \mu S_y & \mu S_z & 0 \\ 0 & -2\mu S_y/3 & \mu S_x & 0 & 0 \\ 0 & -2\mu S_z/3 & 0 & \mu S_x & 0 \\ -kTS_x\rho & 2\mu(2uS_x - vS_y - wS_z)/3 & \mu(vS_x + uS_y) & \mu(wS_x + uS_z) & kTS_x/p \end{bmatrix}$$

$$\tilde{B}_v = \begin{bmatrix} 0 & 0 & 0 & 0 & 0 \\ 0 & \mu S_y & -2\mu S_x/3 & 0 & 0 \\ 0 & \mu S_x & 4\mu S_y/3 & \mu S_z & 0 \\ 0 & 0 & -2\mu S_z/3 & \mu S_y & 0 \\ -kTS_y\rho & \mu(vS_x + uS_y) & 2\mu(2vS_y - uS_x - wS_z)/3 & \mu(wS_y + vS_z) & kTS_y/p \end{bmatrix}$$

$$\tilde{C}_v = \begin{bmatrix} 0 & 0 & 0 & 0 & 0 \\ 0 & \mu S_z & 0 & -2\mu S_x/3 & 0 \\ 0 & 0 & \mu S_z & -2\mu S_y/3 & 0 \\ 0 & \mu S_x & \mu S_y & 4\mu S_z/3 & 0 \\ -kTS_z\rho & \mu(wS_x + uS_z) & \mu(wS_y + vS_z) & 2\mu(2wS_z - vS_y - uS_x)/3 & kTS_z/p \end{bmatrix}$$

When turbulence modelling is intreoduced in the simulations, the eddy viscosity μ_t and the turbulent conductivity k_t are added to the molecular ones.